Detection and Differentiation of Supercooled Large Droplet Icing Conditions
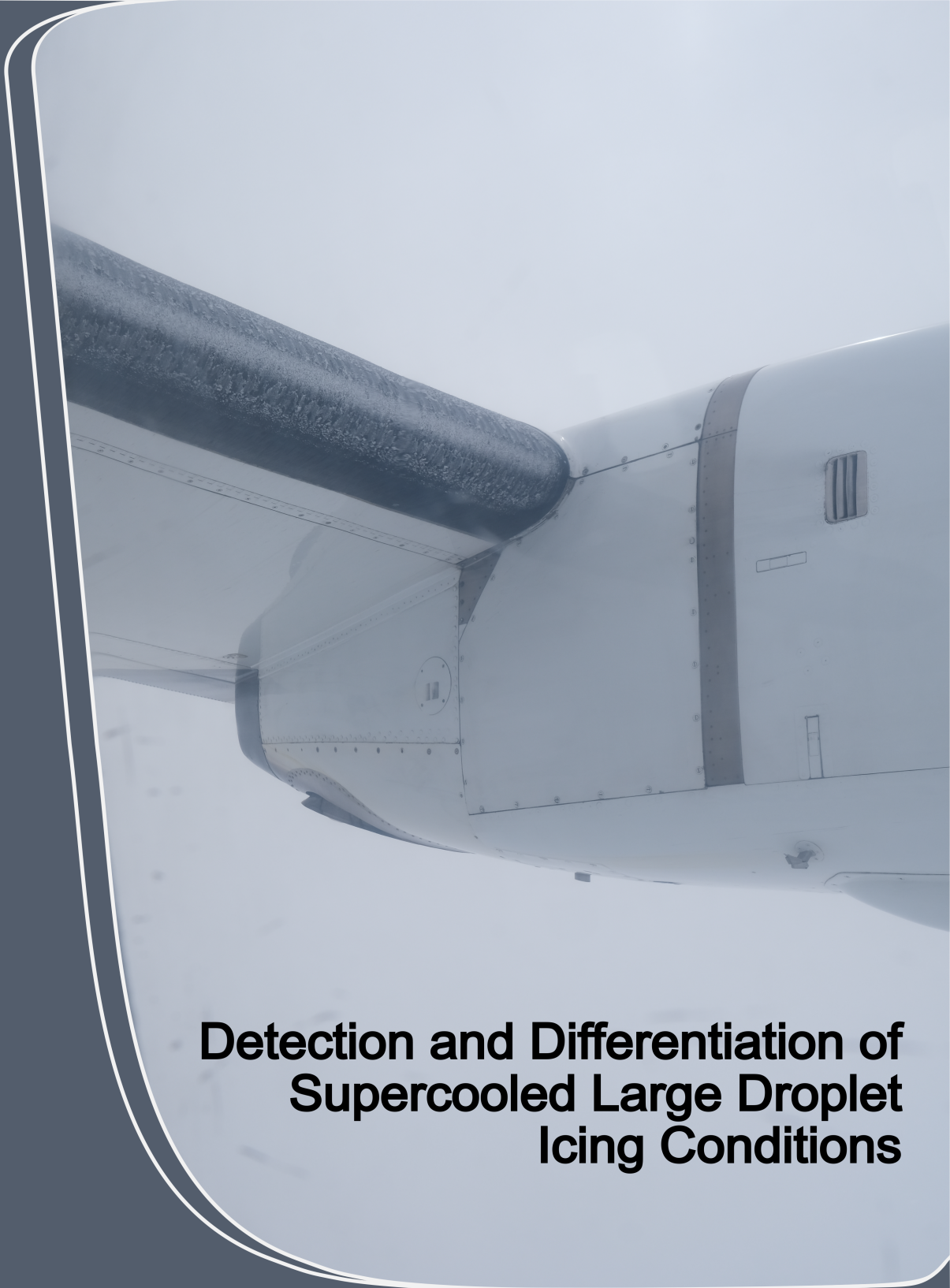
Johannes Lucke

Detection and Differentiation of Supercooled Large Droplet Icing Conditions Johannes Lucke

DETECTION AND DIFFERENTIATION OF SUPERCOOLED LARGE DROPLET ICING CONDITIONS

Dissertation

for the purpose of obtaining the degree of doctor
at Delft University of Technology
by the authority of the Rector Magnificus Prof. dr.ir. T.H.J.J. van der Hagen,
Chair of the Board for Doctorates
to be defended publicly on Monday, 14 October 2024 at 15:00 o'clock

by

Johannes Reinhard LUCKE

Master of Science in Earth Oriented Space Science and Technology
Technical University of Munich, Germany,

born in Berlin, Germany.

This dissertation has been approved by:

promotor: Prof. dr. V. Grewe
promotor: Prof. dr. C. Voigt

Composition of the doctoral committee:

Rector Magnificus,	chairperson
Prof. dr. V. Grewe,	Delft University of Technology
Prof. dr. C. Voigt,	Johannes Gutenberg University Mainz

Independent members:

Prof. dr. M. Kotsonis,	Delft University of Technology
Prof. dr. J. Teuwen,	Delft University of Technology
Dr. H. Jentink,	Netherlands Aerospace Center
Prof. dr. M. R. K. Frövel,	Instituto Nacional de Técnica Aeroespacial
Prof. dr. M. Snellen,	Delft University of Technology (*reserve member*)

Additional members:

Dr. Tina Jurkat-Witschas,	Deutsches Zentrum für Luft- und Raumfahrt

Keywords:	Supercooled large droplets, Atmospheric Icing conditions,
Front & Back:	Front: Ice accretion observed on the ATR-42 aircraft of the French facility for airborne research (SAFIRE). Back: Scientific instruments aboard the SAFIRE ATR-42. Both images were taken during the European SENS4ICE flight campaign. Photo credit: Deniz Menekay.

CONTENTS

SUMMARY

Icing conditions that contain supercooled large droplets (SLDs) represent a hazard for aviation. Due to their large inertia, SLDs impact behind the extent of aircraft ice protection systems where the developing ice accretion cannot be removed. At present, aircraft that are vulnerable to SLD icing need to avoid severe icing conditions in general, leading to increased operating costs. New American and European aviation regulations allow the passage through such conditions if the aircraft carries instruments that can detect the presence of SLDs. Upon detection, the pilots can exit the icing cloud before the situation becomes hazardous.

The mass of liquid water contained in an SLD is several orders of magnitude higher than the mass contained in a typical small cloud droplet. However, the number concentration of SLDs is much lower than that of small cloud droplets, consequently, it is challenging to detect SLDs with instruments. As of now, no instruments for the detection of SLD icing conditions are in use on commercial aircraft.

This thesis investigates a combination of two instruments for the detection of SLD icing conditions. The first instrument is the Nevzorov probe for the measurement of liquid and total water content and the second instrument is the Backscatter Cloud Probe with Polarization Detection (BCPD), a non-invasive laser backscatter probe that measures the size and shape of cloud particles between 2 and 42 µm. The Nevzorov probe used in this work carried a new, 12 mm diameter total water content sensor that was added to the instrument specifically for the measurement of SLD icing conditions. Both instruments, the Nevzorov probe and the BCPD, are first analyzed individually in icing wind tunnel tests. The findings from the tests show that the new 12 mm sensor of the Nevzorov probe captures SLDs effectively. No indication was found of SLD being incompletely evaporated due to splashing or of water being swept out of the cone. The collision efficiency of small droplets with the sensor is low and can be compensated with a correction derived in this work. Intensive atmospheric testing ensued the icing wind tunnel measurements. During measurements in Arctic clouds, it could be shown that the fraction of liquid and glaciated particles can be estimated from the BCPD. Measurements in the South of France were able to demonstrate that the detection and discrimination of SLD icing conditions is possible with the Nevzorov probe and the BCPD for SLD icing encounters that are sufficiently long and contain a high number of SLDs.

The results of this work allow future flight campaigns to use the 12 mm sensor of the Nevzorov probe and benefit from its capture efficiency and better sampling statistics. The comparisons of the Nevzorov probe to other instruments can help scientists choose suitable instrumentation for future icing wind tunnel and flight campaigns. Concerning the BCPD, a new method developed in this thesis to estimate the number of ice and water particles could, with small modifications, also

be employed for other instruments that use polarization filters. For the detection and discrimination of SLD conditions, future work should focus on extending the sample area of the BCPD further outward from the aircraft skin to measure particle size distributions that are unaffected by the aircraft boundary layer. Furthermore, the false alarm rate of the system could be reduced by incorporating an instrument similar to the BCPD but with a larger size range and larger sample area for the direct detection of SLDs.

SAMENVATTING

IJsvorming met onderkoelde grote druppels (SLD's) vormt een gevaar voor de luchtvaart. Door hun grote traagheid komen SLD's achter de ijsbeschermingssystemen van vliegtuigen terecht, waar de zich ontwikkelende ijsafzetting niet verwijderd kan worden. Momenteel moeten vliegtuigen die kwetsbaar zijn voor SLD-ijsvorming ernstige ijsvorming in het algemeen vermijden, wat leidt tot hogere bedrijfskosten. Nieuwe Amerikaanse en Europese luchtvaartreglementen staan de passage door dergelijke omstandigheden toe als het vliegtuig instrumenten aan boord heeft die de aanwezigheid van SLD's kunnen detecteren. Na detectie kunnen de piloten de ijswolk verlaten voordat de situatie gevaarlijk wordt.

De massa vloeibaar water in een SLD is enkele orden van grootte groter dan de massa in een typische kleine wolkendruppel. De concentratie van het aantal SLD's is echter veel lager dan die van kleine wolkendruppeltjes, waardoor het een uitdaging is om SLD's met instrumenten te detecteren. Op dit moment worden er nog geen instrumenten voor de detectie van SLD-ijsvorming gebruikt in commerciële vliegtuigen.

Deze dissertatie onderzoekt een combinatie van twee instrumenten voor de detectie van SLD-ijsvorming. Het eerste instrument is de Nevzorov sonde voor het meten van het vloeibare en totale watergehalte en het tweede instrument is de Backscatter Cloud Probe with Polarization Detection (BCPD), een niet-invasieve laser backscatter sonde die de grootte en vorm van wolkdeeltjes tussen 2 en 42 μm meet. De Nevzorov sonde die in dit werk werd gebruikt, had een nieuwe sensor voor de totale waterinhoud met een diameter van 12 mm die speciaal aan het instrument was toegevoegd voor het meten van SLD ijsvorming. Beide instrumenten, de Nevzorov sonde en de BCPD, zijn eerst afzonderlijk geanalyseerd in windtunneltests bij ijsvorming. De resultaten van de tests laten zien dat de nieuwe 12 mm sensor van de Nevzorov sonde SLD's effectief vastlegt. Er zijn geen aanwijzingen gevonden dat SLD's onvolledig verdampt zijn door spatten of dat water uit de kegel wordt geveegd. De botsingsefficiëntie van kleine druppeltjes met de sensor is laag en kan worden gecompenseerd met een in dit werk afgeleide correctie. Na de ijsvormingmetingen in de windtunnel werden intensieve atmosferische tests uitgevoerd. Tijdens metingen in Arctische wolken kon worden aangetoond dat de fractie vloeibare en geglazuurde deeltjes kan worden geschat uit de BCPD. Metingen in Zuid-Frankrijk toonden aan dat de detectie en het onderscheid van SLD ijsvorming mogelijk is met de Nevzorov sonde en de BCPD voor SLD ijsvorming ontmoetingen die lang genoeg zijn en een hoog aantal SLD's bevatten.

De resultaten van dit werk stellen toekomstige vluchtcampagnes in staat om de 12 mm sensor van de Nevzorov sonde te gebruiken en te profiteren van zijn vangstefficiëntie en betere bemonsteringsstatistieken. De vergelijkingen van de Nevzorov sonde met andere instrumenten kunnen wetenschappers helpen om geschikte in-

strumenten te kiezen voor toekomstige windtunnel- en vluchtcampagnes met ijs-vorming. Wat de BCPD betreft, zou een nieuwe methode die in dit proefschrift ontwikkeld is om het aantal ijs- en waterdeeltjes te schatten, met kleine aanpassin-gen ook gebruikt kunnen worden voor andere instrumenten die polarisatiefilters gebruiken. Voor de detectie en discriminatie van SLD-condities moet toekomstig werk zich richten op het uitbreiden van het monstergebied van de BCPD verder buiten de vliegtuighuid om deeltjesgrootteverdelingen te meten die niet beïnvloed worden door de grenslaag van het vliegtuig. Verder zou het percentage valse alar-men van het systeem kunnen worden verlaagd door een instrument in te bouwen dat vergelijkbaar is met de BCPD, maar met een groter deeltjesgroottebereik en een groter monstergebied voor de directe detectie van SLD's.

1

INTRODUCTION

Atmospheric icing conditions are known to be hazardous to aircraft since the advent of aviation. Despite enormous improvements in the safety of flight over the last decades, icing conditions still contributed to 11% of all fatal aviation accidents of commercial airliners in the period from 2017-2021. Furthermore, icing conditions were an underlying cause in 21% of the in-flight loss of control events that resulted in accidents [1].

Two types of icing conditions can be differentiated: Ice crystal icing and icing from supercooled cloud droplets. The former occurs most often in the upper troposphere at the outflow of convective systems and is especially relevant for aircraft engines and sensors, such as pitot tubes. Blockage of a pitot tube by ice crystals was for instance a contributing factor to the crash of Air France flight 447 over the Atlantic in 2009 [2]. This thesis deals with the latter type, the icing by supercooled cloud droplets. Such icing conditions occur predominantly in low-level clouds where temperatures are slightly below the freezing level. When an aircraft passes through a cloud that contains supercooled droplets, these droplets freeze on impact with the airframe, causing ice accretion. Ice may form on all surfaces that are exposed to the airflow, but accretion on the wings and the control surfaces is especially critical. Among the adverse effects evoked by ice accretion are lower lift, higher drag, higher stall speed and larger fuel consumption [3].

To mitigate these effects, most modern aircraft are equipped with ice protection systems. An image of an ice protection system can be seen in Fig. 1.1. Ice protection systems usually only extend up to the first few percent of the wing chord, while further aft parts of the wing are unprotected. This design is based on certification regulations that resulted from a large number of research, commercial and military flights in icing conditions between the 1940s and 1960s [4]. The regulations recommended that the extent of the ice protection system be determined from the impingement limits of 40 µm diameter droplets, the largest droplet diameter that was expected to be encountered in flight [5]. The largest droplets are critical due to their large inertia, which causes them to be relatively unaffected by drag forces

Figure 1.1: Ice protection system on the wing of the Polar-6 aircraft of Alfred-Wegener Institute. Image courtesy of Christof Lüpkes.

that exist around the wing. Smaller droplets, on the other hand, only impinge close to the leading edge or else are swept around the wing by the airflow.

Concerns that the focus on droplet sizes below 40 μm might be insufficient arose in the 1980s, when Sand *et al.* [6] and Cooper *et al.* [7] reported icing conditions where droplets with diameters as large as 300 μm were encountered. In October 1994 American Eagle flight 4184 crashed with the loss of life of all 68 occupants on board. The subsequent investigation suggested that the aircraft had flown through icing conditions which contained supercooled large droplets (SLDs), i.e. droplets with a diameter larger than 100 μm, prior to the crash [8]. The icing conditions resulted in a ridge of ice behind the extent of the ice protection system, which eventually caused an aileron hinge moment reversal that resulted in a sharp roll and sent the aircraft into a dive toward the ground [9].

The crash initiated numerous scientific flight campaigns aimed at establishing the microphysical properties of SLD icing conditions and understanding their formation process [10]. It was discovered that SLDs occur most of the time in combination with a large number of cloud droplets with ordinary diameters between 10-40 μm. The overall droplet size distribution (DSD) of SLD conditions is consequently very broad. Furthermore, SLD icing conditions are associated with relatively low liquid water contents (LWCs) of about 0.1 to 0.4 $\mathrm{g\,m^{-3}}$.

After the completion of the flight activities, researchers and regulation authorities set out to translate the gained knowledge into a standard that could be used for aircraft certification. This standard was added as Appendix O to American and European aviation regulations in 2014 and 2015, respectively [11, 12]. The SLD icing conditions specified in the standard are therefore referred to as Appendix O conditions.

The new regulations leave aircraft manufacturers with several possible choices regarding the certification of new aircraft. First of all, aircraft manufacturers can

choose not to certify their aircraft for flight in Appendix O conditions. As it is difficult to forecast which icing conditions are Appendix O conditions, this essentially means that the aircraft has to avoid most, if not all icing conditions. This represents a competitive disadvantage for the aircraft type.

Secondly, aircraft manufacturers can attempt to prove that their aircraft can safely operate in the entire scope of Appendix O. Certain aircraft models may not be adversely affected by Appendix O conditions due to their design, such that operational safety is automatically given. Furthermore, aircraft manufacturers could make provisions against Appendix O icing, such as increasing the extent of the ice protection system. This would involve significant changes to the layout of the wing and make the aircraft heavier.

As a third option, aircraft manufacturers may incorporate instruments in the aircraft that are able to detect Appendix O conditions. In this case, it is sufficient to show that the aircraft is capable of flying in Appendix O conditions until these are detected, including a safety margin that allows the aircraft to escape safely from the icing conditions. Alternatively, aircraft manufacturers may also certify their aircraft for a portion of Appendix O, if they incorporate instruments that assess the severity of the icing conditions [11]. The use of instruments for the detection and discrimination of Appendix O conditions is an attractive option for aircraft that are severely affected by Appendix O conditions and where no design changes can be made to the ice protection system. From a sustainability perspective, real-time assessments of the severity of icing conditions are also favorable, because they open the possibility to probe the icing conditions instead of extensively re-routing aircraft around regions with an icing risk.

The work presented in this thesis was performed as part of the activities of the German Aerospace Center (DLR) within the EU project «SENSors and certifiable hybrid architectures for safer aviation in ICing Environment» (SENS4ICE) [13]. The SENS4ICE project aims to address the above-mentioned issue, the detection and discrimination of Appendix O conditions. The project strives to detect and discriminate icing conditions with a hybrid system [14] that consists of sensors for the direct measurement of droplet size or ice accretion and an indirect system that analyzes the aircraft performance to detect ice accretion [15]. The sensors and the hybrid system are tested in relevant icing conditions in an airborne demonstration [16]. The focus of this thesis is on the direct sensors, therefore the indirect system is disregarded in the remainder of this work.

The SENS4ICE consortium includes also icing wind tunnel (IWT) operators that provided their facilities for the testing of the sensors under development. Because Appendix O is a new addition to the certification specifications, IWTs only recently began to upgrade their facilities for the production of Appendix O conditions [18]. Creating realistic Appendix O conditions in IWTs is a challenge of its own that is discussed in Chapter 2. Moreover, no dedicated instruments exist for the measurement of the LWCs and DSDs of Appendix O conditions yet. Currently used instrumentation usually covers only a certain size range of the Appendix O spectrum or has large uncertainties pertaining to either the measurement of the small or the large droplets.
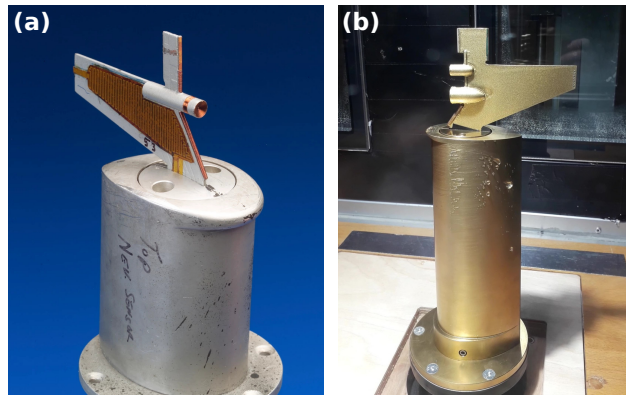
Figure 1.2: Nevzorov probes with the classical (**a**) and the new (**b**) sensor head. Image (**a**) from [17].

However, several instruments were newly devised or upgraded in recent years to allow for the measurement of Appendix O conditions. The established Nevzorov probe [19–21], an instrument for measuring LWC and total water content (TWC) was equipped with a second, larger TWC cone specifically for collecting SLDs (see Fig. 1.2). My first research question concerns this additional cone:

> ## Research question I
>
> How well is the Nevzorov 12 mm Total Water Content collector cone suited for the measurement of supercooled large droplet conditions and how does it compare to other liquid water content instruments?

The Nevzorov 12 mm cone would be perfectly suited for the measurement of SLD conditions if its measurements yielded the true LWC under all possible SLD conditions. Naturally, this is not the case, for instance, due to drag forces in the vicinity of the sensor not all droplets upstream of the sensor actually impact on it. The collision efficiency of droplets is therefore smaller than 1. Furthermore, the possibility exists that large droplets splash on the sensor and are only partially collected. To assess the magnitude of these effects and to evaluate the suitability of the 12 mm cone for measurements in SLD conditions, the Nevzorov probe was tested in three different IWTs. I compare the LWC measured by the new Nevzorov cone to measurements of other instruments. From the comparison, I experimentally derive the collision efficiency of small droplets with the 12 mm cone and assess its ability to capture and retain SLDs.

My second research question concerns another in-situ instrument, the Backscatter Cloud Probe with Polarization Detection (BCPD). The BCPD measures the size of droplets with diameters from 2-42 μm, but not SLDs. The main advantage of the BCPD is that it can be integrated into the fuselage of aircraft and does not protrude

outwards. Unlike underwing probes, which are commonly used during scientific flight campaigns, the BCPD does not cause any additional drag to aircraft.

Furthermore, the BCPD measures the depolarization of the backscattered light. The depolarization differs depending on the shape of the particles. The measurement of depolarization is therefore especially relevant for the differentiation between droplets and ice particles. While methods were developed to separate spherical and aspherical particles from depolarization measurements of some scientific airborne instruments [22–24], no such methods exist as of now for the BCPD.

The BCPD is a new instrument that has not been described in the literature yet, and no comparisons to other scattering probes exist. In the scope of this thesis, it is deployed to measure the phase and shape of cloud particles. Therefore my second research question is:

Research question II

How can measurements of the Backscatter Cloud Probe with Polarization Detection be used to obtain an accurate assessment of the cloud particle size and phase?

To answer the research question, I first compare IWT measurements of the BCPD to that of a Cloud Droplet Probe (CDP). I also use calibration data from the manufacturer to derive corrections to the BCPD's measurements.

Mixed phase conditions, where the determination of the particle phase is especially important, are difficult to simulate in IWTs. Therefore the phase differentiation capabilities of the BCPD are analyzed during a research flight of the HALO-$(AC)^3$ campaign [25]. Based on the data from this flight, a novel approach to separate ice and liquid particles is devised. The results are validated by comparison to LWC and ice water content (IWC) measurements from the Nevzorov probe and from additional established optical airborne instruments that were aboard the aircraft.

Lastly, the ultimate goal of this thesis is to assess whether the combination of the Nevzorov probe and the BCPD can be used to reliably detect Appendix O conditions and discriminate them from other icing conditions. This goal is the subject of the third research question:

Research question III

Can the combined data from the Nevzorov probe and the Backscatter Cloud Probe with Polarization Detection be used to discriminate Appendix O icing conditions from other atmospheric icing conditions?

Various concepts that were previously developed in the thesis are used to an-

1

swer this question. A novel algorithm assesses the phase of clouds based on the combined data from Nevzorov and BCPD and derives information on the presence of Appendix O conditions. Its output is validated with data from the previously mentioned research flight from the HALO-AC³ campaign, during which many different atmospheric conditions, ranging from ice clouds over mixed-phase clouds to purely liquid clouds were sampled. Unfortunately, no Appendix O conditions were encountered during this flight, such that only the false alarm rate of the algorithm can be assessed from the data of that flight. The capability of the algorithm for the detection of Appendix O is evaluated based on a flight from the SENS4ICE campaign that encountered several SLD events associated with the passage of a warm front over the north of France.

In the last part of my thesis, I explain the remaining challenges and provide an outlook on future research questions regarding sensor development, icing detection and the measurement of microphysical properties of supercooled clouds.

REFERENCES

[1] IATA, *2021 Safety Report*, Tech. Rep. (International Air Transport Association, 2022).

[2] Bureau d'Enquêtes et d'Analyses, *Final report on the accident on 1st June 2009 to the Airbus A330-203 registered F-GZCP operated by Air France flight AF 447 Rio de Janeiro–Paris*, Paris: BEA (2012).

[3] A. Heinrich, R. Ross, G. Zumwalt, J. Provorse, V. Padmanabhan, J. Thompson, and J. Riley, *Aircraft Icing Handbook Volume 1 of 3* (U.S. Department of Transportation, 1991).

[4] D. T. Bowden, A. Gensemer, and C. A. Skeen, *Engineering summary of airframe icing technical data*, Tech. Rep. FAA ADS-4 (General Dynamics San Diego Ca Convair Div, 1963).

[5] R. K. Jeck, *Icing Design Envelopes (14 CFR Parts 25 and 29, Appendix C) Converted to a Distance-Based Format*, Tech. Rep. DOT/FAA/AR-00/30 (Federal Aviation Administration, 2002).

[6] W. R. Sand, W. A. Cooper, M. K. Politovich, and D. L. Veal, *Icing Conditions Encountered by a Research Aircraft*, Journal of Climate and Applied Meteorology **23**, 1427 (1984).

[7] W. A. Cooper, W. R. Sand, D. L. Veal, and M. K. Politovich, *Effects of icing on performance of a research airplane*, Journal of Aircraft **21**, 708 (1984).

[8] J. Marwitz, M. Politovich, B. Bernstein, F. Ralph, P. Neiman, R. Ashenden, and J. Bresch, *Meteorological Conditions Associated with the ATR72 Aircraft Accident near Roselawn, Indiana, on 31 October 1994*, Bulletin of the American Meteorological Society **78**, 41 (1997).

[9] National Transportation Safety Board, *In-Flight Icing Encounter and Loss of Control Simmons Airlines, d.b.a. American Eagle Flight 4184 Avions de Transport Regional (ATR) Model 72-212, N401AM Roselawn, Indiana October 31, 1994*, Tech. Rep. NTSB/AAR-96/01 (National Transportation Safety Board, 1996).

[10] G. Isaac, S. Cober, A. Korolev, J. Strapp, A. Tremblay, and D. Marcotte, *Overview of the Canadian Freezing Drizzle Experiment I, II, and III. Preprints*, in *Conf. on Cloud Physics*, pp. 447–450 (1998).

[11] Office of the Federal Register, National Archives and Records Administration, *14 CFR Appendix O to Part 25 - Supercooled Large Drop Icing Conditions*, https://www.govinfo.gov/app/details/CFR-2016-title14-vol1/CFR-2016-title14-vol1-part25-appO (2016).

[12] European Aviation Safety Agency (EASA), *Certification Specifications and Acceptable Means of Compliance for Large Aeroplanes*, https://www.easa.europa.eu/downloads/134259/en (2021).

[13] SENS4ICE, https://www.sens4ice-project.eu/, accessed: 2021-09-13.

[14] C. W. Schwarz, *The SENS4ICE EU project - SENSors and certifiable hybrid architectures for safer aviation in ICing Environment - A project midterm overview*, in *6th International Conference Prospects of Civil Avionics Development* (2021).

[15] C. Deiler and F. Sachs, *Design and Testing of an Indirect Ice Detection Methodology*, in *SAE Technical Paper Series* (SAE International, 2023).

[16] Tina Jurkat-Witschas and Johannes Lucke and Carsten Schwarz and Christoph Deiler and Falk Sachs and Simon Kirschler and Deniz Menekay and Christiane Voigt and Ben Bernstein and Olivier Jaron and Frank Kalinka and Alessandra Zollo and Lyle Lilie and Johanna Mayer and Christian Page and Benoit Vié and Aurelien Bourdon and Rogerio Pereira Lima and Luiz Vieira, *Overview of Cloud Microphysical Measurements during the SENS4ICE Airborne Test Campaigns: Contrasting Icing Frequencies from Climatological Data to First Results from Airborne Observations*, in *SAE Technical Paper Series* (SAE International, 2023).

[17] National Aeronautics and Space Administration, *Icing Research Tunnel Probes - Nevzorov Probe*, https://www.dvidshub.net/image/830847/icing-research-tunnel-probes-nevzorov-probe, accessed: 2023-09-21 (2004).

[18] D. M. Orchard, K. Szilder, and C. R. Davison, *Design of an Icing Wind Tunnel Contraction for Supercooled Large Drop Conditions*, in *2018 Atmospheric and Space Environments Conference* (American Institute of Aeronautics and Astronautics, 2018).

[19] A. V. Korolev, J. W. Strapp, G. A. Isaac, and A. N. Nevzorov, *The Nevzorov Airborne Hot-Wire LWC–TWC Probe: Principle of Operation and Performance Characteristics*, Journal of Atmospheric and Oceanic Technology **15**, 1495 (1998).

1

[20] J. W. Strapp, J. Oldenburg, R. Ide, L. Lilie, S. Bacic, Z. Vukovic, M. Oleskiw, D. Miller, E. Emery, and G. Leone, *Wind Tunnel Measurements of the Response of Hot-Wire Liquid Water Content Instruments to Large Droplets*, Journal of Atmospheric and Oceanic Technology **20**, 791, https://doi.org/10.1175/1520-0426(2003)020<0791:WTMOTR>2.0.CO;2 (2003).

[21] A. Korolev, J. Strapp, G. Isaac, and E. Emery, *Improved airborne hot-wire measurements of ice water content in clouds*, Journal of Atmospheric and Oceanic Technology **30**, 2121 (2013).

[22] A. Costa, J. Meyer, A. Afchine, A. Luebke, G. Günther, J. R. Dorsey, M. W. Gallagher, A. Ehrlich, M. Wendisch, D. Baumgardner, H. Wex, and M. Krämer, *Classification of Arctic, midlatitude and tropical clouds in the mixed-phase temperature regime*, Atmospheric Chemistry and Physics **17**, 12219 (2017).

[23] J. Meyer, *Ice crystal measurements with the new particle spectrometer NIXE-CAPS*, (2011).

[24] L. Nichman, C. Fuchs, E. Järvinen, K. Ignatius, N. F. Höppel, A. Dias, M. Heinritzi, M. Simon, J. Tröstl, A. C. Wagner, R. Wagner, C. Williamson, C. Yan, P. J. Connolly, J. R. Dorsey, J. Duplissy, S. Ehrhart, C. Frege, H. Gordon, C. R. Hoyle, T. B. Kristensen, G. Steiner, N. M. Donahue, R. Flagan, M. W. Gallagher, J. Kirkby, O. Möhler, H. Saathoff, M. Schnaiter, F. Stratmann, and A. Tomé, *Phase transition observations and discrimination of small cloud particles by light polarization in expansion chamber experiments*, Atmospheric Chemistry and Physics **16**, 3651 (2016).

[25] M. Wendisch, M. Brückner, S. Crewell, A. Ehrlich, J. Notholt, C. Lüpkes, A. Macke, J. P. Burrows, A. Rinke, J. Quaas, M. Maturilli, V. Schemann, M. D. Shupe, E. F. Akansu, C. Barrientos-Velasco, K. Bärfuss, A.-M. Blechschmidt, K. Block, I. Bougoudis, H. Bozem, C. Böckmann, A. Bracher, H. Bresson, L. Bretschneider, M. Buschmann, D. G. Chechin, J. Chylik, S. Dahlke, H. Deneke, K. Dethloff, T. Donth, W. Dorn, R. Dupuy, K. Ebell, U. Egerer, R. Engelmann, O. Eppers, R. Gerdes, R. Gierens, I. V. Gorodetskaya, M. Gottschalk, H. Griesche, V. M. Gryanik, D. Handorf, B. Harm-Altstädter, J. Hartmann, M. Hartmann, B. Heinold, A. Herber, H. Herrmann, G. Heygster, I. Höschel, Z. Hofmann, J. Hölemann, A. Hünerbein, S. Jafariserajehlou, E. Jäkel, C. Jacobi, M. Janout, F. Jansen, O. Jourdan, Z. Jurányi, H. Kalesse-Los, T. Kanzow, R. Käthner, L. L. Kliesch, M. Klingebiel, E. M. Knudsen, T. Kovács, W. Körtke, D. Krampe, J. Kretzschmar, D. Kreyling, B. Kulla, D. Kunkel, A. Lampert, M. Lauer, L. Lelli, A. von Lerber, O. Linke, U. Löhnert, M. Lonardi, S. N. Losa, M. Losch, M. Maahn, M. Mech, L. Mei, S. Mertes, E. Metzner, D. Mewes, J. Michaelis, G. Mioche, M. Moser, K. Nakoudi, R. Neggers, R. Neuber, T. Nomokonova, J. Oelker, I. Papakonstantinou-Presvelou, F. Pätzold, V. Pefanis, C. Pohl, M. van Pinxteren, A. Radovan, M. Rhein, M. Rex, A. Richter, N. Risse, C. Ritter, P. Rostosky, V. V. Rozanov, E. R. Donoso, P. S. Garfias, M. Salzmann, J. Schacht, M. Schäfer, J. Schneider, N. Schnierstein,

P. Seifert, S. Seo, H. Siebert, M. A. Soppa, G. Spreen, I. S. Stachlewska, J. Stapf, F. Stratmann, I. Tegen, C. Viceto, C. Voigt, M. Vountas, A. Walbröl, M. Walter, B. Wehner, H. Wex, S. Willmes, M. Zanatta, and S. Zeppenfeld, *Atmospheric and Surface Processes, and Feedback Mechanisms Determining Arctic Amplification: A Review of First Results and Prospects of the (AC)3 Project*, Bulletin of the American Meteorological Society **104**, E208 (2023).

1

2

ATMOSPHERIC ICING CONDITIONS AND THEIR REPLICATION IN WIND TUNNELS

The previous chapter motivated this work and identified the research questions. In this chapter, the fundamental processes of how atmospheric icing conditions form in the atmosphere are explained. Furthermore, the definition of the certification specifications (e.g. those of Appendix O) are provided. These topics are integral for understanding the challenges involved in the detection and discrimination of Appendix O conditions. Lastly, I also explain how realistic icing conditions can be reproduced in icing wind tunnels (IWTs) and the challenges and requirements that are faced when creating artificial Appendix O conditions.

2.1. FORMATION OF SUPERCOOLED CLOUDS

Clouds are clusters of a myriad of droplets or ice crystals. Liquid cloud droplets form in environments where the partial pressure of water vapor exceeds the saturation vapor pressure. The formation is initiated by the condensation of water vapor on small aerosol particles [1, 2]. The condensed water dissolves the constituents of the aerosol and a solution droplet is formed. The presence of the solution is important, as it decreases the saturation vapor pressure next to the droplet and, compared to a pure water droplet, facilitates the initial growth. Once the water droplet reaches a certain radius (usually between 0.1 and 1 µm) [2], it grows spontaneously, because the condensation produces a decrease in the Gibbs free energy of the liquid water-water vapor system. As the droplet grows, the concentration of the solute decreases, which impedes further growth. Also, because the volume is propor-

tional to the third power of the droplet diameter, the time consumed for growth at a given relative humidity increases with droplet size. How large droplets grow by condensation depends on a number of factors, e.g. the local supersaturation, the mass of the solute, atmospheric dynamics and the time over which favorable conditions are sustained. Through condensation, it is generally possible to obtain droplets with diameters of up to 50 μm in under one hour [1]. Once growth by condensation stagnates, cloud droplets can still grow by collision with other cloud droplets. This mechanism is referred to as collision-coalescence, where the term coalescence specifies that the cloud droplets unite after the initial collision. The aerosol particles that act as a seed for droplet growth are known as cloud condensation nuclei (CCNs). Not all aerosol particles are CCNs, and whether an aerosol particle acts as CCN is dependent on the ambient supersaturation.

Cloud droplets do not necessarily freeze once their temperature drops below 0 °C. In fact, supercooled liquid droplets can exist up to a temperature of above approximately -38 °C. Below -38 °C water freezes homogeneously, i.e. in the absence of a nucleus [1, 3]. At temperatures above -38 °C, a small particle, commonly known as an ice nucleating particle (INP) is required to initiate the freezing process. A freezing event that is facilitated by an INP is termed «heterogeneous nucleation».

A wide range of particles can function as INPs, e.g. organic particles like black carbon and amino acids, but also pollen, algae and bacteria [3, 4]. Whether a particle acts as an INP also depends on temperature, certain INPs only function as such once the temperature decreases below a certain limit [3]. Compared to the number of CCN (and therefore also to the number of cloud droplets), the number of INPs is in general very low [1, 5] and the existence of supercooled clouds can be explained by INPs not being readily available for every supercooled droplet.

Hu *et al.* [6] estimate that more than 95% of clouds with temperatures between 0 °C and -15 °C are liquid clouds. Because some particles only function as INPs below a certain temperature, the frequency of occurrence of supercooled clouds decreases with decreasing temperature. At -20 °C for instance, only 10% of clouds are entirely liquid [1].

At equivalent partial pressures of water vapor, the relative humidity is higher over ice than over water [2]. In the presence of just a few ice crystals, a mixed-phase cloud can glaciate rapidly as the ice crystals grow and deplete the available water vapor [7]. Ice crystals can also grow directly by collisions with supercooled droplets [2]. Further contributing to the rapid glaciation of mixed-phase clouds is often a process that is known as secondary ice production [8]. Secondary ice production is an overarching term that describes various pathways in which an ice particle can fragment and produce splintered ice particles, which again can grow either from the vapor phase or through collisions [2].

The persistence of supercooled clouds is therefore essentially governed by the supply rate of water vapor, the rate of evaporation, the uptake of water vapor by ice crystals through diffusion and the removal of liquid droplets through freezing on ice particles [9]. The uptake of water vapor by ice crystals in turn depends on the availability of ice crystals, which is related to the number of INPs. Low numbers of INPs are therefore generally favorable for the longevity of supercooled clouds.

The lifetime of glaciated clouds is shorter than that of supercooled clouds because the large ice crystals sediment much faster than the smaller liquid droplets [10].

2.2. OCCURRENCE OF SUPERCOOLED LARGE DROPLETS

While supercooled clouds are common, the occurrence of supercooled large droplet (SLD) conditions is relatively rare [11, 12] since a combination of peculiar circumstances is required for the formation. Essentially, two distinct processes can produce SLDs [13]:

- Supercooled warm rain process: SLDs form entirely from clouds in the liquid phase, they attain their large size through collision-coalescence processes (see Fig. 2.1a)

- Cold rain process: SLDs form from sedimenting ice hydrometeors which first pass through a layer of air at above 0 °C, where they melt, and then through a layer at subfreezing temperature, where they supercool again (see Fig. 2.1b).

SLD conditions that are created through the supercooled warm rain process are referred to as freezing drizzle [14], while SLD conditions that are created through the cold rain process are referred to as freezing rain [15–18]. Droplet diameters in freezing drizzle conditions only rarely exceed 500 µm. The formation of freezing drizzle conditions is usually associated with relatively warm cloud top temperatures of above -15 °C, where the supercooled droplets are less likely to freeze [19], but also observations at −25 °C and even −29 °C have been reported [20, 21]. Furthermore, for the production of freezing drizzle, the air should contain low numbers of INPs and CCNs [22, 23], as is often the case for clean air masses that originate over the oceans [12]. Significant wind shear is also claimed to be conducive to the formation of drizzle drops [19], although Cober *et al.* [15] also found SLDs formed through collision-coalescence processes near cloud top when no strong wind shear was present.

Freezing rain often occurs in situations where warm air masses ascend over a layer of cold air on the surface, as is the case at a warm front [13]. Droplets in freezing rain conditions can have diameters of up to several millimeters [17]. Freezing rain conditions only occur in a relatively narrow temperature range between 0 °C and −13 °C [17], due to the high likelihood of large droplets freezing at low temperatures and the required warm air layer.

Bernstein *et al.* [24] list a number of meteorological scenarios that facilitate the formation of freezing drizzle: Boundary layer clouds, which are not isolated from sources of CCNs and INPs on the ground, can produce SLDs if the cloud layer is sufficiently deep. In such clouds, the number concentration stays approximately constant in altitude, while the liquid water content (LWC) and the average droplet diameter increase. Hence, at some point, droplet sizes may surpass the threshold to SLDs. More favorable however is the existence of a stable layer, which can for instance form during the passage of a warm front. The warm air ascends over the colder layer and is in this process depleted of CCNs and INPs through precipitation. The inversion which results from the warm air overflowing the cold
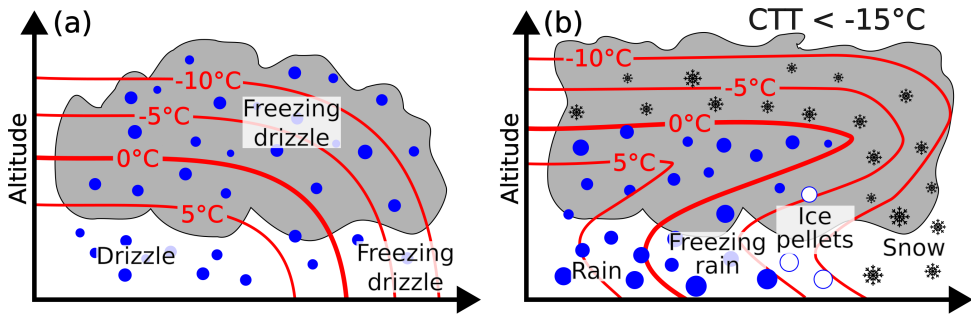
Figure 2.1: Formation of freezing drizzle through the supercooled warm rain process (**a**) and of freezing rain through the cold rain process (**b**). Cloud top temperatures (CTTs) are usually above -15 °C for freezing drizzle formation and below -15 °C for freezing rain formation. Image based on Marwitz *et al.* [14].

layer furthermore blocks CCNs and INPs from the ground from ascending into the cloud.

> ### Droplets or Drops?
>
> No clear size threshold exists for the distinction between a droplet and a drop, according to the Glossary of Meteorology [25]. However, the term droplet is often used to denote non-precipitating liquid particles that remain suspended in a cloud due to their weight being in near equilibrium with drag forces and updrafts, while the term drop implies that the particle is precipitating. Based on this definition, the Glossary of Meteorology suggests 0.2 mm diameter as the threshold between drops and droplets. For this thesis, such a definition is impractical, especially because SLDs would in part be considered as droplets and in part as drops, depending on their size. I therefore distinguish as follows: Small cloud drops and freezing drizzle drops are generally denoted as droplets, also I use the term droplet size distribution instead of drop size distribution. The term «drop» is only used when raindrops are specifically and exclusively mentioned.

SLDs often occur alongside small cloud droplets in bimodal conditions, i.e. two maxima are present in the volume distribution of the cloud liquid water content, one at a diameter typical for small cloud droplets (i.e. between 10 - 40 µm) and a second one at the diameter where the maximum mass of the SLDs is concentrated. The SLDs contribute only a very small number to the overall droplet number concentration, but they can contribute significantly to the overall LWC (for the certification regulations regarding flight in such icing conditions see Section 2.4).

2.3. AIRCRAFT ICING BY SUPERCOOLED DROPLETS

The freezing process of supercooled water droplets that impact the airframe may be instantaneous or may occur after the water dispersed and merged into a liquid layer with the water of other droplets [26]. In the first case, air is trapped during the freezing process, resulting in a whitish, opaque ice accretion called rime ice. In the second case, no air is trapped and the ice accretion appears transparent. This type of ice accretion is called glaze ice [27]. If droplet sizes are large (as is the case for SLDs), the LWC is high and the ambient temperature is not too far below the melting point, the likelihood is high that not all water freezes immediately, hence such conditions are conducive to the formation of glaze ice [26, 28]. Due to its transparent nature, glaze ice is difficult to identify visually and therefore especially dangerous. The delayed freezing process also means that liquid water may flow downstream along the aircraft components and freeze at locations that are not protected against ice accretion. Rime and glaze ice accretions that occurred on the Cloud Combination Probe of DLR during IWT tests are displayed in Fig. 2.2a and b respectively. The different colors of the ice accretions are clearly perceptible. Runback ice can be observed in Fig. 2.2b on the arm of the upper probe component.
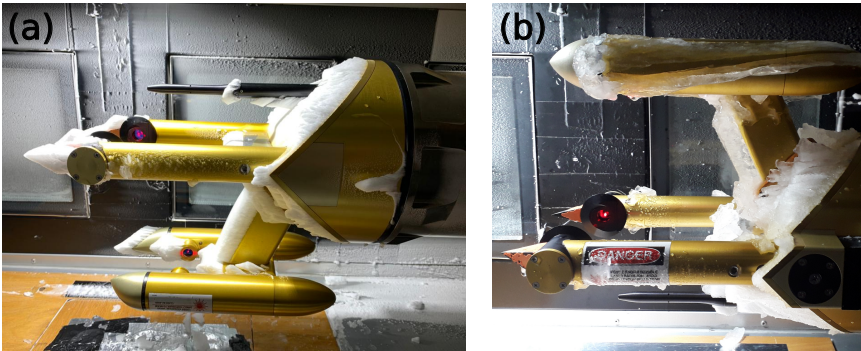
Figure 2.2: Rime ice (**a**) and glaze ice (**b**) accretion on the Cloud Combination Probe during wind tunnel tests at the Technical University of Braunschweig.

For the safety of flight and for aircraft certification it is crucial to know the maximum severity of atmospheric icing. The severity depends on multiple parameters of the icing cloud [26]:

1. Horizontal extent of the icing conditions (in the direction of passage).

2. LWC: The mass of liquid water per unit volume is a key factor to how much ice accretion can occur during passage through a cloud.

3. DSD: The location, the shape and the type (glaze or rime) of the ice accretion depends on the DSD of the cloud that is penetrated. The location where droplets impact is related to the droplet inertia. Small droplets either impinge close to the leading edge or follow the streamlines around the wing. Large droplets, on the other hand, can impinge further aft on the wing, in the least favorable cases even behind the extent of the ice protection system [28].

4. Temperature: The temperature influences the freezing process, e.g. the formation of rime ice or glaze ice and thus also the shape of the ice accretion. The power required by the ice protection system may be temperature-dependent.

Determining a complete description of all possible icing conditions that may be hazardous to aircraft operation is a challenging task that has been intensively investigated for many years [26]. Systematic observations of icing conditions were reported from 1947 on among others by Lewis [29], Lewis and Bergrun [30], Kline [31] and Bowden *et al.* [32]. During these early research activities, it was found that icing conditions vary significantly depending on the cloud type. Cumuliform clouds tend to have larger LWCs but smaller horizontal extents than stratiform clouds.

Regarding the DSDs, almost infinitely many combinations of droplet sizes can occur in icing clouds, each of which would result in a different ice accretion. It is not practical to describe icing conditions through their DSD. Instead, the DSD is usually reduced to a small set of parameters, which are deemed to be representative of the DSD. For the early research activities, the most important parameter (and the only one) is the median volume diameter (MVD). The MVD is the diameter that splits the cumulative mass distribution in half, i.e. half of the liquid water is contained in droplets smaller than the MVD, while the other half is contained in droplets larger than the MVD [32].

A further parameter, which is emphasized especially for the description of SLD conditions (as will be shown later), is the maximum drop diameter (D_{max}). The D_{max} is defined as the diameter at which 99% of the liquid water is contained in droplets smaller than D_{max}. This definition ensures that the D_{max} is a stable property and independent of the sampling time. An illustration of a DSD (measured in a supercooled cloud with an insignificant portion of SLDs), the corresponding cumulative mass distribution and the resulting MVD and D_{max} can be seen in Fig. 2.3. The MVD and D_{max} are easily derived from the cumulative mass distribution in Fig. 2.3b. It is worth noting that SLDs were measured (see Fig. 2.3a), but their contribution to the overall LWC is below 1% and therefore insignificant.

When analyzing the correlation between LWC and MVD, it was found that the largest MVDs do not occur together with the largest LWCs. While MVDs in general range from approximately 15 µm to 50 µm, the largest LWCs are associated with MVDs at the lower end of the stated size range [32]. These high LWCs are usually found in strong convective systems [33, 34]. On average, cloud LWC also decreases with decreasing temperature [26, 35].

For the definition of airworthiness criteria of aircraft, the findings on icing conditions that were explained above needed to be combined practically. This was achieved by the creation of icing envelopes (see Fig. 2.4). These icing envelopes engulf the LWCs, MVDs and temperatures that are associated with icing conditions. The envelopes represent the 99% probability limits, i.e. they were estimated in a way that 99% of the icing conditions that an aircraft is likely to encounter are contained within the envelope limits [35]. These envelopes were added to the Federal Aviation Regulations of the United States in 1955 [36], where they are found in Appendix C to Part 25 [37]. The conditions described in the envelopes are therefore
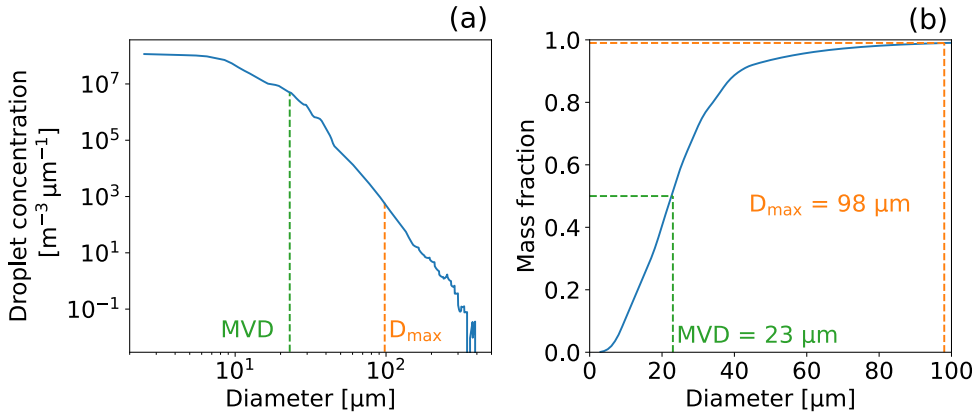
Figure 2.3: Unimodal droplet size distribution (**a**) and the corresponding normalized cumulative mass distribution (**b**).

known as Appendix C conditions and are referred to as such in this work. The same envelopes are also specified in Appendix C of the corresponding European regulations [38].

The Appendix C envelopes are defined for continuous and intermittent maximum icing conditions (see Fig. 2.4). This distinction reflects the difference in LWC and horizontal extent between cumuliform and stratiform clouds [35], which was mentioned earlier in this section. The envelopes for continuous icing conditions are generally associated with stratiform clouds, while the envelopes for intermittent icing conditions are descriptive of cumuliform clouds. It is worth noting that the envelopes are specified for reference distances of 32.2 km for continuous and 4.8 km for intermittent icing conditions. The maximum LWC values from the envelopes must be interpreted as the average LWC that has been measured over the reference distances. It is very unlikely that the maximum LWC specified for intermittent icing conditions exists over tens of nautical miles, as is the case for the LWCs for continuous conditions. Therefore, if distances longer than the reference distance are considered, the maximum LWC values can be lowered, while for distances shorter than the reference distance they must be raised [35]. The exact procedure for aircraft certification depends also on the maneuvers that are expected to be flown, but this is out of the scope of this thesis and I refer the interested reader to the respective documents [37, 38]. The range of LWC values stated in Appendix C for intermittent and continuous icing conditions are also common choices for test conditions in IWTs, as shall be seen in the following chapters of this work.

The Appendix C envelopes do not describe freezing drizzle or freezing rain conditions. In their summary of airframe icing technical data, Bowden *et al.* [32] mentioned that freezing rain can cause ice accretion on aircraft parts that would not be affected during the icing conditions specified in Appendix C and stressed that this should be considered during the design process, but no specific standard was established. This was also because hardly any in-flight data of freezing rain

2
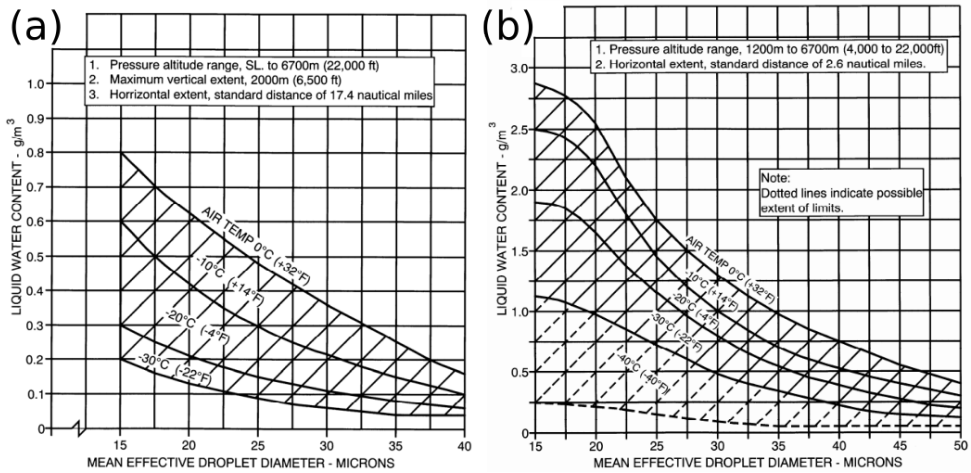
Figure 2.4: Appendix C icing envelopes. The continuous maximum envelopes (**a**) are used for stratiform clouds, while the intermittent maximum envelopes (**b**) are used for cumuliform clouds. The mean effective droplet diameter is equivalent to the MVD [17]. Images from [38].

had been collected. Freezing drizzle conditions are not mentioned by Bowden *et al.* [32], likely because at the time no direct method to detect SLDs in-flight existed. Instead, droplet sizes were derived from rotating cylinders of different sizes (see Chapter 3).

2.4. APPENDIX O ICING CONDITIONS

After the accident of American Eagle flight 4184, which was mentioned in Chapter 1, numerous research activities on SLD icing were initiated. One objective of these activities was to extend the existing Appendix C regulations, such that SLD conditions would be covered. The consensus of the aviation industry was to leave Appendix C unchanged and to create a distinct framework that describes SLD icing environments [39]. The difficulty in creating a new standard lies in the fine line between creating a complete and yet practical standard. Regulations that require certification for unrealistically severe icing conditions can be harmful to the economics of aircraft operations and increase the cost of the certification program, while an incomplete standard poses a threat to flight safety.

In the end, a standard (which is nowadays known as Appendix O, due to being specified in Appendix O of the American federal aviation regulations [40] and the European certification specifications [38]) was developed that separated the SLD conditions by D_{max} and MVD into four distinct subsets [17]. In accordance with the meteorological formation processes of SLDs, Appendix O differentiates between freezing drizzle and freezing rain, where conditions with a $D_{max} < 500$ µm are identified as freezing drizzle, while conditions with $D_{max} > 500$ µm are identified as freezing rain.

Furthermore, for both freezing drizzle and freezing rain conditions, a distinc-
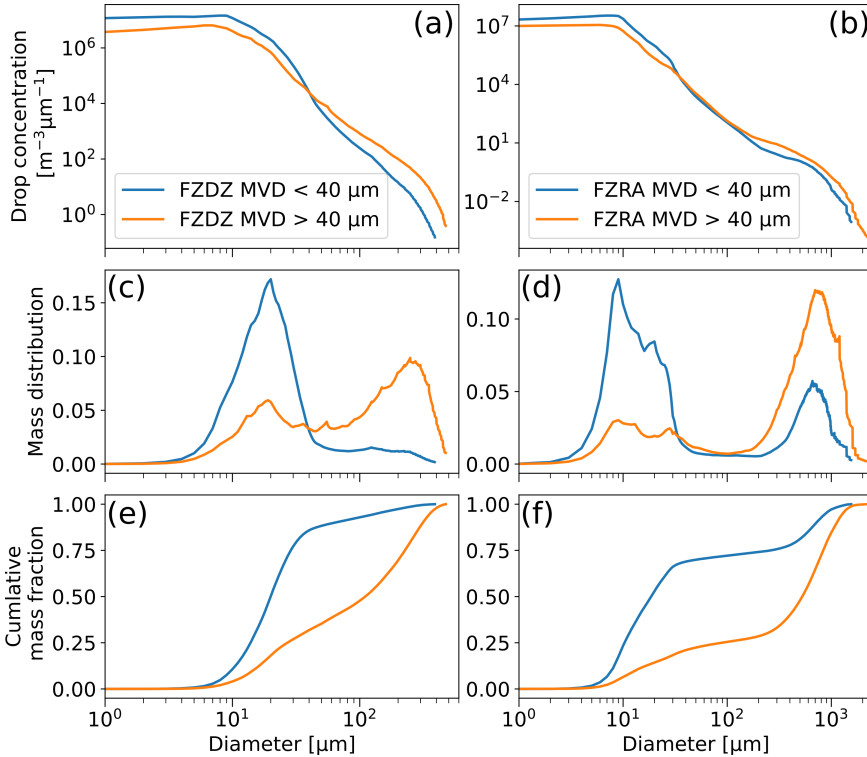
Figure 2.5: Typical distributions of droplet sizes and mass for the four Appendix O regimes. The displayed distributions are averages of all the SLD conditions found in the research activities of Cober and Isaac [17]. The left column shows freezing drizzle (FZDZ) conditions and the right column freezing rain (FZRA) conditions. Panels **a** and **b** display the droplet number concentrations. Only a very small portion of droplets are SLDs. Panels **c** and **d** show the mass distributions. The mass fraction per size-bin has been normalized with the difference between the logarithm of the upper size-bin limit and the lower size-bin limit. This normalization counteracts the distortion caused by the logarithmic scaling of the x-axis. As a consequence, the y-axis units for **c** and **d** are arbitrary and do not contain any information about the absolute LWC. Panels **e** and **f** show cumulative mass distributions. All plots shown in this figure were adapted from Cober and Isaac [17].

tion was made in Appendix O whether the MVD was smaller or larger than 40 µm. This distinction can be interpreted as an evaluation of the contribution of SLDs to the total water content. For cases where the MVD was smaller or equal to 40 µm, SLDs contribute less than 50% to the total LWC, while for the subset of observations with MVDs larger than 40 µm, up to 100% of the LWC may be contained in SLDs. The 40-µm-MVD-threshold was selected to be compatible with the Appendix C regulations. Aircraft manufacturers that certified their aircraft for Appendix C could point to the existing certification to cover the portion of LWC contained in small cloud droplets and would just have to show that their aircraft can handle the remaining portion of LWC contained in droplets larger than 40 µm. Typical distributions of droplet size, droplet volume and cumulative droplet volume for the four subsets of Appendix O conditions can be seen in Fig. 2.5. The comparison of panels **a** and **b** to panels **e** and **f** shows that despite their small number concentration SLDs can contribute significantly to the overall LWC. Furthermore, panels **c** and **d** highlight the typical bimodal nature of Appendix O conditions.

The maximum LWC that can be expected to be encountered in Appendix O conditions is significantly smaller than in Appendix C conditions (compare Fig. 2.4 and Fig. 2.6). Ice accumulation therefore tends to be slower in Appendix O conditions and the difficulty of certifying aircraft for Appendix O lies not in the amount of ice that needs to be handled but rather in the location of the ice accretion.
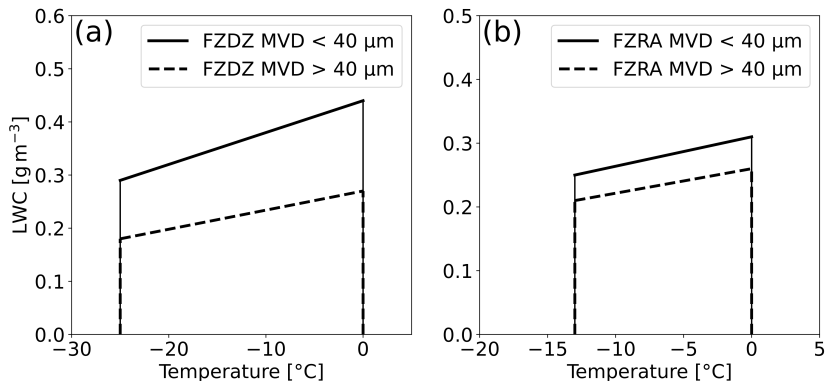
Figure 2.6: Appendix O envelopes for freezing drizzle (FZDZ) (**a**) and freezing rain (FZRA) (**b**).

2.5. REPLICATION OF ICING CONDITIONS IN WIND TUNNELS

Icing wind tunnels (IWTs) are a relatively cheap (compared to the cost of a flight test) and well-controlled means to test airplane components and sensors. In contrast to regular wind tunnels, which are routinely used for studies of aerodynamics, IWTs possess a spray system, which produces the droplet cloud, and a powerful cooling system to achieve temperatures well below 0 °C. The first IWTs were de-

veloped in the 1930s in the United States of America to test wing and propeller deicing systems [36]. IWTs are usually closed-loop wind tunnels, i.e. the cold air is recirculated. The droplet spray is produced by an array of spray nozzles, to which water and air at certain pressures is supplied. The intended droplet size is produced by selecting an appropriate combination of air and water pressure. An increase in the air pressure (while the water pressure remains constant) tends to decrease droplet size, while a decrease in air pressure results in larger droplet sizes. Vice versa also the water pressure can be varied, here a reduction in water pressure results in smaller droplet sizes, while an increase produces larger droplets [41].

IWTs were historically optimized for the production of Appendix C conditions [36, 42]. The addition of Appendix O to aircraft certification standards resulted in a demand for testing facilities with freezing drizzle and freezing rain capabilities. However, several challenges are associated with the production of Appendix O conditions. First of all, droplets need to be produced which are starkly different from those of Appendix C conditions. This is especially apparent if one considers that the droplet volume increases with the third power of the diameter. Depending on the spray system that is employed, a new set of spray nozzles may be required, which, to produce bimodal Appendix O distributions, also needs to be combined with the nozzles that produce the small droplet spray. The large size of SLDs creates however even more critical problems, as has also been discussed in detail in Orchard *et al.* [43]. First of all, according to Stokes law [44], the SLDs sediment much faster than small droplets, hence, the SLD spray may have a very uneven distribution within the tunnel cross section. Secondly, SLDs take much longer than small droplets to supercool. Therefore, it is possible that the SLDs are not sufficiently cold to cause ice accretion when they arrive in the test section. A third issue is the velocity of the SLDs in the test section. Due to their larger inertia, SLDs require more time than small droplets to attain the tunnel velocity [45]. While the second and the third issue could theoretically be solved by increasing the distance between the spray system and the test section (which would likely already require significant changes to the IWT design), the first issue directly contradicts this solution, as longer distances between spray system and test section would result in further sedimentation of SLDs.

An additional problem is the production of uniform Appendix O conditions while maintaining a realistic LWC. The large volume of SLDs means that already a single drop contributes significantly to the overall LWC. The difficulty therefore lies in adjusting the spray nozzles in such a way that very few droplets are produced, which also need to be evenly distributed over the test section. Different importance is assigned by the individual IWT owners to the LWC limits of Appendix O. While some trim their IWTs to respect the limits, others argue that for testing purposes higher LWCs can be simply accounted for by using shorter sampling times.

The above-mentioned issues are relevant for the interpretation of the results presented in subsequent parts of this thesis. IWTs serve as test beds for the atmospheric sensors that are investigated and they permit to test in a multitude of icing conditions that would be practically impossible to obtain during a single flight campaign. However, it is important to understand that especially the Appendix O

2

conditions produced in IWTs are subject to significant uncertainties that can contribute to differences between the readings of individual sensors.

Appendix C and O conditions and their generation in wind tunnels become important again in Chapter 4. For now, I proceed to a presentation of the different measurement techniques that are used to determine parameters such as the MVD and the LWC.

REFERENCES

[1] H. Pruppacher and J. Klett, *Microphysics of Clouds and Precipitation* (Springer Netherlands, 2010).

[2] J. M. Wallace and P. V. Hobbs, *Atmospheric science: An introductory survey*, Vol. 92 (Elsevier, 2006).

[3] S. M. Kreidenweis, M. Petters, and U. Lohmann, *100 years of progress in cloud physics, aerosols, and aerosol chemistry research*, Meteorological Monographs **59**, 11.1 (2019).

[4] Z. A. Kanji, L. A. Ladino, H. Wex, Y. Boose, M. Burkert-Kohn, D. J. Cziczo, and M. Krämer, *Overview of Ice Nucleating Particles*, Meteorological Monographs **58**, 1.1 (2017).

[5] V. I. Khvorostyanov and J. A. Curry, *The Theory of Ice Nucleation by Heterogeneous Freezing of Deliquescent Mixed CCN. Part I: Critical Radius, Energy, and Nucleation Rate*, Journal of the Atmospheric Sciences **61**, 2676 (2004).

[6] Y. Hu, S. Rodier, K. Xu, W. Sun, J. Huang, B. Lin, P. Zhai, and D. Josset, *Occurrence, liquid water content, and fraction of supercooled water clouds from combined CALIOP/IIR/MODIS measurements*, Journal of Geophysical Research **115**, 10.1029/2009jd012384 (2010).

[7] A. Korolev, G. McFarquhar, P. R. Field, C. Franklin, P. Lawson, Z. Wang, E. Williams, S. J. Abel, D. Axisa, S. Borrmann, J. Crosier, J. Fugal, M. Krämer, U. Lohmann, O. Schlenczek, M. Schnaiter, and M. Wendisch, *Mixed-Phase Clouds: Progress and Challenges*, Meteorological Monographs **58**, 5.1 (2017).

[8] P. R. Field, R. P. Lawson, P. R. A. Brown, G. Lloyd, C. Westbrook, D. Moisseev, A. Miltenberger, A. Nenes, A. Blyth, T. Choularton, P. Connolly, J. Buehl, J. Crosier, Z. Cui, C. Dearden, P. DeMott, A. Flossmann, A. Heymsfield, Y. Huang, H. Kalesse, Z. A. Kanji, A. Korolev, A. Kirchgaessner, S. Lasher-Trapp, T. Leisner, G. McFarquhar, V. Phillips, J. Stith, and S. Sullivan, *Chapter 7. Secondary Ice Production: Current state of the science and recommendations for the future*, Meteorological Monographs 10.1175/amsmonographs-d-16-0014.1 (2016).

[9] R. M. Rauber and A. Tokay, *An explanation for the existence of supercooled water at the top of cold clouds*, Journal of Atmospheric Sciences **48**, 1005 (1991).

[10] U. Lohmann and J. Feichter, *Global indirect aerosol effects: A review*, Atmospheric Chemistry and Physics **5**, 715 (2005).

[11] B. C. Bernstein, C. A. Wolff, and F. McDonough, *An Inferred Climatology of Icing Conditions Aloft, Including Supercooled Large Drops. Part I: Canada and the Continental United States*, Journal of Applied Meteorology and Climatology **46**, 1857 (2007).

[12] B. C. Bernstein and C. Le Bot, *An Inferred Climatology of Icing Conditions Aloft, Including Supercooled Large Drops. Part II: Europe, Asia, and the Globe*, Journal of Applied Meteorology and Climatology **48**, 1503 (2009).

[13] G. J. Huffman and G. A. Norman, *The Supercooled Warm Rain Process and the Specification of Freezing Precipitation*, Monthly Weather Review **116**, 2172 (1988).

[14] J. Marwitz, M. Politovich, B. Bernstein, F. Ralph, P. Neiman, R. Ashenden, and J. Bresch, *Meteorological Conditions Associated with the ATR72 Aircraft Accident near Roselawn, Indiana, on 31 October 1994*, Bulletin of the American Meteorological Society **78**, 41 (1997).

[15] S. G. Cober, J. W. Strapp, and G. A. Isaac, *An Example of Supercooled Drizzle Drops Formed through a Collision-Coalescence Process*, Journal of Applied Meteorology **35**, 2250 (1996).

[16] J. V. Cortinas Jr., B. C. Bernstein, C. C. Robbins, and J. W. Strapp, *An Analysis of Freezing Rain, Freezing Drizzle, and Ice Pellets across the United States and Canada: 1976–90*, Weather and Forecasting **19**, 377 (2004).

[17] S. G. Cober and G. A. Isaac, *Characterization of Aircraft Icing Environments with Supercooled Large Drops for Application to Commercial Aircraft Certification*, Journal of Applied Meteorology and Climatology **51**, 265 (2012).

[18] S. A. Tessendorf, A. Rugg, A. Korolev, I. Heckman, C. Weeks, G. Thompson, D. Jacobson, D. Adriaansen, and J. Haggerty, *Differentiating Freezing Drizzle and Freezing Rain in HRRR Model Forecasts*, Weather and Forecasting **36**, 1237 (2021).

[19] B. M. Pobanz, J. D. Marwitz, and M. K. Politovich, *Conditions Associated with Large-Drop Regions*, Journal of Applied Meteorology and Climatology **33**, 1366 (1994).

[20] Silber, Israel and Fridlind, Ann M and Verlinde, Johannes and Ackerman, Andrew S and Chen, Yao-Sheng and Bromwich, David H and Wang, Sheng-Hung and Cadeddu, Maria and Eloranta, Edwin W, *Persistent supercooled drizzle at temperatures below -25 °C observed at McMurdo Station, Antarctica*, Journal of Geophysical Research: Atmospheres **124**, 10878 (2019).

[21] A. Korolev, G. Isaac, J. Strapp, and S. Cober, *Observation of drizzle at temperatures below -20 °C*, in *40th AIAA Aerospace Sciences Meeting & Exhibit*, p. 678 (2002).

[22] R. M. Rasmussen, B. C. Bernstein, M. Murakami, G. Stossmeister, J. Reisner, and B. Stankov, *The 1990 Valentine's Day Arctic Outbreak. Part I: Mesoscale and Microscale Structure and Evolution of a Colorado Front Range Shallow Upslope Cloud*, Journal of Applied Meteorology **34**, 1481 (1995).

[23] D. Rosenfeld, R. Chemke, P. DeMott, R. C. Sullivan, R. Rasmussen, F. McDonough, J. Comstock, B. Schmid, J. Tomlinson, H. Jonsson, K. Suski, A. Cazorla, and K. Prather, *The common occurrence of highly supercooled drizzle and rain near the coastal regions of the western United States*, Journal of Geophysical Research: Atmospheres **118**, 9819 (2013).

[24] B. C. Bernstein, R. M. Rasmussen, F. McDonough, and C. Wolff, *Keys to Differentiating between Small- and Large-Drop Icing Conditions in Continental Clouds*, Journal of Applied Meteorology and Climatology **58**, 1931 (2019).

[25] American Meteorological Society, *Droplet*, in *Glossary of Meteorology* (2022).

[26] A. Heinrich, R. Ross, G. Zumwalt, J. Provorse, V. Padmanabhan, J. Thompson, and J. Riley, *Aircraft Icing Handbook Volume 1 of 3* (U.S. Department of Transportation, 1991).

[27] D. L. Arenberg, *Determination of icing-conditions for airplanes*, Transactions, American Geophysical Union **24**, 99 (1943).

[28] M. K. Politovich, *Predicting glaze or rime ice growth on airfoils*, Journal of aircraft **37**, 117 (2000).

[29] W. Lewis, *A flight investigation of the meteorological conditions conducive to the formation of ice on airplanes*, Tech. Rep. 1393 (National Aeronautics and Space Administration, Ames Research Center, Moffett Field, CA, 1947).

[30] W. Lewis and N. R. Bergrun, *A probability analysis of the meteorological factors conducive to aircraft icing in the United States*, (1952).

[31] D. B. Kline, *Investigation of Meteorological Conditions Associated with Aircraft Icing in Layer-Type Clouds for 1947-48 Winter*, (1949).

[32] D. T. Bowden, A. Gensemer, and C. A. Skeen, *Engineering summary of airframe icing technical data*, Tech. Rep. FAA ADS-4 (General Dynamics San Diego Ca Convair Div, 1963).

[33] R. P. Lawson, S. Woods, and H. Morrison, *The microphysics of ice and precipitation development in tropical cumulus clouds*, Journal of the Atmospheric Sciences **72**, 2429 (2015).

[34] R. C. Braga, D. Rosenfeld, R. Weigel, T. Jurkat, M. O. Andreae, M. Wendisch, M. L. Pöhlker, T. Klimach, U. Pöschl, C. Pöhlker, C. Voigt, C. Mahnke, S. Borrmann, R. I. Albrecht, S. Molleker, D. A. Vila, L. A. T. Machado, and P. Artaxo, *Comparing parameterized versus measured microphysical properties of tropical convective cloud bases during the ACRIDICON–CHUVA campaign*, Atmospheric Chemistry and Physics **17**, 7365 (2017).

[35] R. K. Jeck, *Icing Design Envelopes (14 CFR Parts 25 and 29, Appendix C) Converted to a Distance-Based Format*, Tech. Rep. DOT/FAA/AR-00/30 (Federal Aviation Administration, 2002).

[36] W. M. Leary, *We Freeze to Please: A History of NASA's Icing Research Tunnel and the Quest for Flight Safety*, Vol. 4226 (National Aeronautics and Space Administration, 2002).

[37] Office of the Federal Register, National Archives and Records Administration, *14 CFR Appendix C to Part 25*, https://www.ecfr.gov/pdfs/df8e9886-1ceb-46a8-938a-16a146334e04.pdf (2014).

[38] European Aviation Safety Agency (EASA), *Certification Specifications and Acceptable Means of Compliance for Large Aeroplanes*, https://www.easa.europa.eu/downloads/134259/en (2021).

[39] S. Cober, B. Bernstein, R. Jeck, E. Hill, G. Isaac, J. Riley, and A. Shah, *Data and Analysis for the Development of an Engineering Standard for Supercooled Large Drop Conditions*, techreport DOT/FAA/AR-09/10 (Federal Aviation Administration, 2009).

[40] Office of the Federal Register, National Archives and Records Administration, *14 CFR Appendix O to Part 25 - Supercooled Large Drop Icing Conditions*, https://www.govinfo.gov/app/details/CFR-2016-title14-vol1/CFR-2016-title14-vol1-part25-appO (2016).

[41] V. R. Bora, I. Knop, J. Lucke, and T. Jurkat-Witschas, *Instrumentation for measuring supercooled large droplet cloud distributions in icing wind tunnels*, in *AIAA SCITECH 2023 Forum*, p. 2286, https://arc.aiaa.org/doi/pdf/10.2514/6.2023-2286 (2023).

[42] E. Herman, *Goodrich Icing Wind Tunnel Overview, Improvements and Capabilities*, in *44th AIAA Aerospace Sciences Meeting and Exhibit*, p. 862 (2006).

[43] D. M. Orchard, K. Szilder, and C. R. Davison, *Design of an Icing Wind Tunnel Contraction for Supercooled Large Drop Conditions*, in *2018 Atmospheric and Space Environments Conference* (American Institute of Aeronautics and Astronautics, 2018).

[44] G. G. Stokes, *On the Effect of the Internal Friction of Fluids on the Motion of Pendulums*, Transactions of the Cambridge Philosophical Society **9**, 8 (1851).

[45] V. R. Bora, M. Gallia, I. Knop, and A. Guardone, *Investigation of the Influence of Aero-Thermal Non-equilibrium Conditions of an SLD Cloud on Airfoil Icing*, in *SAE Technical Paper Series*, ICE (SAE International, 2023).

2

3

INSTRUMENTS AND METHODS

The measurement of icing conditions is achieved with scientific instrumentation. A solid understanding of the physical principles of these instruments is key to comprehending the challenges that exist with the measurements. In this chapter, I therefore present techniques and instruments that are used for the determination of cloud particle size, shape, liquid water content (LWC) and total water content (TWC). I focus on the instruments that I operated and evaluated, however, as cross-comparisons between different instruments are standard practice in the icing community, I also give a short overview of alternative measurement methods.

3.1. MEASUREMENT OF LIQUID- AND TOTAL WATER CONTENT

Three widely used techniques for the measurement of LWC exist, accretion-based methods, hot-wire sensors and evaporators [1, 2]. Furthermore, particle sizing methods are at times used to estimate LWCs. The following passages aim to give the reader a short introduction to the fundamentals of each of these techniques and Table 3.1 provides examples.

ACCRETION-BASED METHODS

Estimates of the LWC are obtained from accretion-based methods by measuring the mass of ice that accumulated on a given structure over a period of time. Typical objects used to collect the ice accretion are static and rotating cylinders [3] and icing blades [4] (see Table 3.1). Both methods are still employed in icing wind tunnels [5–7]. A drawback of accretion-based methods is that the LWC cannot be obtained in real-time, instead, after the test, an operator is required to move the cylinder or the blade out of the airflow and then measure the mass of the accreted ice. This is especially impractical for airborne measurements, although, owing to its simplicity, the rotating cylinder method was widely used for the measurement of LWC in the early years of icing research [8, 9].

3

HOT-WIRE SENSORS

Hotwire sensors calculate the LWC and TWC from the power that is required to evaporate the impinging particles. These instruments are often referred to as constant temperature probes because the sensing elements are configured to maintain a constant temperature. Upon impact of a water droplet or an ice particle, the sensing element is cooled, as heat is transferred to the particle until it eventually evaporates (this happens usually very quickly, within a few milliseconds). To compensate for the heat losses and maintain the sensor temperature, additional power is drawn by the probe. From the extra amount of power required, the LWC and TWC can be estimated. One of the first hotwire instruments was the King probe [10, 11], which features one cylindrical sensing element with a diameter of 1.8 μm. The King probe is only suitable for the measurement of liquid particles, as ice particles bounce off the sensor and are consequently not collected. Later hotwire instruments, such as the Nevzorov probe, the WCM-2000 [5] and the Ice Crystal Detector (ICD) [12] also possess sensors that are designed to trap ice particles (see Table 3.1). Furthermore, many hot wire instruments include reference sensors that are protected from particle impingement and aid in estimating convective heat losses in cloudy conditions. The operating principle is very similar for all of these sensors.

EVAPORATORS

Instruments that belong to the class of evaporators vaporize water droplets and ice particles within their sample volume and compare the resulting humidity to the ambient humidity [13]. The difference between the two humidities yields the estimate of the TWC. One instrument that employs this technique is the Isokinetic Probe (IKP), which was designed for the measurement of high ice water contents, where it achieves measurements of TWC with uncertainties of just a few percent. However, measurements of low total water contents in low-level clouds are subject to large uncertainties due to the large humidity values that are compared [14]. The IKP is therefore not commonly used for measurement campaigns in low-level clouds, but it has been operated in high LWC icing wind tunnels and contributes to the comparisons that I perform in Chapter 4.

PARTICLE SIZING METHODS

Data from particle counting and sizing instruments can be used for the measurement of LWC (the operating principles of such instruments are explained in Section 3.2.3, Section 3.2.4 and Section 3.3). Because the volume is related to the third power of the droplet size, all initial errors in the droplet size are amplified, leading to a large uncertainty in the LWC. Estimating the TWC of ice particles is even more difficult because the volume of an ice crystal cannot be easily assessed from a 2D image [15, 16]. Data from particle sizing instruments are therefore usually not used for the measurement of LWC and TWC, instead the three previously mentioned techniques are employed.

The main instrument for the measurement of LWC and TWC in this work is the Nevzorov probe, which I describe in detail in the following. The characteristics of some of the other LWC and TWC instruments, which were mentioned in the brief overview above and are of relevance for this work are listed in Table 3.1.
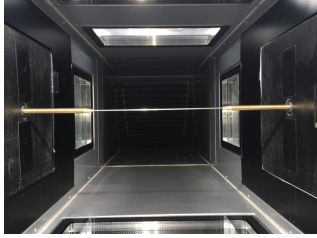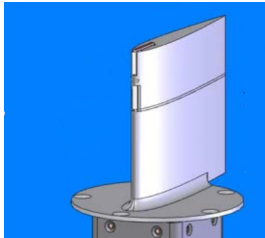
Instrument

Rotating cylinder
Manufacturer: n/a
Measurement technique: Accretion-based
Parameters measured: LWC
Cylinder diameters: Usually 2.5 - 5 mm

Figure source: Institute of Fluid Dynamics of TU Braunschweig

Icing blade
Manufacturer: n/a
Measurement technique: Accretion-based
Parameters measured: LWC
Blade width: Usually 3.125 mm

Figure source: Steen *et al.* [5]

WCM-2000
Manufacturer: SEA, Inc.
Measurement technique: Hot-wire
Parameters measured: LWC, TWC
Sensors (diameter): Wire (0.5 mm), cylinder (2.1 mm), forward-facing half pipe (2.1 mm)

Figure source: Steen *et al.* [5]

Ice Crystal Detector (ICD)
Manufacturer: SEA, Inc.
Measurement technique: Hot-wire
Parameters measured: LWC, TWC
Sensors: One concave, one convex
Sensor diameter: 2.4 mm for both sensors

Figure source: adapted from Lilie *et al.* [12].

Isokinetic Probe (IKP)
Manufacturer: National Research Council of Canada & Environment Canada
Measurement technique: Evaporator
Parameters measured: TWC

Figure source: SEA, Inc.

Table 3.1: LWC and TWC instruments that were used for comparisons to the Nevzorov probe.
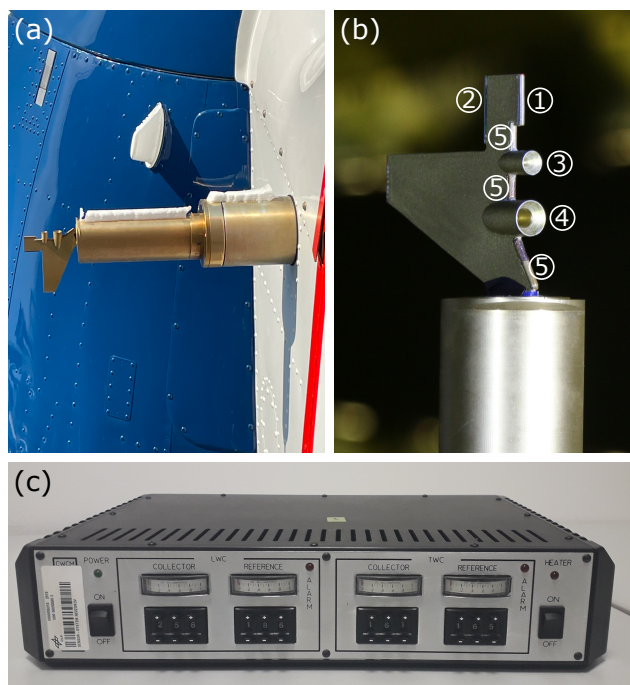
Figure 3.1: Components of the Nevzorov probe. (**a**): Pillar with sensor head, mounted on the Polar 6 aircraft. (**b**): Sensor head, with the individual components listed. Liquid water content (LWC) sensor (1), Reference sensor (2), 8 mm total water content (TWC) cone (3), 12 mm TWC cone (4), Leading edge heaters (5). (**c**): Control box, with the switches that are used to set the resistances visible.

3.1.1. THE NEVZOROV PROBE

The Nevzorov probe is a hotwire instrument for the measurement of cloud LWC and TWC that was conceived in the 1970s by the Cloud Physics Laboratory of the Central Aerological Observatory of the Soviet Union [17]. The Nevzorov probe consists of a sensor head, a pillar and a control box. The pillar is attached to the aircraft fuselage, or in IWTs to one of the walls and extends into the measurement volume (Fig. 3.1a). The sensor head is mounted on top of the pillar and carries the individual sensors (Fig. 3.1b). Typical Nevzorov sensor heads carry three types of sensors for different purposes. The LWC sensor is cylindrical, it collects predominantly water droplets, while ice particles bounce off on its surface. The TWC sensors, on the other hand, have cavities that allow them to retain both water and ice particles (see Fig. 3.2). Finally, reference sensors are protected from cloud particle impact and measure only convective heat losses. Their measurements are used to correct those of the LWC and TWC sensors. The sensor head is mounted on a rotatable disk that is inserted into the upper part of the Nevzorov pillar. This rotatable disk allows the Nevzorov sensor head to compensate for pitch changes during flight. The control box (Fig. 3.1c) contains most of the electronics and an interface that allows the user to set the temperature of the individual sensors.
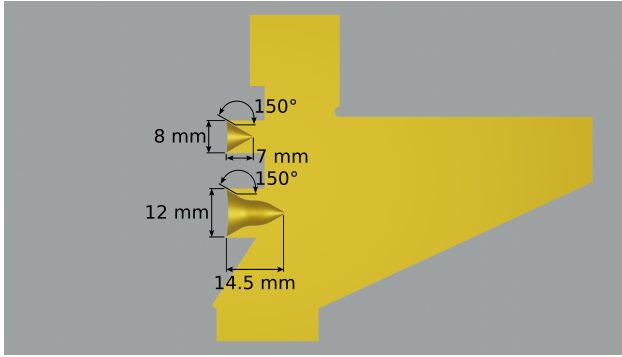
Figure 3.2: cross section of the Nevzorov sensor head, showing the 7 mm deep inverted conical cavity of the 8 mm total water content (TWC) cone and the 14.5 mm deep cavity of the 12 mm TWC cone.

The first version of the instrument was designed to measure only cloud TWC. Later, the cylindrical sensor for LWC measurements was added [17]. In the 1990s and 2000s, the Nevzorov probe saw wide usage during numerous icing wind tunnel and flight campaigns [18–21]. As a consequence of these tests, design improvements were made, the most notable being the introduction of a deeper TWC cone to mitigate splashing and bouncing effects [22]. The newest version of the sensor head, which is investigated in this study, features two TWC cones with diameters of 8 and 12 mm and one cylindrical hotwire. The detailed principle of operation is explained in the following.

PRINCIPLE OF OPERATION

The Nevzorov probe outputs analog signals that correspond to the voltages V_c, V_r and currents I_c, I_r that are required to maintain the temperature of the collector sensors (i.e. the LWC and TWC sensors) and reference sensors. The power drawn by a collector and a reference sensor is $P_c = V_c I_c$ and $P_r = V_r I_r$, respectively. Heat losses of a reference sensor are mainly due to convection hence its power consumption is assumed to be equal to [17]:

$$P_r = \alpha_r S_r (T_r - T_a). \tag{3.1}$$

Here, T_r and T_a are the temperatures of the reference sensor and the ambient air, S_r is the sample area of the reference sensor. The factor α_r is the heat transfer coefficient for the sensor, which in the literature is specified as $\alpha_r = \kappa g_r Nu_r$, where κ is the thermal conductivity of air, g_r the factor which takes into account the surface geometry of the sensor and Nu_r the Nusselt number [17]. In purely liquid clouds, the collector sensors need to heat the droplets from the droplet temperature T_d to the evaporation temperature T_e. The latent heat required for the evaporation at temperature T_e is $L(T_e)$, which can be approximated by the following formula [23]:

$$L(T_e) = 2486.9696 - 2.025056 \cdot T_e - 29.288 \cdot 10^{-4} \cdot T_e^2 \ [\text{Jg}^{-1}]. \tag{3.2}$$
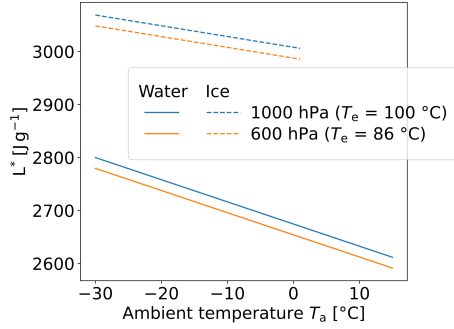
Figure 3.3: The energy needed to vaporize water or ice (L^*) plotted versus the ambient temperature for pressures of 600 and 1000 hPa. Higher energies are required to vaporize ice because the latent heat of fusion needs to be compensated. The dependence of the latent heat on evaporation temperature (and therefore on pressure, see Eq. (3.2)) is minimal and not perceptible from the image.

The specific energy needed for heating and evaporation is termed (L^*) and is given as:

$$L^*(T_e, T_a) = c_w(T_e - T_a) + L(T_e). \tag{3.3}$$

Here, $c_w = 4.1813 \, \mathrm{J\,g^{-1}K^{-1}}$, which is the specific heat capacity of water. T_d can be assumed to be equal to T_a. The dominance of the latent heat term means that even differences of 10 °C between T_d and T_a, which can occur for large droplets in wind tunnels [24], result in an error of less than 2% in L^* for all temperatures and pressures at which atmospheric icing conditions exist. A plot of the dependence of L^* on the ambient temperature is shown in Fig. 3.3.

For ice crystals, which will become relevant in Chapter 5 of this thesis, the energy needed to warm the ice crystals from the ambient temperature to 0 °C and the latent heat of fusion for ice have to be added to Eq. (3.3). For ice crystals the specific energy L_i^* is:

$$L_i^* = -c_i T_a + L_f + c_w T_e + L(T_e), \tag{3.4}$$

where $c_i = 2.027 \, \mathrm{J\,g^{-1}K^{-1}}$ is the specific heat capacity of ice and $L_f = 333.55 \, \mathrm{J\,g^{-1}}$ is the latent heat of fusion. The total power consumption of the collector sensors is calculated by adding the term that describes the convective heat losses to the term that contains the power required for heating and evaporating the impinging water or ice. I refer to the two terms as the dry term and the wet term from now on:

$$P_c = \alpha_c S_c (T_c - T_a) + \varepsilon W L^* S_c U. \tag{3.5}$$

Here, W denotes the water content of the air, S_c is the sensor sample area, U is the airspeed and ε is the collection efficiency of the sensor, which is explained in the subsequent section. A relation between the convective heat losses of the reference sensor and the convective heat losses of the collector sensor can be obtained from measurements in dry air:

$$\frac{P_{c,\mathrm{dry}}}{P_r} = k. \tag{3.6}$$

The ratio k only depends on parameters such as airspeed, pressure and temperature [17]. For time intervals where these parameters are constant, one can rearrange and insert Eq. (3.6) into Eq. (3.5) and solve for W:

$$W = \frac{P_c - kP_r}{\varepsilon L^* S_c U}.$$ (3.7)

COLLECTION EFFICIENCY

The collection efficiency ε in Eq. (3.7) describes how much of the water present in a volume of air upstream of a sensor sample area is collected by the sensor. The minimum value for the collection efficiency is therefore zero (none of the water is collected) and the maximum value is one (all the water is collected). Collection efficiencies can be smaller than 1 for two reasons. First of all, the curvature of the streamlines around the sensor results in drag forces that can alter the trajectory of the particle such that it does not impact. The efficiency that describes this effect is referred to as the collision efficiency. Secondly, splashing or shattering of the particle on impact with the sensor may result in an incomplete collection and thus in an underestimation of the water content. This effect is referred to as the capture efficiency in this manuscript.

The collection efficiencies are in general size-dependent. Let us for now only consider the droplet collision efficiency, which has been thoroughly investigated in the literature [25–29]. A droplet trajectory can be described as a function of two parameters, the droplet inertia parameter K, which relates the droplet inertia to the drag forces that act on the droplet, and the free stream droplet Reynolds number Re [30]. The two parameters are specified in Eq. (3.8) and Eq. (3.9), respectively.

$$K = \frac{1}{9} \frac{d^2 U \rho_w}{c \mu_a}.$$ (3.8)

$$Re = \frac{\rho_a U d}{\mu_a}.$$ (3.9)

In the equations, d denotes the droplet diameter, ρ_a and ρ_w are the densities of air and water, c is the characteristic length of the geometry for which the impingement is calculated and μ_a is the dynamic viscosity of air. If the Reynolds number is held constant, droplet collision efficiencies increase with an increase in the droplet inertia parameter K [30]. Therefore, larger droplets, a larger airspeed and a smaller sensor geometry result in higher collision efficiencies. Collision efficiencies are available from the literature for the LWC sensor and the 8 mm cone of the Nevzorov probe. The shape of the LWC sensor is approximately cylindrical and its collision efficiency can be calculated analytically from the formulae of Finstad *et al.* [29] or Langmuir and Blodgett [25]. In this work, I use the latter, which is also recommended in ARP5905 [31] for the rotating cylinder method. Collision efficiency curves of the 8 mm cone have been derived empirically by Korolev *et al.* [17] for velocities between 100 and 150 $\mathrm{m\,s}^{-1}$ and were computed on the basis of a 2-D fluid simulation by Strapp *et al.* [19] for velocities of 67 and 100 $\mathrm{m\,s}^{-1}$. In this work I always correct 8 mm cone measurements with the collision efficiency curves from
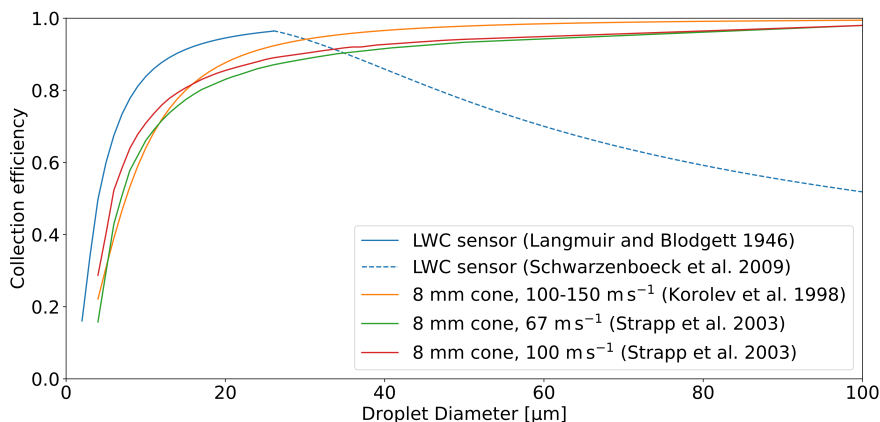
Figure 3.4: Collection efficiencies for the Nevzorov probe sensors that are available from the literature. The curves of Strapp *et al.* [19] (green, red) were only computed up to diameters up to 50 µm and were extrapolated to attain a collection efficiency of 0.98 at a diameter of 100 µm and a collection efficiency of 1 at a diameter of 250 µm. The curve of Schwarzenboeck *et al.* [21] (blue dashed) was computed for the volume mean diameter (VMD) of a cloud, rather than for individual droplet diameters.

Strapp *et al.* [19], using the curve for the velocity value that matches the encountered airspeed best. The reader should note, that these collision efficiency curves may still contain significant errors for small droplet sizes [19]. Regarding the overall collection efficiency of the 8 mm cone, splashing and re-entrainment of water or ice is at present assumed to be irrelevant [22]. On the contrary, significant splashing may occur on the LWC sensor for droplets whose diameter exceeds approximately 30 µm, which leads to a decrease in the capture efficiency of the LWC sensor that has been characterized by Schwarzenboeck *et al.* [21]. All the collection efficiency curves that are available at present are displayed in Fig. 3.4. For the 12 mm cone, which is a new addition to the Nevzorov sensor head, no collection efficiencies have been published up to now. As part of this work, I experimentally derive the collection efficiency of the 12 mm cone from the measurements that were obtained during wind tunnel campaigns.

DATA ACQUISITION

The Nevzorov probe is supplied to customers without a data acquisition system. Hence, as part of this thesis, a suitable acquisition system was selected. In this section, I briefly explain the considerations that influenced the choice and setup of the data acquisition. The Nevzorov probe measures eight different quantities; one voltage and one current, for each of its four sensors. Each of these quantities is derived from a differential measurement between two analog signals which are output by the control box. Consequently, for the data acquisition, 16 different signals need to be recorded and digitized by an analog to digital converter (ADC). The maximum voltage output from the control box is +10 V and -10 V for the positive and negative channels, respectively. For the data acquisition, I chose the LabJack

U6 ADC together with a MUX80 multiplexer, both of which are produced by the LabJack cooperation [32]. This setup can record all 16 channels in a differential configuration. The resolution of the ADC is approximately 300 µV, hence the signals of the Nevzorov probe, which are on the order of several volts, can be very well resolved. The ADC was configured to record data with a frequency of up to 1000 Hz, the high frequency was chosen because it was hypothesized that the impact of individual large droplets might be observable in the Nevzorov signal (this topic is further discussed in Section 4.3.7). Among the data presented in this work, only the icing wind tunnel (IWT) data and the flight data from the European SENS4ICE campaign were acquired with the system described above. During the HALO-AC³ campaign[1], an ADC chosen by Alfred-Wegener Institute was used with a sampling frequency of 100 Hz.

DRY AIR MEASUREMENTS

An accurate estimate of the dry term (Eq. (3.5)) is of utmost importance when evaluating measurements of the Nevzorov probe. It is not unusual that the dry term is by a factor of ten larger than the wet term. In such cases small errors in the dry term lead to significant errors in the LWC or TWC estimate (this is further discussed in Section 4.3.6). In IWTs the dry term of a collector sensor and the factor k (see Eq. (3.6)) can be obtained for a given airspeed and temperature from measurements where the droplet spray is turned off. For the IWT measurements presented in this thesis, the common practice was to collect measurements in dry air for all temperature and airspeed combinations that would be used for the test points. During some IWT measurements droplet impingement on the reference sensor was detected, which contaminated the dry air signal. The impingement was usually caused by an imperfect alignment or oscillations of the sensor head. For those cases, the convective heat losses were estimated from the power consumption before the start of the measurement. As tunnel temperature and airspeed are constant and independent of the droplet spray, the dry term before the start of the spray is very similar to the one after the start of the spray. In-flight, where continuous changes in airspeed, pressure and temperature occur, determination of the dry term is challenging. Nonetheless, a suitable procedure for the evaluation of the in-flight data was found, which is presented in Chapter 5.

The operating principles for instruments that measure the bulk LWC and TWC have now been thoroughly described and an overview of the challenges that affect these measurement principles was given. Furthermore, suitable methods to correct for reduced droplet collection efficiencies were explained. I now proceed to explain the measurement techniques for the two other important features of a cloud, the particle size distribution and the particle shape.

---

[1]The campaign name HALO-AC³ is a combination of two acronyms. HALO is the name of the High-Altitude Long Range Research Aircraft of the German Aerospace Center. The acronym AC³ is short for the project name: «Arctic Amplification: Climate Relevant Atmospheric and Surface Processes and Feedback Mechanisms».

3.2. PARTICLE SIZE MEASUREMENTS WITH SCATTERING PROBES

Instruments that count particles and size them based on the intensity of scattered light are a vital part of this thesis. Such instruments are called scattering probes and are the subject of this section. Before I explain their measurement principle, I use the following two subsections to introduce the necessary parameters to describe an electromagnetic wave and to provide a summary of the fundamentals of light scattering. The descriptions provided in these subsections (Section 3.2.1 and Section 3.2.2) mostly follow those of Bohren and Huffman [33].

All scattering probes use lasers that emit a collimated beam of coherent light and these properties are assumed for the lasers in the following.

3.2.1. DESCRIPTION OF LIGHT RAYS

The light emitted by a laser is an electromagnetic wave [34] whose electric field at time t and the location z along the direction of propagation is [33]:

$$\mathbf{E} = \mathbf{E}_0 \exp(ikz - i\omega t), \tag{3.10}$$

where k is the wave vector and ω is the angular frequency. Sensors, such as photodiodes, do not measure the electric field of electromagnetic radiation, but the power that arrives at the sensor. This power is the Poynting vector $\mathbf{S}$ of an electromagnetic wave:

$$\mathbf{S}(t) = \mathbf{E}(t) \times \mathbf{H}(t), \tag{3.11}$$

where $\mathbf{H}$ is the magnetic field associated with the electromagnetic wave. The Poynting vector varies with the angular frequency ω. Because typical ω values for light waves are very high, sensors usually measure the time average of the Poynting vector [33]. This time average is called irradiance and has the unit Wm^{-2} (irradiance is equivalent to the intensity, but usage of the term intensity may lead to confusion with other quantities such as the radiant intensity or the spectral intensity and is thus avoided from now on). After integration of Eq. (3.11) over at least one period and some additional manipulations the irradiance is calculated as [33]:

$$I = \langle \mathbf{S} \rangle = \frac{k \langle |\mathbf{E}|^2 \rangle}{2\omega\mu}. \tag{3.12}$$

Here, the rectangular brackets signify the time average and μ is the magnetic permeability. Apart from the irradiance, the polarization of electromagnetic waves is especially important for this work. The polarization is commonly specified through the Stokes parameters S_0, S_1, S_2 and S_3, which are stated in the following. At first, the electric field vector of the electromagnetic wave is separated into two orthogonal components [33]:

$$\mathbf{E}_0 = E_\parallel \mathbf{e}_\parallel + E_\perp \mathbf{e}_\perp. \tag{3.13}$$

The electric field component in either direction is a complex number with the complex amplitudes $a_\parallel$ and $a_\perp$ and the phases $\delta_\parallel$ and $\delta_\perp$:

$$E_\parallel = a_\parallel \exp(-i\delta_\parallel) \text{ and } E_\perp = a_\perp \exp(-i\delta_\perp). \tag{3.14}$$

The first Stokes parameter represents the irradiance of the beam (see Eq. (3.12)), it is stated below as the time average of the parallel and perpendicular components of the electric field [33, 35]:

$$S_0 = c\langle E_\parallel E_\parallel^* + E_\perp E_\perp^* \rangle,$$ (3.15)

where c is the factor $k/2\omega\mu$ from Eq. (3.12). The second Stokes parameter represents the difference between the parallel and perpendicular polarized light with respect to the coordinate system of choice:

$$S_1 = c\langle E_\parallel E_\parallel^* - E_\perp E_\perp^* \rangle.$$ (3.16)

The third Stokes parameter also represents the difference between parallel and perpendicular polarized light but for a coordinate system that has been rotated by 45° compared to the coordinate system that was used to specify the second Stokes parameter. The basis vectors of this new coordinate system are [33]:

$$\mathbf{e}_a = \frac{1}{\sqrt{2}}(\mathbf{e}_\parallel + \mathbf{e}_\perp) \text{ and } \mathbf{e}_b = \frac{1}{\sqrt{2}}(\mathbf{e}_\parallel - \mathbf{e}_\perp).$$ (3.17)

The components of the electric field in this coordinate system can be written as:

$$E_a = \frac{1}{\sqrt{2}}(E_\parallel + E_\perp) \text{ and } E_b = \frac{1}{\sqrt{2}}(E_\parallel - E_\perp).$$ (3.18)

The difference between the irradiances in our two new principal directions is found analog to Eq. (3.15), by using the expressions from Eq. (3.18):

$$S_2 = c\langle E_a E_a^* - E_b E_b^* \rangle = c\langle E_\parallel E_\perp^* - E_\perp E_\parallel^* \rangle.$$ (3.19)

Lastly, it is also possible to use left-handed and right-handed circular basis vectors [33]:

$$\mathbf{e}_r = \frac{1}{\sqrt{2}}(\mathbf{e}_\parallel - i\mathbf{e}_\perp) \text{ and } \mathbf{e}_l = \frac{1}{\sqrt{2}}(\mathbf{e}_\parallel + i\mathbf{e}_\perp),$$ (3.20)

where $\mathbf{e}_r$ and $\mathbf{e}_l$ fulfill the following:

$$\mathbf{e}_r^\mathsf{T} \mathbf{e}_r^* = 1 \text{ and } \mathbf{e}_l^\mathsf{T} \mathbf{e}_l^* = 1 \text{ and } \mathbf{e}_r^\mathsf{T} \mathbf{e}_l^* = 0.$$

The representation of the electric field in this coordinate system is:

$$E_r = \frac{1}{\sqrt{2}}(E_\parallel - iE_\perp) \text{ and } E_l = \frac{1}{\sqrt{2}}(E_\parallel + iE_\perp).$$ (3.21)

The last Stokes parameter is the difference between the irradiances of the right-hand and the left-hand circular polarized electric fields [33]:

$$S_3 = ic\langle E_\perp^* E_\parallel - E_\parallel^* E_\perp \rangle.$$ (3.22)

The meaning of the Stokes parameters can be grasped from Fig. 3.5. The first Stokes parameter, which corresponds to the irradiance, is not shown in this image, but for completely polarized light it can be thought of as the length of the arrow. A nonzero value in V indicates the presence of circular polarization.
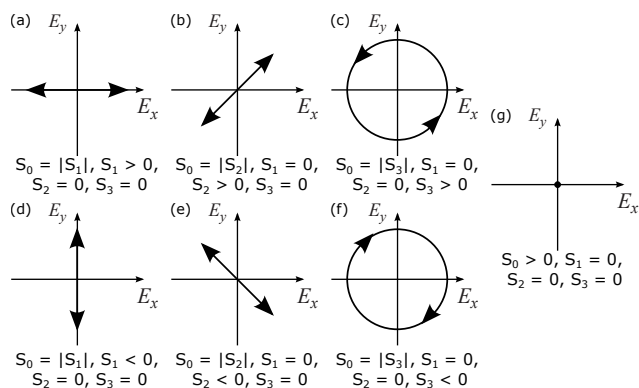
Figure 3.5: Illustration of polarization states that result from nonzero values in one of the three parameters. Plots **(a)** and **(d)** show light that is linearly polarized in the x and y direction, respectively. Plots **(b)** and **(e)** show light linearly polarized with respect to the basis vectors a and b (see Eq. (3.17)). Plots **(c)** and **(f)** display right- and left-hand circularly polarized light, respectively. Plot **(g)** shows (or in fact does not show), the Stokes parameters for the case of unpolarized light, which are all zero, except for S_0. Image adapted from Dan Moulton, CC BY-SA 3.0, via Wikimedia Commons and Cepheiden (https://commons.wikimedia.org/w/index.php?curid=11771529).

3.2.2. LIGHT SCATTERING BY SMALL PARTICLES

In this section, I explain the interaction of electromagnetic waves with small particles. I only consider elastic scattering, i.e. scattering where the wavelength of the light is not changed by the scattering process.

First, let me deliberate on a particle of arbitrary size and shape. At an elementary level, such a particle is composed of electrons, protons and neutrons [33]. If an electromagnetic wave passes through it, the electrical charges contained within the particle (i.e. the electrons and protons) are forced into an oscillatory motion by the electric field of the wave. Energy is transferred from the wave to the electric charges in that process. Through their motion, the electrical charges re-emit electromagnetic energy which gives rise to a new electromagnetic wave, known as the scattered radiation [33].

How exactly the particle responds to exposure to an electromagnetic wave depends on the wavelength of the incident light, the refractive index of both the particle and the surrounding medium, and on the particle size and shape. Usually, the first three properties are known and only the particle size and shape are of interest. Depending on the particle size, different scattering patterns are distinguished. If the particle is small compared to the wavelength of the incident light, all the electric charges within it oscillate approximately in the same phase as the incident light [33, 36]. The resulting scattering pattern is best described by Rayleigh scattering [37]. Rayleigh scattering occurs, for example, in air on molecules such as N_2 and O_2 and on aerosols. For larger objects, such as a water droplet, the assumption that all particles oscillate in the same phase as the incident light no longer holds true. Instead, scattered wavelets from different regions within the object superpose and form a scattering pattern that contains peaks and troughs. Treatment of the scat-

tering phenomena produced (e.g. by a water droplet) can therefore no longer be described by Rayleigh scattering but requires the use of Mie-Theory [38]. Here I do not delve deep into the fundamentals of Mie scattering problems, which have been treated in various textbooks [33, 39, 40]. Instead, I assume that the solution to the Mie scattering problem is available in the following form:

$$\mathbf{S}_s(\theta,\phi) = \mathbf{M}(\theta,\phi)\,\mathbf{S}_i, \tag{3.23}$$

where $\mathbf{S}_i$ is the Stokes vector of the incident light. $\mathbf{M}(\theta,\phi)$ is a so-called Müller-matrix, a 4×4 matrix that describes the transformation of a Stokes vector. It is named after Hans Müller who established the formalism in 1943 [41]. $\mathbf{M}(\theta,\phi)$ represents the differential scattering cross section for the infinitesimal small solid angle element defined by θ and ϕ. The differential scattering cross section relates the irradiance of the incident light to the irradiance of the scattered light that is observed under a given unit solid angle [33, 42] and is defined as:

$$\frac{\mathrm{d}\sigma}{\mathrm{d}\Omega} = \frac{r^2\,I_s(\theta,\phi)}{I_i} = \frac{P_{s,\Delta\Omega}(\theta,\phi)}{I_i}. \tag{3.24}$$

Here, I_i and I_s denote the incident and scattered irradiances, $P_{s,\Delta\Omega}$ is the scattered power per solid angle. $\mathbf{M}(\theta)$ has the units $\mathrm{m^2\,sr^{-1}}$, which means that the Stokes vector of the scattered light S_s from Eq. (3.23) does not specify an irradiance but a radiant intensity.

Most computer codes that are available for the calculation of Mie scattering do not output $\mathbf{M}(\theta,\phi)$, but only $\mathbf{M}(\theta)$. In such cases, ϕ is assumed to be equal to the azimuthal angle under which the observer is positioned. The plane that is spanned by the direction of the incident light (the positive z-direction) and the direction under which the scattered light is observed (given by a vector $\mathbf{r}$) is called the scattering plane (see Fig. 3.6) [43]. The scattering plane is of importance for the definition of the polarization of the incident light, the terms parallel polarized (p-polarized) and perpendicular polarized (s-polarized) usually refer to the polarization of the light with respect to the scattering plane. I also adopt this convention in this work. Fig. 3.7 depicts three plots that show the scattering cross section as a function of the polar angle θ for water droplets with diameters of 0.2, 2 and 20 µm. Each plot contains two scattering cross section curves, one for incident p-polarized light and one for incident s-polarized light. Clearly, the scattering cross sections for p- and s-polarized incident light are dissimilar. It follows that for polarized light no rotational symmetry of the scattering cross section around the z-axis exists (as opposed to unpolarized light, where the scattering cross section is independent of ϕ [44]). If the point of observation was rotated by 90° around the z-axis, and the laser orientation was retained (i.e. the perpendicular polarized light is parallel to the scattering plane), Fig. 3.7 would look exactly the same except that the curves for p- and s-polarized light were switched.

Perfectly spherical particles do not cause any depolarization of the incident wave, i.e. incident p-polarized light (with respect to the scattering plane) results in the scattering of only p-polarized light and incident s-polarized light results in the scattering of only s-polarized light [33].
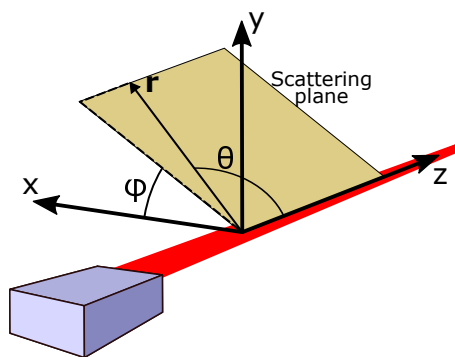
Figure 3.6: Definition of the angles θ and ϕ and of the scattering plane.

The three plots in Fig. 3.7 also demonstrate the following:

- The scattering cross section and consequently also the scattered irradiance are correlated with particle size.

- The scattering pattern becomes more complex with increasing particle size.

- The fraction of light scattered in the forward direction increases with increasing particle size.

The first of these points is the basis of the particle size measurement with scattering probes. A sketch of a possible setup of a scattering probe is shown in Fig. 3.8. Usually, scattering probes possess a single detector that collects light from a fixed range of angles (pairs of θ and ϕ). The position of the detector varies in different probe designs. In the next section, I explain the particle size measurements with forward scattering probes, i.e. scattering probes where the detector is placed at the angle $\theta = 0$ directly on the z-axis. While the focus of this thesis and especially of research question II is on the Backscatter Cloud Probe with Polarization Detection (BCPD), measurements of forward scattering probes are used for several purposes in Chapters 4, 5 and 6. It is therefore important to understand the operating principle, advantages and disadvantages of forward scattering probes. The measurement principle of the BCPD is explained afterward in Section 3.2.4.

3.2.3. FORWARD SCATTERING PROBES

Established forward scattering probes are the Forward Scattering Spectrometer Probe (FSSP) [45, 46], the Cloud Droplet Probe (CDP) [47], the Cloud Aerosol Spectrometer (CAS) [48] and the Fast Cloud Droplet Probe (FCDP) [49] (The CAS measures both, forward- and backscattered light). Here, I provide an overview of the measurement principle of the CDP, which is the forward scattering probe that is used the most in this thesis. The optical setup of CAS, FCDP and FSSP is not described in this work but is relatively similar to that of the CDP [49–51].
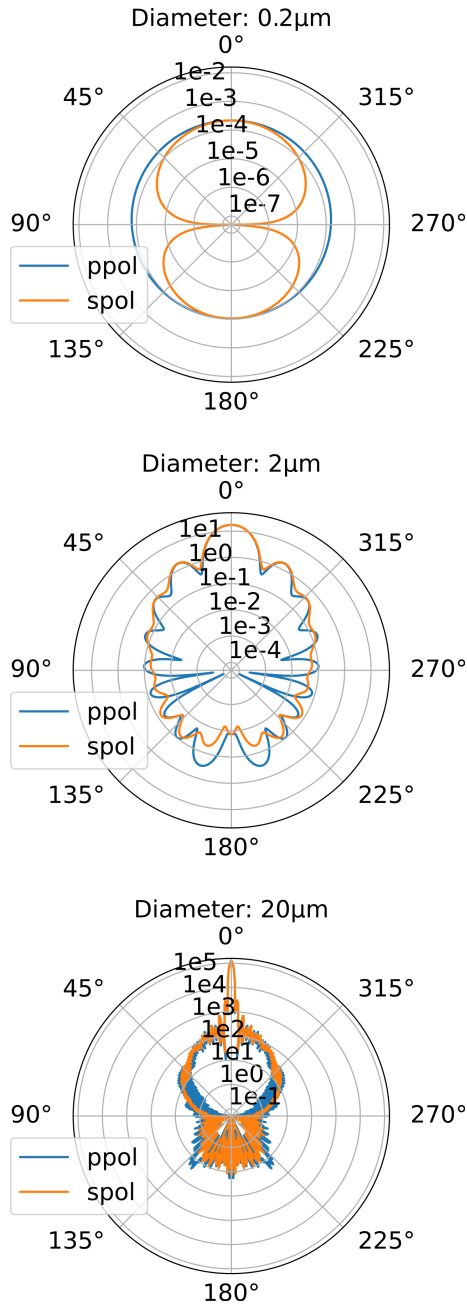
Figure 3.7: Scattering behavior for spherical cloud droplets with 0.2 (top), 2 (middle) and 20 µm (bottom) diameter for incident parallel polarized (p-polarized) and perpendicular polarized (s-polarized) light, plotted in blue and orange, respectively. The angular coordinate shows the angle θ, while the radial coordinate represents the scattering cross section $d\sigma/d\Omega$ in m^2/sr for incident p- and s-polarized light. The scattering behavior of the droplet with 0.2 µm diameter is still well described by Rayleigh scattering, while for the description of the other two scattering patterns Mie-theory is required.
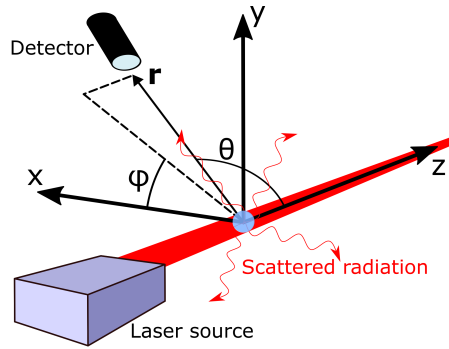
Figure 3.8: Measurement principle of a scattering probe.

MEASUREMENT PRINCIPLE OF FORWARD SCATTERING PROBES

The optical system of a CDP can be seen in Fig. 3.9. The laser beam is produced by a laser diode and reflected on a mirror (upper part of Fig. 3.9). When the laser beam interacts with a droplet, its light is scattered as described in the previous section. The scattered light is collimated by a lens. Forward scattering probes dump the light collected within a small angle from the z-axis ($\theta = 0°$ to $4°$) to avoid measuring the not-scattered, direct laser beam. The light scattered from angles between 4-12° is reflected on a mirror toward another lens, from where the light is projected onto a qualifying and a sizing detector (bottom right Fig. 3.9). The names of these detectors are self-explanatory, the sizer measures the overall irradiance of the incident light, while the qualifier uses an additional slit (qualifier mask), to exclude incident light from out-of-focus particles. A particle is only counted and sized if the ratio between the signals at the qualifying detector and the sizing detector exceeds a certain threshold. If the ratio is too low, the particle is considered to have passed outside of the qualified sample area of the probe and is rejected [47].

The scattering cross section of the annular area between 4-12° from which the scattered light is collected in the CDP, CAS, FCDP and FSSP can be computed from Mie-Theory [38]. Differences between the scattering of p- and s-polarized light need not be considered for the computation of the overall scattering cross sections of these instruments, as they cancel out due to the symmetry of the area from which light is collected around the z-axis. The relationship between the size of spherical water droplets and their scattering cross sections in the direction of the CDP collection angles can be seen in Fig. 3.10. The figure shows that the scattering cross section does not increase monotonously with particle size. Instead, it exhibits many small-scale oscillations, which are due to the interference pattern of the Mie scattering. These oscillations are problematic because they degrade the achievable size resolution. Different droplet diameters can produce the same scattering cross section value (that corresponds to an irradiance measurement at the sizer). Such ambiguous solutions may arise for practically every scattering cross section value of the curve, however, in terms of absolute error, the problem is most severe at droplet
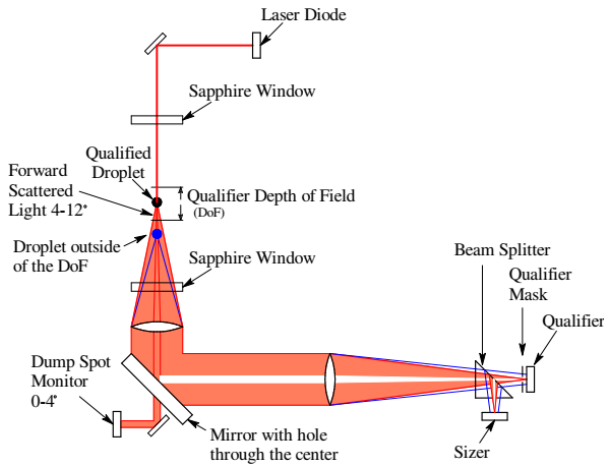
Figure 3.9: Optical system of the CDP. Image from Lance *et al.* [47].

diameters between 2-10 µm, where the slope of the curve is small. This is apparent from Fig. 3.10. A scattering cross section of 10 µm^2 can correspond to several diameters between 3.1 µm and 7.1 µm, the size ambiguity thus extends over 4 µm. A scattering cross section of 320 µm^2 however corresponds to at least a 48.2 µm diameter droplet and at most to a 49.2 µm droplet, the extent of the ambiguity is consequently much smaller. These ambiguities in the solution are referred to as Mie-ambiguities [52].

The CDP is able to size water droplets with diameters between 2 and 50 µm. This size range is typical for scattering probes. The size range of the CDP is chosen such that it can measure the most common cloud droplet sizes [53], but not aerosol particles, which are typically below 2 µm in diameter and also no drizzle or rain drops. The upper size limit of 50 µm is a consequence of multiple design considerations. The sample area and the width of the laser beam would need to be increased to measure droplets larger than 50 µm, which are rare compared to small droplets. The increase of the laser beam width would in turn increase the probability of multiple droplets being in the sample volume simultaneously (this effect is known as coincidence and is further discussed in Section 3.2.3). Also, the size resolution of the individual sizes would be decreased due to limitations in the resolution of the analog-to-digital converter, which records the voltage at the photodetector. Lastly, optical array probes, which are explained in Section 3.3, are more convenient for the measurements of large particles, since their images also provide information about the particle shape. Therefore, it is common practice to measure clouds that include drizzle drops or large ice particles with multiple cloud probes.

It is important to note that the presented scattering cross sections are only valid for spherical water droplets [54]. Ice particles have a different refractive index and most often also shapes that are asymmetric. Consequently, the relationship between size and scattered irradiance depends on ice particle size, shape and orien-
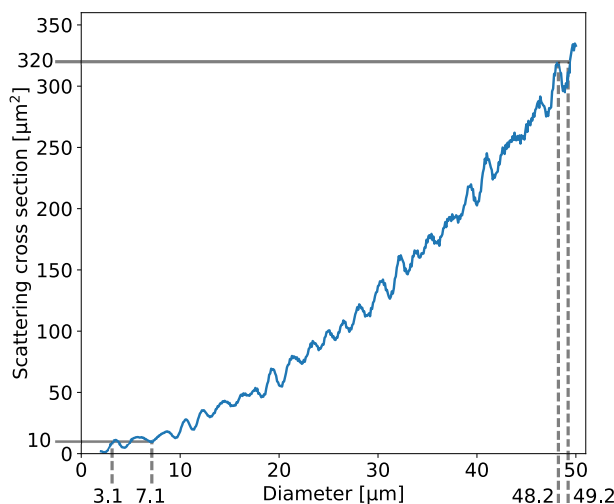
Figure 3.10: Relationship between the diameter of a droplet and the scattering cross section of the particle for $4° \leq \theta \leq 12°$. Many forward scattering probes use this or a very similar range of angles, e.g. the Cloud Droplet Probe (CDP), the Fast Cloud Droplet Probe (FCDP), the Cloud Aerosol Spectrometer (CAS) and the Forward Scattering Spectrometer Probe (FSSP). The influence of the Mie-ambiguities is exemplified for scattering cross section values of 10 and 320 μm^2.

tation [55]. In many cases, different combinations of these parameters cause identical scattered irradiance in the angular range that is measured by the instrument. The ability to derive ice particle sizes is therefore severely limited and shall not be attempted in the scope of this thesis. Also for the BCPD, which is explained in Section 3.2.4, the computed scattering cross sections are only applicable to water droplets.

MEASUREMENT UNCERTAINTIES OF FORWARD SCATTERING PROBES
The measurements of forward scattering probes are subject to measurement errors, which introduce uncertainty. Understanding these uncertainties is important for the interpretation of the results that are presented in subsequent parts of this thesis. In the following, I provide an overview of the relevant uncertainties for the CDP.

Scattering probes measure two important properties of an ensemble of particles, the particle number and the particle size distribution. Consequently, two types of errors are distinguished [56], namely:

- Counting error: The difference between the measured and the true number of particles per unit volume.

- Sizing error: The difference between the measured and the true size of a given particle.

The counting error is defined for measurements of multiple particles, while the sizing error is defined for a single particle. The sizing error usually varies with the droplet size that is investigated (in fact, even the counting error may vary with the

droplet size distribution that is investigated, but more to that later). A statement of a single sizing accuracy value is imprecise, instead, one should generally provide sizing errors for selected droplet sizes.

Faber *et al.* [57] provide one of the most thorough reviews of the measurement errors of a CDP based on laboratory tests with a droplet generator. They measured the response of the CDP to droplets of different sizes across the entire sample area. They report that the relative counting error of the CDP is 2% or smaller in 95% of the sample area. Regarding the sizing error, they find a dependence not only on droplet size but also on the sampling location within the sample area. If the mean measured diameter from all locations within the sample area is considered, the relative sizing error for a droplet of a given diameter is within 10% for all sizes that they investigated. However, for individual droplets, significantly stronger over- and undersizing may occur, depending on the location at which the droplet passes through the sample area. That means that size distributions are erroneously broadened when measured by the CDP. The previously mentioned Mie-ambiguities further contribute to the broadening.

The exact magnitude and direction of this broadening depends on the calibration and the size binning that is applied to the CDP. For most of the measurements presented in this work, a CDP of the German Aerospace Center (DLR) (DLR-CDP) is used, which I calibrated on multiple occasions according to the procedure described in [42]. The DLR-CDP is older than the CDP used by Faber *et al.* [57] and has not been masked with a pin-hole as suggested in Lance [58]. The sizing and counting errors of the DLR-CDP are therefore likely larger than those stated in Faber *et al.* [57].

Laboratory calibrations can only mimic the behavior of an instrument in flight or in an IWT to a limited extent. This is mostly due to the much higher number concentrations that are encountered in such environments. The high number concentrations give rise to a very prominent error source: droplet coincidence. Droplet coincidence occurs when light from multiple droplets affects the sizer at the same instant [47]. This happens either when multiple droplets are within the sample area (standard coincidence), or if a single droplet is within the sample area, but a second droplet is at a nearby location (an area designated as the extended sample area by Lance *et al.* [47]), such that it still affects the signal measured at the sizer. Due to the much larger size of the extended sample area compared to the qualified sample area, the second type of coincidence, which is referred to as extended coincidence [47] is much more common than the first. Droplet coincidence may affect the counting and the sizing error. In the case of standard coincidence (two droplets within the qualified sample area), the two coincident droplets are counted as a single, larger one, thus the coincidence event results in an oversizing and an undercounting. On the contrary, extended coincidence may result in either an oversizing or an undercounting, depending on whether the signal from the droplet in the extended sample area leads to a disqualification of the droplet within the qualified sample area or not [47].

After the general overview of the well-established forward scattering instruments, I now proceed to discuss the BCPD, a slightly different scattering probe

that is the subject of research question II and therefore forms an important part of this thesis.

3.2.4. THE BACKSCATTER CLOUD PROBE WITH POLARIZATION DE-TECTION

Unlike the previously mentioned forward scattering probes, the BCPD is, as the name suggests, an instrument that derives the particle size from the irradiance of the backscattered light. It was developed by the American manufacturer Droplet Measurement Techniques. The BCPD measures droplets with diameters between 2-42 µm, i.e. its size range is relatively similar to that of the CDP but ends at a slightly lower maximum value (the maximum droplet diameter that can be measured with the CDP is 50 µm).

The BCPD is based on the Backscatter Cloud Probe (BCP), the first backscatter instrument that was developed by Droplet Measurement Techniques, which has seen wide use in the In-service Aircraft for a Global Observing System (IAGOS) project [60, 61]. In contrast to the BCP, the BCPD includes a polarization filter to measure the depolarization that occurs in the scattering process. The depolarization can be used for assessments of the particle shape.

The optical setup of the BCPD is shown in Fig. 3.11a. Before I begin with the explanation of the optical setup, let us define the relationship between the BCPD components and the coordinate system as follows (also see Fig. 3.11):

- The lens for collecting the scattered light is centered in the x-z plane, i.e. there is no offset in the y-direction.

- The incident light is perfectly linearly polarized in the x-z plane.

The BCPD collects light within a cone of ±18.5° around a center-line angle of θ = 155°, ϕ = 0°. The collected light is directed onto a polarizing beam splitter, which separates it into a p- and an s-polarized component. The irradiance of each component is measured by a photodetector. The polarizing beam splitter is aligned in such a way that light polarized parallel to the x-z plane is measured as perfectly p-polarized light and light polarized perpendicular to the x-z plane is perfectly s-polarized light.

From the optical design of the BCPD one difference to the CDP is apparent; the BCPD does not contain a qualifying element. This has as a consequence that the sample area of the BCPD is not restricted to the region where the laser beam irradiance is approximately uniform.
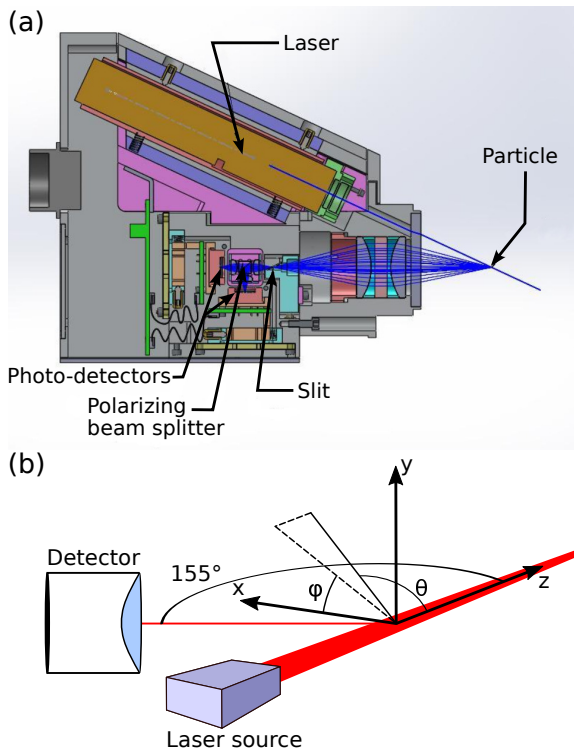
Figure 3.11: **(a)**: Optics of the Backscatter Cloud Probe with Polarization Detection (BCPD) (Figure adapted from the BCPD manual) [62, 63]. **(b)**: Geometry definition for the BCPD.

The sample area of the BCPD was calibrated by the manufacturer Droplet Measurement Techniques, who used a droplet generator to measure the backscatter from a 40 μm diameter droplet across the entire sample area. They proceeded along grid points with a spacing of 50 μm on the z-axis and 25 μm on the y-axis. The result of their calibration is used for this work. I applied a cubic interpolation to estimate the values between the grid points and obtained a smoother and more realistic irradiance distribution of the sample area. The resulting backscattered irradiance pattern can be seen in Fig. 3.12. The backscattered irradiance decreases towards the edges of the sample area. In the z-direction, the irradiance profile remains relatively constant over most of the sample area, before falling to zero over the last 100 μm on each side. In the y-direction, the irradiance profile rises over approximately 50 μm until it reaches a plateau that extends over roughly 120 μm of the innermost portion of the sample area and then again decreases to zero. The lower backscattered irradiance in the outer regions of the sample area means that particles passing through these regions are undersized. This problem also has been encountered and discussed by Beswick *et al.* [60] for the BCP and is investigated further for the BCPD in Section 4.4.2.

For the BCPD a relationship between particle size and scattering cross section,
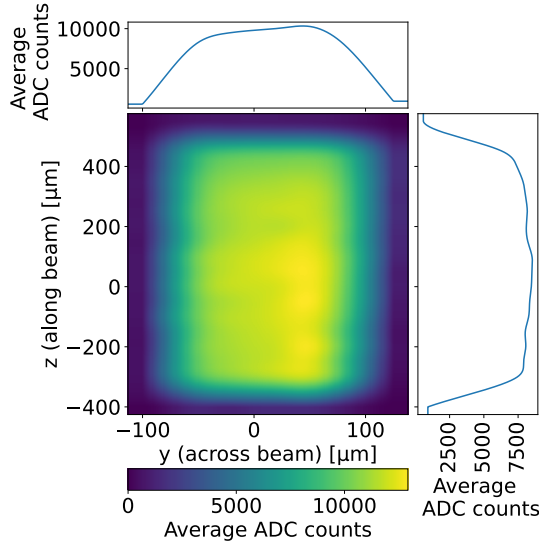
Figure 3.12: Backscattered irradiance from the sample area of the Backscatter Cloud Probe with Polarization Detection, visualized as analog-to-digital converter (ADC) counts.

similar to the one shown for the CDP in Fig. 3.10, needs to be established. Now, the polarization of the incident and scattered light has to be considered. The area from which light is collected is not symmetrical to the z-axis, leading to more complex formulations for the angles θ and ϕ. For the computation of the backscatter signal I use Müller-calculus [41], the coordinate system is defined as shown in Fig. 3.11.

Because the BCPD laser is polarized parallel to the x-z plane for observations with $\phi = 0$ its Stokes vector is:

$$\mathbf{S}_i = \begin{pmatrix} 1 \\ 1 \\ 0 \\ 0 \end{pmatrix}. \tag{3.25}$$

However, as mentioned in Section 3.2.2, Müller matrices and Stokes vectors used in Mie-theory refer to the scattering plane. Hence, for all angles where $\phi \neq 0$ it is necessary to account for the inclination of the polarization direction to the scattering plane:

$$\mathbf{S}'_i = \mathbf{R}(\phi)\,\mathbf{S}_i. \tag{3.26}$$

where $\mathbf{R}$ is [43]:

$$\mathbf{R}(\phi) = \begin{bmatrix} 1 & 0 & 0 & 0 \\ 0 & \cos(2\phi) & \sin(2\phi) & 0 \\ 0 & -\sin(2\phi) & \cos(2\phi) & 0 \\ 0 & 0 & 0 & 1 \end{bmatrix}. \tag{3.27}$$
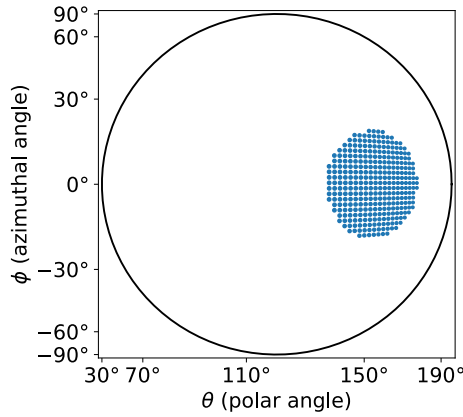
Figure 3.13: Area with individual scattering cross section segments, which are added to obtain the overall scattering cross section that is measured by the Backscatter Cloud Probe with Polarization Detection. Note that, for the actual calculation, a smaller segment size (and therefore higher resolution) was used. The larger segment size in the image is shown to enable the reader to discern the individual segments.

The Stokes vector of the scattered light can now be found as:

$$\mathbf{S}_\mathrm{s} = \int_{136.5°}^{173.5°} \int_{-\cos^{-1}\left(\frac{\theta-155°}{18.5°}\right)\frac{18.5°}{\pi}}^{\cos^{-1}\left(\frac{\theta-155°}{18.5°}\right)\frac{18.5°}{\pi}} \mathbf{M}(\theta)\,\mathbf{R}(\phi)\,\mathbf{S}_\mathrm{i}\,\mathrm{d}\phi\,\mathrm{d}\theta. \tag{3.28}$$

The integration was performed with the pySCATMECH package [64], which has a feature that evaluates the scattering cross section for a given range of angles by dividing the area into very small individual solid angle segments. I used an angular spacing of 0.5° between each segment for my calculations. Trials with smaller spacings yielded no significant changes in the computed cross sections, hence 0.5° is assumed to be appropriate. The pySCATMECH package is by default not able to perform the integration over the individual scattering cross section segments for a Mie-scatterer, it only computes the Mie scattering in the scattering plane, i.e. for a single azimuthal angle ϕ. Therefore, I modified the program such that the scattering cross section can also be computed for an area that contains a range of azimuthal angles while keeping the polarization of the incident light fixed [65].

To evaluate the signal measured at each of the photodetectors, their sensitivity needs to be considered, which can be done with a Stokes vector:

$$\mathbf{U}_{\parallel} = \begin{pmatrix} 1 \\ 1 \\ 0 \\ 0 \end{pmatrix}, \quad \mathbf{U}_{\perp} = \begin{pmatrix} 1 \\ -1 \\ 0 \\ 0 \end{pmatrix}, \tag{3.29}$$

where $\mathbf{U}_{\parallel}$ represents the sensitivity of a detector that only measures p-polarized light while $\mathbf{U}_{\perp}$ denotes the sensitivity of a detector that measures only s-polarized light. Note that the parallel and perpendicular directions for the receivers are defined with respect to the orientation of the polarizing beam splitter, i.e. the elec-
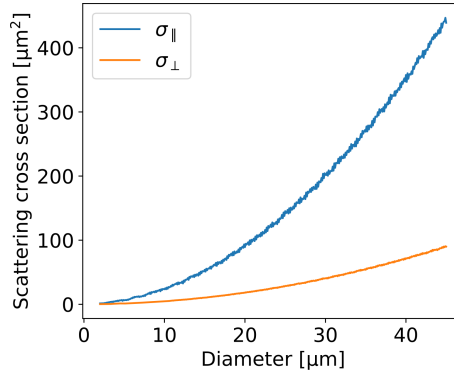
Figure 3.14: Relationship between droplet diameter and the scattering cross sections of scattered p-polarized (blue) and s-polarized (orange) light for the Backscatter Cloud Probe with Polarization Detection. The curves were computed for incident light that is completely p-polarized.

tric field of p-polarized light oscillates in the x-z plane, while the electric field of s-polarized light oscillates perpendicular to the x-z plane. The scattering cross sections that correspond to the irradiance received by the photodetectors are:

$$\sigma_{\parallel} = \mathbf{U}_{\parallel}^{\mathsf{T}} \mathbf{S}_{\mathrm{s}} \,, \tag{3.30}$$

$$\sigma_{\perp} = \mathbf{U}_{\perp}^{\mathsf{T}} \mathbf{S}_{\mathrm{s}} \,. \tag{3.31}$$

Figure 3.14 shows the relationship between droplet diameter and scattering cross section for p- and s-polarized light. In comparison to the scattering cross section curve from the CDP, which was shown in Fig. 3.10, it is striking that the curve of the BCPD is far smoother and exhibits only very small-scale Mie-ambiguities. This is an advantage of the BCPD over the classical forward scattering probes.

Measurements with the different scattering probes that were explained in this section are described in subsequent chapters. As discussed in Section 3.2.3, the size range of scattering probes is restricted to relatively small droplet diameters. Scattering probes are for instance not able to measure supercooled large droplets (SLDs). For this task, optical array probes are needed, which I introduce in the following section.

3.3. PARTICLE SIZE AND SHAPE MEASUREMENTS WITH OPTICAL ARRAY PROBES

Optical array probes form another category of cloud instrumentation that is distinctively different from the scattering probes that were explained in Section 3.2. They are used for the measurement of larger cloud droplets, drizzle and raindrops and ice crystals.

MEASUREMENT PRINCIPLE OF OPTICAL ARRAY PROBES
The measurement principle of optical array probes is illustrated in Fig. 3.15. A laser beam is directed from its source in the body of the probe into one of the arms, where

it is reflected on a mirror at a 90° angle into the airflow. Subsequently, it impacts on the second arm of the probe, where another mirror reflects it at a 90° angle onto an array of photodiodes, from which this category of instruments derives its name. When a particle passes through the laser beam, some of the photodiodes are momentarily shadowed and, if the measured irradiance falls below a certain threshold, the acquisition system of the instrument is triggered. The status of all photodiodes is recorded and an image that contains the degree of shadowing can be created. From this image, particle size and shape are derived. The first optical array probes were developed by Robert G. Knollenberg in the late 1960s at the National Center for Atmospheric Research in Boulder, Colorado [66]. Since then, various models have been built.

The two optical array probes that are most relevant for this thesis are the Cloud Imaging Probe (CIP) and the Precipitation Imaging Probe (PIP), with size ranges from 15-960 μm and 100-6400 μm, respectively [56, 67, 68]. The size range of an optical array probe is dictated by the properties of the optical array. The smallest size that can be measured corresponds to a droplet that shadows a single photodiode sufficiently to be detected. The upper size limit stems from the width of the array, any particle which exceeds the array dimensions cannot be wholly imaged. The array only has an extent perpendicular to the airflow. The particle shape in the direction of the airflow is obtained from multiple subsequent acquisitions of the photodiode array.
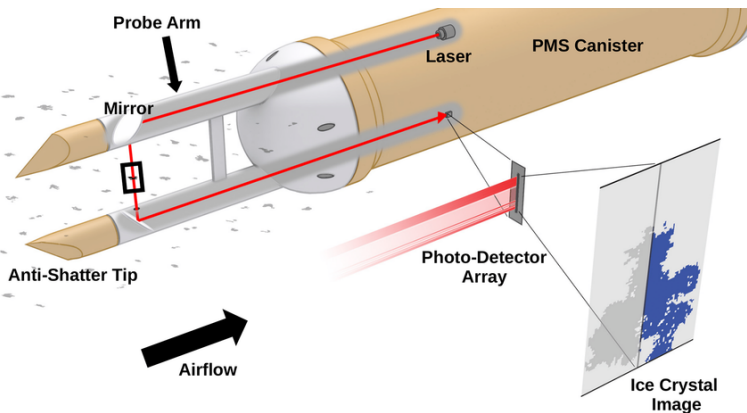
Figure 3.15: Measurement principle of an optical array probe. Image from Wagner and Delene [69].

The instrument category of optical array probes can be divided into monoscale and grayscale probes. Monoscale probes store information about the shadowing in a single bit, and a pixel is classified as shadowed if the incident irradiance measured by a photodiode decreases by more than half [68]. Grayscale probes, on the other hand, use two bits to store information about four different shadowing levels. The sensitivity range of such probes is usually divided into the following equally spaced shadowing levels: Unshadowed (less than 25% irradiance decrease on the diode), 25% shadowed (less than 50% irradiance decrease on the diode), 50% shad-

owed (less than 75% irradiance decrease on the diode) and 75% shadowed (more than 75% irradiance decrease on the diode).

The PIP used in this work is a monoscale probe, while the CIP is a grayscale probe. Fig. 3.16 shows images of various liquid and ice particles imaged with the CIP. The three different grayscale levels are clearly distinguishable in the figure.
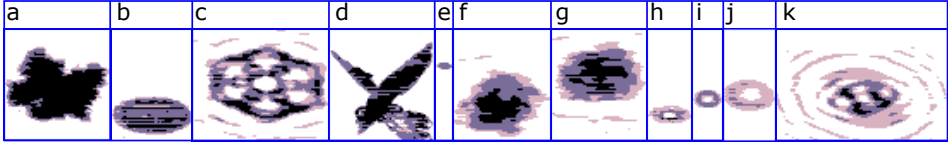
Figure 3.16: Example images of particles collected with the CIP during various flight campaigns. **a-d** show in-focus images of a strongly rimed ice crystal, a large droplet, a plate-like ice crystal and a seagull-type ice crystal, respectively [70]. From the meteorological context in which it was recorded, **e** was determined to be the image of a small droplet. **f** and **g** show slightly out-of-focus images of strongly rimed ice crystals similar to **a**. For **h-j** no definitive classification is possible. The white spot in the center may represent a Poisson spot that is expected for round particles. Image **k** shows the out-of-focus image of a plate-like ice crystal.

One property that is of profound importance for optical array probes is the depth-of-field (DoF). The DoF can be thought of as the width of the sample area of the probe (the height of the sample area is fixed by the height of the array of photodiodes). More precisely, the DoF describes the distance from the object plane in which the probe is sensitive to particles. The term sensitivity depends on a selected shadowing threshold. For instance, if a 50% shadowing threshold is selected, the probe is sensitive to particles that produce at least at one pixel a shadow that exceeds the 50% threshold [71]. Consequently, the DoF is not constant but changes with particle size, as can be seen from Fig. 3.17. Mathematically, the DoF is given as [72]:

$$Z_{\mathrm{DOF}} = 2 \frac{Z_{\mathrm{d,max}}}{\lambda} \left(\frac{d}{2} \right)^2. \tag{3.32}$$

The factor two represents the symmetry of the DoF about the object plane. $Z_{\mathrm{d,max}}$ is a dimensionless number that specifies the distance from the object plane where a disk, which is entirely opaque at the object plane, does not contain any pixels above a selected shadowing threshold. From Fig. 3.17 and Eq. (3.32) it is clear that the sample area is much smaller for small droplets than for large droplets. Therefore, to obtain size distributions from optical array probes, the appropriate sample area for each particle size needs to be used to account for the differences in the DoF.

The object plane of an optical array probe is positioned exactly in the center between the two arms of the probe. Particles that pass through the laser beam in the object plane are perfectly in-focus (while it is impossible to say if they were perfectly in the object plane, the particles in Fig. 3.16a-d at least passed the laser beam at close proximity to the object plane). Particles that pass the laser beam at locations other than the object plane are not in focus (Fig. 3.16f-j). Especially small particles are just accurately imaged if they pass within a very short distance from the object plane (see Eq. (3.32)) [74]. Small particles that pass the laser beam at
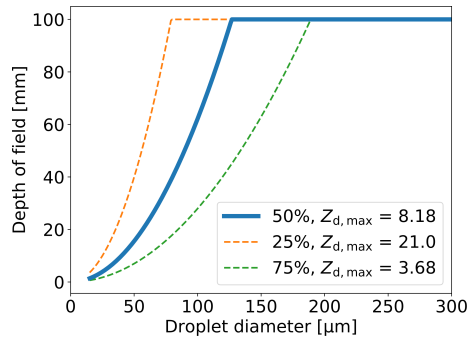
Figure 3.17: Depth of field of a CIP grayscale probe for different droplet diameters and a shadowing threshold of 50%, the DoF curves for 25% and 75% shadowing are shown for comparison. The $Z_{d,max}$ values were taken from Korolev *et al.* [72]. A laboratory calibration of the DLR-CIP yielded the same $Z_{d,max}$ value for 50% [73]. No measurements of the 25% and 75% threshold were performed at DLR. The arm width of the CIP is 100 mm and thus represents a mechanical limit to the DoF for all shadowing thresholds.

locations further away from the object plane are either not imaged at all, or they may appear to be severely distorted and enlarged. Due to diffraction, particles that are imaged out-of-focus, often (depending on their shape) develop one or several unshadowed spots within their perimeter, which are known as Poisson spots (Fig. 3.16h-j) [71, 74]. Conversely, it is however not the case that all particles that show unshadowed spots are imaged out of focus, see Fig. 3.16c, which is an in-focus plate-like ice-crystal that nonetheless exhibits unshadowed spots.

Many attempts have been made to correct out-of-focus images of optical array probes. Korolev *et al.* [75] presented an approach to correct the size of liquid particles based on the size of their Poisson spot, a procedure which is therefore known as the «Korolev correction» and is commonly applied in evaluation software of optical array probes. However, the procedure should not be applied for mixed-phase conditions, as the relation between the size of the Poisson spot and the particle diameter that is used in the procedure is not valid for aspherical particles. Therefore, a solid differentiation between ice- and liquid particles is required for airborne measurements to apply the Korolev correction.

MEASUREMENT UNCERTAINTIES OF OPTICAL ARRAY PROBES

As for the scattering probes, the measurement uncertainties of optical array probes are a consequence of possible counting and sizing errors. The magnitude of these uncertainties is reported for spherical droplets in this paragraph. I do not discuss the uncertainties for ice crystals, as the focus of this thesis is on the measurement of droplets.

The smallest droplet sizes that can be measured with an optical array probe correspond to the shadowing of a single pixel (see Section 3.3). Naturally, that means that the size resolution is poor for small droplets and the maximum error for the smallest size bin is 50%. The sizing uncertainty reduces rapidly as droplet diameters increase, for a droplet of 80 µm diameter the maximum error due to the

resolution of the probe is only 9% [73]. Further sizing errors are introduced due to out-of-focus particles which appear enlarged in optical array probe images. The exact magnitude of these sizing errors is difficult to quantify, as it depends on the corrections that are applied. A review paper by Baumgardner *et al.* [56] reports an overall sizing accuracy of optical array probes of ±20% for particles larger than 100-200 μm. For smaller particles sizing uncertainties may be as large as ±50%. In the same publication Baumgardner *et al.* [56] also provide estimates for the uncertainty in the concentration measurement. These are claimed to be ±50% for particles larger than 100-200 μm and ±100% for particles smaller than 100 μm diameter.

Sections 3.2.3 and 3.3 explained the measurement principles and the uncertainties of forward scattering and optical array probes. These instruments, which often have been used for several decades, serve as input for collision efficiency corrections for the Nevzorov probe and source of comparison for the new BCPD in the subsequent chapters of this thesis. The previous sections showed that also the measurements of the forward scattering and optical array probes are subject to significant uncertainties. But, in contrast to new instruments like the BCPD, their uncertainties are well established and I mitigate them as far as possible (see Section 4.2). Therefore, forward scattering and optical array probes are an appropriate source of comparison to measurements of new instruments such as the BCPD.

REFERENCES

[1] R. F. Ide, *Comparison of liquid water content measurement technquies in an icing wind tunnel*, Tech. Rep. ARL-TR-2134 (National Aeronautics and Space Administration Cleveland OH Lewis Research Center, 1999).

[2] C. Davison, J. MacLeod, and J. Strapp, *Naturally Aspirating Isokinetic Total Water Content Probe: Evaporator Design and Testing*, in *1st AIAA Atmospheric and Space Environments Conference* (American Institute of Aeronautics and Astronautics, 2009).

[3] J. Stallabrass, *An Appraisal of the Single Rotating Cylinder Method of Liquid Water Content Measurement*, Tech. Rep. LTR-LT-92 (National Research Council Canada, 1978).

[4] R. F. Ide, *Liquid Water Content and Droplet Size Calibration of the NASA Lewis Icing Research Tunnel*, in *28th Aerospace Sciences Meeting sponsored by the American Institute of Aeronautics and Astronautics* (1990).

[5] L.-C. E. Steen, R. F. Ide, and J. F. Van Zante, *An Assessment of the Icing Blade and the SEA Multi-Element Sensor for Liquid Water Content Calibration of the NASA GRC Icing Research Tunnel*, in *8th AIAA Atmospheric and Space Environments Conference*, p. 4051, https://arc.aiaa.org/doi/pdf/10.2514/6.2016-4051 (2016).

[6] D. M. Orchard, C. Clark, and G. Chevrette, *Measurement of Liquid Water Content for Supercooled Large Drop Conditions in the NRC's Altitude Icing Wind Tunnel*, in *SAE Technical Paper* (SAE International, 2019).

[7] I. Knop, S. E. Bansmer, V. Hahn, and C. Voigt, *Comparison of different droplet measurement techniques in the Braunschweig Icing Wind Tunnel*, Atmospheric Measurement Techniques **14**, 1761 (2021).

[8] E. J. Dolezel, R. M. Cunningham, and R. E. Katz, *Progress in Icing Research*, Bulletin of the American Meteorological Society **27**, 261 (1946).

[9] W. Lewis, *A flight investigation of the meteorological conditions conducive to the formation of ice on airplanes*, Tech. Rep. 1393 (National Aeronautics and Space Administration, Ames Research Center, Moffett Field, CA, 1947).

[10] W. D. King, D. A. Parkin, and R. J. Handsworth, *A Hot-Wire Liquid Water Device Having Fully Calculable Response Characteristics*, Journal of Applied Meteorology and Climatology **17**, 1809 (1978).

[11] W. D. King, J. E. Dye, D. Baumgardner, J. W. Strapp, and D. Huffman, *Icing Wind Tunnel Tests on the CSIRO Liquid Water Probe*, Journal of Atmospheric and Oceanic Technology **2**, 340 (1985).

[12] L. E. Lilie, D. Bouley, C. P. Sivo, and T. P. Ratvasky, *Test results for the SEA ice crystal detector (ICD) under SLD conditions at the NASA IRT*, (American Institute of Aeronautics and Astronautics, 2021).

[13] T. P. Ratvasky, J. W. Strapp, and L. E. Lilie, *Isokinetic Probe Total Water Content Measurements in the NASA Icing Research Tunnel with Supercooled Large Drop Conditions*, in *AIAA AVIATION 2021 FORUM* (American Institute of Aeronautics and Astronautics, 2021).

[14] C. R. Davison, J. W. Strapp, L. E. Lilie, T. P. Ratvasky, and C. Dumont, *Isokinetic TWC evaporator probe: Calculations and systemic error analysis*, in *8th AIAA Atmospheric and Space Environments Conference*, p. 4060 (2016).

[15] P. R. Brown and P. N. Francis, *Improved measurements of the ice water content in cirrus using a total-water probe*, Journal of Atmospheric and Oceanic Technology **12**, 410 (1995).

[16] A. J. Heymsfield, C. Schmitt, A. Bansemer, and C. H. Twohy, *Improved Representation of Ice Particle Masses Based on Observations in Natural Clouds*, Journal of the Atmospheric Sciences **67**, 3303 (2010).

[17] A. V. Korolev, J. W. Strapp, G. A. Isaac, and A. N. Nevzorov, *The Nevzorov Airborne Hot-Wire LWC–TWC Probe: Principle of Operation and Performance Characteristics*, Journal of Atmospheric and Oceanic Technology **15**, 1495 (1998).

[18] A. V. Korolev, G. A. Isaac, S. G. Cober, J. W. Strapp, and J. Hallett, *Microphysical characterization of mixed-phase clouds*, Quarterly Journal of the Royal Meteorological Society **129**, 39 (2003).

3

[19] J. W. Strapp, J. Oldenburg, R. Ide, L. Lilie, S. Bacic, Z. Vukovic, M. Oleskiw, D. Miller, E. Emery, and G. Leone, *Wind Tunnel Measurements of the Response of Hot-Wire Liquid Water Content Instruments to Large Droplets*, Journal of Atmospheric and Oceanic Technology **20**, 791, https://doi.org/10.1175/1520-0426(2003)020<0791:WTMOTR>2.0.CO;2 (2003).

[20] E. Emery, D. Miller, S. Plaskon, W. Strapp, and L. Lillie, *Ice particle impact on cloud water content instrumentation,* in *42nd AIAA Aerospace Sciences Meeting and Exhibit*, p. 731 (2004).

[21] A. Schwarzenboeck, G. Mioche, A. Armetta, A. Herber, and J.-F. Gayet, *Response of the Nevzorov hot wire probe in clouds dominated by droplet conditions in the drizzle size range*, Atmospheric Measurement Techniques **2**, 779 (2009).

[22] A. Korolev, J. Strapp, G. Isaac, and E. Emery, *Improved airborne hot-wire measurements of ice water content in clouds,* Journal of Atmospheric and Oceanic Technology **30**, 2121 (2013).

[23] Science Engineering Associates, *WCM-2000* (2016).

[24] D. M. Orchard, K. Szilder, and C. R. Davison, *Design of an Icing Wind Tunnel Contraction for Supercooled Large Drop Conditions*, in *2018 Atmospheric and Space Environments Conference* (American Institute of Aeronautics and Astronautics, 2018).

[25] I. Langmuir and K. Blodgett, *A mathematical investigation of water droplet trajectories* (Army Air Forces Headquarters, Air Technical Service Command, 1946).

[26] P. McComber and G. Touzot, *Calculation of the Impingement of Cloud Droplets in a Cylinder by the Finite-Element Method*, Journal of Atmospheric Sciences **38**, 1027 (1981).

[27] E. P. Lozowski, J. R. Stallabrass, and P. F. Hearty, *The Icing of an Unheated, Nonrotating Cylinder. Part I: A Simulation Model*, Journal of Climate and Applied Meteorology **22**, 2053, https://doi.org/10.1175/1520-0450(1983)022<2053:TIOAUN>2.0.CO;2 (1983).

[28] L. Makkonen, *Modeling of Ice Accretion on Wires*, Journal of Applied Meteorology and Climatology **23**, 929 (1984).

[29] K. J. Finstad, E. P. Lozowski, and E. M. Gates, *A Computational Investigation of Water Droplet Trajectories*, Journal of Atmospheric and Oceanic Technology **5**, 160, https://doi.org/10.1175/1520-0426(1988)005<0160:ACIOWD>2.0.CO;2 (1988).

[30] A. Heinrich, R. Ross, G. Zumwalt, J. Provorse, V. Padmanabhan, J. Thompson, and J. Riley, *Aircraft Icing Handbook Volume 1 of 3* (U.S. Department of Transportation, 1991).

[31] AC-9C Aircraft Icing Technology Committee, *Calibration and Acceptance of Icing Wind Tunnels (ARP5905)* (2015).

[32] LabJack Cooperation, *U6 Datasheet* (2016).

[33] C. F. Bohren and D. R. Huffman, *Absorption and scattering of light by small particles,* Absorption and Scattering of Light by Small Particles , 544 (1998).

[34] J. C. Maxwell, *A dynamical theory of the electromagnetic field,* Philosophical transactions of the Royal Society of London , 459 (1865).

[35] K.-N. Liou, *Theory of the scattering-phase-matrix determination for ice crystals,* Journal of the Optical Society of America **65**, 159 (1975).

[36] T. G. Kyle, *Atmospheric transmission, emission and scattering* (Elsevier, 2013).

[37] A. T. Young, *Rayleigh scattering,* Applied Optics **20**, 533 (1981).

[38] G. Mie, *Beiträge zur Optik trüber Medien, speziell kolloidaler Metallösungen,* Annalen der Physik **330**, 377 (1908).

[39] A. Doicu, T. Wriedt, and Y. A. Eremin, *Light scattering by systems of particles: Null-field method with discrete sources: Theory and programs*, Vol. 124 (Springer, 2006).

[40] W. Hergert and T. Wriedt, *The Mie Theory: Basics and Applications*, Springer Series in Optical Sciences (Springer Berlin Heidelberg, 2012).

[41] H. Mueller, *Memorandum on the polarization optics of the photoelastic shutter,* Report of the OSRD project OEMsr-576 **2** (1943).

[42] J. Kleine, *Flugzeuggetragene Messungen von Eis- und Rußpartikeln in Kondensstreifen bei Verwendung konventioneller und synthetischer Treibstoffe*, Ph.D. thesis, Johannes Gutenberg-Universität Mainz (2019).

[43] V. V. Tuchin, L. V. Wang, and D. A. Zimnyakov, *Optical Polarization in Biomedical Applications* (Springer Berlin Heidelberg, 2006).

[44] M. Bass, *Handbook of optics: Volume I - Geometrical and physical optics, polarized light, components and instruments* (McGraw-Hill Education, 2010).

[45] B. A. Gardiner and J. Hallett, *Degradation of In-Cloud Forward Scattering Spectrometer Probe Measurements in the Presence of Ice Particles,* Journal of Atmospheric and Oceanic Technology **2**, 171 (1985).

[46] J.-L. Brenguier, T. Bourrianne, A. A. Coelho, J. Isbert, R. Peytavi, D. Trevarin, and P. Weschler, *Improvements of Droplet Size Distribution Measurements with the Fast-FSSP (Forward Scattering Spectrometer Probe),* Journal of Atmospheric and Oceanic Technology **15**, 1077 (1998).

[47] S. Lance, C. A. Brock, D. Rogers, and J. A. Gordon, *Water droplet calibration of the Cloud Droplet Probe (CDP) and in-flight performance in liquid, ice and mixed-phase clouds during ARCPAC*, Atmospheric Measurement Techniques **3**, 1683 (2010).

[48] D. Baumgardner, J. Brenguier, A. Bucholtz, H. Coe, P. DeMott, T. Garrett, J. Gayet, M. Hermann, A. Heymsfield, A. Korolev, M. Krämer, A. Petzold, W. Strapp, P. Pilewskie, J. Taylor, C. Twohy, M. Wendisch, W. Bachalo, and P. Chuang, *Airborne instruments to measure atmospheric aerosol particles, clouds and radiation: A cook's tour of mature and emerging technology*, Atmospheric Research **102**, 10 (2011).

[49] S. Glienke and F. Mei, *Fast Cloud Droplet Probe (FCDP) Instrument Handbook*, Tech. Rep. SC-ARM-TR-238 (U.S. Department of Energy, 2020).

[50] D. Baumgardner, H. Jonsson, W. Dawson, D. O'Connor, and R. Newton, *The cloud, aerosol and precipitation spectrometer: A new instrument for cloud investigations*, Atmospheric Research **59-60**, 251 (2001).

[51] R. Pinnick, D. Garvey, and L. Duncan, *Calibration of Knollenberg FSSP light-scattering counters for measurement of cloud droplets*, Journal of Applied Meteorology and Climatology **20**, 1049 (1981).

[52] P. D. Rosenberg, A. R. Dean, P. I. Williams, J. R. Dorsey, A. Minikin, M. A. Pickering, and A. Petzold, *Particle sizing calibration with refractive index correction for light scattering optical particle counters and impacts upon PCASP and CDP data collected during the Fennec campaign*, Atmospheric Measurement Techniques **5**, 1147 (2012).

[53] N. L. Miles, J. Verlinde, and E. E. Clothiaux, *Cloud Droplet Size Distributions in Low-Level Stratiform Clouds*, Journal of the Atmospheric Sciences **57**, 295 (2000).

[54] D. Baumgardner, R. Newton, M. Krämer, J. Meyer, A. Beyer, M. Wendisch, and P. Vochezer, *The Cloud Particle Spectrometer with Polarization Detection (CPSPD): A next generation open-path cloud probe for distinguishing liquid cloud droplets from ice crystals*, Atmospheric Research **142**, 2 (2014).

[55] A. Macke, J. Mueller, and E. Raschke, *Single scattering properties of atmospheric ice crystals*, Journal of Atmospheric Sciences **53**, 2813 (1996).

[56] D. Baumgardner, S. J. Abel, D. Axisa, R. Cotton, J. Crosier, P. Field, C. Gurganus, A. Heymsfield, A. Korolev, M. Krämer, P. Lawson, G. McFarquhar, Z. Ulanowski, and J. Um, *Cloud ice properties: In situ measurement challenges*, Meteorological Monographs **58**, 9.1 (2017).

[57] S. Faber, J. R. French, and R. Jackson, *Laboratory and in-flight evaluation of measurement uncertainties from a commercial Cloud Droplet Probe (CDP)*, Atmospheric Measurement Techniques **11**, 3645 (2018).

[58] S. Lance, *Coincidence Errors in a Cloud Droplet Probe (CDP) and a Cloud and Aerosol Spectrometer (CAS), and the Improved Performance of a Modified CDP,* Journal of Atmospheric and Oceanic Technology **29,** 1532 (2012).

[59] J. R. Lucke, T. Jurkat-Witschas, D. Baumgardner, F. Kalinka, M. Moser, E. De La Torre Castro, and C. Voigt, *Characterization of Atmospheric Icing Conditions during the HALO-(AC)³ Campaign with the Nevzorov Probe and the Backscatter Cloud Probe with Polarization Detection,* in *SAE Technical Paper Series* (SAE International, 2023).

[60] K. Beswick, D. Baumgardner, M. Gallagher, A. Volz-Thomas, P. Nedelec, K.-Y. Wang, and S. Lance, *The backscatter cloud probe - a compact low-profile autonomous optical spectrometer,* Atmospheric Measurement Techniques **7,** 1443 (2014).

[61] *In-service Aircraft for a Global Observing System,* https://www.iagos.org/, accessed: 2022-09-17.

[62] D. Baumgardner and R. Newton, *Optical particle detector,* U.S. Patent 2014/0330459 A1, (2014).

[63] Droplet Measurement Technologies, Inc., *Backscatter Cloud Probe with Polarization Detection (BCPD) - Operator Manual* (2020).

[64] T. A. Germer, *pySCATMECH: A Python interface to the SCATMECH library of scattering codes,* in *Reflection, Scattering, and Diffraction from Surfaces VII,* edited by L. M. Hanssen (SPIE, 2020).

[65] National Institute of Standards and Technology, *pyscatmech,* https://github.com/johanneslucke/pySCATMECH (2023).

[66] R. G. Knollenberg, *The optical array: An alternative to scattering or extinction for airborne particle size determination,* Journal of Applied Meteorology (1962-1982) , 86 (1970).

[67] R. C. Braga, D. Rosenfeld, R. Weigel, T. Jurkat, M. O. Andreae, M. Wendisch, U. Pöschl, C. Voigt, C. Mahnke, S. Borrmann, R. I. Albrecht, S. Molleker, D. A. Vila, L. A. T. Machado, and L. Grulich, *Further evidence for CCN aerosol concentrations determining the height of warm rain and ice initiation in convective clouds over the Amazon basin,* Atmospheric Chemistry and Physics **17,** 14433 (2017).

[68] S. J. O'Shea, J. Crosier, J. Dorsey, W. Schledewitz, I. Crawford, S. Borrmann, R. Cotton, and A. Bansemer, *Revisiting particle sizing using greyscale optical array probes: Evaluation using laboratory experiments and synthetic data,* Atmospheric Measurement Techniques **12,** 3067 (2019).

[69] S. W. Wagner and D. J. Delene, *Technique for comparison of backscatter coefficients derived from in situ cloud probe measurements with concurrent airborne lidar,* Atmospheric Measurement Techniques **15,** 6447 (2022).

3

[70] K. Kikuchi, T. Kameda, K. Higuchi, and A. Yamashita, *A global classification of snow crystals, ice crystals, and solid precipitation based on observations from middle latitudes to polar regions*, Atmospheric Research **132-133**, 460 (2013).

[71] A. Korolev, *Reconstruction of the Sizes of Spherical Particles from Their Shadow Images. Part I: Theoretical Considerations*, Journal of Atmospheric and Oceanic Technology **24**, 376 (2007).

[72] A. V. Korolev, J. W. Strapp, and G. A. Isaac, *Evaluation of the Accuracy of PMS Optical Array Probes*, Journal of Atmospheric and Oceanic Technology **15**, 708 (1998).

[73] M. Moser, *Characterization and calibration of an optical array probe and airborne in-situ measurements of mixed-phase clouds*, Master's thesis, Friedrich-Alexander-Universität Erlangen-Nürnberg (2018).

[74] T. V. de Guélis, A. Schwarzenböck, V. Shcherbakov, C. Gourbeyre, B. Laurent, R. Dupuy, P. Coutris, and C. Duroure, *Study of the diffraction pattern of cloud particles and the respective responses of optical array probes*, Atmospheric Measurement Techniques **12**, 2513 (2019).

[75] A. V. Korolev, G. A. Isaac, J. W. Strapp, S. G. Cober, and H. W. Barker, *In situ measurements of liquid water content profiles in midlatitude stratiform clouds*, Quarterly Journal of the Royal Meteorological Society **133**, 1693 (2007).

4

INSTRUMENT CHARACTERIZATIONS IN ICING WIND TUNNELS

The first research question of this thesis concerns the suitability of the new 12 mm cone of the Nevzorov probe (Section 3.1.1) for the measurement of supercooled large droplet (SLD) conditions. As mentioned in Section 2.4, SLD conditions often contain also a large number of small droplets. At present, the collision efficiency of small droplets with the 12 mm cone is unknown (see Section 3.1.1). To use the 12 mm cone for measurements in SLD conditions and to answer the research question, this collision efficiency needs to be determined. Furthermore, the ability of the 12 mm cone to retain and completely evaporate the SLDs needs to be verified. These two analyses are performed experimentally by means of a comparison to other instruments, for which a realistic, yet controlled test environment is required. Icing wind tunnels (IWTs) are essentially the only facilities that are able to produce a droplet cloud with realistic number concentrations, particle sizes and velocities. Three IWT campaigns were performed with the Nevzorov probe and this chapter explains the measurement setup, the evaluation strategy and the results obtained from these activities.

Furthermore, in connection with research question II, the Backscatter Cloud Probe with Polarization Detection (BCPD, see Section 3.2.4) was tested in one IWT

(see Table 4.1) to characterize its sizing and sampling capabilities through a comparison to droplet size distributions (DSDs) of the Cloud Droplet Probe (CDP, see Section 3.2.3). The CDP operation and data evaluation were also part of the work performed within this thesis. In fact, to obtain DSDs across the entire droplet size range, a Cloud Combination Probe (CCP), which consists of a CDP and a Cloud Imaging Probe (CIP, see Section 3.3), was used. These DSDs also serve as input for the collision efficiency corrections of the Nevzorov probe.

The first part of this chapter provides an overview of the IWT campaigns, the instruments that were used and the data available from each tunnel. The second part describes the procedure applied to obtain DSDs from the CCP data. These DSDs are required as input for the third part, where I evaluate the measurements of the Nevzorov probe and establish a methodology to derive the collision efficiency of the 12 mm cone. Lastly, the fourth part shows results from the BCPD measurements.

Icing wind tunnel	Campaign dates	DLR instrumentation
Braunschweig Icing Wind Tunnel (TU Braunschweig)	20th-31st July 2020	Nevzorov, BCPD, CCP
Goodrich Icing Wind Tunnel (Collins Aerospace)	9th-10th Nov. 2020, 16th-19th Feb. 2021	Nevzorov, CCP
Climatic Wind Tunnel Vienna (Rail Tec Arsenal)	26th Apr. 2019, 23rd-24th June 2021	Nevzorov, CAPS

Table 4.1: Overview of the icing wind tunnel campaigns and the instrumentation used. The instruments are abbreviated as follows: Cloud Combination Probe (CCP), Backscatter Cloud Probe with Polarization Detection (BCPD), Cloud Aerosol and Precipitation Spectrometer (CAPS).

In this chapter, I differentiate between the instruments that are the subject of the studies (i.e. the 12 mm cone of the Nevzorov probe and the BCPD) and the reference instrumentation that is used as input for calculations and for comparison to BCPD and 12 mm cone measurements. The measurements from the reference instrumentation are referred to as the reference measurements. Part of the reference measurements were provided by the tunnel operators (this is further explained in the subsequent sections). The reference measurements of the liquid water content (LWC) obtained by the tunnel operators are therefore also referred to as the tunnel LWC reference measurements or in short as the tunnel LWC. The DSD reference measurements with the CCP were always obtained and evaluated by the German Aerospace Center (DLR). An overview of the reference instrumentation used in this chapter can be seen in Table 4.2.

Measurements from the LWC sensor and the 8 mm cone of the Nevzorov probe represent a special case. These sensors are used for the derivation of the collision efficiency of the 12 mm cone and serve there as reference instrumentation but are not used for further comparisons. The reason for this is explained in Section 4.3.2.

4.1. ICING WIND TUNNEL CAMPAIGNS

The IWT measurement campaigns that form the backbone of this chapter were part of two EU projects, SENS4ICE [2, 3] and ICEGENESIS [4]. IWT campaigns were conducted over a total of approximately 5 weeks in the climatic wind tunnel of Rail Tec Arsenal in Vienna, the Braunschweig Icing Wind Tunnel of the Technical University of Braunschweig and the Goodrich Icing Wind Tunnel of Collins Aerospace. An overview of the campaigns and the DLR instruments tested in the tunnels is given in Table 4.1. The IWTs were selected because each of them participated in either of the two EU projects. Furthermore, taken together, they can produce a large variety of icing conditions with distinctively different spray systems. The usage of three IWTs also helps to mitigate the influence of possible biases that are present in just one facility. Another criterion for the selection of the IWTs was the requirement to have DSDs available for all test points.

In Chapter 2 I introduced the Appendix C and Appendix O envelopes that describe atmospheric icing conditions. IWTs have the capability to produce icing conditions that are not found in the atmosphere. Thus, IWT conditions are not constrained to the Appendix C and Appendix O envelopes. The difficulties in recreating Appendix O conditions (see Section 2.5) cause many of the SLD icing conditions produced in IWTs to lie outside the Appendix O envelopes. Therefore, instead of differentiating between Appendix C and Appendix O, different categories are used for the IWT study: Small droplet spray, freezing drizzle and freezing rain. Small droplet spray includes the nominal Appendix C conditions [5] as well as conditions where the LWC and MVD are outside the Appendix C envelopes, but no supercooled large droplet mode (D > 100 µm) is present (see Section 2.3). Freezing drizzle and freezing rain conditions include unimodal and bimodal SLD conditions, some of which fall within the LWC specifications of Appendix O [6], while others exceed the maximum LWC significantly. The distinction between freezing drizzle and freezing rain is made according to the maximum of the LWC distribution in the large droplet mode. If the maximum is positioned at a diameter smaller than 500 µm the condition is identified as freezing drizzle, otherwise as freezing rain. This definition is different from that of Cober and Isaac [6], which was shown in Chapter 2, where freezing rain is defined by a maximum drop diameter (D_{max}) larger than 500 µm. The distribution of the droplet spray produced in IWTs is relatively broad so that sprays with a droplet mode centered around 200 µm still contain a small, but not insignificant (>1% of total LWC) number of droplets larger than 500 µm. Since the large majority of SLDs are nonetheless drizzle drops, I decided that such conditions are better described by the characteristics of freezing drizzle as defined in Cober and Isaac [6] and hence list them as such.

In the following, I give a brief overview of the individual measurement campaigns, the instrumentation used and the mounting positions of the instruments.

4.1.1. MEASUREMENTS IN THE BRAUNSCHWEIG ICING WIND TUNNEL

The Braunschweig Icing Wind Tunnel (BIWT) is a relatively new facility, whose design is described in Bansmer *et al.* [7]. The tunnel was used for numerous research activities on ice crystal- and supercooled liquid water icing in recent years [8, 9]. The layout and the tunnel specifications can be seen in Fig. 4.1. The basic spray system for the production of droplet sprays with MVDs up to 60 µm consists of an array of 5 × 5 spray atomizers [7]. For the production of freezing drizzle conditions, a set of six atomizers suitable for the generation of SLDs was added to the two uppermost spray bars of the spray system [10].
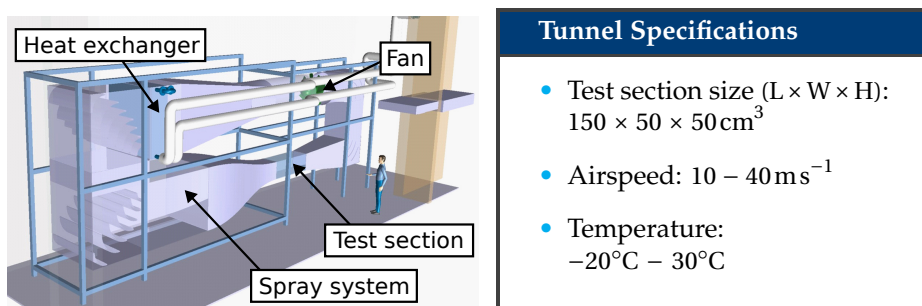
Figure 4.1: Schematic and specifications of the Braunschweig Icing Wind Tunnel (Figure adapted from [10]).

MEASUREMENTS PERFORMED BY THE GERMAN AEROSPACE CENTER

Three DLR instruments were tested in the BIWT, the BCPD (Section 3.2.4), the Nevzorov probe (Section 3.1.1), and the CCP of DLR, which due to its frequent usage on the DLR research aircraft HALO is referred to as HALO-CCP [11–13]. The 50×50 cm^2 cross section of the IWT did not offer the possibility of simultaneous measurements of the HALO-CCP and the Nevzorov probe, hence the measurements were performed consecutively. Simultaneous measurements of the BCPD and Nevzorov probe were possible. The droplet spray is not uniform across the tunnel cross section, hence the results depend on the sampling positions of the instruments. This is especially relevant for Appendix O conditions. As mentioned in Chapter 2, SLDs sediment much faster than smaller cloud droplets. Consequently, uncertainty existed at what height the SLD spray traverses the test section. To establish the optimal measurement position, the Nevzorov probe was mounted on a fixture that could be moved up and down. Freezing drizzle conditions were measured at different heights, as shown in Fig. 4.2. I only display measurements of the 8 mm cone, as it has an acceptable collection efficiency for small and large droplets. The image shows that a relatively strong gradient exists in the LWC at the centerline, which is consequently not a favorable measurement position. At 65 mm above the centerline, the gradient in the LWC is relatively small, hence the Nevzorov sensor head was positioned at that height for all test points. To be more

precise, the 8 mm cone of the Nevzorov probe was positioned 65 mm above the centerline, which led to the LWC sensor and the 12 mm cone being positioned two centimeters above and below, respectively (see Fig. 4.3a).
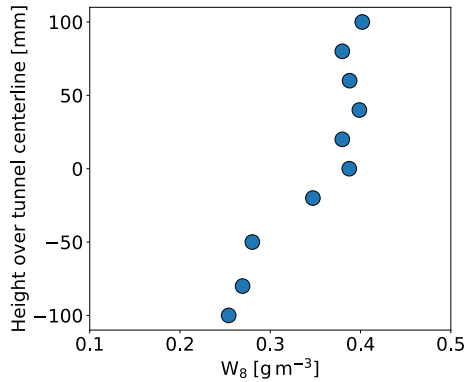
Figure 4.2: Liquid water content measurements of the 8 mm cone of the Nevzorov probe (W_8) at different heights in the Braunschweig Icing Wind Tunnel (BIWT) for a bimodal freezing drizzle condition.

The sample volumes of the CDP and the CIP on the CCP are separated by 13.5 cm. As the CIP detects large droplets, but the CDP measures only the small droplet spray, which is not strongly affected by inhomogeneities, the sample volume of the CIP was positioned at the same height as that of the 8 mm cone, while the CDP was positioned above (see Fig. 4.3b). A horizontal alignment of the arms of the CDP and the CIP was preferred over a vertical alignment (which would have allowed the CDP to be closer to the centerline) because it was assumed that water could accumulate on the upward-facing glass windows and render the measurements unusable.

The BCPD is designed for mounting in an aircraft fuselage and therefore lacks an appropriate canister to position it in the center of the tunnel. Instead, it was mounted to a side wall of the tunnel at the height of the centerline. The BCPD was housed in a plastic casing that protruded approximately 6 cm into the tunnel. The distance of 6 cm was chosen because prior measurements by the BIWT operators showed that at this distance the airflow and the droplet spray would be unaffected by the side wall. To affect the streamlines in the proximity of the BCPD as little as possible, the casing was given a gentle slope in the direction facing the airflow. The result was a shape that bore a resemblance to the beak of a platypus (see Fig. 4.3c). Thus, a trade-off between distance to the centerline and modification of the flow was handled.

Technical problems, such as the icing of spray nozzles and the production of ice instead of water, were repeatedly encountered at the BIWT. All test points I present here have been considered valid after a thorough analysis. It was generally attempted to measure the same test points with all instruments. Due to the removal of invalid measurements, the selection of test points for the Nevzorov probe and the BCPD differ. The test points that are used to analyze each instrument are
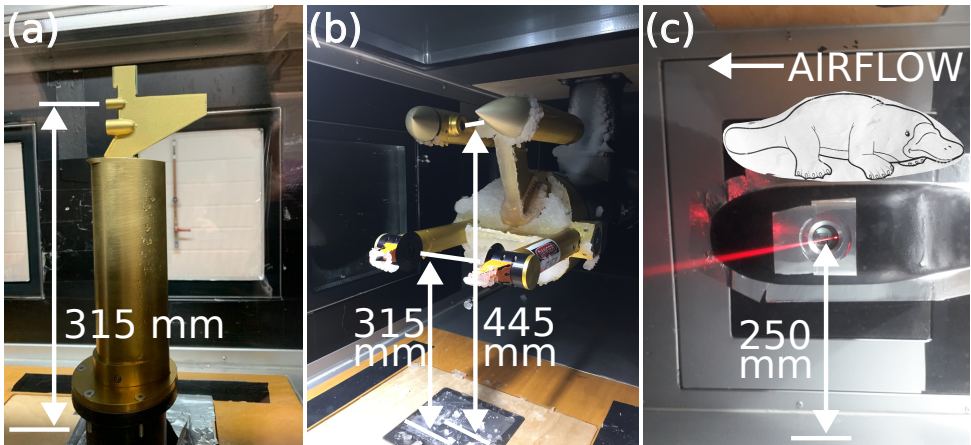
Figure 4.3: Mounting positions of the Nevzorov probe **(a)**, CCP **(b)** and BCPD **(c)** in the Braunschweig Icing Wind Tunnel.

presented in Section 4.3.1 and Section 4.4.1 for the Nevzorov probe and the BCPD, respectively.

ADDITIONAL MEASUREMENTS

Complementary to the measurements of the Nevzorov probe, the CCP and the BCPD, the BIWT operators provided measurements of the LWC based on data from high-accuracy flow meters for their small droplet spray and freezing drizzle conditions (see Table 4.2). Flow meters measure the quantity of water that passes through each nozzle. The overall throughput is then divided by the tunnel cross section to obtain LWC values. These measurements, which were not obtained in the scope of the campaigns listed in Table 4.1, are later used as reference measurements.

4.1.2. MEASUREMENTS IN THE GOODRICH ICING WIND TUNNEL

The Goodrich Icing Wind Tunnel of Collins Aerospace (referred to in this thesis as Collins IWT for brevity) is a well-established facility that has been involved in icing research for decades [14–16]. The spray system for Appendix C conditions has been calibrated as per ARP5905 [17] and can produce icing clouds with MVDs between 15-60 µm and LWCs between 0.15 and 3 gm^{-3}. The tunnel was upgraded to generate freezing drizzle in the scope of the SENS4ICE project. However, the small and the large droplet spray cannot be operated at the same time, such that only unimodal freezing drizzle conditions can be produced by the tunnel.

MEASUREMENTS PERFORMED AS PART OF THE SENS4ICE PROJECT

In the scope of the SENS4ICE project, measurements with the Nevzorov probe of DLR and a CCP, which was provided by Embraer, were performed in the tunnel. Unlike in the BIWT, the Nevzorov probe was mounted from the side wall, such
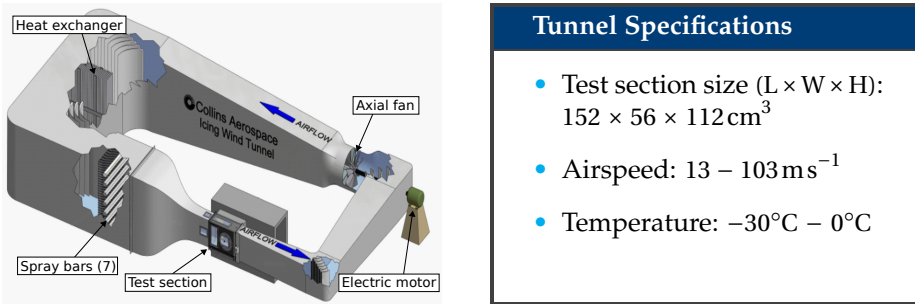
Figure 4.4: Schematic and specifications of the Collins icing wind tunnel (Figure adapted from [15]).

4

that the pillar and the sensor head were in a horizontal orientation. This comes with the advantage that the sedimentation effects of large droplets are similar at the positions of all three sensors. The CCP was also mounted from the side wall, but with the orientation of the arms horizontal as was the case in the BIWT.

ADDITIONAL MEASUREMENTS

For its tunnel calibration, Collins measured the LWC in small droplet spray conditions with an icing blade and the freezing drizzle conditions with a WCM-2000 (see Table 4.2). Only the forward-facing half-pipe element of the WCM-2000 is considered by Collins for the measurement of freezing drizzle conditions, as large droplets are assumed to splash on the other two sensing elements. For the calibration of the freezing drizzle conditions, the WCM-2000 was mounted at the same height as the Nevzorov probe, but 45 cm upstream due to mounting constraints. Regarding the tunnel homogeneity, measurements performed in the Collins IWT before the SENS4ICE measurement campaign showed that the uniformity of both small droplet spray and freezing drizzle conditions is within ±10 % over the spatial extent of the Nevzorov sensor head.

4.1.3. MEASUREMENTS IN THE CLIMATIC WIND TUNNEL OF RAIL TEC ARSENAL

The third set of measurement data originates from the climatic wind tunnel of Rail Tec Arsenal (RTA) in Vienna. The wind tunnel differs from the BIWT and the Collins IWT, especially by its much larger size. The tunnel was originally constructed to test railway vehicles [18]. Its layout and specifications can be seen in Section 4.1.3. RTA has been developing its capabilities to produce Appendix O conditions over several years [19]. For the production of freezing drizzle, it uses the same set of nozzles as for small droplet spray conditions, but with different temperature and pressure settings. To achieve satisfactory homogeneity in freezing rain conditions, RTA developed a special system with rotating spray nozzles, which improve the distribution of the large droplets [20].

MEASUREMENTS PERFORMED BY DLR

The measurements in this tunnel were not part of the SENS4ICE project but of the ICEGENESIS project. As this project's goals differed from those of the SENS4ICE IWT characterization, no measurements for a tunnel intercomparison with the CCP were performed, only Nevzorov probe measurements. In the tunnel, the Nevzorov probe was mounted in two different orientations. For the freezing rain measurements, which took place in 2019, the sensor head was in a vertical orientation, while for the small droplet spray and freezing drizzle measurements, which took place in 2021, the sensor head was in a horizontal orientation.
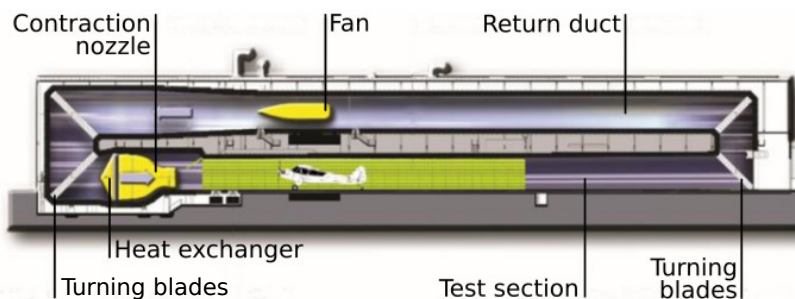
Tunnel Specifications

- Test section size (L × W × H): $90 \times 2.5 \times 3.5\,\mathrm{m}^3$

- Airspeed: $20 - 80\,\mathrm{m\,s}^{-1}$

- Temperature: $-30°C - 5°C$

Figure 4.5: Schematic and specifications of the Rail Tec Arsenal climatic wind tunnel (Figure adapted from [21]).

ADDITIONAL MEASUREMENTS

The climatic wind tunnel of RTA has been calibrated with many instruments. Like Collins, RTA uses icing blades to measure the LWC in small droplet spray conditions. For freezing drizzle conditions, RTA computes the LWC from a combination of measurements from the icing blade, the WCM-2000 (half-pipe element), the Nevzorov probe and Cloud Aerosol and Precipitation Spectrometer. The LWC in freezing rain conditions is determined solely from Isokinetic Probe measurements [22] (see Table 3.1 for an overview of the LWC instruments). The DSDs for the small droplet spray test points are derived from Malvern probe measurements. The DSDs for freezing drizzle and freezing rain are composites of measurements from many different instruments, e.g. from the Malvern, the Fast Cloud Droplet Probe [23, 24], the 2D-Stereo Probe [25], the Cloud Aerosol and Precipitation Spectrometer and the Precipitation Imaging Probe [26] (see Table 4.2).

4.1.4. CONTRIBUTORS TO THE ICING WIND TUNNEL MEASUREMENTS

The evaluation of the data from the Nevzorov probe, the CCP and the BCPD that is presented in the following is my own work. The IWT measurements that were described in the previous sections were a group effort in which multiple people participated. During the measurements at the BIWT, I was supported by Tina Jurkat-Witschas and Raphael Märkl from DLR, as well as Venkateshwar Reddy Bora and Stephan Sattler from the BIWT. At the Collins IWT, the measurements with the Nevzorov probe were conducted by Matthew Hamman and other Collins personnel under my supervision via a remote desktop connection, due to my inability to travel during the COVID-19 pandemic. The measurements with the CCP were performed by Matt Freer with the support of Collins personnel. The measurements at RTA were conducted by Romy Heller and Valerian Hahn of DLR, as well as Wolfgang Breitfuss of RTA.

4

IWT	LWC reference instrumentation			Droplet size reference instrumentation		
	SDS	FZDZ	FZRA	SDS	FZDZ	FZRA
Collins	Icing Blade	WCM-2000		CCP	CCP	
RTA	Icing Blade	Icing blade, WCM-2000 Nevzorov, CAPS	IKP	Malvern	Malvern, FCDP, 2D-S, CAPS	Malvern, FCDP, 2D-S, PIP
BIWT	Flow meters	Flow meters		CCP	CCP	

Table 4.2: Reference instrumentation used by the icing wind tunnels (IWTs) for the measurement of LWC and droplet size in small droplet spray (SDS), freezing drizzle (FZDZ) and freezing rain (FZRA) conditions. The instruments are abbreviated as follows: Cloud Combination Probe (CCP), Isokinetic Probe (IKP), Fast Cloud Droplet Probe (FCDP), 2D-Stereo Probe (2D-S), Cloud Aerosol and Precipitation Spectrometer (CAPS) and Precipitation Imaging Probe (PIP). An overview of the LWC instrumentation can also be found in Table 3.1.

4.2. ICING WIND TUNNEL MEASUREMENTS WITH THE CLOUD COMBINATION PROBE

For the computation of the collision efficiency of the Nevzorov probe and for the comparison to the BCPD measurements, DSDs of the IWT conditions are required. As mentioned in the previous section, a CCP was used in the BIWT and at the Collins IWT for the measurement of DSDs. This section describes the processing steps to obtain DSDs from the data of the two instruments that constitute the CCP, the CDP and the CIP.

The overlap between the size range of the CDP (2-50 μm) and the CIP (15-950 μm) raises the question, of how exactly the data of the two instruments should be combined. The CIP suffers from significant uncertainties at the lower limits of its size range, as was discussed in Chapter 3. However, as shown in Faber *et al.* [27], the CDP uncertainties are low up to a droplet diameter of 46 μm. The first two size bins of the CIP are therefore neglected and only particles that have a min-

imum size of three pixels, equivalent to a diameter of 45 µm, are considered. The threshold value for the CDP is based on the largest size bin in which a sufficient number of particles were counted (At least one particle count per bin per 5-second interval is required). The threshold value fell between 39-47 µm. A threshold value for the CDP larger or equal to 45 µm means that the third size bin of the CIP is also not used. Furthermore, a size binning for liquid droplets based on a laboratory calibration was applied to the lower end of the CDP size range to consider ambiguities caused by the Mie resonances [28, 29]. CIP data were processed with the SODA software [30]. The software incorporates a shattering [31] and a depth of field correction [32]. After combining the data of the two instruments I followed the procedure in Cober and Isaac [6] and performed a logarithmic interpolation between the bin centers to obtain a size distribution with 1 µm bin resolution.

4.3. ICING WIND TUNNEL MEASUREMENTS WITH THE NEVZOROV PROBE

This section characterizes the collision and capture efficiency of the 12 mm cone of the Nevzorov probe. Figure 4.6 displays the methodology used for the characterization. The figure is intended to aid the reader in understanding the relationship between the individual quantities that are computed and to serve as an orientation regarding the step of the methodology that is currently being discussed. The figure will be frequently referred to in the subsequent subsections.

The suitability of the 12 mm cone, which is addressed in research question I, is determined by the accuracy and precision of the collision efficiency corrected LWC measurements of the 12 mm cone. These measurements are denoted as LWC_{12} (see bottom right in Fig. 4.6) and are the final product from the raw 12 mm cone measurements (the raw measurements are denoted as W_{12}).

This section first provides an overview of the IWT test points that are available for the study (Section 4.3.1). Then, the collision efficiency of the 12 mm cone is derived from measurements in small droplet spray conditions (Section 4.3.2). Subsequently, the capture efficiency of the 12 mm cone is analyzed through a comparison to tunnel reference measurements in unimodal SLD conditions (Section 4.3.3). Eventually, the accuracy of LWC_{12} is assessed in bimodal SLD conditions, where both, the collision efficiency and the capture efficiency of the cone, are of importance (Section 4.3.4).

At the end of this section, the remaining uncertainties in the Nevzorov measurements and drawbacks of the probe that were observed during the testing are discussed (Section 4.3.5 and Section 4.3.6). Additionally, a method to estimate the droplet size from the measurements of the Nevzorov probe is presented in Section 4.3.7. The method becomes relevant in Chapter 6, where atmospheric Appendix O conditions need to be distinguished from Appendix C conditions.

4.3.1. OVERVIEW OF THE TEST POINTS

Figure 4.7 and Table A.1 provide an overview of all the test points from the three IWTs used for the study of the 12 mm cone of the Nevzorov probe. At the Collins
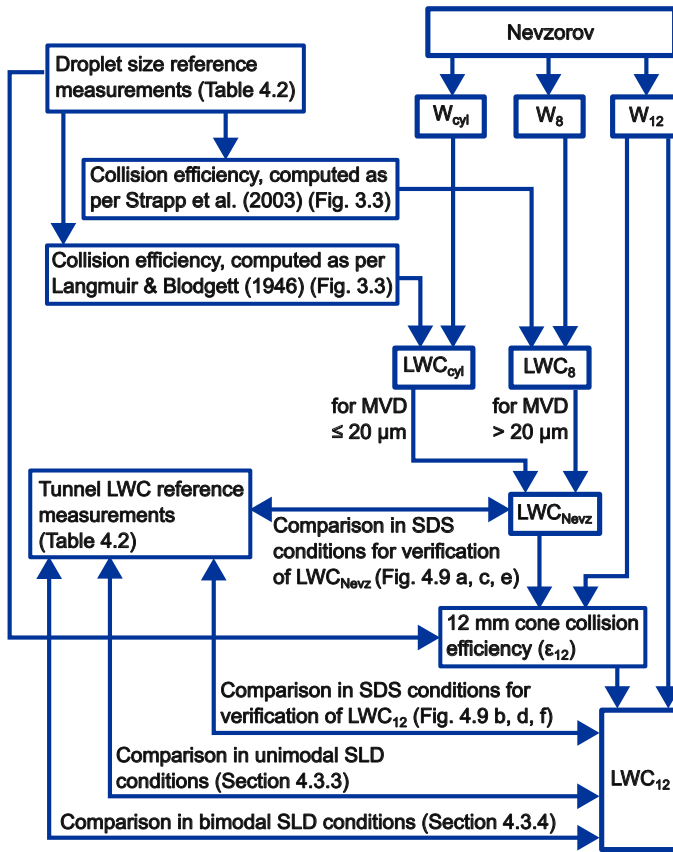
Figure 4.6: Methodology for the characterization of the 12 mm cone of the Nevzorov probe.

IWT, measurements of a total of 21 small droplet spray conditions at airspeeds of 40, 67 and 85 m s^{-1} were performed. Eight different small droplet spray conditions were measured in the BIWT at the maximum tunnel airspeed of 40 m s^{-1}. At RTA, four small droplet spray conditions were measured at an airspeed of 60 m s^{-1}. The small droplet spray conditions were selected in a way that large portions of the Appendix C icing envelopes were covered. Additional small droplet spray test points at MVDs beyond 40 μm were measured to characterize the collision efficiency of the Nevzorov probe for larger droplet sizes.

The freezing drizzle conditions vary significantly between the tunnels. The examined freezing drizzle test points represent the set of conditions that were attainable with the spray system of the IWT and were regarded as suitable under consideration of the trade-off between low LWC and preservation of icing cloud uniformity. The Collins IWT produced unimodal SLD conditions with MVDs between 128 and 221 μm at an airspeed of 76 m s^{-1}. At RTA and the BIWT mostly bimodal freezing drizzle distributions with varying fractions of LWC in the small

and large droplet modes were measured. Currently, of the three IWTs, only RTA is able to produce freezing rain conditions (see Table A.1). I obtained measurements in unimodal as well as bimodal freezing rain conditions at airspeeds of 50 and 60 m s^{-1}.
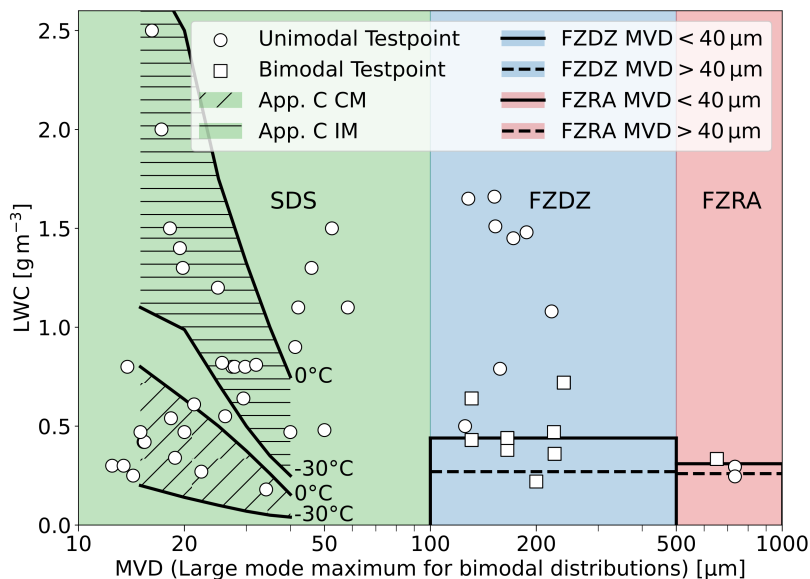
Figure 4.7: IWT test points used in this study, grouped into the categories small droplet spray (SDS), freezing drizzle (FZDZ) and freezing rain (FZRA). For unimodal test points, the markers represent the MVD, while for bimodal test points the diameter at the maximum of the large droplet mode is shown. The Appendix C envelopes for continuous maximum icing conditions (CM) and intermittent maximum icing conditions (IM) and the Appendix O maximum LWC envelopes from Cober and Isaac [6] are also shown for comparison.

4.3.2. Derivation of the collision efficiency of the 12 mm cone of the Nevzorov probe

Section 3.1.1 included a discussion of the factors that influence the collision efficiency of sensors. A larger sensor geometry leads to lower collision efficiencies. Consequently, for the Nevzorov probe, the collision efficiency of the 12 mm cone is expected to be below that of the 8 mm cone. Also, collision efficiencies eventually approach 100% as droplet size increases. Only the small droplet spray conditions are therefore relevant for the derivation of the collision efficiency.

Since the collision efficiency changes with airspeed, I define three groups of measurements in small droplet spray conditions, which are listed in Table 4.3. Group 1 contains measurements at 40 m s^{-1} from the Collins IWT and the BIWT,

Group 2 contains measurements at 60 and 67 ms^{-1} from the Collins IWT and RTA and Group 3 contains measurements at 85 ms^{-1} from the Collins IWT. The measurements in Group 2 differ in airspeed by 7 ms^{-1}. I group these measurements together because I assume that the gain in accuracy of the collision efficiency that is obtained by using more measurements outweighs the inaccuracy that is induced by not differentiating between the airspeeds.

IWT	Group 1 (40 ms^{-1})	Group 2 (60 and 67 ms^{-1})	Group 3 (85 ms^{-1})
Collins	6	9	6
RTA	0	4	0
BIWT	8	0	0
Total	14	13	6

Table 4.3: Number of small droplet spray measurements per airspeed group.

One possibility to derive the collision efficiencies of the 12 mm cone experimentally is to compare its measurements in the IWT with the tunnel LWC reference measurements (see Table 4.2). Collision efficiency curves can then be estimated with a fit through the data points.

Alternatively, the measurement of the Nevzorov LWC sensor and the 8 mm cone can be used as a reference. The collision efficiencies of these two sensors are well characterized, hence their raw measurements (W_{LWC} and W_8, respectively) can be corrected and serve as a benchmark for the true tunnel LWC. The collision efficiency corrected measurements of the LWC sensor and the 8 mm cone are denoted as $\mathrm{LWC}_{\mathrm{LWC}}$ and LWC_8, respectively (see Fig. 4.6). The advantage of using these two sensors as a reference is that they were subjected to the exact same condition as the 12 mm cone, consequently, the comparison is not affected by random fluctuations of the LWC in the IWTs. Therefore, for the derivation of the collision efficiency curve of the 12 mm cone, the LWC sensor and the 8 mm cone of the Nevzorov probe are used instead of the tunnel LWC reference instrumentation.

As mentioned in Section 3.1.1, large droplets tend to splash on the LWC sensor, whereas for the 8 mm cone the collision efficiency of small droplets is low, which makes the LWC estimate prone to large uncertainties. To compute the LWC that was present in the tunnel, I use the appropriate sensor for each measurement. If the MVD is smaller or equal to 20 µm I utilize $\mathrm{LWC}_{\mathrm{LWC}}$, while for an MVD larger than 20 µm LWC_8 is used. In the following this combination of LWC values from the LWC sensor and the 8 mm cone is referred to as the Nevzorov reference LWC and denoted as $\mathrm{LWC}_{\mathrm{Nevz}}$ (see Fig. 4.6).

In an ideal experimental setup the Nevzorov probe would be exposed to monodisperse droplet distributions, the measurements of the 12 mm cone would be compared to $\mathrm{LWC}_{\mathrm{Nevz}}$ and a collision efficiency curve could be derived. Realistic conditions differ from that setup because dispersed droplet distributions are produced. In our experiments, these droplet distributions are derived from the droplet size reference instrumentation (see Table 4.2). The collision efficiency curve of the

12 mm cone can be described by a function $f(d)$, where d is the droplet diameter. For an ideal measurement, the raw LWC measured by the 12 mm cone (W_{12}) is equal to the LWC in the tunnel, which I approximate with LWC_{Nevz}, multiplied by the overall collision efficiency of the 12 mm cone (ε_{12}), see Eq. (4.1).

$$W_{12} = \varepsilon_{12} \cdot \text{LWC}_{\text{Nevz}} = \sum_{d_i = d_{\min}}^{d_{\max}} f(d_i) \cdot v(d_i) \cdot \text{LWC}_{\text{Nevz}} \tag{4.1}$$

Here, $v(d_i)$ is the fraction of the total LWC in size bin i, calculated from the available DSDs. The question arises what kind of analytical function $f(d)$ should be. Korolev *et al.* [33] suggested Eq. (4.2) for $f(d)$, where D_0 is the free parameter, which can be adjusted depending on the sensor that is modeled. I also experimented with other functional forms, but the resulting curves tended to be less realistic (in the sense that the curve shape did not match the sensor ratios of W_{12} to LWC_{LWC} or LWC_8). Hence, Korolev's curve was used.

$$f(d) = \frac{d^2}{\left(D_0^2 + d^2\right)} \tag{4.2}$$

In the next step, I formulate a system of equations for each airspeed group, where each equation represents one measurement and is of the form of Eq. (4.1). I minimize the sum of squared residuals (*RSS*, see Eq. (4.3)) with respect to D_0 to find the optimal solution for D_0 for each airspeed group:

$$RSS = \sum_{j=1}^{n} \left(\frac{W_{12, \text{TP}_j}}{\text{LWC}_{\text{Nevz}, \text{TP}_j}} - \sum_{d_i = d_{\min}}^{d_{\max}} f(d_i, D_0) \cdot v_{\text{TP}_j}(d_i) \right)^2. \tag{4.3}$$

In the equation above, TP_j denote the individual test points. The results of the least squares estimation are shown in Table 4.4.

Group	G1	G2	G3
D_0	18.3 ± 1.1	18.7 ± 0.6	17.6 ± 1.3

Table 4.4: D_0 values computed from the curve fit for the different airspeed groups. The uncertainties represent the 1σ intervals that are associated with the curve fit.

Figure 4.8 shows the computed collision efficiency curves. The three curves for the three different airspeed groups lie very close together so that they are hardly distinguishable. The collision efficiency of a 10 μm diameter droplet is only 0.2, but it then rises steeply to 0.5 for 20 μm droplets. Beyond 20 μm its slope decreases continuously and the collision efficiency attains 0.7 for 30 μm droplets and 0.9 for 60 μm droplets. The collision efficiency curve for group 1 (40 ms^{-1}) is slightly higher than that of group 2 (60 to 67 ms^{-1}). This is unexpected because a higher airspeed leads to higher momentum and therefore results in a higher collision efficiency, in line with equations (3.8) and (3.9). However, within the stated error

margins also the scenario $D_{0,G1} < D_{0,G2}$ is possible. Figure 4.9 shows the comparison between LWC_{12}, LWC_{Nevz} and the tunnel LWC for the small droplet spray test points (compare Fig. 4.6). For all measurements, the collision efficiency was computed using the full DSD. Each row of Fig. 4.9 contains a different airspeed group. The left panels depict the ratio of LWC_{Nevz} to the tunnel LWC, i.e. they compare how well the reference measurements from the Nevzorov probe and the tunnel LWC reference measurements agree (see Fig. 4.6). The shaded areas denote 10% and 20% deviation from the tunnel LWC measurements. The comparisons show a good agreement between LWC_{Nevz} and the tunnel LWC, where, across all airspeed groups, 58% and 94% of the Nevzorov measurements fall within ±10% and ±20% of the tunnel LWC respectively. The scatter of the data points can be explained through the combined uncertainties of the Nevzorov probe and the IWT (the Nevzorov uncertainties are further discussed in Section 4.3.6).

The right panels show the ratio of LWC_{12} to the tunnel LWC. For airspeed group 2 (Fig. 4.9d), LWC_{12} exhibits a similarly good agreement to the tunnel LWC as LWC_{Nevz} (Fig. 4.9c). For airspeed groups 1 and 3 (Fig. 4.9b and 4.9f), the discrepancies between LWC_{12} and the tunnel LWC are a bit larger than between LWC_{Nevz} and the tunnel LWC (Fig. 4.9a and 4.9e). Across all airspeed groups, 42% and 79% of the LWC_{12} values fall within ±10% and ±20% of the tunnel LWC, respectively. The outliers at low MVDs are mostly data points with high LWCs.

There has been an ongoing discussion concerning the ability of the Nevzorov probe to evaporate all of the impinging water. For an earlier, shallower version of the Nevzorov's cone Emery *et al.* [34] observed that a pool of water formed inside the cone and was occasionally swept out, which led to an underestimate of the LWC. The effect occurred during ice shaver conditions run at an airspeed of 67 m s^{-1} and a TWC larger than 2.1 g m^{-3}. For this work, a thorough analysis of the data found no evidence of pooling. Pooling and subsequent underestimates of LWC should be a function of LWC flux. While LWC_{12} is lower than the tunnel LWC for some of the high LWC flux test points, it is equal or higher for many others (see Fig. 4.9 and Table A.1). The discrepancy between LWC_{12} and the tunnel LWC for the low MVD and high LWC points can in part be explained through droplet coincidence effects in the CDP (see Section 3.2.3). The number concentrations for these test points exceeded 2000 cm^{-3} and droplet coincidence [28, 35] was present (see Appendix A.3). Droplet coincidence results in a shift towards larger droplets in the size distribution, which in turn decreases the applied collision efficiency. The magnitude of the effect and its exact influence on LWC_{12} could not be determined, because the inter-arrival time data, which is used to correct for coincidence, was not available for the measurements at the Collins IWT.

4.3.3. Measurements in unimodal supercooled large droplet conditions

The Nevzorov probe was tested in unimodal SLD conditions to characterize its capture efficiency of SLD, see Table A.1 and Fig. 4.6. These test points provide valuable information on the response of the Nevzorov sensors to large drops. Figure 4.10 shows the results of the measurements in comparison to the tunnel LWC,
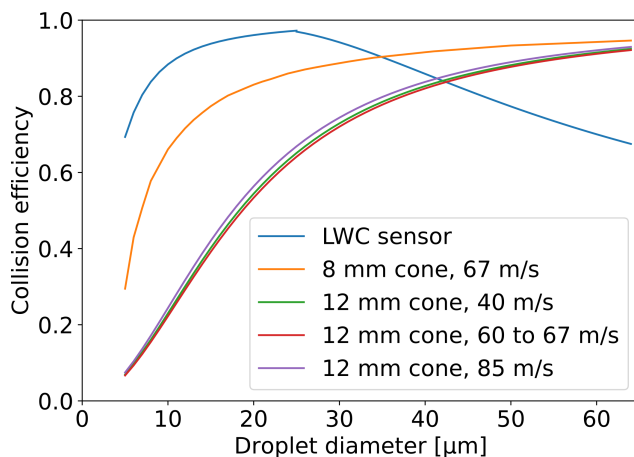
Figure 4.8: Collision efficiency curves of the Nevzorov 12 mm cone for the three airspeed groups, the collision efficiencies of the LWC sensor and the 8 mm cone from the literature are shown for comparison.

determined with the WCM-2000 instrument for the freezing drizzle cases (except for the freezing drizzle test point with the lowest MVD, which was measured at RTA with multiple instruments) and with the Isokinetic Probe for the freezing rain test points (see Table 4.2). No collision efficiency corrections were applied to any of these measurements because the droplet diameters were deemed to be sufficiently large for collision efficiency effects to be irrelevant (hence $LWC_{12} = W_{12}$, $LWC_8 = W_8$). The overall agreement between the Nevzorov and the tunnel LWC in Fig. 4.10 is good, all LWC_8 values and all but one LWC_{12} value fall within ±20% of the tunnel LWC. The LWC_8 and LWC_{12} values generally follow a similar trend in comparison to the tunnel LWC, but LWC_{12} is on average 6.5% higher than LWC_8. For the freezing drizzle test points, where the tunnel LWC was determined with the WCM-2000, LWC_8 and LWC_{12} increasingly exceed the tunnel LWC with increasing MVD values. This does not apply to the freezing rain test points, for which the tunnel LWC was determined with the Isokinetic Probe.

The results suggest that the Nevzorov TWC sensors are better suited than the WCM-2000 for the collection of droplets with diameters of approximately 200 μm or more. A possible explanation is the greater depth and width of the Nevzorov sensors, which allows them to retain most of the large droplets. Splashing and bouncing effects, similar to those described by Korolev *et al.* [36] for an earlier, shallower version of the Nevzorov TWC cone might occur on the 2.1 mm wide WCM-2000 TWC sensor. In line with these observations, a comparison of the WCM-2000 and the Isokinetic Probe showed that the LWC measurements of the Isokinetic Probe exceeded those of the WCM-2000 [22], in freezing rain conditions even by as much as 65%.

Other factors can also cause or contribute to the discrepancies between Nevzorov and WCM-2000, such as the different mounting positions of the two instruments or an uneven distribution of the large droplet spray. Additionally, the high
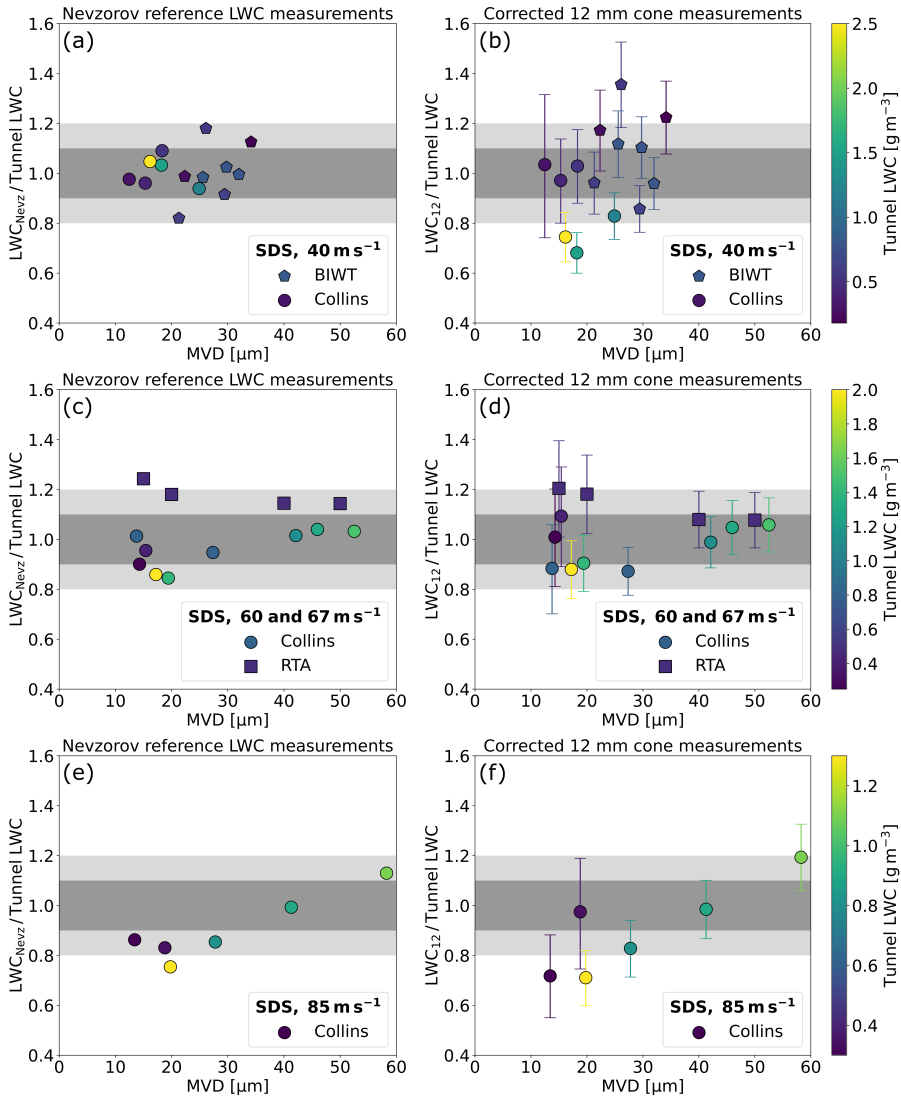
Figure 4.9: Comparison of the Nevzorov reference LWC (LWC_{Nevz}) and the corrected 12 mm cone LWC (LWC_{12}) to the tunnel LWC for different MVD and the three different airspeed groups (top, middle, bottom). The error bars incorporate all uncertainty sources of the Nevzorov probe as detailed in Section 4.3.6, including the uncertainty in the collision efficiency curve, which is described by the standard deviation of D_0 (see Table 4.4). The error bars do not consider uncertainties not related to the Nevzorov probe, e.g. the IWT variability.

LWC of the large droplet spray at the Collins IWT led to oscillations of the sensor head that may have affected the measurements.

The fact that LWC_{12} is on average higher than LWC_8 suggests that, due to its larger depth and smaller perimeter-to-area ratio, the capture efficiency of the 12 mm

cone is larger than that of the 8 mm cone. However, the difference between the two cones is still within the uncertainty range of the instrument, so no definitive statement can be made.

Now, both the collision efficiency of the 12 mm cone and its capture efficiency have been characterized individually. In the subsequent section, the accuracy of the 12 mm cone is analyzed in bimodal SLD conditions, i.e. in an environment where both the collision efficiency and the capture efficiency are relevant.
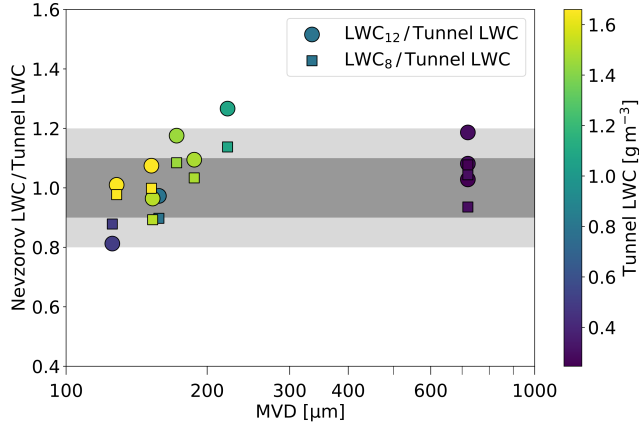
Figure 4.10: Measurements of the 12 mm cone (LWC_{12}) and the 8 mm cone (LWC_8) in comparison to the tunnel LWC in unimodal freezing drizzle and freezing rain conditions. The tunnel LWC is based on WCM-2000 measurements for all the freezing drizzle test points and on Isokinetic Probe measurements for the freezing rain test points.

4.3.4. MEASUREMENTS IN BIMODAL SUPERCOOLED LARGE DROPLET CONDITIONS

Bimodal SLD conditions were measured in the BIWT and the RTA climatic wind tunnel (see Table A.1). An overview of the cumulative LWC from the bimodal DSDs measured with the CCP in the BIWT can be seen in Fig. 4.11. Often, collision efficiencies of DSDs are approximated by using the MVD as a representative diameter for the entire distribution. This has been shown to work well for small cylindrical sensors and unimodal droplet distributions [37, 38]. Recently, Sokolov and Virk [39] found that Langmuir A-J distributions [40] with similar MVDs had very different collision efficiencies on a 30 mm cylinder at an airspeed of 4 m s^{-1}. Furthermore, larger errors can be introduced when using the MVD approximation for bimodal distributions [41]. Van Zante *et al.* [42] also caution that bimodal distributions cannot be represented by the MVD only. In Fig. 4.11 I investigate the magnitude of the errors introduced by using the MVD approximation for droplet collision efficiency for five bimodal distributions measured with the HALO-CCP in the BIWT (shown in Fig. 4.11a). The distributions with the MVDs of 16, 18, and 61 μm have a small droplet mode centered around 15 μm and a large droplet mode at approximately 230 μm. They differ mainly in the ratio of liquid water contained

in small droplets to liquid water contained in large droplets. The distributions with MVDs of 24 and 34 µm have their small droplet mode centered at 20 and 30 µm, respectively, and their large droplet mode at 166 µm. Figure 4.11b shows the relative error in the LWC when the MVD approximation for droplet collision efficiency is used. It highlights the importance of computing the collision efficiency from the entire DSD, especially for sensors such as the 12 mm cone where a large collision efficiency correction is applied. In one bimodal distribution, the error from the usage of the MVD approximation for droplet collision efficiency exceeds 30%. The relative error is not a function of the MVD but rather depends on how well the MVD represents the DSD. As a consequence of the findings presented above, I use the full DSD as input to the collision efficiency function when computing LWC_{12} and LWC_8.
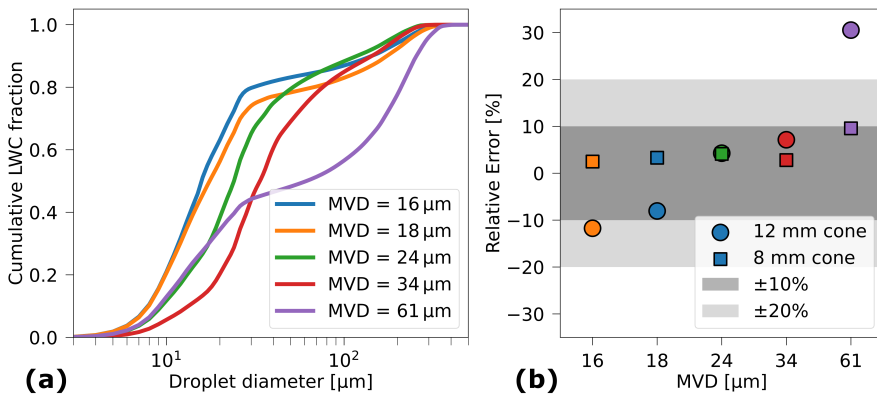
Figure 4.11: **(a)**: Cumulative liquid water content of the bimodal DSDs measured with the HALO-CCP (see Section 4.2) in the BIWT. **(b)**: Relative error of the LWC estimate that is introduced when approximating the collision efficiency from the MVD as compared to the collision efficiency estimated using the DSDs shown on the left side.

The application of the collision efficiencies for bimodal SLD conditions has now been clarified, hence I proceed to the comparison of LWC_{12} to the tunnel LWC in bimodal freezing drizzle and freezing rain conditions (see Fig. 4.6). The results are shown in Fig. 4.12 and Table 4.5. The LWC_8 values are also provided. The results show that both, LWC_{12} and LWC_8, agree within ±20% with the tunnel LWC for all but one test point. The measurements of the two Nevzorov cones, LWC_{12} and LWC_8, coincide closely with each other once the MVD exceeds 24 µm. At lower MVDs, LWC_{12} and LWC_8 diverge into opposite directions from the tunnel LWC.

The results prove that reliable measurements of LWC in bimodal SLD conditions can be achieved with the 12 mm TWC cone of the Nevzorov probe. The collision efficiency correction appears to be very accurate once the MVD exceeds 24 µm. The divergence of LWC_{12} and LWC_8 from the tunnel LWC at lower MVDs can be seen as an indication that minor errors still exist in the collision efficiency curve of the 12 mm cone and possibly also in that of the 8 mm cone, as acknowl-

edged by Strapp *et al.* [43]. The analytical form for the collision efficiency curve of the 12 mm cone is simple, therefore it is probable that the curve cannot accurately represent the collision efficiency for all diameters. Furthermore, the collision efficiency at small diameters is low, so that even a small offset in the curve introduces large errors in the result. For the test point at an MVD of 61 µm, both LWC_{12} and LWC_8 exceed the tunnel LWC by approximately the same value and the offset is consistent for both measurements that were made in this condition. This indicates that the discrepancy is not due to a problem with the Nevzorov probe or the collision efficiency correction, but more likely a larger uncertainty in the tunnel calibration exists for this point. It is important to remember that the accuracy of the collision efficiency also depends on the DSD. The DSD is subject to the uncertainties of the reference instruments. Errors in the DSD, which is used as an input for the computation of the collision efficiency, propagate into the errors of the LWC. The measurement uncertainties of the Nevzorov probe are further discussed in Section 4.3.6.
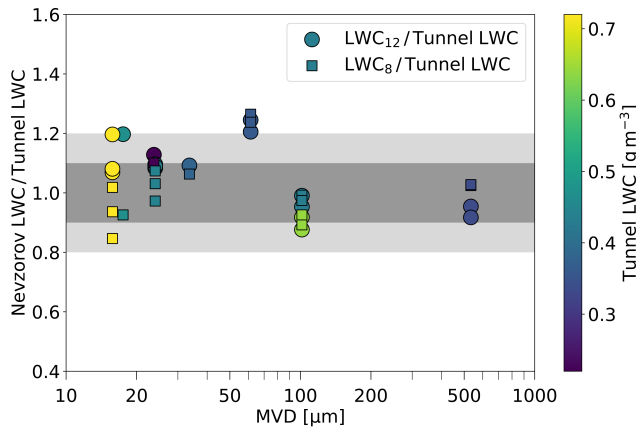
Figure 4.12: Same as Fig. 4.10 but for bimodal SLD conditions and with collision efficiencies applied. For the freezing drizzle test points from the BIWT, the tunnel LWC is based on flow meter measurements. The tunnel LWC of the freezing drizzle test points from RTA was determined from a combination of icing blade and WCM-2000 measurements. The tunnel LWC of the freezing rain test points from RTA stems from a combination of icing blade and Isokinetic Probe measurements. Table 4.5 lists the IWTs where the individual test points originated.

4.3.5. BIASES BETWEEN SENSOR HEADS

Two different sensor heads of the Nevzorov probe with serial numbers SN416 and SN433 were used during testing in the BIWT. Some test points were measured with both sensor heads. During the comparison of the measurements, a curious effect was noted. It appears that the 8 mm cone of the sensor head with serial number SN416 measured consistently higher values than the 8 mm cone of the sensor head SN433. This can be seen in Fig. 4.13. The relative difference between the 8 mm cone measurements is in general the largest of the three values (largest meaning also the least negative, as in the case of test point 418). Generally, it is not surprising if dif-

Test point	Tunnel	MVD [μm]	LWC_8/Tunnel LWC	LWC_{12}/Tunnel LWC	ε_{12mm}
522	BIWT	16	0.94	1.07	0.49
521	BIWT	18	0.93	1.16	0.53
524	BIWT	24	1.02	1.06	0.61
U13	RTA	24	1.10	1.10	0.66
525	BIWT	34	1.06	1.07	0.72
537	BIWT	61	1.25	1.21	0.70
U15	RTA	102	0.91	0.89	0.85
U18	RTA	102	0.98	0.95	0.84
TP7	RTA	534	1.02	0.95	0.90
TP8	RTA	534	1.02	0.91	0.90

Table 4.5: Comparison of the collision efficiency corrected LWC of the 12 mm cone (LWC_{12}) to the tunnel LWC and the collision efficiency corrected LWC of the 8 mm cone (LWC_8). The values of test points that were measured multiple times were averaged.

ferences between the two sensor heads exist, this may be completely unrelated to the sensor head and instead caused by tunnel variability. However, if they are due to tunnel variability, the differences should be approximately equal for the three sensors. This is not the case. The mean relative difference between the measurements of the two LWC sensors is just 0.2%, for the two 12 mm cones it is -1.2%, but for the two 8 mm cones it is 9.2%, as can be seen from the the last column of Fig. 4.13.
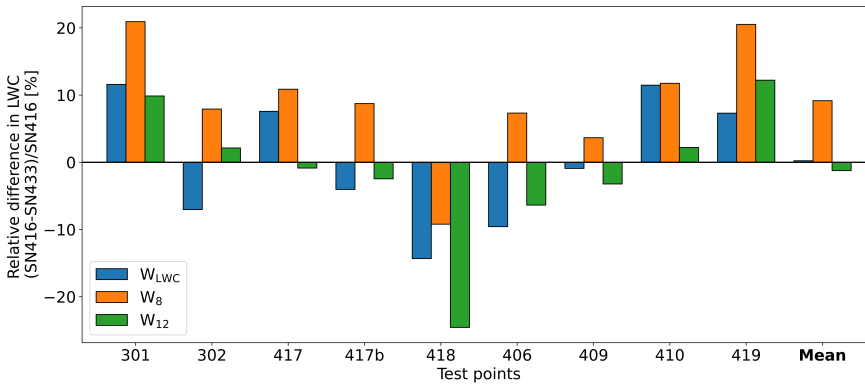
Figure 4.13: Relative differences between the LWCs measured by the Nevzorov sensor head SN416 and the Nevzorov sensor head SN433 for the LWC sensor (W_{LWC}, blue), the 8 mm cone (W_8, orange) and the 12 mm cone (W_{12}, green). The differences are shown for several test points measured at the BIWT.

The difference between the measurements of the two 8 mm cones means that one of the cones consumes more power than the other. This could be related to either the convective heat losses or the energy needed for the heating and evaporation of droplets. I noticed that the convective heat losses of the sensors are not the same. This can be due to several reasons, e.g. slightly different shapes of the cones

or slightly different temperatures of the sensors. However, I computed the convective heat losses separately for each sensor head and verified that the signals from all sensors were close to zero before the start of the droplet spray. All differences that exist between the convective heat losses of the two 8 mm cones are therefore removed and cannot explain the difference in measured LWC. Consequently, the bias only occurs in the presence of the droplet spray, which means that one of the sensors evaporates more liquid water than the other. A logical explanation would be that the sample areas of the sensors are unequal, but measurements showed that they are of nearly identical size.

In the end, measurements at the Collins IWT helped to solve this conundrum. During several of these measurements, especially during those which were run at a temperature of -20 °C and at an airspeed of 85 $\mathrm{m\,s}^{-1}$, ice build-up was observed on the cones at some point after the start of the measurement. At the same time, an increase in the LWC measured by the cones (that corresponds to an increase in power) could be observed. The measurements of the cones are affected by the build-up of ice (see Fig. 4.14). The outside of the cone is not hot enough to melt the ice at the same rate at which it is accreting, but some power is nonetheless expended. This shows that the insulation of the Nevzorov sensor head is incomplete towards the outside of the cone. During the measurements in the BIWT, no ice build-up was observed on the outside of the cone. However, while the spray was active water flowed along the side of the cones and cooled the outside of the cone. As is the case for ice, this leads to a higher power consumption of the respective sensor. Given that the Nevzorov sensor heads are handmade, there may be some differences in the insulation of the individual cones. This difference in insulation can explain the bias between the two sensors.

4.3.6. UNCERTAINTIES

The bias that was discussed in the previous section is one of the uncertainties that affect the Nevzorov probe. In this section, I assess the overall accuracy that is achievable with the Nevzorov probe. While the literature usually estimates the accuracy of the Nevzorov probe to be between ±10% and ±15% [33, 44], no thorough compilation of all the uncertainties and their dependence on atmospheric and flight parameters exists. Therefore, I begin with a categorization of the uncertainties that affect the Nevzorov probe measurements.

GENERAL SENSOR ACCURACY

This category comprises all the uncertainties that are intrinsically connected to the sensor, e.g. uncertainties related to the response of the electronics, slight differences in the sensor geometry or sensor biases as the one that was discussed in the previous section. Uncertainties of the response of the electronics are mostly eliminated through the subtraction of the convective heat loss term. As mentioned in Section 4.3.5, no large differences in the sensor geometry were found. Based on the discussion of the sensor bias in Section 4.3.5, I estimate the general accuracy of the LWC measurement as ±10%.
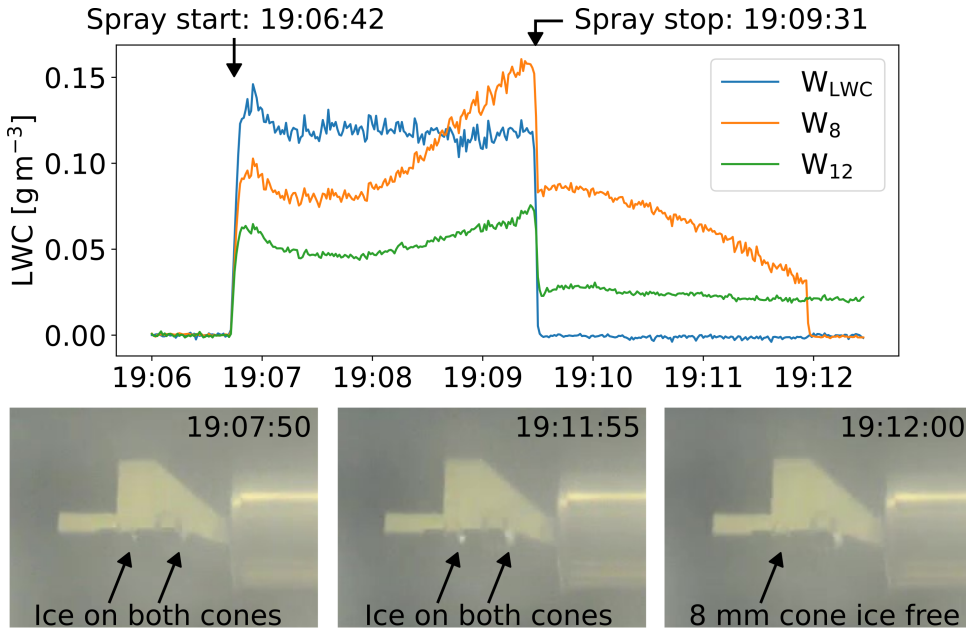
Figure 4.14: Temporal evolution of W_{LWC} (blue), W_8 (orange) and W_{12} (green) for test point C8 (see Table A.1) and images of the Nevzorov probe sensor head during the measurement.

ACCURACY OF THE CONVECTIVE HEAT LOSS TERM

The convective heat losses depend on airspeed (U), ambient temperature (T_a), pressure and the sensor geometry. I disregard the influence of pressure changes here, as the pressure remained constant in the IWTs. Generally, a higher airspeed, lower ambient temperature and larger sensor geometry lead to larger convective heat losses. To assess how an inaccuracy in the estimated convective heat losses affects the overall LWC measurement, I need to consider the contribution of the convective heat loss term to the total power expenditure. The contribution of the convective heat loss term decreases with increasing LWC, hence the relative error caused by an inaccuracy in the estimated convective heat losses is smaller for high LWC test points than for low LWC test points. To ensure comparability, I state all uncertainties with respect to an LWC value of $0.2\,\mathrm{g\,m^{-3}}$.

The 8 mm cone and the 12 mm cone have larger absolute convective heat losses than the LWC sensor, however, they also capture significantly more liquid water due to their larger sample area. Figure 4.15 displays the convective heat losses of each sensor for different airspeeds. To consider the different sample areas, the values have been normalized by the sampling volume of each sensor, which is derived from the airspeed multiplied by the sensor sample area. The convective heat losses per volume of air are lowest for the 12 mm cone, followed by the 8 mm cone. Their inverted-conical shape inhibits the airflow and thus reduces convective heat losses. The convective heat losses of the LWC sensor are 2.5 to 3 times that of the 8 mm and 12 mm cone. Also, the convective heat losses per unit volume decrease

with airspeed, while the liquid water content per unit volume is independent of airspeed. Consequently, the ratio of dry term to wet term (see Eq. (3.5)) is larger for measurements at high airspeed, hence their accuracy is less affected by errors in the convective heat loss term.

For the IWT test points, I was able to determine the factor k (see Eq. (3.6)) with an uncertainty below 2%. The error that results from this uncertainty can amount to approximately 11% for the LWC sensor under the least favorable conditions (T_a = −20 °C, U = 40 m s^{-1}). For the 8 mm and 12 mm cone, the uncertainties for this condition are 5% and 3.5%, respectively. In favorable conditions, such as T_a = −10 °C, U = 85 m s^{-1}, the uncertainties due to convective heat losses for the LWC, 8 mm cone and 12 mm cone sensors are only 7%, 2.5% and 2%, respectively.

ACCURACY OF THE COLLISION EFFICIENCY

The formulations of Langmuir and Blodgett [40] and Finstad *et al.* [45] for the flow of droplets around a cylinder agree within two percent for the droplet sizes that are relevant for this study. Hence I assume that the uncertainty in the LWC collision efficiency estimate is not greater than that value. Strapp *et al.* [43] did not publish any uncertainties for their collision efficiency curve of the 8 mm cone but noted that the curve may contain significant errors at small droplet diameters. I found that the values of LWC$_8$ indeed fall significantly below that of the tunnel LWC and LWC$_{LWC}$ at small droplet diameters (see Fig. 4.16). A downward shift of the collision efficiency curve by 0.14 and 0.07 yielded the best agreement of LWC$_8$ with the tunnel LWC and LWC$_{LWC}$ respectively, if only test points with an MVD < 20 μm were considered. Above 20 μm the agreement between LWC$_8$ and the tunnel LWC is good, only a slight downward shift of the collision efficiency curve by 0.02 would lead to marginally lower residuals between the tunnel LWC and LWC$_8$ (I did not compare LWC$_8$ to LWC$_{LWC}$ because I considered the measurement of the LWC sensor unreliable because of possible splashing effects). I, therefore, assume that the collision efficiency curve of Strapp *et al.* [43] is accurate to within ±0.02 for diameters of 20 μm or larger.

OVERALL UNCERTAINTY

I consider all the above-mentioned uncertainties to be uncorrelated biases that are Gaussian-distributed. They are combined following the procedure suggested in AGARD-AR-304 [46]. For LWC$_{LWC}$ the maximum combined uncertainty that I expect for MVDs between 10 and 20 μm is ±15%, in IWT conditions which are more favorable in terms of the magnitude of the convective heat losses, the uncertainty decreases to approximately ±12%. For LWC$_8$ the maximum uncertainty in the MVD range from 20 to 60 μm is ±11%. The uncertainty in LWC$_{12}$ at small MVDs is inevitably large and reaches up to ±29% at an MVD of 12 μm and U = 40 m s^{-1}. However, the uncertainty rapidly decreases to ±19% at an MVD of 15 μm and to ±14% at an MVD of 22 μm. Uncertainties in the convective heat losses of the 12 mm cone are small compared with the other uncertainty sources, therefore changes in airspeed or temperature should only cause minor differences in the stated uncertainties.
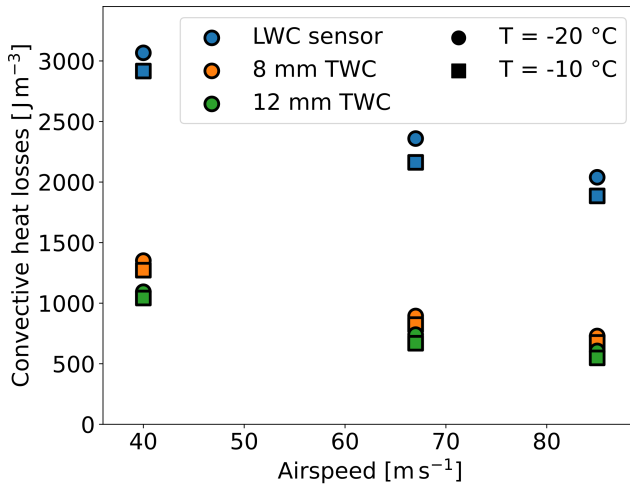
Figure 4.15: Convective heat losses of the Nevzorov sensors for different airspeeds per volume of air.
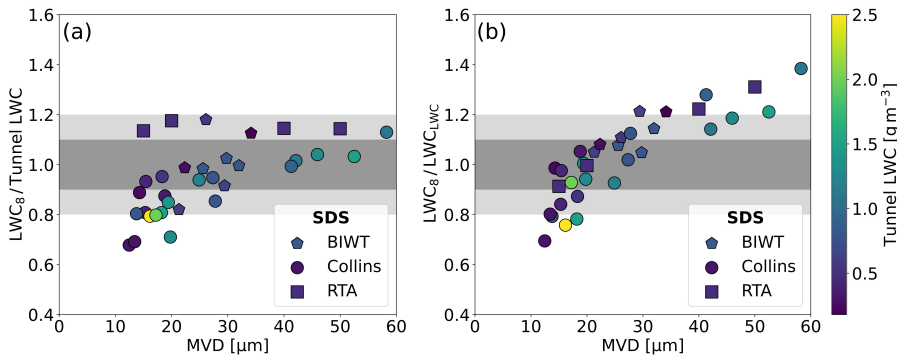
Figure 4.16: Comparison of the collision efficiency corrected 8 mm cone measurements (LWC_8) to the tunnel LWC **(a)** and to the collision efficiency corrected LWC sensor measurements (LWC_{LWC}) **(b)**.

This study found that the capture efficiency of the cones either does not decrease with increasing droplet size or, as may be the case for the 8 mm cone, is only marginally reduced (see Section 4.3.3). This is in agreement with the observations from Korolev *et al.* [36] that the number of ice particles that bounce from the 8 mm cone is small.

In SLD conditions with large LWCs, the sensor head exhibited high-frequency flutter around its axis of rotation. This flutter led to (very short-term) deflections of the sensor head of up to ±20°, which may introduce additional uncertainty into the measurement. The change in sample area caused by the flutter is however just a few percent. The previously mentioned uncertainty sources, e.g. the convective heat loss term and sensor biases, are not increased in SLD conditions compared to small droplet spray conditions. The uncertainty of the collision efficiency in SLD

conditions is very close to zero, because the collision efficiency of SLDs is essentially 100%. Considering all this, I conclude that the measurement uncertainties of the 12 mm and 8 mm cone of the Nevzorov probe in SLD conditions are smaller or at most equal to those in small droplet spray conditions.

4.3.7. DEDUCTION OF DROPLET SIZE

In consideration of research question III, it is necessary to detect large droplets without an optical instrument, because the size range of the BCPD extends only from 2-42 μm. Hence, a solution needs to be found on how the presence of large droplets can be inferred from measurements of the Nevzorov probe.

The previous sections showed that the droplet collision efficiency is related to droplet size. Consequently, an estimate of droplet size can be obtained from ratios between the three sensors. Apart from this, another possibility exists. The amount of liquid water contained in large droplets is significantly higher than in small droplets. When a large droplet impacts on a Nevzorov sensor, the power consumption increases momentarily as the sensor aims to maintain its temperature. This effect becomes apparent when one analyzes the standard deviation of the Nevzorov sensor signals. This can be seen in Fig. 4.17. For both the 8 mm cone and the 12 mm cone, a clear correlation exists between the MVD and the standard deviation of the sensor signal. Standard deviations of the 8 mm cone signal are in general larger than those of the 12 mm cone. This is plausible, because due to the smaller surface area of the 8 mm cone, a single droplet influences the LWC measurement of the 8 mm cone more than that of the 12 mm cone. The plots also distinguish between the different droplet conditions. The unimodal freezing drizzle conditions cause on average the highest standard deviation, although there are some significant differences between the tunnels, the unimodal freezing drizzle test points collected at the Collins IWT (all of which are in both plots found in the upper right corner) have significantly higher standard deviations than those observed at RTA at similar MVDs (compare also Table A.1). Bimodal freezing drizzle test points with very low LWCs have higher standard deviations than small droplet spray test points with comparable MVDs. This is to be expected because the few large droplets cause spikes in the sensor readings and lead to higher standard deviations. However bimodal freezing drizzle test points with high MVDs have lower standard deviations than comparable unimodal test points of similar MVDs. This effect is unexpected, especially because also the absolute difference between the observations is large. At this point, the most likely conclusion is that some differences in the spray system also influence the standard deviation. This might for instance be related to the frequency at which spray nozzles produce droplets. If the homogeneity of the icing cloud that is produced differs between the IWTs, the observed standard deviation is also affected. Usage of the standard deviation as an indication of droplet size therefore requires a calibration for each environment, which relates the standard deviation with the MVD.
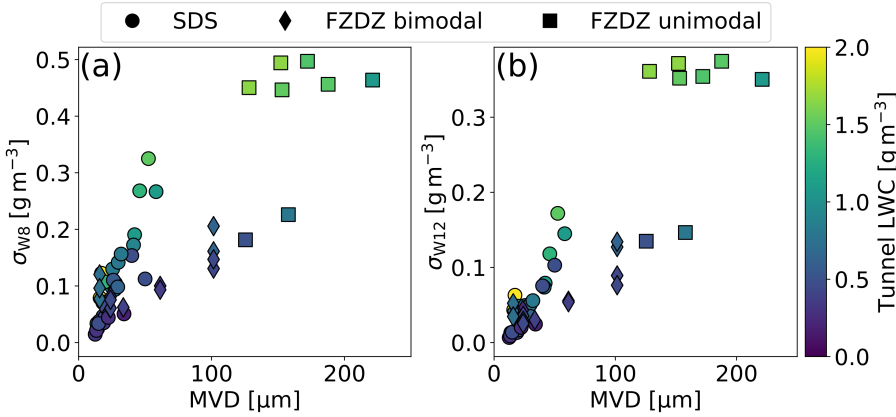
Figure 4.17: Standard deviations of the measurements from the 8 mm cone of the Nevzorov probe (σ_{W8}, **a**) and the 12 mm cone of the Nevzorov probe (σ_{W12}, **b**) plotted against the MVD. Measurements from all tunnels were used for this plot. Circular markers designate small droplet spray (SDS) test points, diamond and quadratic-shaped markers designate test points in bimodal and unimodal freezing drizzle (FZDZ) conditions, respectively.

4.4. ICING WIND TUNNEL MEASUREMENTS WITH THE BACKSCATTER CLOUD PROBE WITH POLARIZATION DETECTION

The goal of the IWT measurements with the Backscatter Cloud Probe with Polarization Detection (BCPD) was to characterize its sizing and counting properties in comparison to those of the CDP component of the CCP (see Section 4.2), under consideration of all the uncertainties listed in Chapter 3. The characterization of the BCPD is an important step for answering research question II. This section at first shows the results of the instrument comparison and then elaborates on necessary corrections to the data.

4.4.1. COMPARISON BETWEEN THE BACKSCATTER CLOUD PROBE WITH POLARIZATION DETECTION AND THE CLOUD DROPLET PROBE

Table 4.6 lists the measured number concentrations and MVDs of the CDP and the BCPD for all common and valid test points of the two instruments. The number concentrations and MVDs of the CDP have been adjusted to the BCPD size range (see Section 3.2.4), i.e., they were computed considering only droplets with diameters between 2 and 42 μm. The subscript $2-42$ has therefore been added to the CDP parameters. At a later stage, I apply corrections to the BCPD data. To distinguish uncorrected and corrected parameters, a tilde symbol is added to the uncorrected parameters. A visual comparison of the measured parameters of the two instruments is depicted in Fig. 4.18. From Table 4.6 and Fig. 4.18 two clear observations can be made:

Test point	$N_{CDP,2\text{-}42}$ [cm^{-3}]	$MVD_{CDP,2\text{-}42}$ [µm]	$\tilde{N}_{BCPD}$ [cm^{-3}]	$\tilde{MVD}_{BCPD}$ [µm]
402	619	22	237	23
406	374	22	167	23
407	708	21	301	22
409	914	21	346	21
410	553	25	281	25
415	197	29	63	29
416	440	26	223	27
417	539	26	173	28
418	1159	24	330	26
521	704	15	317	16

Table 4.6: Common test points of the Cloud Droplet Probe (CDP) and the Backscatter Cloud Probe with Polarization Detection (BCPD) measured in the Braunschweig Icing Wind Tunnel. To make the measurements of the BCPD and the CDP comparable, the number concentration (N) and the median volume diameter (MVD) of the CDP are computed only for the size bins that fall into the size range of the BCPD.

1. The number concentrations of CDP and BCPD are not in agreement at all. Depending on the data point, the concentration measured by the CDP is by a factor two to four larger than that of the BCPD.

2. The MVDs of CDP and BCPD agree within ±10% in all cases. The MVD from the BCPD is on average just 4% higher than that of the CDP.

The difference between the number concentrations measured by BCPD and CDP appears to be uncorrelated with both the MVD and the absolute value of the number concentration, although the two data points with the highest number concentration in Fig. 4.18a hint that the BCPD number concentration is going into saturation at about 400 cm^{-3}. There can be numerous explanations for the lower number concentrations measured by the BCPD. These are listed and investigated below individually:

1. The sample area of the BCPD is too small in general.

2. The number concentrations differ only for small droplet sizes. This explains also the agreement of the MVDs, which are relatively unaffected by errors in the concentration of small droplets.

3. Undersizing effects, such as described in Beswick *et al.* [47] result also in undercounting, as the sample area of the BCPD for small droplets is smaller than assumed.

The first explanation would be consistent with the two observed effects. However, the sample area of the BCPD was calibrated by the manufacturer, Droplet Measurement Techniques, as shown in Fig. 3.12. It is certainly possible that errors still exist in the sample area calibration, also because the airspeeds during the calibration were on the order or 10 ms^{-1} and therefore far from realistic airspeeds.

However, I consider it unlikely that the error in the calibration is 100% or more, which would be required to explain the observed underestimate.
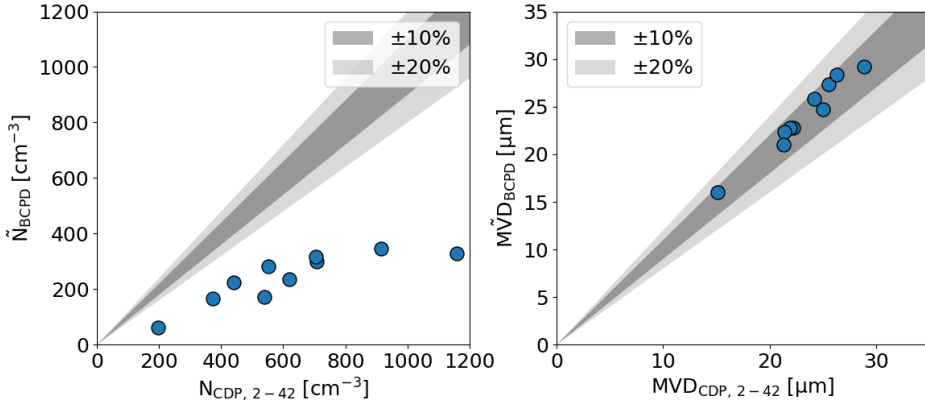
Figure 4.18: Comparison of the number concentrations (N) (**a**) and median volume diameters (MVDs) (**b**) measured by the Cloud Droplet Probe (CDP) and the Backscatter Cloud Probe with Polarization Detection (BCPD). The tilde symbol above the BCPD parameters signifies that no correction for undersizing effects (see Section 4.4.2) has been applied. The subscript 2-42 for the CDP parameters specifies that the size range for the CDP has been adjusted to match that of the BCPD.

To investigate the second point, the ratio between the number concentrations of the CDP and the BCPD in the individual size bins is plotted in Fig. 4.19. The BCPD measures lower number concentrations across the entire size range. There is hardly any droplet diameter where the BCPD measures a higher number concentration than the CDP. I can therefore conclude that the problem is not only present in a specific size range. There are however size bins, where the difference in number concentration is especially large, e.g. between 7-10 μm. The large differences there can be due to Mie-ambiguities in the CDP measurements. As mentioned in Section 3.2.3, the size resolution of droplets below 10 μm is low for the CDP, so the observed difference can be explained by too many droplets being assigned to this size bin of the CDP, while too few droplets are assigned to the CDP size bins smaller than 5 μm.

Finally, I investigate the last of the possible causes. Undersizing and resulting undercounting effects that occur for droplets that pass through the fringes of the sample were briefly mentioned already in Section 3.2.4. There, Fig. 3.12 showed that the backscattered irradiance near the fringes of the sample area is significantly lower than at the center. The procedure to account for undersizing effects is lengthy and I dedicate the following section to it.

4.4.2. Inversion of the droplet size distribution

In Section 3.2.4 I showed that the backscattered irradiance varies across the BCPD sample area. This was visualized in Fig. 3.12, which displays the backscattered irradiance of 40 μm droplets depending on the location where they pass through the
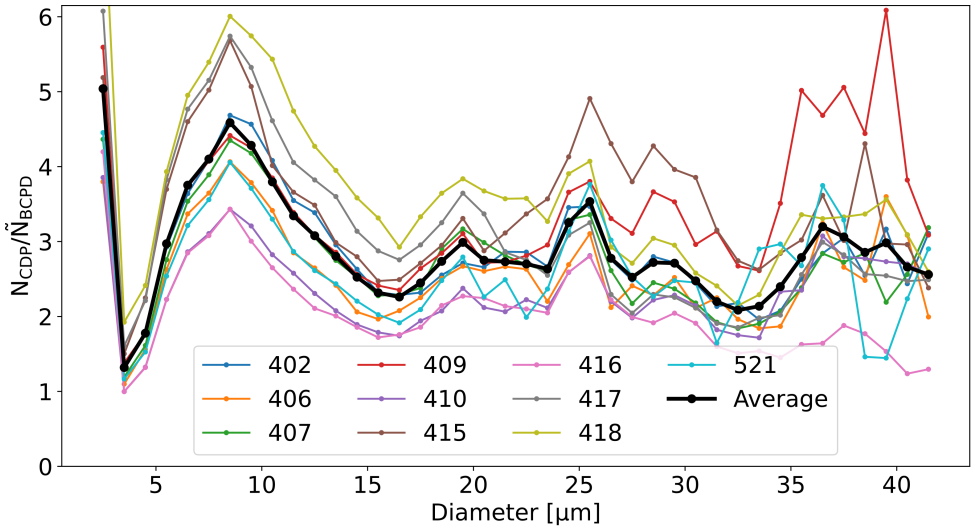
Figure 4.19: Ratio between the number concentrations (N) per size bin of the Cloud Droplet Probe (CDP) and the Backscatter Cloud Probe with Polarization Detection (BCPD) for all the test points in the Braunschweig Icing Wind Tunnel. Dots mark the midpoints of the BCPD size bins.

sample area. The irradiance decreases towards the edges of the sample area, which means that a 40 μm droplet may be sized as a much smaller particle in these regions. This is not only the case for 40 μm droplets but for all sizes. Very small droplets may even fall below the detection threshold of the BCPD if they pass through the outer regions of the sample area, in that case they are not counted at all [47]. The irradiance distribution can be normalized into a map of the percentage of backscattered irradiance (see Fig. 4.20). To do this, I use a reference analog to digital converter (ADC) count $ADC_{40,ref}$ = 12878, which represents the average backscattered irradiance of a 40 μm diameter droplet in the inner section of the sample area according to the calibration. As $ADC_{40,ref}$ is an average value, there are small spots in the sample area where the backscattered irradiance is slightly larger than 100%. This corresponds to an oversizing.

I assume that the scaled irradiance distribution applies to all droplet sizes, i.e. a 20 μm diameter droplet will produce the same relative irradiance distribution as a 40 μm diameter droplet. Following this assumption, the irradiance distribution can also be translated into a matrix **A**, which displays the probability that a droplet of size i is measured as a particle of size j [47]. A graphical representation of the matrix is shown in Fig. 4.21. The triangular shape of the nonzero entries is visible. Almost all elements below the diagonal are zero, which signifies that a small particle cannot be sized as a larger particle. The few elements below the diagonal which are not exactly zero are caused by the previously mentioned normalization, which assumes that slight oversizing may occur at the center of the sample area. The sum of a column of A is always one or less. A sum (S) smaller than one indicates that (1-S)*100% of droplets are undersized so severely that they do not exceed the min-
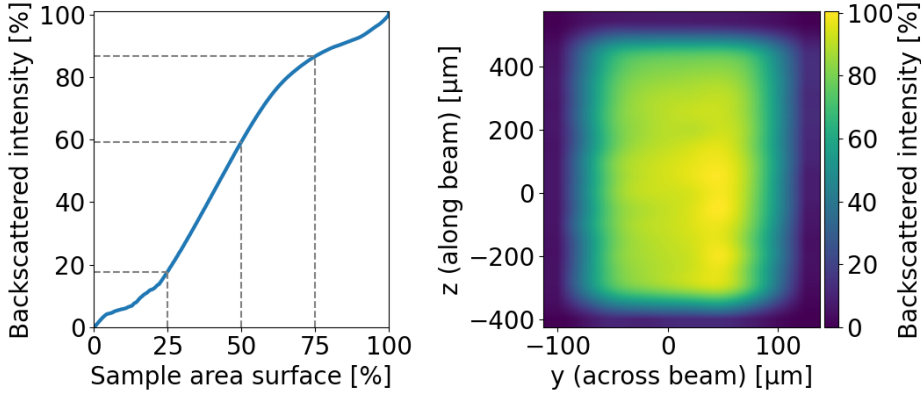
Figure 4.20: Backscattered irradiance from the sample area in percent of the reference irradiance for a 40 μm droplet. The left plot illustrates the undersizing effects that take place. Within 25% of the sample area, droplets backscatter less than 17% of the irradiance that they would scatter according to the calibration by Droplet Measurement Techniques. In 50% of the sample area they backscatter 60% or more of their calibrated irradiance and in 25% of the sample area they backscatter 87% or more of their calibrated irradiance.

imum sizing threshold and are not recorded. The matrix $\mathbf{A}$ therefore automatically accounts for the size dependence of the BCPD sample area. More generally speaking, matrix $\mathbf{A}$ describes the instrument behavior. If the true DSD is $\mathbf{x}$, then the BCPD measures a size distribution $\mathbf{y}$ [47]:

$$\mathbf{y} = \mathbf{A}\mathbf{x} \tag{4.4}$$

The dimensions of the constituents of the equation are as follows: $\mathbf{y}$ contains m measured size bins, while $\mathbf{x}$, which is in theory not a discrete property, is divided into n size bins for practical purposes. Consequently $\mathbf{A}$ is an $m \times n$ matrix. Under the assumption that the DSD measured by the CDP is $\mathbf{x}$, the effect of the undersizing behavior described by matrix $\mathbf{A}$ can be assessed. I find that the undersizing cannot account for the differences between CDP and BCPD (see Appendix A.2). Consideration of the undersizing does improve the agreement of the number concentration to some extent, but it also degrades the agreement of the MVDs. The MVD from the BCPD is now on average 18% higher than that of the CDP.

Nonetheless, according to the sample area calibration, the undersizing correction is necessary. Therefore I proceed with an explanation of how the original DSD can be retrieved from BCPD measurements. The BCPD parameters that have been corrected for undersizing do not carry a tilde symbol and can thus be distinguished from the uncorrected parameters.

For the retrieval of the true size distribution, $\mathbf{A}$ needs to be inverted. The inversion of $\mathbf{A}$ is an ill-posed problem[48]. Beswick *et al.* [47] previously faced the same challenge for the BCP and I follow their approach and implement an inversion algorithm that was originally developed by Twomey [49] and improved by
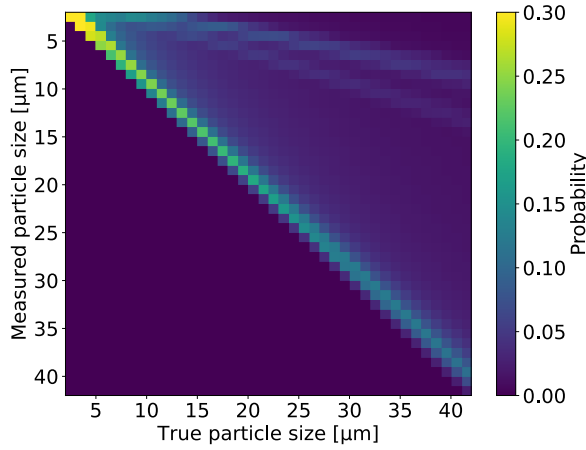
Figure 4.21: The Matrix A that describes the measurement behavior of the Backscatter Cloud Probe with Polarization Detection.

Markowski [50]. The algorithm is therefore also known as the smooth Twomey algorithm (STWOM). It implements the following steps [50]:

1. Compute the vector ξ, which relates the measured size distribution to the solution which is computed from the trial solution of iteration k: $\xi^k = \mathbf{y}/(\mathbf{A}\mathbf{x}^k)$

2. Compute the updated trial solution: $\mathbf{x}^{k+1} = [1 + (\xi^k - 1)\mathbf{A}]\mathbf{x}^k$. Here, the term $(\xi^k - 1)$ serves as a correction to the previous trial solution. It is zero for rows where the elements of $\mathbf{y}$ and $\mathbf{x}$ are in agreement.

3. Repeat steps 1 and 2 until $\sigma < 1$, where: $\sigma = \left(\left((\mathbf{y} - \mathbf{A}\mathbf{x}^{k+1})/\mathbf{e} \right)^{\top} \left((\mathbf{y} - \mathbf{A}\mathbf{x}^{k+1})/\mathbf{e} \right) \right)/m$. $\mathbf{e}$ contains the error tolerances for each element of $\mathbf{y}$.

4. Check if the roughness of the current trial solution has decreased enough. The roughness is defined as the average of the absolute values of the second derivative: $R = \left(\sum_{i=2}^{m-1} |x_{i+1} + x_{i-1} - 2x_i| \right)/(m-2)$. If the roughness has decreased enough, terminate the algorithm, if not, proceed to step 5.

5. Smooth the trial solution. The smoothing is performed for each element in $\mathbf{x}$ as follows: $x_{i,s} = \frac{x_{i-1}}{4} + \frac{x_i}{2} + \frac{x_{i+1}}{4}$. For the first and the last element of $\mathbf{x}$, where only a single adjacent value is available, the factors 3/4 and 1/4 are used for the endpoint and its sole neighbor, respectively.

6. Check if $\sigma < 1$. If yes, repeat the smoothing. If not, execute another iteration of the algorithm starting from step 1 and using the current value of $\mathbf{x}$.

The quality of the reconstructed BCPD size distribution can be analyzed by evaluating the residuals $\mathbf{r} = \mathbf{A}\mathbf{x} - \mathbf{y}$. This can be seen in Fig. 4.22, where the residuals

were divided by **Ax** to obtain a measure for the relative error in the reconstructed
size distribution. The error in the reconstruction is most of the time smaller than
20%. There is however a mismatch in the reconstructed number of droplets from
the first to third size bin. Too many droplets are assigned to the first size bin in the
reconstructed solution, while too few droplets are assigned to the second and third
size bin in the reconstructed solution. This can be explained by uncertainties in the
irradiance distribution across the sample area which propagate into the matrix **A**.
Since the scattering cross section increases only slowly in the low size range (see
Fig. 3.14), the differences between the ADC count thresholds associated with the
respective bins are small. A small error in the backscattered irradiance profile can
easily make the difference whether a large particle is undersized as e.g. a 3 μm or
a 4 μm diameter droplet.

The BCPD does not measure droplets larger than 42 μm, hence the number
concentration of these droplets is assumed to be zero, even though, in reality, they
are almost certainly present, but in low numbers. They may, when undersized,
appear as a droplet with a diameter of e.g. 42 μm, which is recorded in **y**. This
explains the very large residuals that are observed for large droplets.

Another important question is how large the error margins for the solution are
allowed to be. Per Markowski [50] the error margins can be standard deviations
of **y** that were observed during the experiment. In this study, the choice of the val-
ues of **e** was mostly dictated by the convergence of the algorithm, too low values
yielded no convergence at all. I chose a value of 0.4 for all elements of **e** for the
IWT investigation. I did not vary the values of **e** for the individual elements, as I
have no information about the possible errors per bin. Furthermore, the number of
smoothing iterations (step 5), can be varied and limited. I found that a maximum
of two smoothing iterations usually yields a smooth solution with small residuals.
Increases in the number of smoothing iterations lead to higher residuals. The num-
ber of iterations of the whole block (Steps 1-6) is limited to 10. If no solution that
satisfies the constraint $\sigma < 1$ is found, the inversion process is considered to have
failed and no reconstructed size distribution is produced.
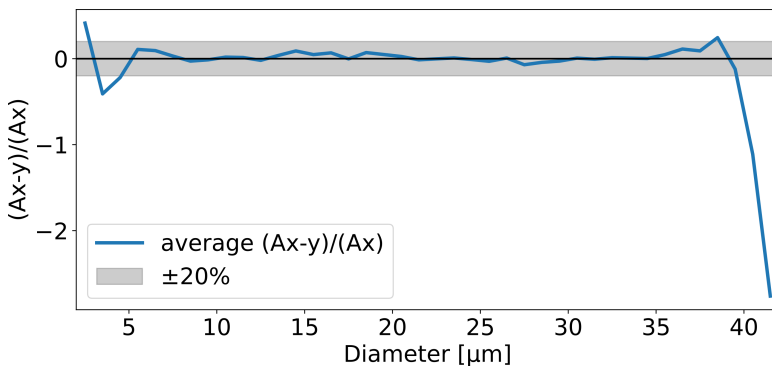
Figure 4.22: Average values of the normalized residuals between the elements of **Ax** and **y**, shown here
for BCPD test point 407.

4.5. CONCLUSIONS FROM THE ICING WIND TUNNEL MEASUREMENTS

This chapter established the collision efficiency and the capture efficiency of the 12 mm cone of the Nevzorov probe. The collision efficiency is low for small droplet diameters, only about 0.2 for 10 μm diameter droplets and 0.5 for 20 μm droplets. The correspondingly large collision efficiency correction that needs to be applied affects the accuracy in this range. Measurements with the 12 mm cone at an MVD of 12 μm carry an uncertainty of almost 30%. For larger droplet diameters this uncertainty decreases rapidly, attaining approximately 14% when the MVD is 22 μm.

The 12 mm cone is effective in capturing SLDs (Section 4.3.3). No losses due to splashing effects could be detected from comparisons to the tunnel reference instruments. In fact, the 12 mm cone measured higher LWCs in SLD conditions than the WCM-2000 probe. This indicates that the half-pipe-shaped sensing element of the WCM-2000 (see Table 3.1) is still affected by droplet splashing effects, while the deeper 12 mm cone of the Nevzorov probe is not.

Concerning research question I, I can state that the Nevzorov 12 mm cone is appropriate for measurements of SLD conditions that are either unimodal (i.e. the mass distribution has only one maximum at a droplet diameter close to or larger than 100 μm), or are bimodal but have the center of the small droplet mode located at diameters larger than 22 μm. The 12 mm cone is better suited than the WCM-2000 for the measurement of SLD conditions but does not provide a significant advantage over the 8 mm cone of the Nevzorov probe.

Furthermore, I showed that it is possible to draw conclusions on the droplet size from the standard deviations of the Nevzorov probe measurements (Section 4.3.7). This finding is important when it comes to differentiating Appendix C and Appendix O conditions in flight. It remains to be seen if the standard deviation can be used as an indication of droplet size in natural cloud conditions, where the droplet number concentrations are lower, mixed-phase conditions can be present and cloud encounters can be short and variable.

The analysis of the BCPD data showed that MVDs from the BCPD and the CDP agree within ±10% in all cases but large discrepancies between the number concentrations of the CDP and the BCPD exist, with the BCPD measuring values which are by a factor 2 to 4 below those of the CDP (Section 4.4.1). Several possible reasons for this were investigated, but none of them could provide a conclusive explanation.

According to the manufacturer calibration, a procedure is required to correct undersizing effects in the BCPD measurements that are caused by an uneven intensity distribution of the laser beam across the sample area. An inversion procedure was developed and implemented (Section 4.4.2). The inversion procedure obtains a solution for the true size distribution that is for almost all droplet diameters within ±20% of what would be expected based on the measured size distribution and the matrix that describes the undersizing behavior. The undersizing behavior of the BCPD can however not explain the difference in number concentration between the BCPD and the CDP.

The description of the IWT measurements is now complete. The next chapter

presents airborne in-situ measurements of clouds from the BCPD and the Nev-zorov probe. The findings of this chapter are considered there and open issues, such as the difference in number concentration between CDP and BCPD, are further analyzed.

REFERENCES

[1] J. Lucke, T. Jurkat-Witschas, R. Heller, V. Hahn, M. Hamman, W. Breitfuss, V. R. Bora, M. Moser, and C. Voigt, *Icing wind tunnel measurements of super-cooled large droplets using the 12 mm total water content cone of the Nevzorov probe,* Atmospheric Measurement Techniques **15**, 7375 (2022).

[2] C. W. Schwarz, *The SENS4ICE EU project - SENSors and certifiable hybrid architectures for safer aviation in ICing Environment - A project midterm overview,* in *6th International Conference Prospects of Civil Avionics Development* (2021).

[3] C. Schwarz, *SENS4ICE EU project preliminary results,* in *SAE Technical Paper Series* (SAE International, 2023).

[4] A.-C. Billault-Roux, J. Grazioli, J. Delanoë, S. Jorquera, N. Pauwels, N. Viltard, A. Martini, V. Mariage, C. Le Gac, C. Caudoux, *et al.*, *ICE GENESIS: Synergetic Aircraft and Ground-Based Remote Sensing and In Situ Measurements of Snowfall Microphysical Properties,* Bulletin of the American Meteorological Society **104**, E367 (2023).

[5] R. K. Jeck, *Icing Design Envelopes (14 CFR Parts 25 and 29, Appendix C) Converted to a Distance-Based Format*, Tech. Rep. DOT/FAA/AR-00/30 (Federal Aviation Administration, 2002).

[6] S. G. Cober and G. A. Isaac, *Characterization of Aircraft Icing Environments with Supercooled Large Drops for Application to Commercial Aircraft Certification,* Journal of Applied Meteorology and Climatology **51**, 265 (2012).

[7] S. E. Bansmer, A. Baumert, S. Sattler, I. Knop, D. Leroy, A. Schwarzenboeck, T. Jurkat-Witschas, C. Voigt, H. Pervier, and B. Esposito, *Design, construction and commissioning of the Braunschweig Icing Wind Tunnel,* Atmospheric Measurement Techniques **11**, 3221 (2018).

[8] B. M. Esposito, W. D. Bachalo, D. Leroy, A. Schwarzenboeck, T. Jurkat, C. Voigt, and S. Bansmer, *Wind Tunnel Measurements of Simulated Glaciated Cloud Conditions to Evaluate Newly Developed 2D Imaging Probes,* in *SAE Technical Paper Series* (SAE International, 2019).

[9] I. Knop, S. E. Bansmer, V. Hahn, and C. Voigt, *Comparison of different droplet measurement techniques in the Braunschweig Icing Wind Tunnel,* Atmospheric Measurement Techniques **14**, 1761 (2021).

[10] V. R. Bora, I. Knop, J. Lucke, and T. Jurkat-Witschas, *Instrumentation for measuring supercooled large droplet cloud distributions in icing wind tunnels,* in *AIAA*

SCITECH 2023 Forum, p. 2286, https://arc.aiaa.org/doi/pdf/10.2514/6.2023-2286 (2023).

[11] C. Voigt, U. Schumann, A. Minikin, A. Abdelmonem, A. Afchine, S. Borrmann, M. Boettcher, B. Buchholz, L. Bugliaro, A. Costa, J. Curtius, M. Dollner, A. Dörnbrack, V. Dreiling, V. Ebert, A. Ehrlich, A. Fix, L. Forster, F. Frank, D. Fütterer, A. Giez, K. Graf, J.-U. Grooß, S. Groß, K. Heimerl, B. Heinold, T. Hüneke, E. Järvinen, T. Jurkat, S. Kaufmann, M. Kenntner, M. Klingebiel, T. Klimach, R. Kohl, M. Krämer, T. C. Krisna, A. Luebke, B. Mayer, S. Mertes, S. Molleker, A. Petzold, K. Pfeilsticker, M. Port, M. Rapp, P. Reutter, C. Rolf, D. Rose, D. Sauer, A. Schäfler, R. Schlage, M. Schnaiter, J. Schneider, N. Spelten, P. Spichtinger, P. Stock, A. Walser, R. Weigel, B. Weinzierl, M. Wendisch, F. Werner, H. Wernli, M. Wirth, A. Zahn, H. Ziereis, and M. Zöger, *ML-CIRRUS: The Airborne Experiment on Natural Cirrus and Contrail Cirrus with the High-Altitude Long-Range Research Aircraft HALO*, Bulletin of the American Meteorological Society **98**, 271 (2017).

[12] T. Jurkat-Witschas, C. Voigt, R. Braga, D. Rosenfeld, and C. Mahnke, *Impact of aerosol on droplet number at cloud base and on the altitude of freezing in convective clouds*, in *SAE International Conference on Icing of Aircraft, Engines, and Structures 2019* (2019).

[13] C. Voigt, J. Lelieveld, H. Schlager, J. Schneider, J. Curtius, R. Meerkötter, D. Sauer, L. Bugliaro, B. Bohn, J. N. Crowley, *et al.*, *Cleaner skies during the COVID-19 lockdown*, Bulletin of the American Meteorological Society (2022).

[14] E. Herman, *Goodrich Icing Wind Tunnel Overview, Improvements and Capabilities*, in *44th AIAA Aerospace Sciences Meeting and Exhibit*, p. 862 (2006).

[15] Collins Aerospace, *Icing Wind Tunnel*, https://www.goodrichdeicing.com/services/icing-wind-tunnel, accessed: 2021-09-08.

[16] M. Hamman, E. H. Ridouane, G. Botura, and A. Taylor, *Collins IWT Capabilities and Icing Characterization*, https://www.sens4ice-project.eu/sites/sens4ice/files/media/2021-05/SENS4ICE_SAE_AC-9C_Meeting_Collins_IWT_Capabilities_and_Icing_Characterization_April2021.pdf (2021).

[17] AC-9C Aircraft Icing Technology Committee, *Calibration and Acceptance of Icing Wind Tunnels (ARP5905)* (2015).

[18] G. Haller, *Klimatests an Schienenfahrzeugen*, Eisenbahntechnische Rundschau (2005).

[19] H. Ferschitz, M. Wannemacher, O. Bucek, F. Knöbel, and W. Breitfuß, *Development of SLD Capabilities in the RTA Icing Wind Tunnel*, SAE International Journal of Aerospace **10**, 12 (2017).

[20] W. Breitfuß, M. Wannemacher, F. Knöbl, and H. Ferschitz, *Aerodynamic comparison of freezing rain and freezing drizzle conditions at the RTA icing wind tunnel*, (SAE International, 2019).

[21] Rail Tec Arsenal, *Klima-Wind-Kanal Wien*, https://www.rta.eu/anlage/kundenbereich/icing-wind-tunnel-iwt, accessed: 2022-11-28.

[22] B. Lang, W. Breitfuss, S. Schweighart, P. Breitegger, H. Pervier, A. Tramposch, A. Klug, W. Hassler, and A. Bergmann, *Photoacoustic hygrometer for icing wind tunnel water content measurement: Design, analysis, and intercomparison*, Atmospheric Measurement Techniques **14**, 2477 (2021).

[23] S. Glienke and F. Mei, *Fast Cloud Droplet Probe (FCDP) Instrument Handbook*, Tech. Rep. SC-ARM-TR-238 (U.S. Department of Energy, 2020).

[24] S. Kirschler, C. Voigt, B. Anderson, R. Campos Braga, G. Chen, A. F. Corral, E. Crosbie, H. Dadashazar, R. F. Ferrare, V. Hahn, *et al.*, *Seasonal updraft speeds change cloud droplet number concentrations in low level clouds over the Western North Atlantic*, Atmospheric Chemistry and Physics Discussions , 1 (2022).

[25] R. P. Lawson, D. O'Connor, P. Zmarzly, K. Weaver, B. Baker, Q. Mo, and H. Jonsson, *The 2D-S (Stereo) Probe: Design and Preliminary Tests of a New Airborne, High-Speed, High-Resolution Particle Imaging Probe*, Journal of Atmospheric and Oceanic Technology **23**, 1462 (2006).

[26] D. Baumgardner, S. J. Abel, D. Axisa, R. Cotton, J. Crosier, P. Field, C. Gurganus, A. Heymsfield, A. Korolev, M. Krämer, P. Lawson, G. McFarquhar, Z. Ulanowski, and J. Um, *Cloud ice properties: In situ measurement challenges*, Meteorological Monographs **58**, 9.1 (2017).

[27] S. Faber, J. R. French, and R. Jackson, *Laboratory and in-flight evaluation of measurement uncertainties from a commercial Cloud Droplet Probe (CDP)*, Atmospheric Measurement Techniques **11**, 3645 (2018).

[28] S. Lance, C. A. Brock, D. Rogers, and J. A. Gordon, *Water droplet calibration of the Cloud Droplet Probe (CDP) and in-flight performance in liquid, ice and mixed-phase clouds during ARCPAC*, Atmospheric Measurement Techniques **3**, 1683 (2010).

[29] P. D. Rosenberg, A. R. Dean, P. I. Williams, J. R. Dorsey, A. Minikin, M. A. Pickering, and A. Petzold, *Particle sizing calibration with refractive index correction for light scattering optical particle counters and impacts upon PCASP and CDP data collected during the Fennec campaign*, Atmospheric Measurement Techniques **5**, 1147 (2012).

[30] A. Bansemer, *SODA2*, https://github.com/abansemer/soda2, accessed: 2022-01-14 (2013).

4

[31] P. R. Field, A. J. Heymsfield, and A. Bansemer, *Shattering and Particle Inter-arrival Times Measured by Optical Array Probes in Ice Clouds*, Journal of Atmospheric and Oceanic Technology 23, 1357 (2006).

[32] A. Korolev, *Reconstruction of the Sizes of Spherical Particles from Their Shadow Images. Part I: Theoretical Considerations*, Journal of Atmospheric and Oceanic Technology 24, 376 (2007).

[33] A. V. Korolev, J. W. Strapp, G. A. Isaac, and A. N. Nevzorov, *The Nevzorov Airborne Hot-Wire LWC–TWC Probe: Principle of Operation and Performance Characteristics*, Journal of Atmospheric and Oceanic Technology 15, 1495 (1998).

[34] E. Emery, D. Miller, S. Plaskon, W. Strapp, and L. Lillie, *Ice particle impact on cloud water content instrumentation*, in *42nd AIAA Aerospace Sciences Meeting and Exhibit*, p. 731 (2004).

[35] S. Lance, *Coincidence Errors in a Cloud Droplet Probe (CDP) and a Cloud and Aerosol Spectrometer (CAS), and the Improved Performance of a Modified CDP*, Journal of Atmospheric and Oceanic Technology 29, 1532 (2012).

[36] A. Korolev, J. Strapp, G. Isaac, and E. Emery, *Improved airborne hot-wire measurements of ice water content in clouds*, Journal of Atmospheric and Oceanic Technology 30, 2121 (2013).

[37] J. Stallabrass, *An Appraisal of the Single Rotating Cylinder Method of Liquid Water Content Measurement*, Tech. Rep. LTR-LT-92 (National Research Council Canada, 1978).

[38] K. J. Finstad, E. P. Lozowski, and L. Makkonen, *On the Median Volume Diameter Approximation for Droplet Collision Efficiency*, Journal of Atmospheric Sciences 45, 4008 (1988).

[39] P. Sokolov and M. S. Virk, *Droplet distribution spectrum effects on dry ice growth on cylinders*, Cold Regions Science and Technology 160, 80 (2019).

[40] I. Langmuir and K. Blodgett, *A mathematical investigation of water droplet trajectories* (Army Air Forces Headquarters, Air Technical Service Command, 1946).

[41] FAA, *Advisory Circular 25-28 - Compliance of Transport Category Airplanes with Certification Requirements for Flight in Icing Conditions*, https://www.faa.gov/regulations_policies/advisory_circulars/index.cfm/go/document.information/documentid/1019691 (2014).

[42] J. F. Van Zante, J. W. Strapp, B. Esposito, D. Orchard, A. Korolev, T. P. Ratvasky, and J. T. Riley, *SLD Instrumentation in Icing Wind Tunnels – Investigation Overview*, in *AIAA AVIATION 2021 FORUM* (American Institute of Aeronautics and Astronautics, 2021).

[43] J. W. Strapp, J. Oldenburg, R. Ide, L. Lilie, S. Bacic, Z. Vukovic, M. Oleskiw, D. Miller, E. Emery, and G. Leone, *Wind Tunnel Measurements of the Response of Hot-Wire Liquid Water Content Instruments to Large Droplets*, Journal of Atmospheric and Oceanic Technology **20**, 791, https://doi.org/10.1175/1520-0426(2003)020<0791:WTMOTR>2.0.CO;2 (2003).

[44] SkyPhysTech Inc., *Operating Manual - Nevzorov Hotwire LWC/TWC Probe (CWCM-U4.1)* (2020).

[45] K. J. Finstad, E. P. Lozowski, and E. M. Gates, *A Computational Investigation of Water Droplet Trajectories*, Journal of Atmospheric and Oceanic Technology **5**, 160, https://doi.org/10.1175/1520-0426(1988)005<0160:ACIOWD>2.0.CO;2 (1988).

[46] AGARD-AR-304, *Quality assessment for wind tunnel testing,* Advisory Group for Aerospace Research & Development (1994).

[47] K. Beswick, D. Baumgardner, M. Gallagher, A. Volz-Thomas, P. Nedelec, K.-Y. Wang, and S. Lance, *The backscatter cloud probe - a compact low-profile autonomous optical spectrometer,* Atmospheric Measurement Techniques **7**, 1443 (2014).

[48] A. Tarantola, *Inverse problem theory and methods for model parameter estimation* (SIAM, 2005).

[49] S. Twomey, *Introduction to the mathematics of inversion in remote sensing and indirect measurement,* Amsterdam, Elsevier Scientific Publishing Co. (Developments in Geomathematics , 253 (1977).

[50] G. R. Markowski, *Improving Twomey's algorithm for inversion of aerosol measurement data,* Aerosol science and technology **7**, 127 (1987).

4

5

AIRBORNE MEASUREMENTS OF ICING CONDITIONS

Flight testing is the most crucial trial for atmospheric sensors. While icing wind tunnel (IWT) testing is helpful in the development process, eventually it needs to be proven that the sensors operate correctly and reliably during flight. Testing in IWTs cannot replace atmospheric measurements entirely for several reasons. First of all, particle size distributions (PSDs) produced in IWTs can differ substantially from those that exist in the atmosphere. This is illustrated in Fig. 5.1, where PSDs from an IWT and a natural cloud are compared. The shapes are distinctively different, even though the median volume diameters (MVDs) are similar. Secondly, atmospheric icing conditions are often found in mixed-phase clouds, i.e. clouds that contain supercooled droplets and ice crystals. While some IWTs are able to produce ice crystals (e.g. in cloud chambers) [2], the variety of ice crystal shapes and sizes that exist in the atmosphere cannot be replicated.

The goal of this chapter is to develop evaluation routines for airborne measurements of the Nevzorov probe and the Backscatter Cloud Probe with Polarization Detection (BCPD). For the BCPD, a procedure for the differentiation of particle phase, which is the subject of research question II, is established. The routine that is developed for the Nevzorov probe serves the purpose of obtaining accurate liquid water content (LWC) and total water content (TWC) values. Due to the possible presence of mixed-phase clouds, LWC and TWC are, unlike in the IWTs, not equal anymore.

For this thesis, the derived LWC and TWC are used as reference values for the verification of the phase differentiation with the BCPD, but, in general, they were also used by atmospheric scientists involved in the airborne measurements for their research [3, 4]. The routines are developed for the Nevzorov probe and the BCPD individually, the combination of Nevzorov probe and BCPD data for the detection and discrimination of Appendix O conditions is established in Chapter 6. This chapter furthermore continues to analyze the sizing performance of the BCPD through comparisons to Cloud Droplet Probe (CDP) data, this time for airborne measurements.

The accurate distinction between LWC and ice water content (IWC) with the Nevzorov probe in mixed-phase clouds is challenging as will be explained in Section 5.4.2. Some strategies for the distinction exist [5, 6], but I revisit the topic here and develop an approach that corrects the collision efficiency of the Nevzorov probe with the PSDs from the reference instruments (that are explained in Section 5.1).

The BCPD has not been tested at all in conditions that contain glaciated particles and the advantages of the polarization filter have not been exploited yet. Here, the challenge lies in effectively separating liquid and ice particles and estimating their number concentration.

The test case in this chapter is an approximately five-hour long flight from the HALO-AC³ campaign[1] [7]. The flight was the thirteenth research flight of the campaign and is abbreviated as RF13. It was selected for this study due to the multitude of atmospheric conditions that it encountered, ranging from purely supercooled clouds over mixed-phase clouds to entirely glaciated clouds. The HALO-AC³ campaign focused on understanding the causes of arctic amplification, i.e. the phenomenon that the Arctic has been warming almost four times as fast as the global average between 1979 and 2021 [8, 9]. One possible contribution to the arctic amplification are feedback processes associated with mixed-phase clouds [10]. Therefore, icing conditions in mixed-phase clouds were frequently sampled during the campaign. Appendix O conditions were neither targeted nor encountered. It was decided to test the Nevzorov probe and the BCPD during this campaign because, due to COVID-19, the original SENS4ICE flight campaign was postponed by a year. The combination of the two sensors for the detection of Appendix O conditions is attempted in the subsequent chapter based on the first evaluation of data from a research flight of the SENS4ICE campaign.

This chapter is structured as follows: The first section provides an overview of the instrumentation that is used for the data analysis in this chapter. The second section describes the research flight and the meteorological conditions that were encountered. The third section explains general considerations on appropriate sampling and averaging times for atmospheric measurements. Thereafter, the data evaluation procedure that was developed for the Nevzorov probe is explained.

---

[1]The campaign name HALO-AC³ is a combination of two acronyms. HALO is the name of the High-Altitude Long Range Research Aircraft of the German Aerospace Center. The acronym AC³ is short for the project name: «Arctic Amplification: Climate Relevant Atmospheric and Surface Processes and Feedback Mechanisms».
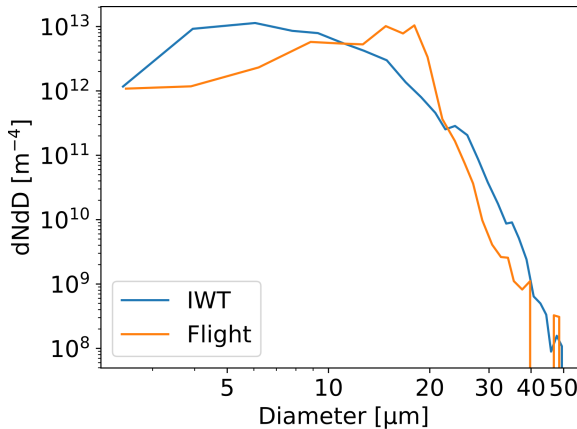
Figure 5.1: Example of a size distribution from an IWT (blue) and from a natural cloud (orange), both with an MVD of 15 μm.

Subsequently, the behavior of the BCPD during the flight testing is described and a method to separate ice and water particles is introduced.

5.1. INSTRUMENTATION

The research flight that is the focus of this chapter was performed with the Polar 6 BT-67 research aircraft of Alfred-Wegener Institute. The Polar 6 was equipped with various instruments for the measurements of cloud particles, CCNs and INPs. A detailed description of all instruments integrated on the aircraft can be found on the HALO-AC³ website [11]. In this chapter, five different instruments, all of them owned and operated by the German Aerospace Center (DLR) are used. All but one of these instruments were tested during the IWT measurements presented in Chapter 4. The instruments and their installation location on the Polar 6 aircraft are listed below and an overview of the aircraft configuration is shown in Fig. 5.2:

- The Nevzorov probe. Mounting location: The Nevzorov pillar was attached to the noseboom. The Nevzorov sensor head was consequently positioned approximately 30 cm away from the noseboom mount (see Fig. 3.1).

- The Backscatter Cloud Probe with Polarization Detection (BCPD). Mounting location: On the bottom of the fuselage, slightly below the wings.

- The Cloud Combination Probe (CCP), consisting of the Cloud Droplet Probe (CDP) and the Cloud Imaging Probe (CIP). Mounting location: In the right underwing pod on the right wing.

- The Precipitation Imaging Probe (PIP). Mounting location: In the left underwing pod on the right wing.

The integration, operation and maintenance of the DLR cloud instrumentation for the HALO-AC³ campaign was a group effort of DLR employees in which I partic-

Figure 5.2: : Installation locations of the DLR instruments during the HALO-AC³ campaign. The BCPD was located in the fuselage behind a roller-door system that was opened during the flight.
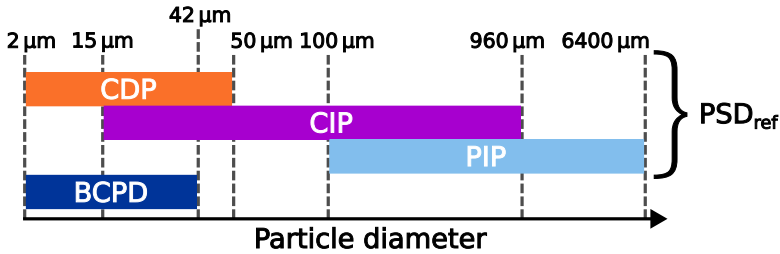
Figure 5.3: Size ranges of the scattering probes and the optical array probes that are used in this chapter.

ipated. Concerning the data evaluation, I was responsible for the measurements of the Nevzorov probe and the BCPD. The CDP, CIP and PIP measurements were merged into combined PSDs by Manuel Moser and a detailed description of how they were obtained can be found in Moser *et al.* [12]. These PSDs extend from 2-6400 µm. Similar to Chapter 4, CDP, CIP and PIP are used as the reference instrumentation that is compared to the BCPD data and serves as input for the collision efficiency correction of the Nevzorov probe. An overview of the size ranges of the instruments can be seen in Fig. 5.3. Because the size range of the BCPD only overlaps with that of the CDP, the BCPD measurements are usually compared to those of the CDP (for which size bins larger than 42 µm are ignored).

In the following sections of this chapter, cloud microphysical parameters such as LWC and MVD are derived from the above-mentioned instruments. In some cases, corrections need to be applied, consequently, raw and corrected parameters are available. Overall, this gives a relatively large set of parameters that might

be difficult to memorize. For the convenience of the reader, the most important parameters are listed and explained in Table 5.1.

Table 5.1: Explanation of important parameters used in this chapter.

Parameter	Unit	Instrument	Description
W_{LWC}	gm^{-3}	Nevzorov	Liquid water content measurement of the LWC sensor, no collision efficiencies are applied. An entirely liquid cloud is assumed for the computation.
W_8	gm^{-3}	Nevzorov	Liquid water content measurement from the 8 mm TWC cone, no collision efficiencies are applied. An entirely liquid cloud is assumed for the computation.
W_{12}	gm^{-3}	Nevzorov	Liquid water content measurement from the 12 mm TWC cone, no collision efficiencies are applied. An entirely liquid cloud is assumed for the computation.
W_{TWC}	gm^{-3}	Nevzorov	Generic term for a liquid water content measurement from a Nevzorov TWC sensor (i.e., it is not specified whether it is an 8 mm TWC cone or a 12 mm TWC cone). No collision efficiencies are applied to the measurement and an entirely liquid cloud is assumed for the computation.
$\mathrm{LWC}_{\mathrm{Nevz}}$	gm^{-3}	Nevzorov	Liquid water content estimate from the iteration procedure described in Section 5.4.2. Collision efficiencies and the cross-sensitivity of the Nevzorov LWC sensor to ice are accounted for in this estimate.
$\mathrm{IWC}_{\mathrm{Nevz}}$	gm^{-3}	Nevzorov	Ice water content estimate from the iteration procedure described in Section 5.4.2. Collision efficiencies and the cross-sensitivity of the Nevzorov LWC sensor to ice are accounted for in this estimate.

Table 5.1 – continued from previous page

Parameter	Unit	Instrument	Description
TWC_{Nevz}	gm^{-3}	Nevzorov	Total water content estimate from the iteration procedure described in Section 5.4.2. Collision efficiencies and the cross-sensitivity of the Nevzorov LWC sensor to ice are accounted for in this estimate.
LWC_{50}	gm^{-3}	CDP, CIP	Liquid water content of all particles with diameters smaller than 50 µm. Calculated as described in Moser *et al.* [12].
IWC_{50}	gm^{-3}	CIP, PIP	Ice water content of all particles with diameters larger than 50 µm. Calculated as described in Moser *et al.* [12].
PSD_{ref}	m^{-4}	CDP, CIP, PIP	Particle size distribution from the reference instrumentation. Calculated as described in Moser *et al.* [12].
N_{ref}	cm^{-3}	CDP, CIP, PIP	Number concentration from the reference instrumentation. Calculated as described in Moser *et al.* [12].
MVD_{ref}	µm	CDP, CIP, PIP	Median volume diameter from the reference instrumentation. Calculated based on the assumption that all observed particles are spherical [12].
N_{CDP}	cm^{-3}	CDP	Number concentration measured by the CDP. An optional subscript specifies the size range in micrometer that is considered for the parameter. If no subscript is specified the entire size distribution from 2-50 µm is considered in the calculation.
MVD_{CDP}	µm	CDP	Median volume diameter measured by the CDP. An optional subscript specifies the size range in micrometer that is considered for the parameter. If no subscript is specified the entire size distribution from 2-50 µm is considered in the calculation.

<div align="right">Continued on next page</div>

Table 5.1 – continued from previous page

Parameter	Unit	Instrument	Description
LWC_{CDP}	gm^{-3}	CDP	Liquid water content measured by the CDP. An optional subscript specifies the size range in micrometer that is considered for the parameter. If no subscript is specified the entire size distribution from 2-50 µm is considered in the calculation.
N_{BCPD}	cm^{-3}	BCPD	Number concentration measured by the BCPD. The underlying size distribution has been corrected for undersizing and undercounting with the STWOM algorithm.
MVD_{BCPD}	µm	BCPD	Median volume diameter measured by the BCPD. The underlying size distribution has been corrected for undersizing and undercounting with the STWOM algorithm.
LWC_{BCPD}	gm^{-3}	BCPD	Liquid water content measured by the BCPD. The underlying size distribution has been corrected for undersizing and undercounting with the STWOM algorithm.

5.2. OVERVIEW OF THE RESEARCH FLIGHT

The research flight took place on April 10, 2022, out of Longyearbyen Airport (LYR) on the Svalbard archipelago. The weather situation on that day was dominated by a high-pressure system located over the central Arctic and a low-pressure system positioned over Northern Scandinavia. This resulted in winds from east to northeast over the Fram Strait (see Fig. 5.4). The aircraft first flew west towards Waypoint 1 (WP1), which it reached at 10 UTC. On the track towards WP2 it first encountered very thin clouds and after surpassing WP6 also thick stratus clouds. During the racetrack pattern (see Appendix A.6 for an explanation of the flight patterns) between WPs 2-5 over the ice, very thin ice clouds were measured. A sawtooth pattern was flown through increasingly thick stratiform mixed-phase clouds between WP5 and WP6. The second racetrack pattern (WPs 6-9) was parallel to a convergence line. In the northwestern part of the pattern, stratiform mixed-phase clouds were present, while in the south-eastern part, shallow convection was observed by the crew, which resulted in strong precipitation below the cloud. The racetrack pattern was concluded at approximately 13 UTC and the aircraft headed directly back to LYR from WP9. A timeline of flight altitude, temperature as well as number concentration and MVD observed by the reference instrumentation (N_{ref} and MVD_{ref}, respectively), can be seen in Fig. 5.5. The MVD_{ref} has been computed under
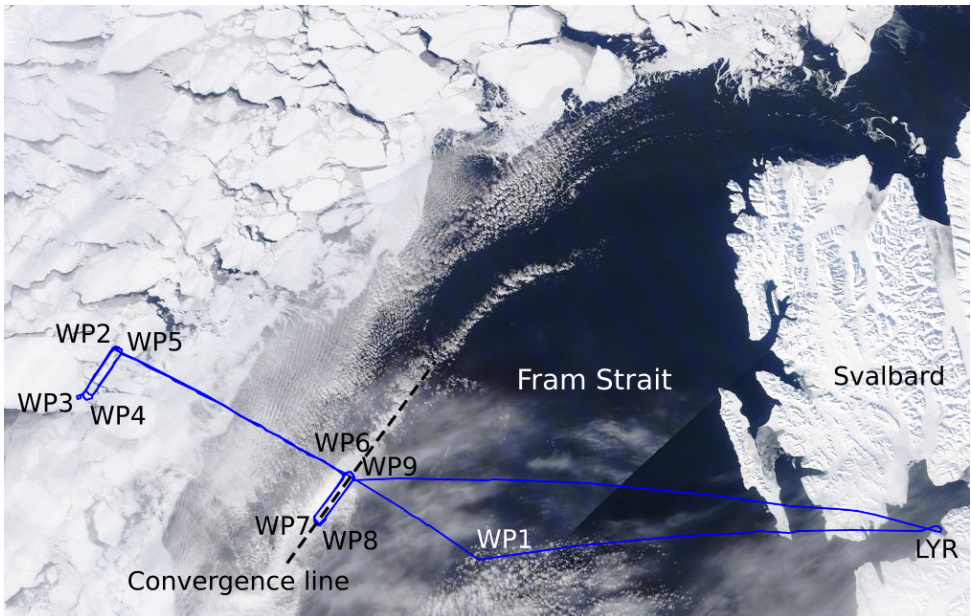
Figure 5.4: Flight track of research flight 13 on April 10, 2022, during the HALO-AC³ campaign. The aircraft departed from Longyearbyen Airport (LYR) on the Svalbard archipelago and then flew westwards over the Fram Strait towards the sea ice. Racetrack patterns were performed between Waypoints (WPs) 2 to 5 and 6 to 9.

the assumption that all particles are spherical, which is certainly not true. It is only shown to indicate the presence of glaciated clouds, that have a very low number concentration and would otherwise not be evident in the plot.

5.3. SAMPLING TIME CONSIDERATIONS

During passage through a cloud, only a tiny amount of the droplets that constitute the cloud is actually sampled by the instruments. This raises the question of how many droplets of a cloud should be measured to obtain a representative sample. Longer sampling times yield larger samples, but also decrease the spatial resolution and may smooth out small-scale characteristics of a cloud. The appropriate sampling time first of all depends on the research question. For large scale studies of cloud properties it may be perfectly acceptable to average over several tens of kilometers. But for the detection of icing conditions it is desirable to obtain indications of ice accretion as timely as possible. The appropriate averaging time also depends on cloud type (e.g. whether the cloud is dense or patchy, whether it has a high number concentration or a low number concentration) and on the sampling pattern flown. The cloud parameters likely remain more stable during an in-cloud segment at constant altitude than during a sawtooth pattern (see Fig. A.8 for an explanation of the most common flight patterns).

The research flight contains racetrack and sawtooth patterns and a large variety
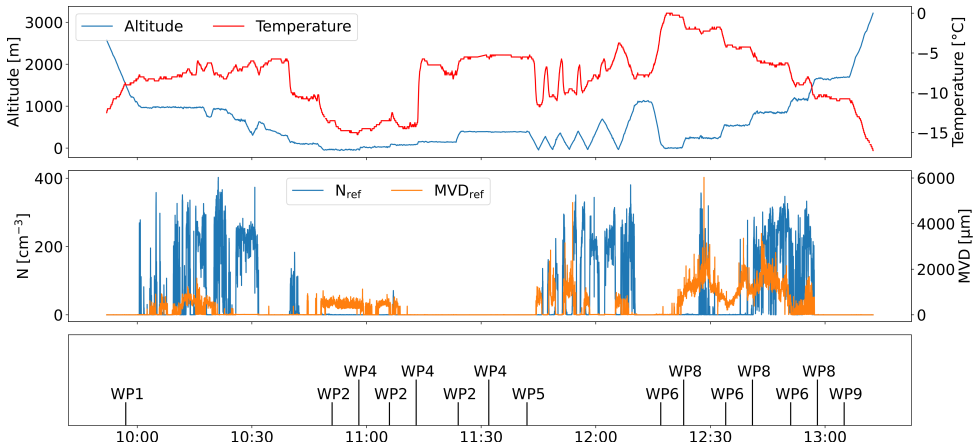
Figure 5.5: Timeline of the research flight. The topmost panel shows altitude and temperature, the middle panel shows the number concentration (N_{ref}) and the median volume diameter (MVD_{ref}) from the reference instrumentation and the bottommost panel shows the location of the waypoints (WPs). The MVD has been computed under the assumption that all particles are spherical. It is shown to visualize the presence of thin ice clouds, such as those visible between 10:50 and 11:10.

of cloud types from very thin ice clouds to dense stratus clouds. It would be very complex to select a sampling time for each scenario. Therefore, I select a sampling time that gives high accuracy for most segments.

The instruments that are used in this study have very different sample areas. Large droplets or ice crystals, which are rare but carry a high water content may therefore be detected by one instrument in a specific sampling interval and not by another, simply due to statistics.

For the discussion on an appropriate sampling time, cloud droplets are assumed to be Poisson-distributed, in line with many other publications [13, 14]. For a selected flight segment with a given start time, I can compute an average particle count distribution (PCD, analog to a PSD, but containing particle counts instead of concentrations) for a number of differently long intervals, e.g. a one-second, a five-second and a sixty-second interval, all starting from the same start time. These PCDs are from now on referred to as the original PCDs. The number of particles in each size bin of each of these PCDs is assumed to be the expectation λ_i of the Poisson-distributed particle count per bin (i). That means each PCD (e.g. for one, five or sixty seconds) is a vector of expectation values, i.e.:

$$\boldsymbol{\lambda} = [\lambda_1, \lambda_2, ... \lambda_n],$$

where n is the number of size bins.

Longer sampling times yield larger values in $\boldsymbol{\lambda}$ and, as the standard deviation of Poisson-distributed parameters only increases with the square root of the expectation, smaller coefficients of variation.

For microphysical parameters like the MVD and the LWC, it is difficult to predict how large uncertainties due to sampling statistics are after a given sampling
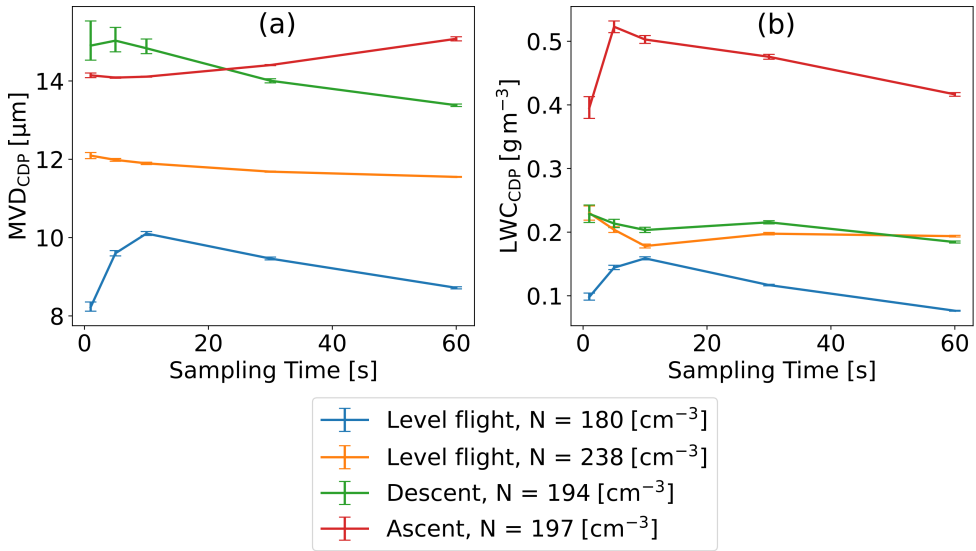
Figure 5.6: Median volume diameters (MVDs) (**a**) and liquid water contents (LWCs) (**b**) computed by the Cloud Droplet Probe (CDP) for several flight segments after different sampling times. The sampling time of each segment begins at the same point in time. Error bars indicate the intervals into which 99% of the simulated MVDs and LWCs fall.

time, because the standard deviations of these values depend on the uncertainty of the particle count of each size bin. Furthermore, the uncertainties of the individual particle counts need to be weighted by droplet volume, large standard deviations of the counts in the smallest size bin have little effect on the overall uncertainty of the MVD, while large standard deviations in the number of counts of the largest bin affect the MVD and LWC significantly.

To simulate the uncertainties in the MVD and LWC, I draw random samples from the original PCDs (1000 random samples were used for the plots in Fig. 5.6 and Fig. 5.7). Each of these samples is in itself a PCD. As these PCDs were not measured, but randomly drawn, I refer to them as simulated PCDs. If the MVD and the LWC are evaluated for a sufficient number of these simulated PCDs, the spread of the simulated MVD and LWC values around the original MVD and LWC should provide a good approximation to the uncertainty due to sampling statistics.

This procedure was performed for four different flight segments of the research flight and for sampling times ranging from one second to sixty seconds. A thousand samples were drawn from the original PCDs for each sampling time that was investigated. The uncertainty of the MVD and LWC of the CDP due to sampling statistics as well as the variation due to spatial inhomogeneity can be seen in Fig. 5.6.

Error bars in Fig. 5.6 show the two-sided 99% confidence intervals of the MVDs computed from the simulated PCDs, i.e. they show the most extreme deviations that can be expected for the MVD due to sampling statistics.

The variations of the MVD due to insufficient statistics are nearly completely irrelevant compared to the variations that can occur due to spatial inhomogeneity. The largest variations in MVD are observed for a sampling time of one second for the case where the MVD is approximately 15 µm. Even there the uncertainty is only ±0.5 µm. Due to spatial inhomogeneities, the MVD can change easily by more than 1 µm within a few seconds, such a change for instance causes the variation in MVD in the blue curve.

For the LWC, uncertainties due to sampling statistics for a sampling time of one second can amount to approximately ±6%, but reduce 3% or less in all cases for sampling times of five seconds. There is consequently little benefit in using long sampling times for measurements of the CDP (and also for the BCPD, whose sample area and measurement range are comparable), instead, a sampling time of five seconds is sufficient. The plot does not include very high MVD values, because no larger droplets were measured during the research flight. The Poissonian variance certainly increases with higher MVD and lower number concentration and for such cases longer averaging times may be necessary.

Analogous plots to Fig. 5.6 can be seen for the 8 mm cone and the 12 mm cone of the Nevzorov probe in Fig. 5.7. The uncertainties due to sampling statistics are significantly larger than those shown for the LWC of the CDP in Fig. 5.6b for the level-flight case shown in blue and the ascent case shown in red. For the one-second intervals, the uncertainties reach up to approximately 44% for the 8 mm cone and 25% for the 12 mm cone. It can be seen from Fig. 5.7c that this is due to large, rare particles like ice crystals that impact only occasionally on the Nevzorov cones but carry a large water content.

The comparison of Fig. 5.7a and 5.7b also provides a clear example of how uncertainties due to sampling statistics are reduced for the 12 mm cone compared to the 8 mm cone because of the larger sample area of the former.

In general, sampling times longer than ten seconds seem to offer little benefit over shorter sampling times. Even for sampling times of five seconds uncertainties are within ±10% for almost all of the presented cases. I therefore choose a sampling time of five seconds for this chapter.

5.4. AIRBORNE MEASUREMENTS WITH THE NEVZOROV PROBE

The evaluation of the Nevzorov probe is more challenging for airborne measurements than for IWT tests, especially because of the changing ambient conditions, which affect the dry term, and due to the existence of mixed-phase clouds [5, 6]. This section explains the approach that was developed in this thesis to obtain accurate LWC and TWC values from airborne measurements of the Nevzorov probe.

5.4.1. ESTABLISHING THE DRY TERM IN CLOUDS

The first step for the evaluation of in-flight measurements of the Nevzorov probe is the determination of the dry term ratio k (see Section 3.1.1) between the dry term of the collector sensors and the dry term of the reference sensor (see Fig. 3.1
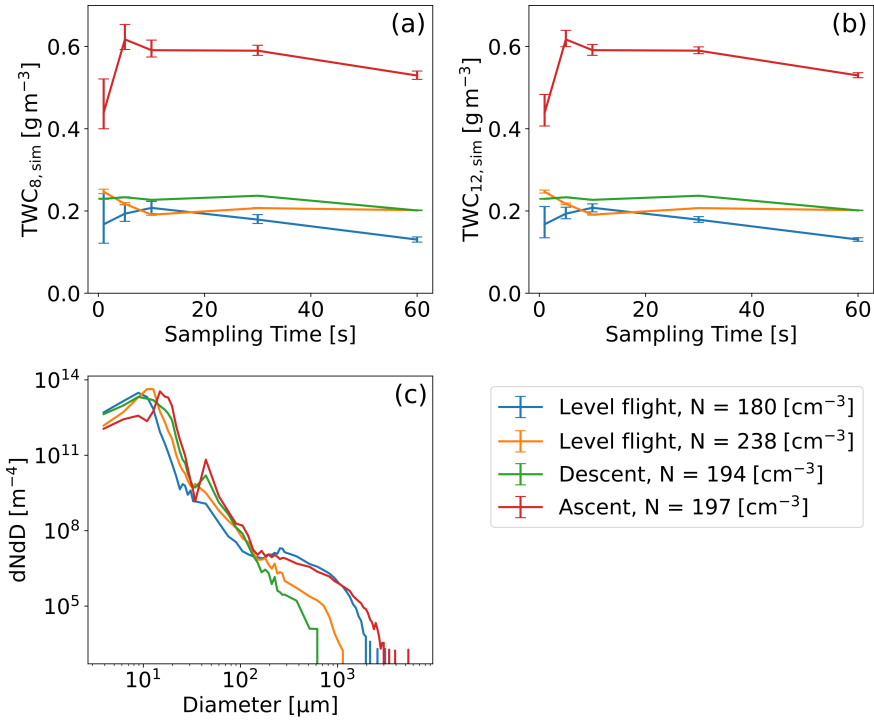
Figure 5.7: Simulated total water content (TWC_{sim}) measurements for the 8 mm cone (**a**) and the 12 mm cone (**b**) derived from the particle size distributions (PSDs) that stem from the reference instrumentation. The PSDs are pictured in panel **c**. Error bars demonstrate the two-sided 99% confidence intervals of the TWC_{sim} values.

for an illustration of the sensors). High accuracy of the dry term ratio is important (see Section 4.3.5). Unlike in IWTs, airspeed, temperature and pressure vary during flight, hence the dry term ratio cannot be assumed constant. Instead, for each combination of airspeed, pressure and temperature a separate dry term ratio is required. Korolev *et al.* [15] estimate that a change in airspeed of $10\,\mathrm{m\,s^{-1}}$ alters the dry term ratio by the equivalent of a water content of 0.002 and $0.003\,\mathrm{g\,m^{-3}}$, respectively. A change in altitude affects the dry term ratio with the equivalent of $0.005\,\mathrm{g\,m^{-3}}$ per km, which is mostly due to the pressure change and only to a minor degree due to the temperature difference [15].

As suggested in [16] and [6], I established a database with measurements in known dry air conditions. Dry air conditions were determined to be present whenever the standard deviation of the measurements fell below a certain threshold. The exact procedure is described in Appendix A.4.

Further following McFarquhar *et al.* [16], a curve fit was performed to the measurements of the dry term ratio to approximate it in cloudy conditions. I experimented with different functional forms but found that none of them was able to represent the values of the dry term ratio sufficiently well across the entire range

of airspeeds, pressures and altitudes. The problem with a curve fit procedure is that all observations are weighted equally. Long stretches of cloud-free air at constant airspeed, temperature and pressure bias the curve fit to attain a very close agreement with the observed dry term ratio, while the dry term ratio for other conditions, which have been measured less frequently, is approximated poorly.

To avoid this problem, I established a method that is independent of the number of measurements that exist for the different atmospheric conditions. The method creates a three-dimensional data array that contains bins of airspeed, pressure and temperature. Bin widths of 4 m s^{-1}, 20 hPa, and 3 °C are used, respectively. Subsequently, each observed dry term ratio is sorted into the corresponding bin and mean values are computed. Dry term ratios for in-cloud segments that correspond to a bin for which no dry air observations exist are approximated from a linear interpolation in all three dimensions between the nearest bins that contain dry air observations.

The binned data is shown in Fig. 5.8 for the LWC sensor, the 8 mm cone and the 12 mm cone respectively. Figures 5.8c - 5.8f demonstrate that the dry term ratio of the TWC sensors increases with decreasing pressure and airspeed (the decrease in the dry term ratio means that the convective heat losses of the TWC sensors do not increase as much as those of the Nevzorov reference sensor). The changes of the dry term ratio with pressure and airspeed are relatively large, values range from 0.78 to 0.88 and from 1.45 to 1.65 for the 8 mm and 12 mm cone, respectively. On the other hand, the range of the dry term ratio for the LWC sensor is tiny, the minimum observed value is 1.355 and the maximum observed value is 1.385 (Fig. 5.8a). There does not appear to be a clear dependence on airspeed or pressure, instead, the values appear to be fluctuating randomly. It is therefore not adequate to use the interpolation technique for the dry term ratio of the LWC sensor. However, the dry term ratio of the LWC sensor depends weakly on temperature (see Fig. 5.8b). Hence, I applied a linear fit of the formulation $mT + c$ to the temperature-binned data (where T is the temperature) and obtained the coefficients m = 1.3916 and c = 0.00102. In the following, all dry term ratios of the LWC sensor are estimated from this linear fit, while dry term ratios for the TWC sensor are computed from the interpolation.

The approach presented above results in a sensitivity of the Nevzorov probe of approximately 0.025 gm^{-3} during airborne measurements (see Appendix A.5). For this reason, the value of 0.025 gm^{-3} is used as the lower threshold for the detection of an in-cloud segment.

5.4.2. COMPUTATION OF LIQUID AND TOTAL WATER CONTENT IN MIXED-PHASE CLOUDS

While the evaluation of the Nevzorov probe measurements is relatively straightforward in pure liquid conditions, it is more complicated in mixed-phase conditions. Due to the possible presence of ice particles, LWC and TWC are no longer equivalent, and both parameters need to be estimated. The distinction between LWC and TWC is made possible by the LWC sensor, which collects predominantly liquid particles.
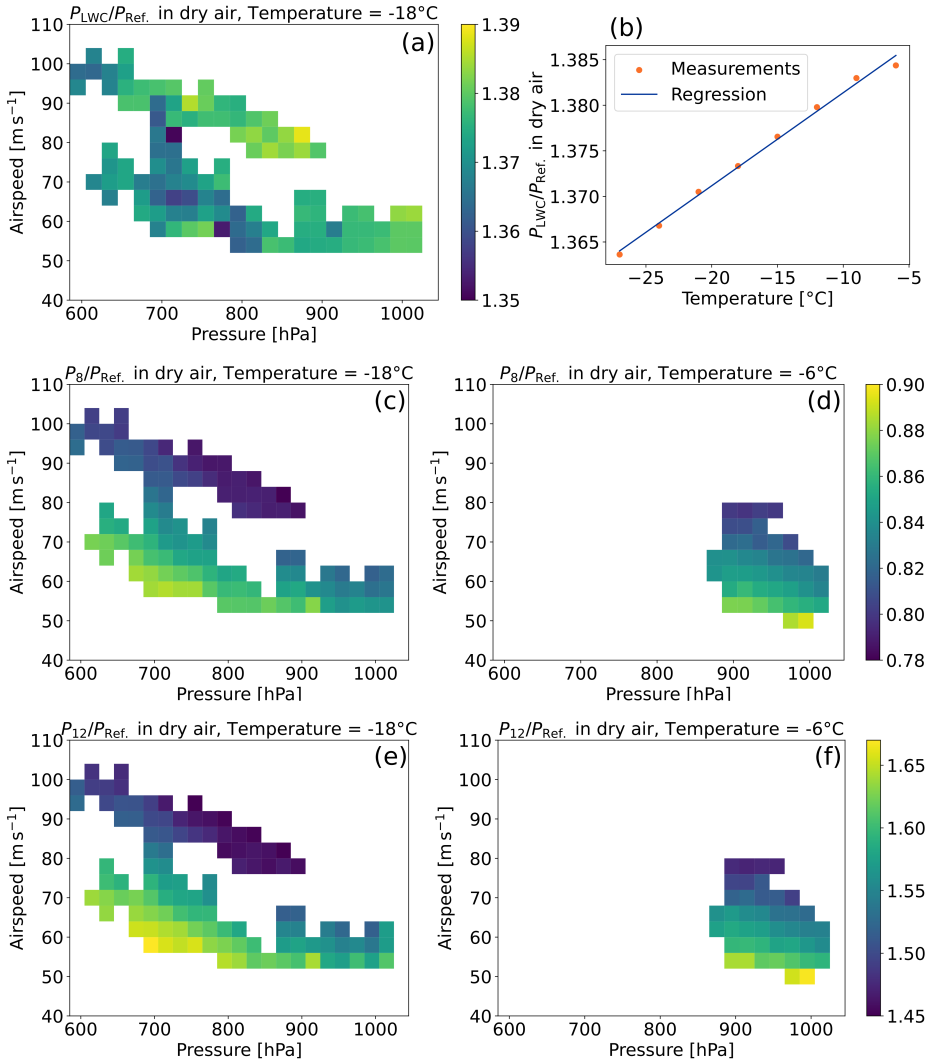
Figure 5.8: Dry term ratio k (see Eq. (3.6)) between the power drawn by the Nevzorov probe collector sensors (LWC sensor, 8 mm cone and 12 mm cone with the respective powers $P_{\mathrm{LWC}}, P_8, P_{12}$) and the power of the Nevzorov reference sensor (P_{ref}) in dry air. Dry term ratios in the figures were determined with the binning approach presented in Section 5.4.1. The first row depicts dry term ratios of the LWC sensor. The correlation between the dry term ratio and airspeed and pressure is plotted for a temperature of -18 °C in panel (a), while panel (b) depicts the temperature dependence averaged over all airspeeds and pressures. The second row shows how the dry term ratios of the 8 mm cone correlate with airspeed and pressure, plotted for temperatures of -18 °C and -6 °C in panels (c) and (d), respectively. Likewise, the bottom row depicts the correlation of the dry term ratio of the 12 mm cone with airspeed and pressure, again for temperatures of -18 °C and -6 °C in panels (e) and (f), respectively.

The problem can be formulated as a system of equations [5], which is shown in Eq. (5.1) and Eq. (5.2). The equations describe how collision efficiency corrected LWC and TWC values (LWC$_{\text{Nevz}}$ and TWC$_{\text{Nevz}}$) can be computed from the raw measurements of the LWC sensor (W_{LWC}) and of a TWC sensor (W_{TWC}). The terms that refer to the TWC sensor are generic and do not contain information about the sensor diameter. For now, this is sufficient to illustrate the problem.

Four different collection efficiencies are included in the system of equations: $\varepsilon_{\text{l,LWC}}$, $\varepsilon_{\text{l,TWC}}$, $\varepsilon_{\text{i,TWC}}$ and β. Each of them describes the response of either the LWC sensor or a TWC sensor to water or ice [17]. The factor β represents the residual response of the LWC sensor to ice particles which is stated in the literature as 11 to 15% at airspeeds below 100 ms^{-1} but also depends strongly on the type of ice crystals that are present [15, 17]. In this work $\beta = 0.11$ is assumed, similar to Schwarzenboeck *et al.* [6], who also evaluated the Nevzorov probe in Arctic clouds. Furthermore, Eq. (5.1) and Eq. (5.2) feature a value κ, which represents the ratio of the energies required to heat and evaporate ice and water (L_i^* / L_l^*, see Eq. (3.3) and Eq. (3.4)).

$$\text{LWC}_{\text{Nevz}} = \frac{\beta W_{\text{TWC}} - \varepsilon_{\text{i, TWC}} W_{\text{LWC}}}{\kappa * \left(\varepsilon_{\text{l, TWC}} \beta - \varepsilon_{\text{l, LWC}} \varepsilon_{\text{i, TWC}}\right)}. \tag{5.1}$$

$$\text{TWC}_{\text{Nevz}} = \frac{\left(\varepsilon_{\text{l, TWC}} - \varepsilon_{\text{i, TWC}}\right) W_{\text{LWC}} + \left(\beta - \varepsilon_{\text{l, LWC}}\right) W_{\text{TWC}}}{\kappa * \left(\varepsilon_{\text{l, TWC}} \beta - \varepsilon_{\text{l, LWC}} \varepsilon_{\text{i, TWC}}\right)}, \tag{5.2}$$

The collection efficiencies in Eq. (5.1) and Eq. (5.2) depend on the PSD (see Section 3.1.1) and on the phase of the individual particles in the PSD (e.g. the collection efficiency of the LWC sensor of the Nevzorov probe is approximately 0.92 for a 20 µm droplet and 11% for an ice particle). In most mixed-phase clouds, liquid droplets have diameters between 1 and 50 µm while ice crystal sizes can range from 1 µm to 10^4 µm Korolev *et al.* [18]. Ice crystal number concentrations are usually several orders of magnitude lower than number concentrations of liquid droplets. Therefore, I make the following assumption: The lower part of the size distribution is entirely liquid, up to a threshold diameter (d_{thres}), while the upper part with particle diameters larger than d_{thres} is composed entirely of ice particles. This assumption is certainly a simplification because the possibility exists (and has been observed by e.g. Lawson *et al.* [19]) that small ice particles exist alongside supercooled large droplets (SLDs). The natural abundance of CCNs and the scarcity of INPs however guarantee that, if present, the liquid particles make up the large majority of the small particles. I further assume that $\varepsilon_{\text{i,TWC}} = 1$, because the majority of the ice water content (IWC) is usually contained in large ice particles.

Nevzorov probe and PSD measurements are used to determine the transition threshold from ice to water. The liquid fraction of the cloud water content, μ_l, is defined as the ratio of LWC to TWC:

$$\mu_l = 1 - \mu_i = \frac{\text{LWC}}{\text{TWC}}, \tag{5.3}$$

with μ_i as the ice fraction of the cloud water content. The liquid fraction can also be described through the liquid part of the size distribution (which extends up to

d_thres):

$$\mu_\text{l} = \frac{\sum_{d_i=d_\text{min}}^{d_\text{thres}} x(d_i)\pi d_i^3}{6\,\text{TWC}}, \tag{5.4}$$

where x is the PSD, i.e. it contains the number concentrations of the size bins that are represented by the diameters d_i. The threshold between the water and the ice phase can be determined by inserting Eq. (5.3) into Eq. (5.4) and solving for d_thres. This requires PSDs that extend at least up to the phase transition threshold as well as estimates for LWC and TWC. Here, PSD_ref, which extends up to 6400 µm (see Fig. 5.3), i.e. well above the size range where liquid cloud droplets exist, is used as the PSD. W_LWC and W_TWC can be initial estimates for the LWC and the TWC in Equations 5.3 and 5.4.

If Equations 5.3 and 5.4 are used for determining d_thres it is required that the integrated LWC from the PSD is comparable to the LWC from the Nevzorov probe. This is not trivial, since small biases in the measured size distribution may result in large errors in the computed LWC because the particle diameter enters into the LWC formulation with the power of three. To verify if this condition is satisfied, I compare the integrated LWC of the CDP to W_LWC. These quantities are comparable because both, the CDP and the LWC sensor of the Nevzorov probe, are insensitive to large ice particles (i.e. they represent an LWC measurement) and the collision efficiency of the Nevzorov LWC sensor is close to unity for the MVDs between 10 and 25 µm that were primarily observed in the small droplet mode during the HALO-AC³ campaign.

The correlation between W_LWC and the LWC from the CDP, both computed for five-second intervals, can be seen in Fig. 5.9a. Only measurements where both, W_LWC and the LWC from the CDP, exceeded 0.025 gm^{-3} were used for the two plots of Fig. 5.9. Furthermore, because the Nevzorov LWC sensor does not collect ice particles, it was required that $\mu_\text{l} > 0.9$ (the μ_l values are derived from the algorithm that is presented here, hence the plot was created after running the algorithm). Figure 5.9b shows that the mean ratio of the LWC measurements of the two instruments is approximately 1.06, which indicates either a slight high bias of the CDP or a slight low bias of the LWC sensor of the Nezvorov probe (or a combination of both). The cause of the offset is likely that no collision efficiency corrections have been applied to W_LWC (cf. Table 5.1). The spread of the data points is such that 67% of all ratios fall between 0.93 and 1.27. The large spread can be explained by the different mounting positions of the instruments. Overall, I conclude from Fig. 5.9 that the combination of Nevzorov LWC and CDP LWC can at least be used as a first approximation to the phase transition diameter.

Having confirmed that the Nevzorov and CDP data are suitable to determine the phase transition diameter, the problem of how to compute LWC_Nevz and TWC_Nevz from Eq. (5.1) - Eq. (5.4) persists. The system of equations is nonlinear because the collision efficiencies ($\varepsilon_\text{l,LWC}$, $\varepsilon_\text{l,TWC}$) are nonlinear functions of μ_l. Also, due to measurement uncertainties, in many cases no solution to the system of equations exists. Thus, I attempt to obtain LWC_Nevz, TWC_Nevz and μ_l with an iteration technique (see Fig. 5.10).
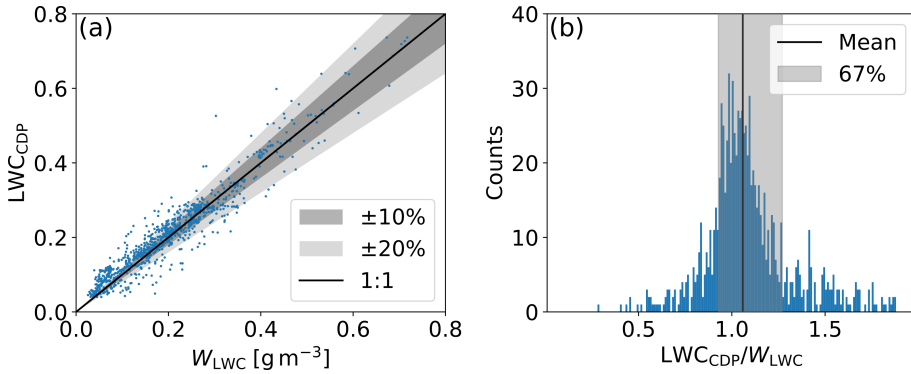
Figure 5.9: Comparison of the raw liquid water content (LWC) measured by the Nevzorov LWC sensor (W_{LWC}) and the LWC measured by the Cloud Droplet Probe (LWC_{CDP}) during segments of the research flight with predominantly liquid clouds ($\mu_l > 0.9$). The liquid fraction μ_l is obtained from the corrected Nevzorov LWC and TWC values, which are computed in this section. Panel **(a)** shows the correlation between the raw Nevzorov LWC sensor measurement and the LWC_{CDP}. Panel **(b)** depicts the distribution of the ratios of LWC_{CDP} to the raw Nevzorov LWC.
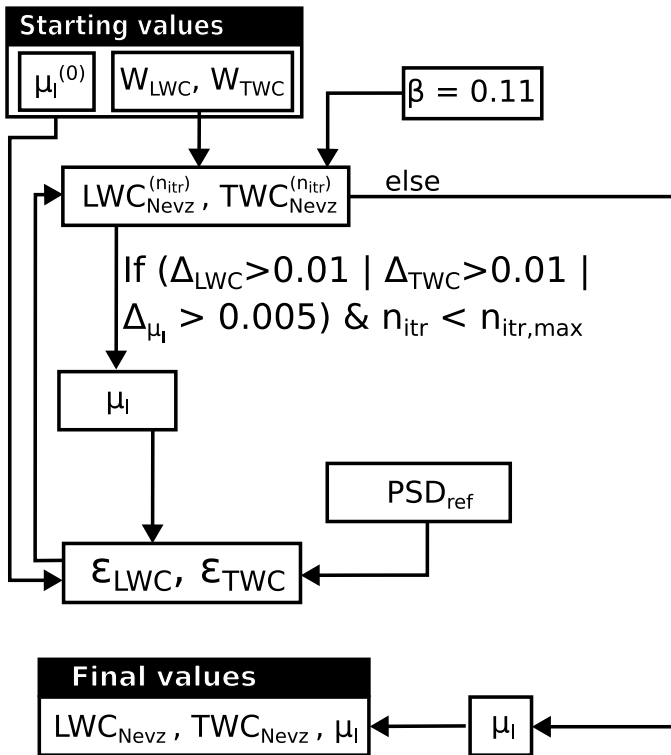
Figure 5.10: Algorithm for the evaluation of atmospheric Nevzorov probe measurements.

I start with the raw sensor measurements W_{LWC} and W_{TWC} and the estimate $\mu_1^{(0)} = 1$, for the fraction of liquid water, i.e. purely liquid clouds. The fraction of liquid water, $\mu_1^{(k)}$, is subject to iteration and the superscript k signifies the iteration step. Collision efficiency corrected estimates of the TWC in mixed-phase conditions can be computed from Eq. (5.5):

$$\text{TWC}_{\text{Nevz}}^{(k+1)} = \frac{\mu_1^{(k)}}{\varepsilon_{1,\text{TWC}}^{(k)}} W_{\text{TWC}} + (1 - \mu_1^{(k)}) \frac{W_{\text{TWC}}}{\kappa}. \tag{5.5}$$

The collision efficiencies in Eq. (5.5) and the following equation are a function of μ_1 and the expression $\varepsilon^{(k)}$ is used for brevity and signifies $\varepsilon(\mu_1^{(k)})$. Collision efficiency corrected estimates for the LWC in mixed-phase conditions can be computed as:

$$\text{LWC}_{\text{Nevz}}^{(k+1)} = \frac{1}{\varepsilon_{1,\text{LWC}}^{(k)}} \left(W_{\text{LWC}} - \kappa \beta (1 - \mu_1^{(k)}) \text{TWC}_{\text{Nevz}}^{(k+1)} \right). \tag{5.6}$$

Updated values of μ_1 are obtained from the ratio of LWC to TWC:

$$\mu_1^{(k+1)} = \frac{\text{LWC}_{\text{Nevz}}^{(k+1)}}{\text{TWC}_{\text{Nevz}}^{(k+1)}}. \tag{5.7}$$

The new μ_1 value is then used to compute new collision efficiencies, which are subsequently applied in Eq. (5.5) and Eq. (5.6) (see Fig. 5.10). The iteration is terminated once changes in both TWC_{Nevz} (Δ_{TWC}) and LWC_{Nevz} (Δ_{LWC}) are smaller than 0.01 gm^{-3} and changes in the liquid fraction (Δ_{μ_1}) are smaller than 0.005. Alternatively, the iteration is also terminated if a maximum number of iterations (n_{itr}) is exceeded, in this work, a maximum of eleven iterations were allowed.

An exact solution usually does not exist due to the various error sources that affect the measurements of W_{LWC}, W_{TWC} and PSD_{ref}, as well as uncertainties in the collision efficiencies. Should the iterative process fail to fulfill the termination criteria of the iteration within the specified n_{itr}, a different approach is chosen. I minimize

$$\min_{\mu_1} \left(\mu_1 \text{TWC}_{\text{Nevz}}(\mu_1) - \text{LWC}_{\text{Nevz}}(\mu_1) \right)^2 \tag{5.8}$$

and step through μ_1 in intervals of 0.05. This approach takes slightly longer than the algorithm previously presented, but it is able to find values for LWC_{Nevz}, TWC_{Nevz} and μ_1 even when the uncertainties in the individual input parameters are large or when they do not correspond well, which can for example be the case if the clouds are very patchy and inhomogeneous.

Till now I have used the generic expression for the Nevzorov TWC measurement. A straightforward strategy to create a single estimate from the measurements of two cones would be:

$$\text{TWC}_{\text{Nevz}} = \frac{1}{2} \text{TWC}_8 + \frac{1}{2} \text{TWC}_{12}. \tag{5.9}$$
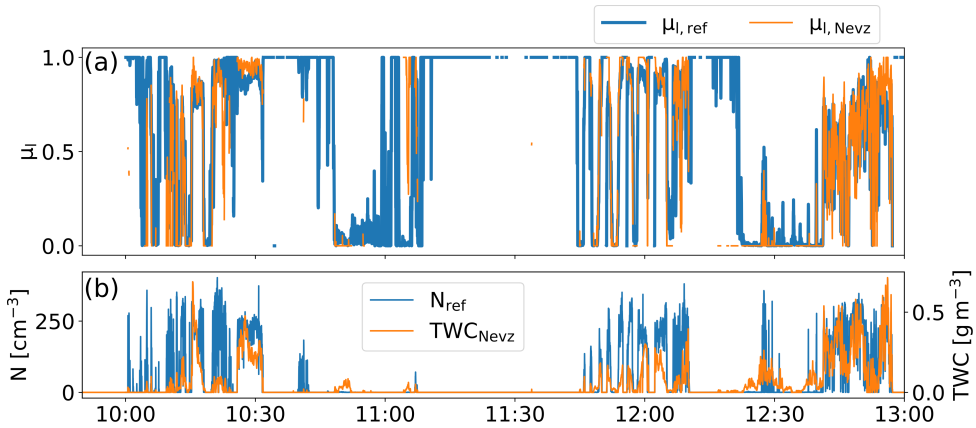
Figure 5.11: Panel **(a)** shows the comparison of the liquid fractions (μ_l) computed from the Nevzorov probe with the algorithm that was developed in this chapter (orange) and from the reference instrumentation, i.e. from the LWC_{50} and IWC_{50} values from CDP, CIP and PIP (blue). Panel **(b)** shows the number concentration (N) from the reference instrumentation (blue) and the total water content (TWC) from the Nevzorov probe (orange).

Here TWC_8 and TWC_{12} are the outputs delivered by Eq. (5.5) for the 8 mm and the 12 mm TWC cone, respectively. However, as discussed in Chapter 4, the uncertainty of the 12 mm cone measurements is large for small droplet sizes, which, as mentioned before, were predominant during the whole HALO-AC³ campaign. The collision efficiencies for the 12 mm cone that resulted from these small droplet sizes were often below 0.4. It was found that usage of the 12 mm cone in liquid and in mixed-phase clouds led to TWCs that were unrealistically high, e.g. in one segment with an MVD of 14 µm, TWC_{12} and TWC_8 differed by 37%. This divergence between TWC_{12} and TWC_8 at small droplet diameters occurred also during the wind tunnel measurements (compare Fig. 4.12). Because the TWC_{12} carries this large uncertainty, for the evaluation of this research flight only the TWC_8 measurements are used.

The fraction of liquid water, μ_l, can also be approximated from the reference instrumentation. Manuel Moser, who evaluated the reference instrumentation, computed the LWC with a fixed $d_{thres} = 50$ µm and used the formulation of Heymsfield *et al.* [20] to compute the IWC of the particles larger than d_{thres}. The corresponding LWC and IWC values are denoted as LWC_{50} and IWC_{50}, respectively (see Table 5.1). A comparison of μ_l obtained with the algorithm from the Nevzorov data (denoted as $\mu_{l,Nevz}$ now for clarity) to the μ_l value that is derived from the LWC_{50} and IWC_{50} (denoted as $\mu_{l,ref}$) can be seen in Fig. 5.11a. In the figure, $\mu_{l,Nevz}$ and $\mu_{l,ref}$ follow the same trend, although local differences exist and attain 0.1 and 0.2 in some instances. The $\mu_{l,Nevz}$ values are missing over large parts of the flight. These segments result from TWC_{Nevz} values equal to zero (see Fig. 5.11b). The low number concentration during these segments confirms that either no or just a very thin cloud, which fell below the detection threshold of the Nevzorov probe, was present.

Overall, the agreement between $\mu_{l,Nevz}$ and $\mu_{l,ref}$ is in 67% of the cases within
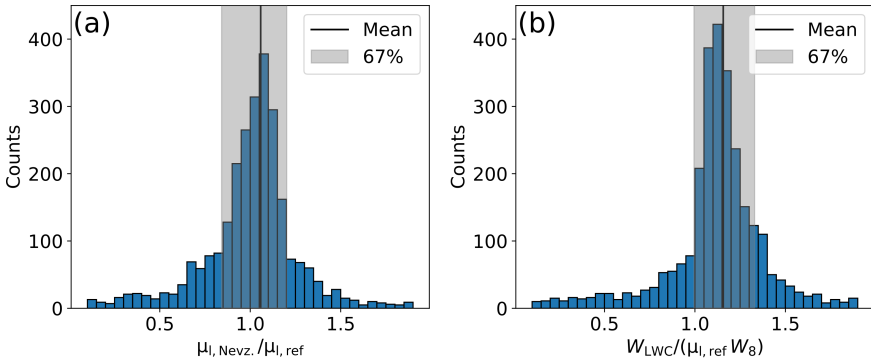
Figure 5.12: Ratios between the liquid fraction (μ_l) observed with the Nevzorov probe and the liquid fraction observed with the reference instrumentation. Panel **a** shows a comparison of $\mu_{l,Nevz}$, the liquid fraction computed from LWC_{Nevz} and TWC_{Nevz}, which were derived with the algorithm, to $\mu_{l,ref}$, which is the liquid fraction obtained from LWC_{50} and IWC_{50} (see Table 5.1). Panel **b** shows the liquid fraction that would be obtained from the raw Nevzorov measurements W_{LWC} and W_8 (assuming that the former represents the LWC and the latter the TWC) in comparison to $\mu_{l,ref}$.

$\pm 18\%$. On average $\mu_{l,Nevz}$ is 3% higher than $\mu_{l,ref}$ (see Fig. 5.12a). To put these values into perspective, in Fig. 5.12b the agreement of the liquid fraction derived from the raw Nevzorov measurements W_{LWC} and W_8 (where the former quantity is assumed to represent the LWC and the latter is assumed to represent the TWC) with $\mu_{l,ref}$ is shown. The liquid fraction from the raw Nevzorov measurements is on average 13% higher than $\mu_{l,ref}$.

It is important to remember that the $\mu_{l,ref}$ values are also only estimates. Likely, they are even less reliable than $\mu_{l,Nevz}$, due to uncertainties in the mass-dimension relations of ice particles [20–22], which affect IWC_{50}, and errors in the droplet diameter entering with the third power into the calculation of LWC_{50}. The good agreement between $\mu_{l,Nevz}$ and $\mu_{l,ref}$ however confirms that the algorithm delivers plausible results and the increased liquid fraction computed from the raw Nevzorov probe measurements is expected due to the low collision efficiency of the 8 mm cone.

The direct effect of the collision efficiency correction on the liquid fraction can be seen in Fig. 5.13. The plot shows the frequency with which a certain μ_l was observed for all five-second intervals of RF13 where TWC_{Nevz} exceeded the threshold sensitivity of the Nevzorov probe. Two histograms are overlaid, one for which no collision efficiency correction was applied to the Nevzorov data and another one where the Nevzorov probe collision efficiency was corrected with the algorithm previously presented. After the collision efficiency correction, a significant part of the cases, which were previously detected as purely liquid, are assessed to be mixed-phase conditions. The classification as mixed-phase mostly corresponds with the visual assessment of the particles from the CIP images, where ice crystals were observed in almost every flight segment. The collision efficiency corrections that are applied are quite large due to the small droplet diameters that were present, therefore significant uncertainties may be present in TWC_{Nevz}, in line with
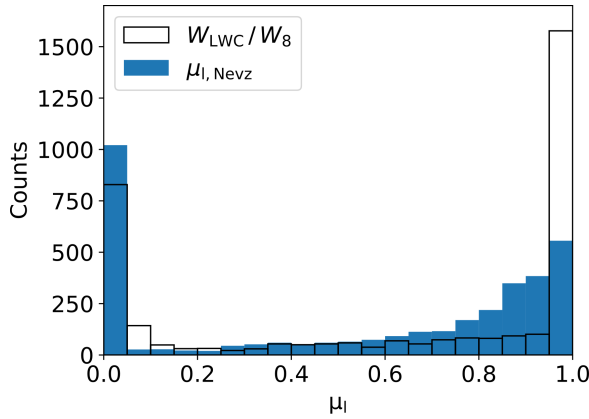
Figure 5.13: Effect of the corrections to the Nevzorov data on the computed liquid fraction μ_l. The liquid fraction from the raw measurements (based on W_{LWC} and W_8) is shown with the transparent bars, the liquid fraction from the corrected measurements ($\mu_{l,Nevz}$) is shown with blue bars.

the discussion in Section 4.3.5. While it is certain that most of the segments were mixed-phase, the exact μ_l may therefore be subject to some errors.

The algorithm removes the effects of the cross-sensitivity of the LWC sensor to ice. It can be seen that the algorithm decreases the counts in the bin of μ_l between 0.05 and 0.1 and increases the portion in the very first bin (μ_l between 0 and 0.05), which essentially represents pure ice.

Finally, it is worth noting that μ_l is constrained to between zero and one. Especially if no collision efficiency is applied, μ_l can significantly exceed one. All instances where μ_l was larger than one were assigned to the uppermost bin in the histogram.

The data evaluation procedure to obtain LWC_{Nevz} and TWC_{Nevz} in mixed-phase clouds is now established. Because the corrected Nevzorov measurements LWC_{Nevz} and TWC_{Nevz} are likely more accurate than LWC_{50} and IWC_{50}, I use LWC_{Nevz} and TWC_{Nevz} as the reference data for the subsequent sections.

5.5. Airborne measurements with the Back- scatter Cloud Probe with Polarization Detection

The measurement principle of the BCPD was explained in Chapter 3 and IWT measurements shown in Chapter 4 provided comparisons of the BCPD measurements to the CDP. This section presents airborne measurements collected with the BCPD. I begin with a comparison of the microphysical parameters measured by the CDP and the BCPD to verify if the observations are similar to those from the IWT measurements (see Section 4.4.1) and to potentially identify a reason for the lower number concentration measured by the BCPD. Then, I establish a framework for using the polarization filter of the BCPD for the discrimination of particle shape, which
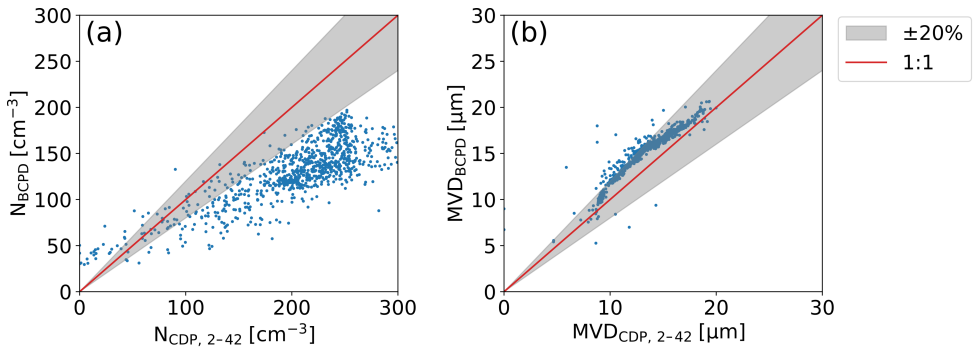
Figure 5.14: Comparison of the number concentration (N) (**a**) and the median volume diameter (MVD) (**b**) measured by the Cloud Droplet Probe (CDP) and the Backscatter Cloud Probe with Polarization Detection (BCPD) during predominantly liquid segments of the research flight.

in turn provides information on the phase of cloud particles.

5.5.1. MEASUREMENT OF PARTICLE SIZE

Similar to the wind tunnel measurements, I compare the microphysical parameters observed by the BCPD during the research flight to those observed by the CDP (see Section 3.2.3). Because no scattering cross section curves for ice particles exist for either of the two instruments (as discussed in Section 3.2.2), only predominantly liquid segments where $\mu_{l,Nevz}$ is larger than 0.9 are used for the comparison. As in Chapter 4, only overlapping portions of the CDP and BCPD size distributions are used, i.e., only CDP size bins till 42 μm are considered. The inversion method, which was presented in Section 4.4.2, is applied to the data to correct for under-sizing effects and to account for the particle size dependence of the sample area.

A comparison of the microphysical parameters measured by the CDP and the BCPD can be seen in Fig. 5.14. The plot is similar to Fig. 4.18 from Section 4.4.1. Significant discrepancies are apparent also here between the number concentrations of the BCPD (N_{BCPD}) and the CDP (N_{CDP}) despite the correction of undersizing effects of the BCPD (Fig. 5.14a). The number concentration of the BCPD is on average only 62% of the number concentration of the CDP, approximately similar to the observations made in the IWT. As for the IWT measurements, I list possible error sources:

- The airflow is significantly altered at the measurement position of the BCPD, which is just 3 cm away from the aircraft skin.

- A significant error exists in the sample area calibration of the manufacturer.

The risk that the airflow is significantly altered at the sampling position of the BCPD exists, but the reduced number concentration of the BCPD was also observed in the IWT. In the IWT the airflow was likely not significantly altered, because the sampling position of the BCPD was close to the front of the casing and the casing

itself protruded 6 cm into the tunnel (see Fig. 4.3c). The possibility that there is
an error in the sampling area calibration of the manufacturer also exists (as was
mentioned in Section 4.4.1), but could not be verified in the scope of this thesis.

The relationship between the MVDs of the BCPD and the CDP (MVD$_{BCPD}$ and
MVD$_{CDP}$, respectively) appears to follow a curve shape (see Fig. 5.14a). MVDs from
the BCPD are about 10% larger than those of the CDP for diameters between 8-10
µm. Beyond 10 µm diameter up to about 15 µm MVDs from the BCPD are consis-
tently almost 20% larger than those of the CDP, while between 15-20 µm the ratio
between the two MVD measurements decreases again, until it attains almost unity
at 20 µm. The range of MVD values that were observed during the research flight
extended from approximately 8 µm to 20 µm, it was therefore much lower than the
range of MVDs measured in the IWTs, which extended from approximately 15 µm
to 29 µm (see Table 4.6 and Fig. 4.18b). Hence, it cannot be determined if the two
plots show similar trends.

These observations mean that the BCPD data from the HALO-AC³ campaign
cannot be used to obtain reliable measurements of the absolute particle number
concentration and derived properties such as the LWC. The MVD measured by the
BCPD on the other hand appears to be a reasonable indications of the droplet size
that is present. The findings are discussed at a later stage again after the measure-
ments from the SENS4ICE campaign have been presented. The subsequent section
focuses on one of the core features of the BCPD, the analysis of the polarization
state of the backscattered light, which can be used to draw conclusions on the par-
ticle shape.

5.5.2. PHASE DIFFERENTIATION

The phase of cloud particles (i.e. liquid or glaciated) is extremely important, espe-
cially for the case of airframe icing, where only liquid particles present a hazard.
Small water droplets are essentially always spherical, while ice particles are most
often aspherical. Järvinen *et al.* [23] reported observations of quasi-spherical ice
particles that formed from aspherical ice after passage through ice-subsaturated
regions. However, these observations were made in tropical convective systems
at significantly lower temperatures and higher altitudes than present during the
HALO-AC³ flight.

Conditions that lead to the formation of spherical ice particles were conse-
quently very likely not present, hence it is assumed from now on that all spher-
ical particles are liquid and all aspherical particles are ice. The terms ice/glaciated
and water/liquid are used synonymously with aspherical and spherical particles,
respectively.

The shape of cloud particles can be deduced from the depolarization of the
light that is backscattered by the observed particles. I describe the depolarization
through the polarization ratio $\delta = (S - P)/(S + P)$ of the backscattered light [24]. Here
P and S are the analog to digital converter (ADC) counts measured at the photode-
tectors that receive p- and s-polarized light, respectively. P and S are consequently
proportional to the scattering cross sections $\sigma_{\parallel}$ and $\sigma_{\perp}$ (see Eq. (3.30) and Eq. (3.31)).
It is important to remember that the incident laser light on the particle is perfectly

p-polarized (if δ of the incident laser beam was measured, its value would be -1).

What values does δ take for spherical and aspherical particles? The answer to this question can be seen in Fig. 5.15. For the image, δ values were assigned to polarization ratio bins with a width of 0.05, which are represented by their midpoint diameter δ_k. Figure 5.15a shows color-coded probability mass functions $p(\delta_k, D)$ for given measured particle diameters (D_i) in an entirely liquid cloud. Figure 5.15b shows the same probability distributions as Fig. 5.15a, but in a predominantly glaciated cloud. Figure 5.15c is based on the same data as Fig. 5.15a, but displays the probabilities for δ_k independent of the particle size. Instead, two different probability mass functions are shown, one for all measured particles and another one for all particles with diameters larger than 10 µm. Similarly, Fig. 5.15d shows the same distributions as Fig. 5.15c, but for the predominantly glaciated cloud.

From Figures 5.15a and 5.15c it is apparent that the vast majority of particles in a liquid cloud scatter light with δ values within a narrow interval between -0.75 and -0.6, especially for diameters larger than 10 µm. This is in excellent agreement with the theoretical δ values for spherical water droplets that can be calculated from the scattering cross section curves derived in Chapter 3 and are plotted in orange in Fig. 5.15a.

The snake-like oscillating pattern in the δ_k distribution that can be observed in Fig. 5.15a upwards from 10 µm is due to small-scale Mie-ambiguities and in part also correspond to the theoretical predictions. No particles larger than 36 µm were observed in the liquid cloud, hence no polarization ratios are displayed.

At the lowest droplet sizes, from 2 µm up to approximately 10 µm, δ varies more than for larger diameters. Here, δ values can fall between -1 and and 0. This can in part be attributed to larger Mie-ambiguities in the small droplet range (see Fig. 3.14). Additionally, the wide spread in δ values can result from undersized large particles, which passed through the fringes of the sample area, where the depolarization differs from the computed value due to the shift in the observation angle.

The distribution of δ_k values for the glaciated cloud (Fig. 5.15b and d) is dissimilar to that of the liquid cloud. The observed δ values are scattered over a wide range from -1 to approximately 0.6. There is a very small hump visible around $\delta = -0.65$ and particle diameters below 6 µm, which is due to a small number of spherical particles (likely liquid), which distorts the pattern but is ignored for the subsequent discussion. When considering just the particles larger than 10 µm it is apparent that the δ_k probability distribution peaks at approximately -0.3.

How can spherical and aspherical particles be separated? The matter is complicated because the probability distributions of spherical and aspherical particles overlap. In previous works [23, 25, 26], which investigated similar problems (for a Cloud Aerosol Spectrometer with Depolarization Option (CAS-DPOL)), fixed polarization ratio thresholds were used for the distinction. Due to the overlap, there is inevitably some confusion between the two regimes when using a fixed threshold. Assuming that here the threshold would be positioned at approximately $\delta = -0.5$, which is likely the most sensible choice, a case with only aspherical particles would nonetheless be detected as containing a large number of spherical particles.
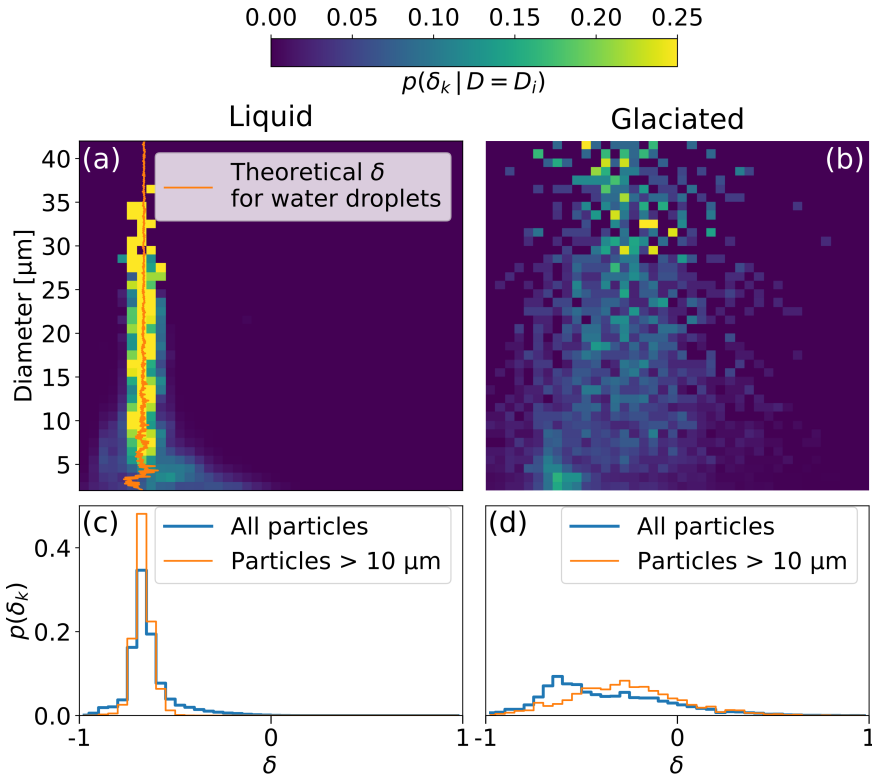
Figure 5.15: Distribution of the polarization ratio δ in liquid and glaciated conditions. The observed δ values were assigned to bins that are denoted through their midpoint polarization ratio δ_k. Panels **a** and **b** show color-coded probability mass functions $p(\delta_k, D)$ for different particle diameters (D_i). Panels **c** and **d** are a reduction of the upper plots to just the x-axis, i.e. the probability mass function now represents the overall likelihood for a given δ_k if all measured particles are considered (blue) and if only particles larger than 10 µm are considered (orange).

Therefore, a different approach is required. I consider the overlap in the low size range as too strong and distinguish only between spherical and aspherical particles with diameters larger than 10 µm. From measurements in pure liquid and pure glaciated conditions (which were also collected during flight campaigns other than HALO-AC³), the characteristic probability distributions of the two regimes are known. The distribution of liquid particles can be described by a very narrow Gaussian distribution $\mathcal{N}_\mathrm{l}$ with mean $\mu = -0.685$ and standard deviation $\sigma = 0.04$. The distribution of ice particles, on the other hand, can be modeled with a Gaussian $\mathcal{N}_\mathrm{i}$ with $\mu = -0.33$ and $\sigma = 0.35$. I fit $\mathcal{N}_\mathrm{i}$ to the observed distribution of ice through the usage of a scaling factor a_i, which is determined from a least squares approach:
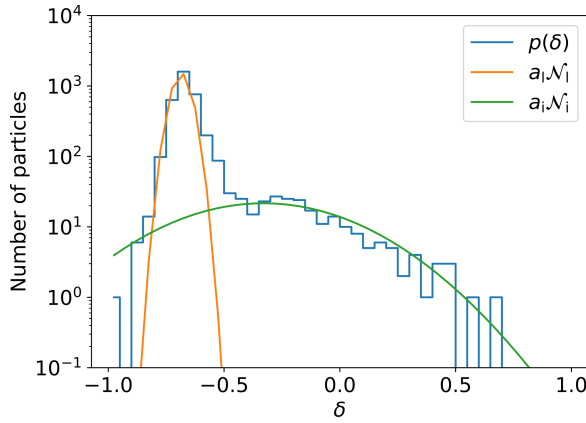
Figure 5.16: Approximation of the measured polarization ratio distribution $p(\delta)$ (blue) through the fit functions for spherical particles (orange) and aspherical particles (green).

$$\min_{a_i}\left(\sum_{\delta_k=\delta_0}^{\delta_{28}}\left(p(\delta_k)-a_i\Delta_\delta\,\mathcal{N}_i(\delta_k)\right)^2\right),$$

$$\text{with } \Delta_\delta = 0.05 \text{ and } \delta_k = -0.425 + k\Delta_\delta,\ k \in \{0,1,...,28\}. \quad (5.10)$$

Here Δ_δ is 0.05, i.e. the bin width associated with one δ_k value. The fit is performed only for the 29 δ_k values from -0.425 upwards to avoid the influence of liquid particles on $p(\delta_k)$. Once a_i has been obtained, I perform a similar fit to the part of $p(\delta_k)$ where liquid particles could be present to determine a scaling factor a_l for the Gaussian distribution of liquid particles. However, here the possible presence of ice particles needs to be considered. The minimization problem therefore reads:

$$\min_{a_l}\left(\sum_{\delta_k=\delta_0}^{\delta_{39}}\left(p(\delta_k)-a_l\Delta_\delta\,\mathcal{N}_l(\delta_k)-a_i\Delta_\delta\,\mathcal{N}_i(\delta_k)\right)^2\right),$$

$$\text{with } \Delta_\delta = 0.05 \text{ and } \delta_k = -0.975 + k\Delta_\delta,\ k \in \{0,1,...,39\}. \quad (5.11)$$

To determine the number of spherical and aspherical particles (n_i and n_w) the integral under the curves $a_l\mathcal{N}_l$ and $a_i\mathcal{N}_i$ is computed. An example of how the fit works can be seen in Fig. 5.16. Furthermore, a comparison of n_i to the IWC measurement from the Nevzorov can be seen in Fig. 5.17. The comparison is purely qualitative, as IWC and n_i are not directly comparable, but it is apparent that ice is detected with the BCPD whenever the Nevzorov probe measures an IWC larger than zero. The plot highlights that the number of ice crystals remains unaffected by the presence of liquid particles. This is the main strength of the algorithm and solves the problem present in works such as those from Meyer [25] and Costa *et al.* [26], where necessarily some ice particles are detected as water.
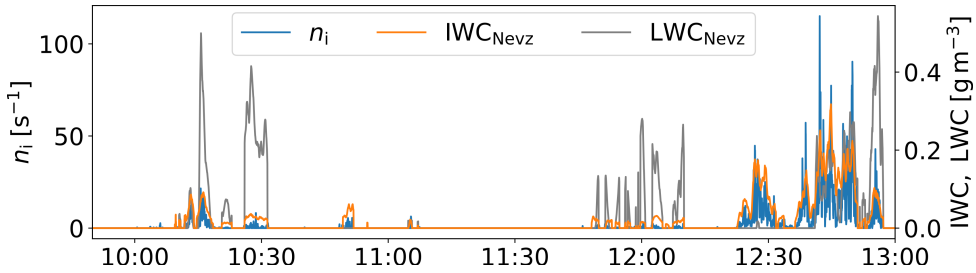
Figure 5.17: Comparison of the number of aspherical particles observed with the Backscatter Cloud Probe with Polarization Detection (n_i, blue) to the ice water content (IWC, orange) and the liquid water content (LWC, grey) from the Nevzorov probe.

It is important to understand that the presented approach operates with a bulk measurement of particles. The procedure of fitting curves to particle distributions can only be used once sufficiently many particles are present that, as an ensemble, exhibit the characteristic shapes of the ice and water distributions. Here, a minimum number of 100 particles is required to separate the distributions of the two regimes. The value of 100 particles was derived empirically and was found to work well in practice.

In many cases, less than 100 particles are measured per second. To apply the phase differentiation algorithm also to thinner clouds and considering the discussion on the sampling time in Section 5.3, the phase differentiation was always performed for rolling intervals of five seconds.

The estimation of n_i and n_w does not yield information on the phase of individual particles. The measurement of the δ of a single particle is often ambiguous, with one notable exception: Particles with a measured diameter larger than 13 μm and $\delta > -0.45$ are certainly ice (at larger δ values also smaller particles can be unambiguously classified as ice). This is known from wind tunnel testing and the theoretical calculations shown in Section 3.2.4. The exact region where it is possible to unambiguously identify particles as ice is shown in the Appendix in Fig. A.9. To detect ice particles at very low concentrations, it is favorable to analyze this region for the presence of particles.

The phase separation technique becomes important again in the next chapter where the cloud phase and the icing risk are assessed.

5.5.3. SHATTERING OF ICE PARTICLES ON THE FUSELAGE

The comparison of the particle number concentrations measured by the CDP in the underwing canister as opposed to the measurement of the BCPD at the fuselage (see Section 5.5.1) brought to light another intriguing effect. While the BCPD usually measured lower number concentrations than the CDP, in conditions with high ice water contents the BCPD particle counts significantly exceeded those of the CDP. This is shown in Fig. 5.18. Such conditions were related to the occurrence of a large number of ice crystals and snowflakes without small droplets being present. The size of the ice crystals was outside the measurement range of the
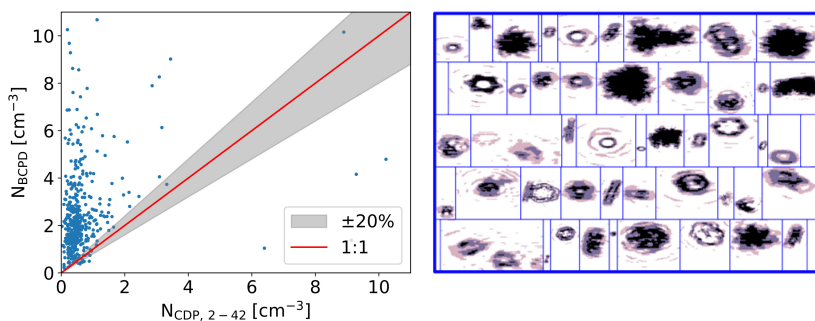
Figure 5.18: Number concentration (N) of the Cloud Droplet Probe (CDP) and the Backscatter Cloud Probe with Polarization Detection (BCPD) in conditions where the Nevzorov ice water content was larger than 90% of the Nevzorov total water content measurement. The right side shows a random sample of particles observed in these conditions.

BCPD, hence they should not have been detected by the instrument. Therefore, we deduce that the particles measured by the BCPD result from the shattering of ice particles on impact with the fuselage. Shattering has been a problem for other cloud instrumentation in the past [27, 28] and was mentioned as a potential cause for abnormally high number concentrations measured by the IAGOS aircraft in cirrus clouds [29]. Usually, shattering events are detected from an analysis of inter-particle times, which are approximately Poisson-distributed and related to the particle number concentration [30]. The shattering of a particle causes the almost simultaneous passage of the splintered fragments and consequently very small inter-particle times. These short inter-particle times manifest themselves as a second mode in the inter-particle time distribution. In the BCPD data, no second mode was detected (see Fig. A.10). This is likely because the particles impact the fuselage significantly ahead of the BCPD and the fragments then disperse in multiple directions. Nonetheless, Fig. 5.18 is clear evidence of shattering and it should be noted that for instruments integrated in the fuselage shattering effects may not manifest themselves as a second mode in the inter-particle times.

The shattering effect makes it impossible to use the BCPD for the detection of ice crystals that actually fall into its size range since there cannot be certainty, whether an ice particle resulted from a shattering event or not. However, shattering is not necessarily only a disadvantage for the BCPD. In a setup where the BCPD is the only cloud probe on an aircraft, the detection of shattered ice particles at least provides information about the presence of ice crystals, which might otherwise not be detected due to their large size, their low number concentration and the small sample volume of the BCPD.

5.6. Conclusions from the airborne measurements

This chapter demonstrated evaluation techniques of airborne measurements of the Nevzorov probe and the BCPD. At first, a procedure to estimate the convective heat

losses of the Nevzorov probe was established that enables the detection of LWCs and TWCs as low as $0.025\,\mathrm{gm}^{-3}$. Subsequently, I developed an iteration technique to determine collision efficiency corrected LWC and TWC values with the Nevzorov probe. The results of the iteration technique yield values of the liquid fraction which are on average within three percent of the liquid fraction that is computed from the reference instrumentation. This represents an improvement compared to the liquid fraction from the raw measurements of the LWC sensor and the Nevzorov 8 mm TWC cone, which is on average 13% higher than the value computed from the reference instrumentation. The new Nevzorov LWC and TWC data are likely also more accurate than those computed from the reference instrumentation itself because the reference instrumentation consists of particle sizing instruments that carry a large uncertainty due to the diameter-volume relationship. Therefore, the corrected LWC and TWC values serve as reference for the assessment of the icing risk in the next chapter.

Furthermore, a technique was conceived how the particle phase and the overall cloud phase can be derived from the BCPD data, an important part of research question II. The number of ice and water particles is determined based on their characteristic polarization ratio distributions. The technique yields results that correspond to the observations made with the Nevzorov probe, i.e. flight segments that have a liquid fraction close to 1 were also assessed by the BCPD to contain hardly any ice particles. It is important to understand that the BCPD delivers only indications on the cloud phase that is present and does not provide microphysical parameters like LWC and TWC. The computation of such parameters from the BCPD is not feasible due to shattering effects of ice crystals on the fuselage and by large uncertainties in the number concentration. The measurement data of the BCPD can therefore be helpful in combination with that of other instruments, e.g. the Nevzorov probe.

The necessary evaluation techniques for airborne measurements of the BCPD and the Nevzorov probe are now sufficiently established and a combination for the detection and discrimination of Appendix O conditions is attempted in the next chapter.

REFERENCES

[1] J. R. Lucke, T. Jurkat-Witschas, D. Baumgardner, F. Kalinka, M. Moser, E. De La Torre Castro, and C. Voigt, *Characterization of Atmospheric Icing Conditions during the HALO-(AC)³ Campaign with the Nevzorov Probe and the Backscatter Cloud Probe with Polarization Detection*, in *SAE Technical Paper Series* (SAE International, 2023).

[2] S. E. Bansmer, A. Baumert, S. Sattler, I. Knop, D. Leroy, A. Schwarzenboeck, T. Jurkat-Witschas, C. Voigt, H. Pervier, and B. Esposito, *Design, construction and commissioning of the Braunschweig Icing Wind Tunnel*, Atmospheric Measurement Techniques **11**, 3221 (2018).

[3] N. Maherndl, M. Moser, J. Lucke, M. Mech, N. Risse, I. Schirmacher,

and M. Maahn, *Quantifying riming from airborne data during HALO-(AC)3*, 10.5194/egusphere-2023-1118 (2023).

[4] B. Kirbus, I. Schirmacher, M. Klingebiel, M. Schäfer, A. Ehrlich, N. Slättberg, J. Lucke, M. Moser, H. Müller, and M. Wendisch, *Thermodynamic and cloud evolution in a cold air outbreak during HALO-(AC)3: Quasi-Lagrangian observations compared to the ERA5 and CARRA reanalyses*, 10.5194/egusphere-2023-2989 (2023).

[5] A. Korolev and J. Strapp, *Accuracy of measurements of cloud ice water content by the Nevzorov probe*, in *40th AIAA Aerospace Sciences Meeting & Exhibit* (American Institute of Aeronautics and Astronautics, 2002).

[6] A. Schwarzenboeck, G. Mioche, A. Armetta, A. Herber, and J.-F. Gayet, *Response of the Nevzorov hot wire probe in clouds dominated by droplet conditions in the drizzle size range*, Atmospheric Measurement Techniques **2**, 779 (2009).

[7] A. Walbröl, J. Michaelis, S. Becker, H. Dorff, I. Gorodetskaya, B. Kirbus, M. Lauer, N. Maherndl, M. Maturilli, J. Mayer, H. Müller, R. A. J. Neggers, F. M. Paulus, J. Röttenbacher, J. E. Rückert, I. Schirmacher, N. Slättberg, A. Ehrlich, M. Wendisch, and S. Crewell, *Environmental conditions in the North Atlantic sector of the Arctic during the HALO–(AC)³ campaign*, 10.5194/egusphere-2023-668 (2023).

[8] M. Rantanen, A. Y. Karpechko, A. Lipponen, K. Nordling, O. Hyvärinen, K. Ruosteenoja, T. Vihma, and A. Laaksonen, *The arctic has warmed nearly four times faster than the globe since 1979*, Communications Earth & Environment **3**, 168 (2022).

[9] M. Wendisch, M. Brückner, S. Crewell, A. Ehrlich, J. Notholt, C. Lüpkes, A. Macke, J. P. Burrows, A. Rinke, J. Quaas, M. Maturilli, V. Schemann, M. D. Shupe, E. F. Akansu, C. Barrientos-Velasco, K. Bärfuss, A.-M. Blechschmidt, K. Block, I. Bougoudis, H. Bozem, C. Böckmann, A. Bracher, H. Bresson, L. Bretschneider, M. Buschmann, D. G. Chechin, J. Chylik, S. Dahlke, H. Deneke, K. Dethloff, T. Donth, W. Dorn, R. Dupuy, K. Ebell, U. Egerer, R. Engelmann, O. Eppers, R. Gerdes, R. Gierens, I. V. Gorodetskaya, M. Gottschalk, H. Griesche, V. M. Gryanik, D. Handorf, B. Harm-Altstädter, J. Hartmann, M. Hartmann, B. Heinold, A. Herber, H. Herrmann, G. Heygster, I. Höschel, Z. Hofmann, J. Hölemann, A. Hünerbein, S. Jafariserajehlou, E. Jäkel, C. Jacobi, M. Janout, F. Jansen, O. Jourdan, Z. Jurányi, H. Kalesse-Los, T. Kanzow, R. Käthner, L. L. Kliesch, M. Klingebiel, E. M. Knudsen, T. Kovács, W. Körtke, D. Krampe, J. Kretzschmar, D. Kreyling, B. Kulla, D. Kunkel, A. Lampert, M. Lauer, L. Lelli, A. von Lerber, O. Linke, U. Löhnert, M. Lonardi, S. N. Losa, M. Losch, M. Maahn, M. Mech, L. Mei, S. Mertes, E. Metzner, D. Mewes, J. Michaelis, G. Mioche, M. Moser, K. Nakoudi, R. Neggers, R. Neuber, T. Nomokonova, J. Oelker, I. Papakonstantinou-Presvelou, F. Pätzold, V. Pefanis, C. Pohl, M. van Pinxteren, A. Radovan, M. Rhein, M. Rex, A. Richter, N. Risse, C. Ritter, P. Rostosky, V. V. Rozanov, E. R. Donoso,

P. S. Garfias, M. Salzmann, J. Schacht, M. Schäfer, J. Schneider, N. Schnierstein, P. Seifert, S. Seo, H. Siebert, M. A. Soppa, G. Spreen, I. S. Stachlewska, J. Stapf, F. Stratmann, I. Tegen, C. Viceto, C. Voigt, M. Vountas, A. Walbröl, M. Walter, B. Wehner, H. Wex, S. Willmes, M. Zanatta, and S. Zeppenfeld, *Atmospheric and Surface Processes, and Feedback Mechanisms Determining Arctic Amplification: A Review of First Results and Prospects of the (AC)3 Project*, Bulletin of the American Meteorological Society **104**, E208 (2023).

[10] I. Tan and T. Storelvmo, *Evidence of strong contributions from mixed-phase clouds to arctic climate change*, Geophysical Research Letters **46**, 2894 (2019).

[11] *HALO-AC3*, https://halo-ac3.de/halo-ac3/p5-p6/, accessed 2023-06-05.

[12] M. Moser, C. Voigt, T. Jurkat-Witschas, V. Hahn, G. Mioche, O. Jourdan, R. Dupuy, C. Gourbeyre, A. Schwarzenboeck, J. Lucke, Y. Boose, M. Mech, S. Borrmann, A. Ehrlich, A. Herber, C. Lüpkes, and M. Wendisch, *Microphysical and thermodynamic phase analyses of Arctic low-level clouds measured above the sea ice and the open ocean in spring and summer*, Atmospheric Chemistry and Physics **23**, 7257 (2023).

[13] H. Pruppacher and J. Klett, *Microphysics of Clouds and Precipitation* (Springer Netherlands, 2010).

[14] W. T. Scott, *Poisson Statistics in Distributions of Coalescing Droplets*, Journal of Atmospheric Sciences **24**, 221 (1967).

[15] A. V. Korolev, J. W. Strapp, G. A. Isaac, and A. N. Nevzorov, *The Nevzorov Airborne Hot-Wire LWC–TWC Probe: Principle of Operation and Performance Characteristics*, Journal of Atmospheric and Oceanic Technology **15**, 1495 (1998).

[16] G. M. McFarquhar, D. Baumgardner, A. Bansemer, S. J. Abel, J. Crosier, J. French, P. Rosenberg, A. Korolev, A. Schwarzoenboeck, D. Leroy, J. Um, W. Wu, A. J. Heymsfield, C. Twohy, A. Detwiler, P. Field, A. Neumann, R. Cotton, D. Axisa, and J. Dong, *Processing of Ice Cloud In Situ Data Collected by Bulk Water, Scattering, and Imaging Probes: Fundamentals, Uncertainties, and Efforts toward Consistency*, Meteorological Monographs **58**, 11.1 (2017).

[17] A. V. Korolev, G. A. Isaac, S. G. Cober, J. W. Strapp, and J. Hallett, *Microphysical characterization of mixed-phase clouds*, Quarterly Journal of the Royal Meteorological Society **129**, 39 (2003).

[18] A. Korolev, G. McFarquhar, P. R. Field, C. Franklin, P. Lawson, Z. Wang, E. Williams, S. J. Abel, D. Axisa, S. Borrmann, J. Crosier, J. Fugal, M. Krämer, U. Lohmann, O. Schlenczek, M. Schnaiter, and M. Wendisch, *Mixed-Phase Clouds: Progress and Challenges*, Meteorological Monographs **58**, 5.1 (2017).

[19] R. P. Lawson, S. Woods, and H. Morrison, *The microphysics of ice and precipitation development in tropical cumulus clouds*, Journal of the Atmospheric Sciences **72**, 2429 (2015).

5

[20] A. J. Heymsfield, C. Schmitt, A. Bansemer, and C. H. Twohy, *Improved Representation of Ice Particle Masses Based on Observations in Natural Clouds*, Journal of the Atmospheric Sciences **67**, 3303 (2010).

[21] P. R. Brown and P. N. Francis, *Improved measurements of the ice water content in cirrus using a total-water probe,* Journal of Atmospheric and Oceanic Technology **12**, 410 (1995).

[22] B. Baker and R. P. Lawson, *Improvement in Determination of Ice Water Content from Two-Dimensional Particle Imagery. Part I: Image-to-Mass Relationships*, Journal of Applied Meteorology and Climatology **45**, 1282 (2006).

[23] E. Järvinen, M. Schnaiter, G. Mioche, O. Jourdan, V. N. Shcherbakov, A. Costa, A. Afchine, M. Krämer, F. Heidelberg, T. Jurkat, C. Voigt, H. Schlager, L. Nichman, M. Gallagher, E. Hirst, C. Schmitt, A. Bansemer, A. Heymsfield, P. Lawson, U. Tricoli, K. Pfeilsticker, P. Vochezer, O. Möhler, and T. Leisner, *Quasi-Spherical Ice in Convective Clouds*, Journal of the Atmospheric Sciences **73**, 3885 (2016).

[24] D. Baumgardner, R. Newton, M. Krämer, J. Meyer, A. Beyer, M. Wendisch, and P. Vochezer, *The Cloud Particle Spectrometer with Polarization Detection (CPSPD): A next generation open-path cloud probe for distinguishing liquid cloud droplets from ice crystals*, Atmospheric Research **142**, 2 (2014).

[25] J. Meyer, *Ice crystal measurements with the new particle spectrometer NIXE-CAPS,* (2011).

[26] A. Costa, J. Meyer, A. Afchine, A. Luebke, G. Günther, J. R. Dorsey, M. W. Gallagher, A. Ehrlich, M. Wendisch, D. Baumgardner, H. Wex, and M. Krämer, *Classification of Arctic, midlatitude and tropical clouds in the mixed-phase temperature regime*, Atmospheric Chemistry and Physics **17**, 12219 (2017).

[27] A. V. Korolev, E. F. Emery, J. W. Strapp, S. G. Cober, G. A. Isaac, M. Wasey, and D. Marcotte, *Small Ice Particles in Tropospheric Clouds: Fact or Artifact? Airborne Icing Instrumentation Evaluation Experiment*, Bulletin of the American Meteorological Society **92**, 967 (2011).

[28] G. M. McFarquhar, J. Um, M. Freer, D. Baumgardner, G. L. Kok, and G. Mace, *Importance of small ice crystals to cirrus properties: Observations from the Tropical Warm Pool International Cloud Experiment (TWP-ICE),* Geophysical research letters **34** (2007).

[29] K. Beswick, D. Baumgardner, M. Gallagher, A. Volz-Thomas, P. Nedelec, K.-Y. Wang, and S. Lance, *The backscatter cloud probe - a compact low-profile autonomous optical spectrometer*, Atmospheric Measurement Techniques **7**, 1443 (2014).

[30] P. R. Field, A. J. Heymsfield, and A. Bansemer, *Shattering and Particle Inter-arrival Times Measured by Optical Array Probes in Ice Clouds*, Journal of Atmospheric and Oceanic Technology **23**, 1357 (2006).

6

ASSESSMENT OF ICING RISK AND CLOUD PHASE

The previous chapter investigated the accuracy and phase discrimination properties of the Nevzorov probe and the Backscatter Cloud Probe with Polarization Detection (BCPD) separately. Now, in connection with research question III, the data of the two instruments are combined and evaluated with a novel algorithm to identify the cloud phase and to detect icing and Appendix O conditions. The new algorithm is referred to as the Icing Risk Assessment Algorithm.

The Icing Risk Assessment Algorithm serves two purposes, to inform pilots about the presence of icing and Appendix O conditions and to retrieve information on the cloud phase in general. The cloud phase is of importance for climatological observations and nowcasting purposes and is therefore considered to be a valuable by-product of the sensor combination.

As discussed in Section 5.3, the detection of icing conditions should be timely but also stable, i.e. it should not change immediately when very short variations in the cloud composition occur. To generate a stable output, measurements used for the algorithm are averaged over thirty seconds, unlike over the five-second interval that was used in Chapter 5. For typical Appendix C and Appendix O icing conditions as they are encountered in the atmosphere, an icing indication within 30 seconds is sufficient [2].

The following sections first discuss the cloud conditions that are differentiated with the Icing Risk Assessment Algorithm, then they explain the detection thresh-

olds that are used. Subsequently, the research flight from the HALO-AC³ campaign that was presented in Chapter 5 is evaluated with the algorithm and the results are analyzed and discussed. In the last section, data from the SENS4ICE campaign are presented. These data include Appendix O encounters, hence the detection rate of Appendix O conditions of the Icing Risk Assessment Algorithm can be evaluated.

6.1. CATEGORIZATION OF CLOUD CONDITIONS

The Icing Risk Assessment Algorithm differentiates six conditions:

1. No cloud and no precipitation (NO)

2. Liquid cloud or precipitation at positive temperatures (WARM)

3. Ice cloud or frozen precipitation (ICE)

4. Mixed-phase cloud (MP)

5. Pure supercooled liquid water cloud containing only small droplets and no supercooled large droplets (LQD SD)

6. Appendix O cloud (App. O)

The rationale behind selecting these conditions is that each of them has a certain significance for the risk of icing and for climatological observations. The first three categories represent no risk for airframe icing. Nonetheless, it is useful to differentiate between the absence of clouds and warm clouds to obtain statistics on cloud occurrences, similar to what is done in the In-service Aircraft for a Global Observing System (IAGOS) program [3]. The detection of ice clouds is also of importance. Ice clouds are sometimes predicted as liquid clouds that carry an icing risk in icing forecasting tools [1]. Aircraft may then choose to fly around the predicted icing conditions. The real-time identification of ice clouds can therefore help to avoid unnecessary reroutings of aircraft.

Mixed-phase clouds and purely supercooled clouds that contain only small droplets both represent an icing risk. Mixed-phase clouds typically do not contain a significant number of supercooled large droplets (SLDs), due to the depletion of the available water vapor by the ice crystals (see Section 2.1). The two conditions are distinguished here because the information on whether a cloud is entirely liquid or partially glaciated is relevant for the characterization of Arctic clouds that is attempted in the HALO-AC³ project [4, 5]. Finally, Appendix O conditions need to be distinguished as was explained in the motivation for this thesis (see Chapter 1).

6.2. DIFFERENTIATION OF CLOUD CONDITIONS

Here, I explain the detection thresholds that are used for identifying the cloud conditions defined in Section 6.1. Two data sources are distinguished, the measurements from the Nevzorov probe and the measurements from the BCPD. For clarity, I explain the decision tree for the BCPD data first and afterward present the overall decision tree of the Icing Risk Assessment Algorithm that includes the data from both the BCPD and the Nevzorov probe.
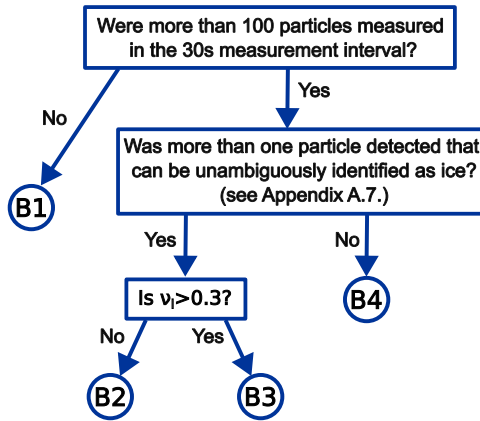
Figure 6.1: Decision tree for the measurements of the Backscatter Cloud Probe with Polarization Detection (BCPD).

6.2.1. DIFFERENTIATING CLOUD CONDITIONS WITH THE BACKSCATTER CLOUD PROBE WITH POLARIZATION DETECTION

An indication for the cloud phase of the BCPD is derived based on the presence of a sufficient number of particles and on the number of water and ice particles that are detected. The particle size measurements of the BCPD are not used, the reason for this being the low confidence in the size measurements, which is further elaborated on in Section 6.4.1.

The decision tree for the BCPD measurements can be seen in Fig. 6.1. Four possible outcomes exist, which are labeled as B1, B2, B3 and B4. As mentioned in Section 5.5.2, the phase differentiation is only performed if more than 100 particles were detected within a 30-second interval. Correspondingly, category B1 specifies that an insufficient number of particles were detected, which is usually the case in an out-of-cloud segment.

In case a sufficient number of particles were present, further assessment of the measurements is performed, which is explained in the following. There is no clear definition of the minimum number of ice particles that need to be present in a cloud for it to be considered a mixed-phase cloud [6]. During the research flight, maximum ice particle concentrations, based on the particle size distribution from the reference instrumentation (PSD_{ref}) and the number of particles larger than 50 μm, were approximately 0.27 cm^{-3}, but often ice particles occurred in much lower concentrations. Given an ice particle concentration of 0.1 cm^{-3} and an airspeed of 67 ms^{-1}, on average 16 ice particles pass the sample volume of the BCPD every second. The maximum number of ice particles detected by the BCPD with the technique from Section 5.5.2 is approximately 100 per second (within the BCPD size range, which is however not well defined for ice particles, see Section 3.2.2). The high number of ice crystals measured by the BCPD is first of all further evidence for shattering. Secondly, in this case, the shattering is favorable, because it allows to detect the presence of ice crystals in lower number concentrations than would

be possible without shattering.

The question arises of what threshold should be used to distinguish mixed-phase and pure supercooled clouds. Given that the water content of large ice crystals can constitute a considerable portion of the overall water content of a cloud even for ice crystal number concentrations well below 0.01 cm^{-3}, it is sensible to opt for a low threshold. I, therefore, decided that every thirty-second segment with two or more ice particles should be classified as mixed-phase. Again using an airspeed of 67 m s^{-1} and assuming that each ice crystal produces one fragment that falls within the size range of the BCPD, the minimum ice crystal number concentration of a cloud that is detected as mixed-phase is approximately 0.001 cm^{-3}. If ice crystals produced on average more than one fragment within the BCPD size range, the minimum ice crystal number concentration would be lower.

Vice versa pure supercooled clouds, which form category B4 in the decision tree (see Fig. 6.1), need to contain no more than one ice particle per thirty-second interval. The low threshold means that the separation of mixed-phase and pure supercooled clouds is subject to a certain randomness. However, I consider this randomness to be favorable compared to a threshold selection where only mixed-phase clouds with high ice particle concentrations can be detected.

Lastly, an indication of whether a cloud is completely glaciated (category B2) or mixed-phase (category B3) is derived from the BCPD data (see Fig. 6.1). For completely glaciated clouds, it is required that:

$$v_l = \frac{n_l}{(n_i + n_l)} \leq 0.3.$$

The threshold of 0.3 implies that a certain portion of liquid droplets can still be present. It was sometimes observed (e.g. see Fig. 5.15b and d) that a small number of liquid particles was present in an almost completely glaciated cloud. These particles are usually less than 10 µm in diameter and do not pose an icing threat.

6.2.2. ICING RISK ASSESSMENT WITH THE NEVZOROV PROBE AND THE BACKSCATTER CLOUD PROBE WITH POLARIZATION DETECTION

Now, the complete Icing Risk Assessment Algorithm, which assigns the observations to the categories introduced in Section 6.1 is explained. Both, the Nevzorov probe data and the BCPD data, which has already been categorized in the previous section, are considered. The thresholds used here are empirical values that are based on the icing wind tunnel (IWT) and flight tests described in Chapter 4 and Chapter 5. A graph that depicts all decisions that lead to the detection of a specific cloud condition is shown in Fig. 6.2. For a definition of the parameters used in the decision tree and in the following paragraphs see Table 5.1.

The absence of clouds (condition NO) is always detected when the average value of the uncorrected total water contents (TWCs) from the Nevzorov probe 8 mm and 12 mm cone (W_8 and W_{12}) is below or equal to 0.025 g m^{-3}. Furthermore, NO is identified if the BCPD condition B1 (less than 100 particles measured in 30 seconds) is detected (see Section 6.2.1).
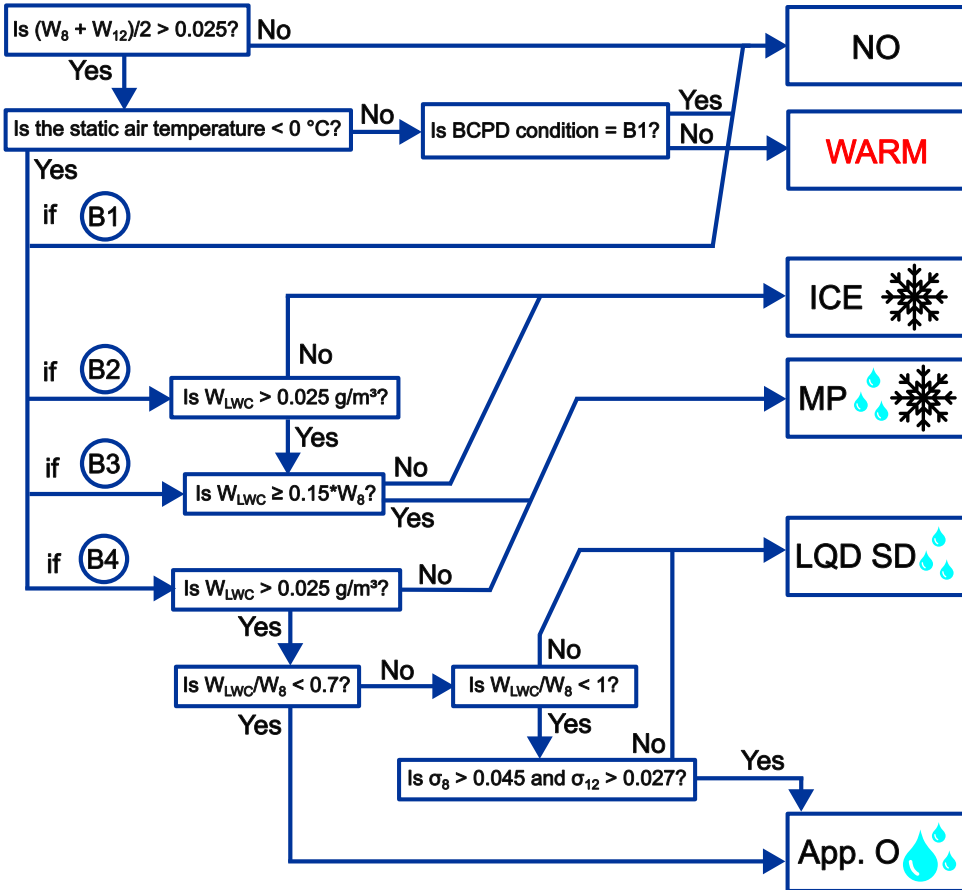
Figure 6.2: Decision tree for the Icing Risk Assessment Algorithm. As described in Section 6.1, six different conditions are distinguished: No clouds (NO), warm clouds (WARM), entirely glaciated clouds (ICE), mixed-phase clouds (MP), purely supercooled clouds that contain only small droplets (LQD SD) and Appendix O conditions (App. O). For a definition of the parameters see Table 5.1.

In case clouds are present (i.e. the cloud condition is not NO), warm clouds (WARM) are identified if the static air temperature is 0 °C or higher. The decisions that lead to the identification of glaciated clouds, mixed-phase clouds, pure liquid clouds and Appendix O conditions are more complex. They are explained in the following. From now on it is assumed that cold clouds were detected (i.e. the cloud condition is not NO or WARM). Entirely glaciated clouds are identified when one of the following statements is true:

- The condition derived from the BCPD is B2 and $W_{\mathrm{LWC}} \leq 0.025\,\mathrm{gm}^{-3}$.

- The condition derived from the BCPD is B2, $W_{\mathrm{LWC}} > 0.025\,\mathrm{gm}^{-3}$ and $W_{\mathrm{LWC}} < 0.15\,W_8$.

- The condition derived from the BCPD is B3 and $W_{\mathrm{LWC}} < 0.15\,W_8$.

Here, W_{LWC} denotes the uncorrected measurement from the liquid water content (LWC) sensor of the Nevzorov probe (see Table 5.1). The first statement relies on the detection of the BCPD and verifies that no significant LWC was detected with the Nevzorov probe. The second statement assures that glaciated conditions are correctly identified even if the overall TWC is high such that, due to the response of the LWC sensor to ice crystals, a W_{LWC} value above the threshold sensitivity is measured. The third statement verifies whether, even though the cloud was detected as B3 by the BCPD, the W_{LWC} value is so low that it shows likely just the response of the Nevzorov LWC sensor to ice. In such a case hardly any liquid water is present and the cloud is better described as glaciated.

Mixed phase clouds are identified if any of the statements below are true:

- The cloud condition detected by the BCPD is B3 and $W_{\mathrm{LWC}} \geq 0.15\,W_8$.

- The cloud condition is detected as B4 but $W_{\mathrm{LWC}} \leq 0.025\,\mathrm{gm}^{-3}$.

The first statement relies on the detection of the BCPD and ensures that the measured LWC is not due to the response of the LWC sensor to ice particles. The second statement on the other hand considers conditions that were identified as almost entirely liquid by the BCPD but where W_{LWC} is below W_8 and below the detection threshold of the Nevzorov probe. For such observations, a few large ice particles were likely present but were not detected by the BCPD.

Lastly, Appendix O conditions are identified when the cloud condition detected by the BCPD is B4 and one of the two statements below is true:

- $W_{\mathrm{LWC}} > 0.025\,\mathrm{gm}^{-3}$ and the ratio of W_{LWC}/W_8 is smaller than 0.7.

- $W_{\mathrm{LWC}} > 0.025\,\mathrm{gm}^{-3}$, the ratio of W_{LWC}/W_8 is between 0.7 and 1, and the standard deviations σ_8 and σ_{12} are larger than 0.045 and 0.027, respectively.

The first case relies solely on the sensor ratio between the LWC sensor and the 8 mm cone. If a sufficient number of SLDs are present, splashing of droplets on the LWC sensor occurs and collision efficiency effects on the 8 mm cone become irrelevant (see Section 3.1.1), shifting the ratio W_{LWC}/W_8 towards smaller values. The second

case considers that in bimodal SLD conditions, the decrease in W_{LWC}/W_8 is not as strong, due to the presence of numerous small droplets. For this reason, also the standard deviations are analyzed, which can serve as an indication for droplet size, as was shown in Section 4.3.7. All observations that are identified as BCPD condition B4 but do not match either of the above statements are identified as purely supercooled clouds without SLDs (LQD SD).

6.3. RESULTS OF THE ICING RISK ASSESSMENT ALGORITHM FOR THE HALO-AC³ RESEARCH FLIGHT

Now the Icing Risk Assessment Algorithm is applied to the data of the research flight from the HALO-AC³ campaign that was described in Chapter 5. It is important to remember that the analysis of the data of the reference instrumentation showed that no Appendix O conditions were encountered during the flight. Hence, the detection of Appendix O cannot be verified from that flight, but the false alarm rate of the Icing Risk Assessment Algorithm can be assessed. Furthermore, the temperature during the entire flight was below 0 °C, consequently, no warm clouds existed (see Fig. 5.5).

The conditions detected by the Icing Risk Assessment Algorithm over the different phases of the research flight are shown in Fig. 6.3a. The corrected Nevzorov measurements LWC_{Nevz} and TWC_{Nevz} derived with the algorithm from Section 5.4.2 are plotted for comparison. These are the most accurate available estimates for the LWC and TWC and therefore serve as the reference for this comparison. The performance of the Icing Risk Assessment Algorithm can be best evaluated from panels b-d of Fig. 6.3. There, for the cloud types that occurred (i.e. ICE, MP, LQD SD), the liquid fraction from the corrected Nevzorov measurements ($\mu_{l,Nevz}$) is plotted in a histogram. Ideally, no bars of the histograms should lie within the red-hatched areas. It can be seen that the Icing Risk Assessment Algorithm is very accurate in recognizing ice clouds, for 94% of the detected cases the reference liquid fraction $\mu_{l,Nevz}$ is between 0 and 0.05. For clouds identified as mixed-phase by the BCPD (Fig. 6.3c) μ_l values fall anywhere between 0 and 1. Ideally, the conditions where $\mu_{l,Nevz}$ falls between 0 and 0.05, and between 0.95 and 1 should be identified as ICE or LQD SD, respectively. Especially the classification of liquid clouds as mixed-phase appears to be common. According to the implementation of the Icing Risk Assessment Algorithm, all of these clouds contain ice particles, but likely their water content is insufficient to reduce $\mu_{l,Nevz}$ below 0.95 (see the requirements for the detection of mixed-phase clouds in Fig. 6.2). The clouds which are classified as purely liquid by the Icing Risk Assessment Algorithm (Fig. 6.3d), are in 57% of the cases mixed-phase clouds according to the $\mu_{l,Nevz}$ values from the Nevzorov probe, albeit mostly with low ice fractions. The differences in classification are likely due to the small sample volume of the BCPD which means that low numbers of ice particles cannot be detected. It is also possible that certain ice particles do not break into small fragments and therefore cannot be detected by the BCPD due to its insufficient size range. Regarding Appendix O conditions, it is clear that the false alarm rate is zero. No cloud conditions are identified as Appendix O.
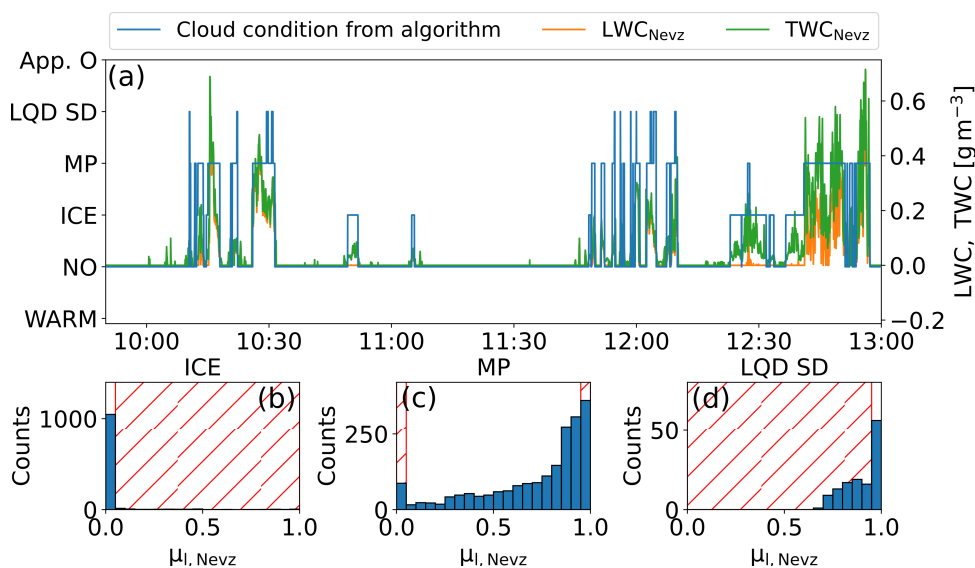
Figure 6.3: **a**: Cloud conditions detected with Icing Risk Assessment Algorithm and comparison to the liquid water content (LWC) and total water content (TWC) from the Nevzorov probe. **b-d**: Liquid fraction $\mu_{l,Nevz}$ from the Nevzorov probe for the three cloud conditions that are differentiated. The red-hatched areas indicate the regions in which in an ideal case zero counts would exist in the histogram.

6

The data from this research flight provided a suitable initial test bed for the Icing Risk Assessment Algorithm. It was observed that glaciated, mixed-phase and purely supercooled clouds can be differentiated. The differentiation of glaciated conditions works robustly. The differentiation between mixed-phase and liquid conditions is limited by the sample volume of the BCPD, which is too small to detect low number concentrations of ice particles. It was verified that no false alarms on the presence of Appendix O conditions were raised. The following section tests the detection of Appendix O conditions.

6.4. FIRST RESULTS FROM THE EUROPEAN SENS4ICE FLIGHT CAMPAIGN

Due to COVID-19, the European SENS4ICE campaign, which was initially planned for April 2022, was shifted to April 2023. The flight campaign was performed on the ATR-42 aircraft of the French facility for airborne research (SAFIRE) [7]. The instrumentation of the aircraft was similar to that of the HALO-AC³ campaign (Section 5.1), with measurements from the Nevzorov probe, the BCPD, the HALO-CCP and the Precipitation Imaging Probe (PIP) all being available. As in the previous chapter, the measurements from the HALO-CCP serve as reference instrumentation, but the PIP is not used, which is acceptable because particle sizes were mostly within the size range of the Cloud Imaging Probe (CIP). The particle size distributions (PSDs) and the particle images from the reference instruments are used to

derive a flag that indicates the presence of Appendix O conditions (referred to as Appendix O flag in the following). Details on the Appendix O flag can be found in the SENS4ICE project deliverable D4.3 [8]. The evaluation of the reference measurements is at the time of this writing still a work in progress and their data should be considered preliminary.

It is however certain that Appendix O conditions were encountered numerous times, enabling a first, though preliminary evaluation of the sensor combination of the Nevzorov probe and BCPD. Results from one flight that carry important implications for the capability of the suggested sensor combination are presented here. The results confirm and explain some of the observations made earlier. First, I describe observations from the measurements of the BCPD and the Nevzorov probe individually, then I assess the performance of the Icing Risk Assessment Algorithm.

6.4.1. Measurements of the Backscatter Cloud Probe with Polarization Detection

The comparison of the BCPD and Cloud Droplet Probe (CDP) measurements till now yielded no conclusive explanation for the differences that were observed in the number concentration and median volume diameter (MVD). In Section 5.5.1, I observed that the agreement between the MVDs of the CDP and the BCPD (MVD_{CDP} and MVD_{BCPD}) followed a curve shape. The same observation was made for the SENS4ICE campaign, but, because larger MVDs were encountered, the curve can be extended. This can be seen in Fig. 6.4b, where MVD_{CDP} and MVD_{BCPD} are compared. The ratio between the number concentrations of the two instruments is shown as the color code. Between 10 µm < MVD_{CDP} < 20 µm a similar trend as in Fig. 5.14b can be observed, with MVD_{CDP} and MVD_{BCPD} reaching parity at approximately 20 µm. Upwards from an MVD_{CDP} of 20 µm, MVD_{BCPD} does not increase at all. In fact, during flight segments where the mode of the PSD lies at approximately 40 µm, not a single 40 µm droplet was observed by the BCPD (not shown).

Figure 6.4a shows the comparison of the number concentrations of the CDP and the BCPD (N_{CDP} and N_{BCPD}), with MVD_{CDP} as the color code. For MVD_{CDP} < 20 µm, N_{CDP} tends to exceed N_{BCPD} as was observed during the HALO-AC³ campaign (see Fig. 5.14a). For larger MVDs, N_{BCPD} is multiple times larger than N_{CDP}.

From the IWT tests, it is known that the BCPD can detect 40 µm droplets. If no 40 µm droplets are detected, this consequently means that none were present. As mentioned previously, the sampling position of the BCPD is just three centimeters from the aircraft fuselage. During the HALO-AC³ campaign, the BCPD was mounted relatively far aft at the bottom of the aircraft (see Fig. 5.2) and for the SENS4ICE campaign, the BCPD was mounted in a side window several meters from the aircraft nose. At both locations, the airflow was possibly influenced by the aircraft body. The deflection of the airflow on the aircraft body can lead to «shadow zones», where no particles of a certain size are present [9]. Similarly, it may also lead to an enrichment of particles of a certain size [10]. Both effects were likely present, according to Fig. 6.4 the BCPD sample volume likely fell within a shadow zone for particles larger than approximately 25 µm diameter, while enrichment of particles of 10-20 µm occurred in that zone. The existence of such shadow and en-
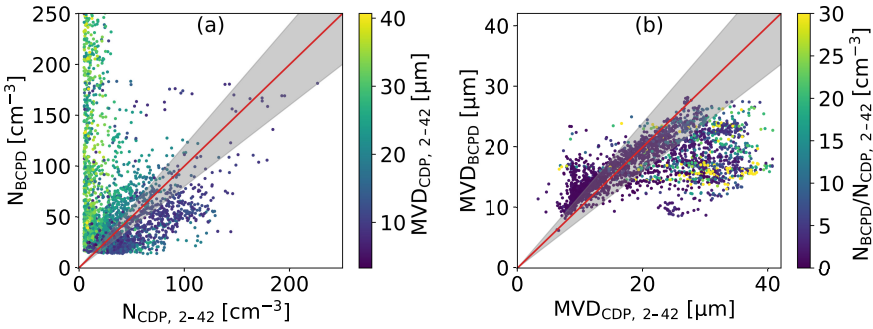
Figure 6.4: Similar to Fig. 5.14, but for the SENS4ICE campaign. The left plot shows the comparison of the number concentration (N) of the Backscatter Cloud Probe with Polarization Detection (BCPD) and the Cloud Droplet Probe (CDP). The right plot compares the median volume diameter (MVD) observed by the BCPD and the CDP. Only predominantly liquid segments (according to the polarization ratio of the BCPD) were considered for this graph.

richment zones is the most plausible explanation for the difference between CDP and BCPD measurements, in MVD as well as in number concentration. Only for the IWT measurements (see Section 4.4.1), where MVDs matched well but number concentrations did not, the existence of such a shadow zone is unlikely and no explanation for the lower number concentrations that were observed could be determined in this thesis.

The risk that the BCPD sample volume might lie in a zone where the airflow is severely altered was known when the installation position was selected. Positions further in the front of the aircraft, ideally directly in the nose, would have been preferred, but none were available, due to space constraints and conflicts with existing avionic equipment at the positions. In a retrospective view, fluid simulations should be conducted prior to integration of the BCPD at any location, but such simulations would have exceeded the scope of this thesis.

6.4.2. MEASUREMENTS OF THE NEVZOROV PROBE

The evaluation of the Nevzorov probe during airborne measurements was established in Section 5.4. I use the same procedure as described there for the removal of the dry air term in the SENS4ICE measurements. The computation of the corrected LWC and TWC values from Section 5.4.2 could not be performed due to time constraints, because, due to the large MVDs observed during SENS4ICE, adaptations to the procedure would have been necessary to account for the effects of droplet splashing on the LWC sensor (see Section 3.1.1). All required inputs to the Icing Risk Assessment Algorithm from Section 6.2 are however available.

In Section 4.3.7 the usage of the standard deviation of the Nevzorov measurements to obtain an indication of the droplet size was discussed. Before the Icing Risk Assessment Algorithm is applied to the Nevzorov data, it is verified that the relationship is also valid during SENS4ICE. The relationship observed in the SENS4ICE data between the standard deviations of the Nevzorov probe TWC cone signals and MVD_{CDP} can be seen in Fig. 6.5. The standard deviation increases with
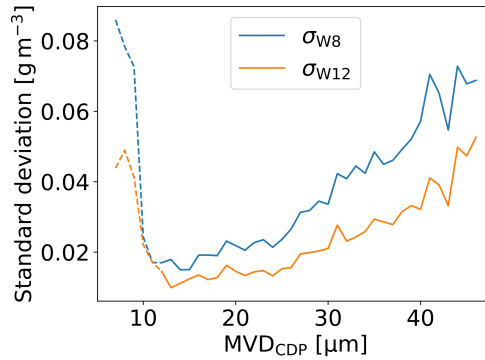
Figure 6.5: Relationship between the median volume diameter (MVD) from the Cloud Droplet Probe (CDP) and the median standard deviations of the Nevzorov 8 mm cone (σ_{W8}, blue) and 12 mm cone (σ_{W12}, orange) signals as observed during the European SENS4ICE campaign.

increasing MVD. The readings below approximately 12 µm should be considered invalid because hardly any such conditions were encountered. Based on this observation I proceed to the application of the Icing Risk Assessment Algorithm to the measurements of the SENS4ICE research flight.

6.4.3. DETECTION OF APPENDIX O CONDITIONS

The algorithm from Fig. 6.5 is applied to the data of a SENS4ICE research flight that was performed on April 27, 2023.

As mentioned before, Appendix O conditions were encountered many times in spring-time clouds during the SENS4ICE campaign, however, most of these encounters were under one minute long. The research flight I selected here had some of the longest and most stable encounters of all flights during the campaign. One extended encounter of approximately three minutes and several short encounters occurred. The results from the Icing Risk Assessment Algorithm and the Appendix O flag from the reference data can be seen in Fig. 6.6. The figure shows the cloud condition detected with the Icing Risk Assessment Algorithm in blue and the Appendix O flag from the reference instrumentation (which is 1 if Appendix O is present and otherwise 0) in orange.

For the interpretation of the results, it is important to consider that the exact entry time into Appendix O conditions is not always clearly identifiable. Both, the Appendix O flag from the reference data and the output from the Icing Risk Assessment Algorithm are based on a rolling mean of thirty seconds [8, 11]. Consider the following example: The aircraft had been flying in clear air but has entered Appendix O conditions in five seconds ago. Due to the averaging the observed parameters are a mixture of clear air conditions and Appendix O conditions. Whether or not the Appendix O flag is raised depends on the severity of the Appendix O conditions and on the parameters that are observed. Entry into very severe Appendix O conditions can lead to the flag being immediately raised, while entry into Appendix O conditions that are weak or are close to Appendix C can cause the flag
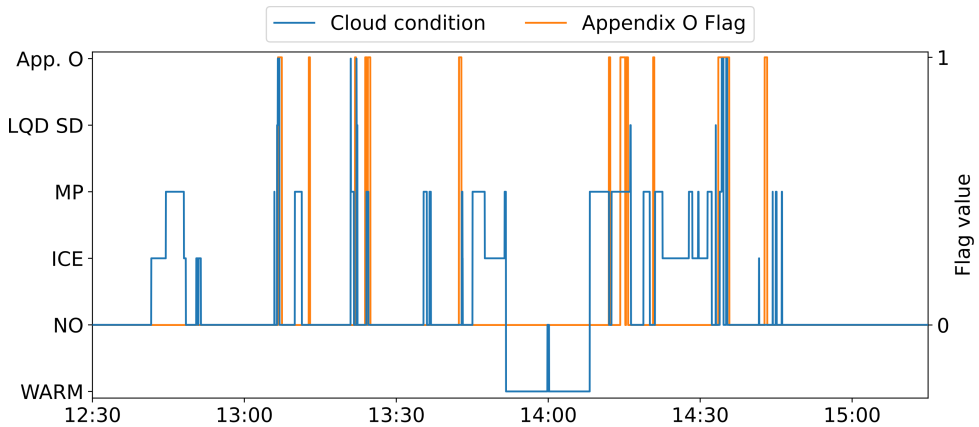
Figure 6.6: Cloud condition detected from the Icing Risk Assessment Algorithm (blue) and Appendix O flag from the reference data (orange).

to be raised several seconds after the first encounter. Because the parameters that are used to detect the presence of Appendix O conditions differ between the Icing Risk Assessment Algorithm and the reference instrumentation, it is expected and acceptable if the two methods detect Appendix O conditions only at approximately the same time.

Regarding the detection of Appendix O conditions, the three-minute encounter around 14:33 is correctly identified as Appendix O by the Icing Risk Assessment Algorithm. In fact, the Icing Risk Assessment Algorithm detects two separate Appendix O encounters, between 14:33 and 14:36. Indeed, it was found that two separate encounters existed in that time frame, which are not individually resolved in the reference measurements. The detected encounters had an MVD of 44 μm and LWCs around $0.15\,\mathrm{g m^{-3}}$ according to the reference measurements. From images of the CIP it was verified that no ice particles were present during the encounters (see Appendix A.9).

A few other, shorter encounters are also detected as Appendix O. However, several Appendix O encounters are missed, especially the approximately one-minute-long encounter at 14:14. The encounter is not detected, because ice particles are measured by the BCPD (i.e. condition B3 is detected, see Fig. 6.1 and Fig. 6.2). From the CIP images I was able to visually verify that ice crystals were indeed present, but also SLDs (see Appendix A.9). The Icing Risk Assessment Algorithm excludes the possibility of the presence of SLDs once ice particles are observed. This exclusion is necessary, because ice particles, like SLDs, decrease the ratio between the LWC sensor and the 8 mm cone sensor, which is used to distinguish LQD SD and Appendix O (see Fig. 6.2).

Positively, one can remark that the false alarm rate of the Icing Risk Assessment Algorithm is practically zero, at no instance are Appendix O conditions erroneously detected (excluding cases where the detection is merely shifted by a few seconds, such as at 13:21).

6.5. Conclusions on the icing risk and cloud phase assessment

In connection with research question III, this chapter presented a technique to determine the icing risk and the cloud phase from the measurements of the Nevzorov probe and the BCPD. At first, a categorization of the cloud conditions that are distinguished was developed and motivated. Then, possible methods and considerations that are crucial for the differentiation of icing risk and cloud phase were discussed, at first only for the BCPD and then for the BCPD and the Nevzorov probe together. The outcome is an algorithm that differentiates between Appendix O, pure supercooled droplet conditions, mixed-phase, glaciated and warm clouds. The algorithm is referred to as the Icing Risk Assessment Algorithm.

The Icing Risk Assessment Algorithm was first tested on data from the HALO-AC³ research flight that was described in Chapter 5. The results confirmed that it is possible to correctly distinguish glaciated clouds from mixed-phase and pure supercooled liquid water clouds. The distinction between mixed-phase and pure supercooled liquid water clouds is also possible, but some confusion between the two conditions exists when ice particle concentrations are below the detection threshold of the BCPD.

Since the HALO-AC³ research flight did not encounter Appendix O conditions, one flight from the SENS4ICE flight campaign, where Appendix O conditions were encountered, was also evaluated. It was found that Appendix O conditions that do not contain ice crystals can be identified with the Icing Risk Assessment Algorithm. However, because ice crystals affect the measurements of the Nevzorov probe LWC and TWC sensors in a similar way as SLDs, small-scale Appendix O conditions, which are embedded into mixed-phase conditions, cannot be detected with the Icing Risk Assessment Algorithm. Suggestions on improving the detection are discussed in the outlook.

References

[1] J. R. Lucke, T. Jurkat-Witschas, D. Baumgardner, F. Kalinka, M. Moser, E. De La Torre Castro, and C. Voigt, *Characterization of Atmospheric Icing Conditions during the HALO-(AC)³ Campaign with the Nevzorov Probe and the Backscatter Cloud Probe with Polarization Detection*, in *SAE Technical Paper Series* (SAE International, 2023).

[2] EUROCAE, *ED-103A/B - Minimum operating performance standards for an inflight icing detection system*, Tech. Rep. (2017).

[3] K. Beswick, D. Baumgardner, M. Gallagher, A. Volz-Thomas, P. Nedelec, K.-Y. Wang, and S. Lance, *The backscatter cloud probe - a compact low-profile autonomous optical spectrometer*, Atmospheric Measurement Techniques **7**, 1443 (2014).

[4] I. Tan, G. Sotiropoulou, P. C. Taylor, L. Zamora, and M. Wendisch, *A review of the factors influencing Arctic mixed-phase clouds: Progress and outlook*, Earth

and Space Science Open Archive, https://doi. org/10.1002/essoar **10508308** (2021).

[5] M. Wendisch, M. Brückner, S. Crewell, A. Ehrlich, J. Notholt, C. Lüpkes, A. Macke, J. P. Burrows, A. Rinke, J. Quaas, M. Maturilli, V. Schemann, M. D. Shupe, E. F. Akansu, C. Barrientos-Velasco, K. Bärfuss, A.-M. Blechschmidt, K. Block, I. Bougoudis, H. Bozem, C. Böckmann, A. Bracher, H. Bresson, L. Bretschneider, M. Buschmann, D. G. Chechin, J. Chylik, S. Dahlke, H. Deneke, K. Dethloff, T. Donth, W. Dorn, R. Dupuy, K. Ebell, U. Egerer, R. Engelmann, O. Eppers, R. Gerdes, R. Gierens, I. V. Gorodetskaya, M. Gottschalk, H. Griesche, V. M. Gryanik, D. Handorf, B. Harm-Altstädter, J. Hartmann, M. Hartmann, B. Heinold, A. Herber, H. Herrmann, G. Heygster, I. Höschel, Z. Hofmann, J. Hölemann, A. Hünerbein, S. Jafariserajehlou, E. Jäkel, C. Jacobi, M. Janout, F. Jansen, O. Jourdan, Z. Jurányi, H. Kalesse-Los, T. Kanzow, R. Käthner, L. L. Kliesch, M. Klingebiel, E. M. Knudsen, T. Kovács, W. Körtke, D. Krampe, J. Kretzschmar, D. Kreyling, B. Kulla, D. Kunkel, A. Lampert, M. Lauer, L. Lelli, A. von Lerber, O. Linke, U. Löhnert, M. Lonardi, S. N. Losa, M. Losch, M. Maahn, M. Mech, L. Mei, S. Mertes, E. Metzner, D. Mewes, J. Michaelis, G. Mioche, M. Moser, K. Nakoudi, R. Neggers, R. Neuber, T. Nomokonova, J. Oelker, I. Papakonstantinou-Presvelou, F. Pätzold, V. Pefanis, C. Pohl, M. van Pinxteren, A. Radovan, M. Rhein, M. Rex, A. Richter, N. Risse, C. Ritter, P. Rostosky, V. V. Rozanov, E. R. Donoso, P. S. Garfias, M. Salzmann, J. Schacht, M. Schäfer, J. Schneider, N. Schnierstein, P. Seifert, S. Seo, H. Siebert, M. A. Soppa, G. Spreen, I. S. Stachlewska, J. Stapf, F. Stratmann, I. Tegen, C. Viceto, C. Voigt, M. Vountas, A. Walbröl, M. Walter, B. Wehner, H. Wex, S. Willmes, M. Zanatta, and S. Zeppenfeld, *Atmospheric and Surface Processes, and Feedback Mechanisms Determining Arctic Amplification: A Review of First Results and Prospects of the (AC)3 Project*, Bulletin of the American Meteorological Society **104**, E208 (2023).

[6] A. Korolev, G. McFarquhar, P. R. Field, C. Franklin, P. Lawson, Z. Wang, E. Williams, S. J. Abel, D. Axisa, S. Borrmann, J. Crosier, J. Fugal, M. Krämer, U. Lohmann, O. Schlenczek, M. Schnaiter, and M. Wendisch, *Mixed-Phase Clouds: Progress and Challenges*, Meteorological Monographs **58**, 5.1 (2017).

[7] C. Schwarz, *SENS4ICE EU project preliminary results*, in *SAE Technical Paper Series* (SAE International, 2023).

[8] J. Lucke, A. L. Zollo, B. Bernstein, and T. Jurkat-Witschas, *SENS4ICE deliverable D4.3: Final report on airborne demonstration and atmospheric characterization*, Tech. Rep. (2024).

[9] A. Afchine, C. Rolf, A. Costa, N. Spelten, M. Riese, B. Buchholz, V. Ebert, R. Heller, S. Kaufmann, A. Minikin, C. Voigt, M. Zöger, J. Smith, P. Lawson, A. Lykov, S. Khaykin, and M. Krämer, *Ice particle sampling from aircraft – influence of the probing position on the ice water content*, Atmospheric Measurement Techniques **11**, 4015 (2018).

6

[10] T. P. Ratvasky, J. W. Strapp, L. E. Lilie, D. B. Bouley, and C. P. Sivo, *Simultaneous Ice Water Content Measurements at Multiple Locations on the NASA DC-8 Aircraft during the 2018 HIWC RADAR Flight Campaign*, in *2021 AIAA Aviation Forum and Exhibition*, E-19981 (2021).

[11] J. Lucke, T. Jurkat-Witschas, D. Menekay, C. Schwarz, C. Deiler, S. Kirschler, R. Heller, J. Mayer, C. Voigt, A. Bourdon, B. Vie, O. Jaron, F. Kalinka, B. Bernstein, D. M. da Silva, L. A. Vieira, C. Sliveira, R. de Lima, and L. Lilie, *Meteorological conditions and microphysical properties that lead to aircraft icing as observed during the SENS4ICE campaigns*, https://www.sens4ice-project.eu/sites/sens4ice/files/media/2023-10/SENS4ICE_DLRK2023_Meteorological_Conditions_DLR_September2023.pdf (2023).

6

7

CONCLUSION

This thesis pursued the goal of detecting atmospheric conditions that lead to ice accretion on aircraft. Especially supercooled large droplet (SLD) conditions, i.e. icing conditions that contain droplets with diameters larger than 100 μm, need to be detected and discriminated from other icing conditions. The combination of two instruments was investigated for this task:

- The Nevzorov probe, an established instrument for the measurement of liquid water content (LWC) and total water content (TWC).

- The Backscatter Cloud Probe with Polarization Detection (BCPD), a new and lightweight instrument that can be integrated into the fuselage of aircraft and thus causes no additional drag. The BCPD measures the size and shape of particles with diameters between 2 and 42 μm.

The Nevzorov probe usually carries two sensors, a cylindrical LWC sensor that is insensitive to glaciated particles and a TWC sensor with an inverted conical cavity for the collection of both liquid and glaciated particles. The classical TWC sensor has a diameter of 8 mm and is generally referred to as the «8 mm cone». In this work, a Nevzorov probe that carried an additional 12 mm TWC sensor was used (referred to as the «12 mm cone»). The sensor was designed with a great depth to retain SLDs. The accuracy and precision of the 12 mm cone for the measurement of small droplets and SLDs had not been analyzed prior to this thesis.

At first, individual evaluations of the two instruments were performed. For the Nevzorov probe, this thesis focused on the new 12 mm cone. More specifically I investigated two main properties of the cone, the collision efficiency, which determines what percentage of the liquid water upstream of the sensor sample area actually impacts on the sensor (see Section 3.1.1), and the capture efficiency for SLDs (i.e. to what extent the liquid water contained in the SLDs is retained by the sensor). Measurements of the Nevzorov probe that were obtained in the scope of three different icing wind tunnel (IWT) campaigns contributed to the study. A wide

149

range of icing conditions, comprising unimodal small droplet spray conditions as well as unimodal and bimodal freezing drizzle and freezing rain conditions were simulated in the IWTs (Section 4.3.1). Planning, testing and data evaluation of these campaigns constituted a large portion of the work presented in this thesis. The following findings were obtained:

- The collision efficiency of the 12 mm cone is significantly smaller than that of the 8 mm cone and the LWC sensor. This is to be expected due to the larger size of the 12 mm cone and the larger resulting drag forces in its vicinity (Section 3.1.1). LWC values measured by the 12 mm cone are consequently lower than those from the LWC sensor and the 8 mm cone of the Nevzorov probe in conditions where predominantly small cloud droplets are present (Section 4.3.2). The reduced collision efficiency requires characterization and correction.

- This thesis experimentally derived a collision efficiency curve for the 12 mm cone. Therefore, for the first time, the reduced collision efficiency of the 12 mm cone can be compensated. The curve was determined through a comparison to the measurements of the well-characterized LWC sensor and the 8 mm cone (Section 4.3.2). The correction that needs to be applied affects the uncertainty in the LWC estimated from the 12 mm cone, it can attain up to ±29% at droplet diameters of 12 µm. Thus, it is not recommended to rely solely on measurements of the 12 mm cone in conditions with high concentrations of droplets with small diameters (Section 4.3.4). The uncertainty decreases to ±14% at droplet diameters of 22 µm.

- The capture efficiency of SLDs of the 12 mm cone is estimated to be on the same order as that of the 8 mm cone. No evidence of droplet splashing on impact with the cone or re-entrainment of liquid water into the airflow was found throughout the entire size spectrum of SLDs from 100-2500 µm (Section 4.3.3).

- Especially for bimodal size distributions, it is important to apply collision efficiencies based on the entire droplet size distribution (DSD) and not only on the median volume diameter (MVD). In extreme cases, using collision efficiencies based solely on the MVD can lead to errors as large as ±30%. It is therefore discussed and recommended in this thesis to always complement the Nevzorov probe LWC and TWC measurements with measurements of the full DSD (Section 4.3.4).

- Sensor head-specific biases of the Nevzorov probe have been detected and characterized in this thesis. The biases were detected after analyzing a series of test conditions that were measured with two different sensor heads. The bias was only observed for the 8 mm cone and was on the order of 9%. The likely reason for the bias is the imperfect insulation of the heating wires of the probe towards the outside of the cone. Additional cooling of the outside of the cone (by ice accretion or liquid water streaming along the side) therefore

increases the power consumption of the sensor. The observed bias can be explained through differences in the insulation of the individual sensors. The sensors are hand-made and the existence of such manufacturing differences is plausible (Section 4.3.5).

Research question I investigated the following: «How well is the Nevzorov 12 mm total water content collector cone suited for the measurement of SLD conditions and how does it compare to other LWC instruments?» I can conclude that the 12 mm cone provides a high capture efficiency that is likely close to 100%, hence it is excellent for measuring SLD. The low collision efficiency of the 12 mm cone can be compensated with the correction derived in this thesis. This is recommended once the center of the small droplet mode of the DSD exceeds 22 µm (Section 4.3.6). For SLD conditions where the small droplet mode is located at smaller diameters, the 12 mm cone can also be used, but its measurements should be verified with those of the 8 mm cone of the Nevzorov probe. Due to its large capture efficiency, the 12 mm cone is preferable to the WCM-2000 sensor (see Table 3.1) for the measurement of SLD conditions. Compared to the 8 mm cone, the 12 mm cone does not provide a significant benefit, because the capture efficiencies of the two cones are similar but the measurements of small droplets with the 12 mm cone are more uncertain.

For the BCPD, at first, the size dependence of the scattering cross section and the polarization ratio for water droplets were determined with the help of a Mie-Scattering software, which needed to be modified for that purpose to account for the asymmetry of the scattering problem. Subsequently, the BCPD was integrated, operated and tested in one wind tunnel and on two research aircraft for flight campaigns in Svalbard and France. For all these campaigns comparisons to measurements from the well-characterized and established Cloud Droplet Probe (CDP) were performed. The following can be stated:

- The scattering cross section of the BCPD contains few Mie-ambiguities. The angular range under which the BCPD collects light is favorable, as the size resolution for small droplets is high. If the laser irradiance was perfectly equal across the entire sample area, the droplet diameter could be unambiguously measured with an accuracy of ±1 µm. This is an advantage of the geometry of the BCPD, especially in comparison to classical forward scattering probes like the CDP and the Cloud Aerosol Spectrometer (Section 3.2.4).

- In IWTs, the sizing performance for droplets of the BCPD is consistent with that of the CDP. The IWT measurements showed that MVDs from the BCPD fall within ±10% of those of the CDP (Section 4.4.1).

- The BCPD number concentrations measured in the IWT amounted on average to 39% of the number concentrations measured by the CDP for the same test points. It was observed that the discrepancy in number concentration extends across the entire size range of the BCPD and is not due to a lower sensitivity of the BCPD for one specific droplet size (Section 4.4.1). Several

possible causes for the discrepancy, such as insufficient wind tunnel uniformity, were investigated and could be ruled out. One of the remaining possibilities is that an error exists in the calibration of the sample area. The sample area was calibrated by the manufacturer of the BCPD and could not be independently verified in the scope of this thesis.

- The sample area of the BCPD, which defines the sample volume, is size dependent (Section 3.2.4). Small droplets that pass close to the edge of the sample area fall below the detection threshold and are not sized at all. If not corrected, this leads to undersizing and undercounting effects. A correction of the undersizing and undercounting effect was developed in this thesis based on the Smooth-Twomey routine [1–3]. It was shown that the application of the algorithm leads to an improved agreement of the number concentrations. For the IWT measurements, the number concentration of the BCPD now amounts on average to 50% of that of the CDP. However, the agreement between CDP and BCPD MVDs worsens, with MVDs of the BCPD now exceeding those of the CDP by 12-22% (Section 4.4.2).

- Particle size and number concentration measurements of the BCPD were compared to those of the CDP for two flight campaigns. The comparisons showed that MVDs from the BCPD are generally higher than those of the CDP in the range from approximately 10-20 μm. Only data from one flight campaign contained cloud encounters where droplet diameters significantly exceeded 20 μm. The data showed that BCPD MVDs hardly increased once CDP MVDs exceeded approximately 20 μm. Likely, inertial separation occurs near the aircraft fuselage and large particles are deflected such that they do not pass the sample volume of the BCPD, which is just 3 cm from the aircraft fuselage (Sections 5.5.1 and 6.4.1). A recommendation from this thesis is to install the instrument in regions with less influence of the boundary layer of the aircraft.

- The polarization ratio of the light that is backscattered from particles towards the BCPD was used to obtain indications on the particle shape, which in turn allows to draw conclusions on the particle phase (Section 5.5.2). The polarization ratio does not provide an unambiguous result whether a specific particle is liquid or glaciated (with some exceptions, see Appendix A.7), but the number of liquid and glaciated particles can be obtained from a probabilistic approach that was developed in this thesis (Section 5.5.2). The approach is advantageous because it does not classify a fraction of the glaciated particles as liquid, as is the case for techniques that use a separation line [4–6] for the distinction.

- Shattering of ice crystals occurs on the fuselage of the aircraft. High number concentrations of ice particles observed by the BCPD are likely to be artifacts from such shattering events. The shattering takes place many meters ahead of the BCPD sample volume and cannot be detected through an analysis of inter-particle times (Section 5.5.3).

Research question II investigated the following: «How can measurements of the Backscatter Cloud Probe with Polarization Detection be used to obtain an accurate assessment of the cloud particle size and phase?» I can conclude that in the current setup, the BCPD can be used to distinguish ice, mixed-phase and purely liquid clouds, hence it is appropriate to assess cloud particle phase. Even though it is theoretically well suited for accurate measurements of particle size, the proximity of its sampling area to the aircraft fuselage means that its measurements are within the boundary layer and are also affected by artifacts from ice particle shattering. The particle size distributions and number concentrations measured by the BCPD are therefore not representative of the cloud.

Finally, research question III investigated: «Can the combined data from the Nevzorov probe and the Backscatter Cloud Probe with Polarization Detection be used to discriminate Appendix O icing conditions from other atmospheric icing conditions?» Appendix O icing conditions are the subset of SLD conditions that is expected to be encountered in the atmosphere (see Section 2.4).

An algorithm was conceived that distinguishes atmospheric conditions based on the measurements of the Nevzorov probe and the BCPD. It differentiates between warm, glaciated, mixed-phased and purely supercooled clouds. Within the category of purely supercooled clouds it further differentiates between clouds that contain only small droplets and Appendix O conditions. The icing risk is derived from the output of the algorithm.

The BCPD and the Nevzorov probe do not deliver direct measurements of SLDs, instead, the presence of SLDs is indirectly deduced. From the individual investigation of the instruments it was known that the 8 mm cone and the 12 mm cone collect SLD efficiently, while, due to splashing of SLDs, the Nevzorov LWC sensor collects only a portion of the liquid water. In the presence of a significant number of SLDs, this results in LWC measurements that are lower than those of the Nevzorov TWC sensors. The ratio between the LWC sensor measurement and the measurement of the 8 mm cone can be used as an indication for the presence of large droplets. A second method involves the analysis of the standard deviations of the Nevzorov 8 mm and 12 mm cone sensors. Large droplets can be detected because they produce larger deviations in the sensor's signal (see Sections 4.3.7 and 6.4.2).

Both methods yield indications about the presence of SLDs, but without providing exact size. Both methods are also ambiguous to observations of ice crystals impacting the sensors. Here, the BCPD data proves valuable, as it contains information on the presence of ice crystals. Appendix O conditions are only detected if the above-mentioned changes in the sensor ratios occur in the absence of ice crystals.

The approach was verified for two flights, one from the HALO-AC³ campaign, which sampled predominantly mixed-phase conditions, and another one from the SENS4ICE campaign, which encountered Appendix O conditions. From the measurement of the HALO-AC³ campaign, the algorithm could be configured in such a way that no false alarms for Appendix O occur in mixed-phase or glaciated conditions. The detection of Appendix O during SENS4ICE works for clouds that

contain a significant amount of SLDs, do not contain ice crystals, and exhibit low spatial variability, i.e. the conditions that are sampled remain approximately constant (see Section 6.4.3).

The limiting factor of the Appendix O detection capabilities of the algorithm is the relatively small size of the sample volume of the BCPD. Cases may arise where no ice particles are detected, even though ice particles were present in low number concentrations. In such cases, a false alarm may be raised. Vice versa, Appendix O conditions that are intertwined with mixed-phase clouds can cause missed alarms because it is assumed that the changes in the measurements of the Nevzorov probe are due to ice crystals. This was observed on some occasions during the SENS4ICE flight that was analyzed (Section 6.4.3).

Overall, this thesis demonstrated various pathways for the retrieval of microphysical parameters from the Nevzorov probe and the BCPD. Furthermore, it was explained how the combination of the two sensors can be employed to detect SLD icing conditions. The current set-up is not applicable right away for operational use, this would require design changes in the instruments. However, it forms the basis for further developments in this direction that are discussed in the subsequent outlook.

REFERENCES

[1] S. Twomey, *Introduction to the mathematics of inversion in remote sensing and indirect measurement*, Amsterdam, Elsevier Scientific Publishing Co. (Developments in Geomathematics , 253 (1977).

[2] G. R. Markowski, *Improving Twomey's algorithm for inversion of aerosol measurement data*, Aerosol science and technology **7**, 127 (1987).

[3] K. Beswick, D. Baumgardner, M. Gallagher, A. Volz-Thomas, P. Nedelec, K.-Y. Wang, and S. Lance, *The backscatter cloud probe - a compact low-profile autonomous optical spectrometer*, Atmospheric Measurement Techniques **7**, 1443 (2014).

[4] J. Meyer, *Ice crystal measurements with the new particle spectrometer NIXE-CAPS*, (2011).

[5] E. Järvinen, M. Schnaiter, G. Mioche, O. Jourdan, V. N. Shcherbakov, A. Costa, A. Afchine, M. Krämer, F. Heidelberg, T. Jurkat, C. Voigt, H. Schlager, L. Nichman, M. Gallagher, E. Hirst, C. Schmitt, A. Bansemer, A. Heymsfield, P. Lawson, U. Tricoli, K. Pfeilsticker, P. Vochezer, O. Möhler, and T. Leisner, *Quasi-Spherical Ice in Convective Clouds*, Journal of the Atmospheric Sciences **73**, 3885 (2016).

[6] A. Costa, J. Meyer, A. Afchine, A. Luebke, G. Günther, J. R. Dorsey, M. W. Gallagher, A. Ehrlich, M. Wendisch, D. Baumgardner, H. Wex, and M. Krämer, *Classification of Arctic, midlatitude and tropical clouds in the mixed-phase temperature regime*, Atmospheric Chemistry and Physics **17**, 12219 (2017).

8

OUTLOOK

Supercooled liquid water icing will remain an active topic of research in the future, but the challenges and the corresponding solutions will evolve. In this last chapter, I first provide an overview of the topics and challenges that still exist or currently emerge in the field of atmospheric icing. Subsequently, I comment on advances in measurement technology that are required to address these challenges. In the last section, unrelated to the two topics discussed before, I explain possible uses for the data from the SENS4ICE flight campaigns.

8.1. EMERGING TOPICS IN ICING RESEARCH

There are many emerging topics in the field of icing research. This section provides an overview of four important topics which are currently a focus of the icing community and which are likely to be the subject of future coordinated research activities.

8.1.1. CERTIFICATION FOR APPENDIX O CONDITIONS

The SENS4ICE project has now been concluded but significant tasks and challenges still exist before sensors for the detection and discrimination of Appendix O conditions can be integrated on commercial aircraft. At the beginning of this thesis, several options for dealing with Appendix O conditions were outlined. The option to detect (with sensors such as those developed within SENS4ICE) and exit Appendix O conditions requires to be able to operate in a portion of Appendix O. Here, one of the remaining challenges comes into play. The time that the aircraft can operate in Appendix O is a function of the droplet size distribution (DSD) and the liquid water content (LWC). These two parameters result in an ice accretion of a certain shape and thickness that influences aerodynamics. The exact ice accretion that results from a given droplet size distribution is very difficult to predict, numerical models usually exhibit large variations in the calculated ice accretions and icing wind tunnel (IWT) tests in Appendix O conditions carry large uncertainties (as mentioned

155

in Section 2.5). Therefore, flight tests would be required that assess the sensor and aircraft performance for a large set of test points within Appendix O. Such flight tests would be extremely expensive and are therefore shunned by aircraft manufacturers. Currently, most aircraft manufacturers attempt to certify their aircraft for Appendix O through similarity analysis to existing aircraft models. It therefore remains to be seen how Appendix O certifications will be performed for completely new aircraft models that differ significantly from existing designs. IWTs can likely not be used in the near future for certification. The remaining uncertainties and the difficulties in producing realistic supercooled large droplet (SLD) conditions are so fundamental that they require completely new IWT designs, like vertical wind tunnels.

8.1.2. UNMANNED AERIAL VEHICLE OPERATIONS IN ICING CONDITIONS

Not only for new commercial aircraft but also for unmanned aerial vehicles (UAVs) new icing certifications will be required. The icing on UAVs differs from that of manned aircraft. Often, UAVs fly slower than commercial aircraft and at very different altitudes [1, 2]. Due to their slow speed, they may be more susceptible to freezing precipitation. Also, even a thin ice layer represents a significant weight penalty for small, lightweight UAVs.

The installation of an ice protection system is often not feasible for UAVs due to the large weight and high power consumption of such a system. However, a detect and exit approach, similar to what is foreseen in the Appendix O regulations, could be feasible to improve the safety of drone operations at subfreezing temperatures. In Section 8.2.1, an overview of the potential of hotwire sensors for a detect and exit approach and the corresponding design considerations for such ice detection sensors are discussed.

8.1.3. WIND TURBINE ICING

The topic of icing is also of great interest to the wind energy sector. The similarity of wind turbine blades and aircraft wings means that wind turbines face similar problems with icing as aircraft. Surface roughening due to ice accretion reduces the lift of the turbine blade and increases the drag [3]. Very slight ice accretion on the blades can already result in power losses of 20% [4, 5]. Fatigue due to an imbalance of ice accretion on the blades reduces the turbine lifetime [3]. Furthermore, to avoid danger to people and property, wind turbines often need to be stopped if icing conditions are present [6]. In regions that experience frequent icing, losses can amount to more than 10% of the annual energy production [7]. Sensors that can accurately detect if and where ice accretion is present on wind turbine blades could reduce deicing power consumption and allow extended operating times, both of which in turn reduce operating costs and increase the availability of green energy.

8.1.4. AIRCRAFT OBSERVATIONS OF METEOROLOGICAL PARAMETERS

Lastly, already now, aircraft observations of meteorological parameters such as temperature, wind speed and turbulence contribute significantly to weather pre-

diction models and to flight operations planning [8]. Currently, most of the weather prediction models only predict the mass mixing ratio of liquid water and not the particle number concentration [9], hence yielding no information on the average particle size. In recent years, attempts have been made to use double-moment schemes that predict both the mass-mixing ratio and the number concentration [9, 10]. Predicting the mass-mixing ratio and the number concentration implies that an average droplet size can be derived. If commercial aircraft carried sensors that record cloud droplet size and number concentration their data could validate predictions from double moment schemes. If the measurement data were available in real-time they could even be used as initial values to improve the predictive skill of the scheme. This would benefit short-term forecasts, especially in regions around airfields, where accurate weather forecasts are of large importance.

8.2. Measurement technology

I proceed to discuss possible design alterations and improvements that can be made to adapt existing sensors for the future applications outlined in the section before.

8.2.1. Suggestions for future hotwire sensors

Many of the properties and issues of the Nevzorov probe that were investigated in this thesis apply to the entire category of hotwire probes. I therefore provide suggestions that concern design considerations for hotwire probes in general. The ideal hot-wire probe would have the following properties:

1. High collision efficiency.

2. High collection efficiency.

3. Low convective heat losses.

4. High power, to instantly evaporate impinging droplets.

5. Large sample area.

Some of these properties directly contradict each other. As was discussed in Section 3.1.1, a high collision efficiency requires a small sensor geometry, while a large collection efficiency is usually associated with a large and deep structure, like the cavities of the Nevzorov TWC cones. Similarly, the requirement for low convective heat losses conflicts with the need for high power.

Hotwire sensors on commercial aircraft

The design considerations have to be viewed in light of the planned application of the probe. For commercial aircraft low drag is one of the most important factors, consequently, a sensor like the Nevzorov probe is not feasible. LWC measurements to assess the severity of icing conditions could be made with hot-wire sensors that are flush-mounted (or almost flush-mounted [11]) with the aircraft

skin. SLDs could be detected by mounting these hotwire sensors at strategic locations on the aircraft, as suggested by AeroTex [11]. While such sensors can provide indications on the LWC, their readings likely represent significant underestimates when splashing of droplets occurs, as is the case in SLD conditions.

On several new aircraft, electro-thermal ice protection systems are used [12]. These systems use heaters embedded into the wing. If the power consumption of the heaters is measured, the system can function as one large hotwire sensor. Indications on the DSD could be derived from measuring the power consumption for specific sections of the ice protection system, e.g. for the position directly at the leading edge and for positions slightly above and below the leading edge. A hotwire sensor that is part of the ice protection system of aircraft would consume little additional power, have high collision and collection efficiencies (at least at certain locations of the airfoil) and a large sample area.

In general, it would be beneficial to have sensors that measure the LWC, and not only detect ice accretion, on commercial aircraft. From the measured LWC it would be possible to determine the exact power that is required to melt or evaporate ice accretion and only provide the necessary amount to the ice protection system. This would reduce the energy consumption of the aircraft and likely also increase the lifetime of the heating elements.

HOTWIRE SENSORS ON UNMANNED AERIAL VEHICLES

It is difficult to give general recommendations for hotwire sensors for UAVs, due to the large variety of vehicles that exist. This section focuses on rotary-wing UAVs. Rotary-wing UAVs usually fly at airspeeds below 20 m s^{-1}. For battery-powered rotary-wing UAVs low power consumption is one of the most important properties. Based on existing hot-wire sensors (e.g. [11, 13]) it is reasonable to assume that sensors with a power consumption below 1W (at typical airspeeds) can be manufactured. This is likely a feasible value for most drones that are heavier than 1 kg and that carry batteries that store a few 100 kJ[14]. For rotary-wing UAVs the direction of motion varies, hence multiple sensors are necessary for the detection of icing conditions. To keep power consumption low, reference sensors should be avoided, instead, the convective heat losses can be estimated based on a database of measurements in dry air. Unlike for the database that was used for the Nevzorov probe (see Section 5.4.1), where the convective heat loss term was assumed to depend only on airspeed, pressure and temperature (horizontal flight was assumed), the convective heat loss term for rotary-wing UAVs depends on airspeed components in all three directions and on yaw, roll and pitch angles additionally to the pressure and the temperature. Calibration of the convective heat losses would therefore be complex.

While hot-wire sensors on rotary-wing UAVs can serve for the detection of icing, the accurate measurement of the LWC is likely not possible, because of the following reasons. First of all, due to the low airspeed, the collision efficiency of droplets with the hotwire sensors will be relatively low (see Section 3.1.1). Secondly, the low airspeed means that the convective heat losses dominate over heat losses due to evaporation and heating of impinging droplets (see Section 4.3.6).

Hence, the measurement of LWC will be affected by large uncertainties, also due to the difficulty of computing accurate estimates of the convective heat losses. If campaigns for the characterization of icing clouds are to be performed with hotwire sensors mounted on UAVs, fixed wing UAVs should be preferred over rotary-wing UAVs.

HOTWIRE SENSORS FOR RESEARCH AIRCRAFT

For the precise measurement of cloud LWC and cloud TWC hotwire probes remain one of only a few options. Existing hot-wire probes show different solutions to the design trade-offs mentioned in Section 8.2.1. The TWC sensor of Science Engineering Associates's Ice Crystal Detector (ICD) probe for instance is integrated into a strut with larger dimensions (see Table 3.1). The location of the sensor at the center of the strut leads to a collision efficiency close to 100% [15] and the depth of the sensor ensures a large capture efficiency, though, from preliminary data evaluated from the North American SENS4ICE campaign, there are indications that not all ice crystals are entirely collected by the sensor. The depth of the sensor also decreases convective heat losses. Similarly to the ICD, the design of the Nevzorov TWC cones is also advantageous regarding convective heat losses (see Section 4.3.6). The shape of the sensor however results in a low collision efficiency, especially in the case of the 12 mm cone (see Section 4.3.2). Using the positive properties of both sensor geometries, a combination of the ICD and the Nevzorov probe cones could be envisaged that integrates the cones into an airfoil shape. The sensor head could be made rotatable but should feature springs that dampen oscillatory motions.

For the evaluation of future flight and IWT campaigns, it would be beneficial to agree on one hotwire probe as an industry and research standard, which should be universally used and evaluated with standardized routines. As shown in this thesis, the composition of mixed-phase clouds changes significantly when collision efficiencies are applied to the Nevzorov probe measurements. Agreement on a standard sensor and evaluation strategy would ensure comparability between the results of individual flight campaigns and greatly reduce the workload for the data evaluation.

8

8.2.2. SUGGESTIONS FOR FUTURE BACKSCATTER PROBES

Backscatter probes are in general more complex and heavier than hotwire sensors due to the laser and the optical components required. Their larger weight makes them unsuitable for the small rotary-wing UAVs for which the applications of hotwire sensors were discussed in the previous section. On commercial aircraft, optical sensors like the BCPD can serve to provide real-time meteorological data [16, 17], as discussed in Section 8.1. Even though the BCPD covers only the size spectrum of small cloud droplets, this size range is very important to understand the evolution of cloud systems.

Future optical sensors for commercial aircraft should be similar in geometry to the BCPD, to make use of the few Mie-ambiguities and the low drag, but the sample area needs to lie further away from the aircraft fuselage to avoid effects from the shattering of ice crystals and the aircraft boundary layer. An increase in

the size range of a scattering probe like the BCPD that allows it to detect SLDs is not achievable without greatly increasing coincidence effects and thus reducing accuracy (see Section 3.2.3). A dedicated instrument is needed for the detection of SLDs and ice particles. A pulsed lidar that detects the backscatter from large droplets and ice crystals is currently being developed by Collins Aerospace [18] and appears to be essentially the only viable optical method to detect larger cloud particles in a setup that does not have components that extend into the airflow and cause significant additional drag. A similar setup is currently also being developed by Honeywell [19]. No results from these sensors have been published to date.

Of course, prior flight tests that compare these new sensors to existing underwing probes are required. Ideally, such an instrument combination would be paired with a hotwire sensor for the measurement of LWC and TWC. All of these sensors together would provide an excellent measurement suite for every type of cloud. If this sensor combination was standard equipment on commercial aircraft it would allow to obtain an enormous number of measurements of clouds that can serve as the desired inputs to the double moment numerical weather prediction schemes mentioned in Section 8.1. Furthermore, while data collected during dedicated flight campaigns are only representative of the season and the weather situation during which they were recorded, the regularity of aircraft observations means that a dataset from commercial aircraft is truly representative of the regions where it is collected [16].

The suggestions presented in this section are essentially an appeal for an upgrade of the IAGOS package. The presently used package has greatly contributed to research [20–23], but needs for upgrades and improvements have also been identified [17]. These would greatly help in evaluating the influence of clouds on the radiation budget of the earth and the effects that occur due to climate change, one of the main open questions of this era.

8.3. Measurement data from the European SENS4ICE campaign

A large data set of over 50 flight hours, more than 12 of which were flown in icing conditions, was collected during the European SENS4ICE flight campaign with the ATR-42 aircraft of the French facility for airborne research (SAFIRE) [24]. Besides the sensors that were developed within the SENS4ICE program, the aircraft carried a large suite of scientific airborne instrumentation. The instrumentation was not limited to LWC and particle size measurements but included also a Ultra-High Sensitivity Aerosol Spectrometer (UHSAS) [25] for the measurement of aerosols and a Water Vapor Sensing System (WVSS-II) [26] for the measurement of atmospheric water vapor. A complete list of the instrumentation can be found in Table 8.1.

The data from the European campaign are special because they were collected in the vicinity of Toulouse, France during April. The timing of the campaign meant that, due to relatively high temperatures at ground level, icing conditions were expected and encountered at much higher altitudes than during campaigns performed in January or February [27, 28]. The icing conditions were often associated

Instrument	Operator	Parameters measured
CDP	DLR	Particle size (2-50 µm diameter)
CDP	SAFIRE	Particle size (2-50 µm diameter)
BCPD	DLR	Particle size and shape (2-42 µm diameter)
CIP	DLR	Particle size and shape (15 - 960 µm diameter, grayscale)
CIP	SAFIRE	Particle size and shape (15 - 960 µm diameter, monoscale)
PIP	DLR	Particle size and shape (100 - 6400 µm diameter, monoscale)
HSI	DLR	Particle size and shape (20 - 2000 µm diameter)
UHSAS	SAFIRE	Particle size (0.06 - 1 µm diameter)
Nevzorov	DLR	LWC, TWC
Robust probe	SAFIRE	TWC
Gerber	SAFIRE	LWC
WVSS-II	SAFIRE	Water vapor mixing ratio

Table 8.1: Scientific instrumentation aboard the SAFIRE ATR-42 aircraft during the European SENS4ICE campaign.

with frontal systems.

The current Appendix O envelopes were established based on data from North America only, therefore the new SENS4ICE measurements from Europe can be used to verify that the Appendix O envelopes are also suitable for other geographic regions.

As mentioned already in Section 6.4, the evaluation of the reference measurements of the microphysical data from the campaign has started but is not yet complete. An in-house code of the German Aerospace Center (DLR) is used to classify the images of the Cloud Imaging Probe as small droplets (diameter smaller than 100 µm), SLDs or ice crystals [28–30]. The final product will contain separate particle size distributions for liquid and ice, provide information on the median volume diameter and the maximum diameter and indicate the presence of Appendix C and Appendix O conditions.

These reference data will be useful for several purposes. The accurate measurements allow the SENS4ICE sensor developers to validate their new technologies, in a similar way as was described for the combination of Nevzorov probe and BCPD in Section 6.4.3.

The radiative properties and lifetimes of purely supercooled, mixed-phase and glaciated clouds differ strongly [31, 32]. Some of the largest uncertainties in climate models are therefore associated with the description of the conversion from supercooled clouds to mixed-phase and glaciated clouds [33]. Studies that describe the glaciation process of a supercooled cloud (or the absence of a glaciation process) are therefore of large importance. The SENS4ICE data contains a wealth of measurements that can be used to study the persistence of supercooled clouds and their conversion to mixed-phase clouds.

One flight of the SENS4ICE campaign is especially well suited for such a study. During that flight, the aircraft tracked an incoming warm front in a Lagrangian pattern. Icing conditions in the same air mass were first sampled over the ocean and subsequently over the land (see Fig. 8.1). A comparison of the icing conditions

8

along the flight path is planned to understand the evolution of the particle size, particle number concentration and ice water content. The comparison shall also consider the aerosol concentrations below the cloud to draw conclusions on the influence of cloud condensation nuclei on the cloud structure.

Figure 8.1: Lagrangian pattern flown during a SENS4ICE research flight. On the day of the flight, a warm front moved from the Atlantic coast toward Toulouse. The flight pattern was chosen such that it approximately matched the speed of the warm front. The blue arrows indicate the flight direction of the aircraft. Map from OpenStreetMap.

The SENS4ICE data can also help to verify numerical weather prediction models. Over France, the AROME[1] model produces weather forecasts with a resolution of 2.5 km [34]. AROME is a single-moment scheme, but its high-resolution forecasts are extremely important to predict severe, local weather events, such as hailstorms and flash floods. The AROME model predicts microphysical parameters of clouds, such as the mass mixing ratios of water droplets, ice crystals, rain, graupel and snow. These mass mixing ratios can also be derived from the SENS4ICE data. Thus, a valuable comparison between the model and reality can be performed.

The icing forecast tool ADWICE of the German weather service (DWD) is another product that could benefit from the usage of the SENS4ICE data [35, 36]. A comparison of the HALO-(AC)³ research flight that was presented in this thesis to the predictions of the tool was already performed in Lucke *et al.* [37]. It was found that the majority of icing conditions were correctly forecast and that regions with higher LWC were associated with a higher predicted icing severity. On some occasions, ADWICE forecasted an icing risk in entirely glaciated clouds. This false alarm results from ADWICE being a «careful» algorithm that predicts an icing risk once the forecast relative humidity exceeds 85% [35]. Comparisons of SENS4ICE data to ADWICE can help the DWD to adjust the parameters that determine the

---

[1]AROME is an acronym for: Application of Research to Operations at Mesoscale

forecast of supercooled liquid water and thus improve the prediction of icing conditions. This in turn will allow aircraft operators to optimize their flight planning, thereby reducing the fuel consumption and the carbon dioxide emissions of the aircraft and increasing operational safety.

REFERENCES

[1] R. Hann, *Atmospheric ice accretions, aerodynamic icing penalties, and ice protection systems on unmanned aerial vehicles*, Ph.D. thesis, Norwegian University of Science and Technology (2020).

[2] R. Hann, A. Enache, M. C. Nielsen, B. N. Stovner, J. van Beeck, T. A. Johansen, and K. T. Borup, *Experimental Heat Loads for Electrothermal Anti-Icing and De-Icing on UAVs*, Aerospace **8**, 83 (2021).

[3] T. Wallenius and V. Lehtomäki, *Overview of cold climate wind energy: Challenges, solutions, and future needs*, Wiley Interdisciplinary Reviews: Energy and Environment **5**, 128 (2015).

[4] F. Lamraoui, G. Fortin, R. Benoit, J. Perron, and C. Masson, *Atmospheric icing impact on wind turbine production*, Cold Regions Science and Technology **100**, 36 (2014).

[5] J. Rong and N. Bose, *Power reduction from ice accretion on a horizontal axis wind turbine*, in *Proc. 12th British Wind Energy Association Conf*, pp. 77–86 (1990).

[6] S. Rastayesh, L. Long, J. D. Sørensen, and S. Thöns, *Risk assessment and value of action analysis for icing conditions of wind turbines close to highways*, Energies **12**, 2653 (2019).

[7] C. Ribeiro and T. Beckford, *Icing losses—what can we learn from production and meteorological data*, Proceedings of the Wind Europe Summit (2016).

[8] E. P. James, S. G. Benjamin, and B. D. Jamison, *Commercial-Aircraft-Based Observations for NWP: Global Coverage, Data Impacts, and COVID-19*, Journal of Applied Meteorology and Climatology **59**, 1809 (2020).

[9] P. R. Field, A. Hill, B. Shipway, K. Furtado, J. Wilkinson, A. Miltenberger, H. Gordon, D. P. Grosvenor, R. Stevens, and K. Van Weverberg, *Implementation of a double moment cloud microphysics scheme in the UK met office regional numerical weather prediction model*, Quarterly Journal of the Royal Meteorological Society **149**, 703 (2023).

[10] S. Muench and U. Lohmann, *Developing a Cloud Scheme With Prognostic Cloud Fraction and Two Moment Microphysics for ECHAM-HAM*, Journal of Advances in Modeling Earth Systems **12**, 10.1029/2019ms001824 (2020).

[11] I. Roberts, R. Gent, C. Hatch, and R. Moser, *Development of the Atmospheric Icing Patch (AIP) under the SENS4ICE Programme*, in *SAE Technical Paper Series*, ICE (SAE International, 2023).

8

[12] B. G. Falzon, P. Robinson, S. Frenz, and B. Gilbert, *Development and evaluation of a novel integrated anti-icing/de-icing technology for carbon fibre composite aerostructures using an electro-conductive textile*, Composites Part A: Applied Science and Manufacturing **68**, 323 (2015).

[13] Science Engineering Associates, *WCM-2000* (2016).

[14] J. Zhang, J. F. Campbell, D. C. Sweeney II, and A. C. Hupman, *Energy consumption models for delivery drones: A comparison and assessment*, Transportation Research Part D: Transport and Environment **90**, 102668 (2021).

[15] B. M. Esposito, W. D. Bachalo, D. Leroy, A. Schwarzenboeck, T. Jurkat, C. Voigt, and S. Bansmer, *Wind Tunnel Measurements of Simulated Glaciated Cloud Conditions to Evaluate Newly Developed 2D Imaging Probes*, in *SAE Technical Paper Series* (SAE International, 2019).

[16] A. Petzold, V. Thouret, C. Gerbig, A. Zahn, C. A. M. Brenninkmeijer, M. Gallagher, M. Hermann, M. Pontaud, H. Ziereis, D. Boulanger, J. Marshall, P. Nédélec, H. G. J. Smit, U. Friess, J.-M. Flaud, A. Wahner, J.-P. Cammas, A. Volz-Thomas, and I. TEAM, *Global-scale atmosphere monitoring by in-service aircraft – current achievements and future prospects of the European Research Infrastructure IAGOS*, Tellus B: Chemical and Physical Meteorology **67**, 10.3402/tellusb.v67.28452, https://doi.org/10.3402/tellusb.v67.28452 (2015).

[17] K. Beswick, D. Baumgardner, M. Gallagher, A. Volz-Thomas, P. Nedelec, K.-Y. Wang, and S. Lance, *The backscatter cloud probe - a compact low-profile autonomous optical spectrometer*, Atmospheric Measurement Techniques **7**, 1443 (2014).

[18] Collins Aerospace, http://https://www.collinsaerospace.com/, accessed: 2023-11-30.

[19] P. Badin, V. Hamada, and M. Wiebold, *Short Range Particulate*, https://www.sens4ice-project.eu/sites/sens4ice/files/media/2023-11/SENS4ICE_SAE_AC-9C_Honeywell_20231024.pdf, accessed: 2023-12-01 (2023).

[20] L. Hu, D. J. Jacob, X. Liu, Y. Zhang, L. Zhang, P. S. Kim, M. P. Sulprizio, and R. M. Yantosca, *Global budget of tropospheric ozone: Evaluating recent model advances with satellite (OMI), aircraft (IAGOS), and ozonesonde observations*, Atmospheric Environment **167**, 323 (2017).

[21] H. Petetin, B. Sauvage, M. Parrington, H. Clark, A. Fontaine, G. Athier, R. Blot, D. Boulanger, J.-M. Cousin, P. Nédélec, *et al.*, *The role of biomass burning as derived from the tropospheric CO vertical profiles measured by IAGOS aircraft in 2002–2017*, Atmospheric Chemistry and Physics **18**, 17277 (2018).

[22] K.-D. Gottschaldt, H. Schlager, R. Baumann, D. S. Cai, V. Eyring, P. Graf, V. Grewe, P. Jöckel, T. Jurkat-Witschas, C. Voigt, *et al.*, *Dynamics and composition*

8

of the Asian summer monsoon anticyclone, Atmospheric Chemistry and Physics **18**, 5655 (2018).

[23] J. Pletzer, D. Hauglustaine, Y. Cohen, P. Jöckel, and V. Grewe, *The climate impact of hydrogen-powered hypersonic transport*, Atmospheric Chemistry and Physics **22**, 14323 (2022).

[24] C. Schwarz, *SENS4ICE EU project preliminary results*, in *SAE Technical Paper Series* (SAE International, 2023).

[25] R. H. Moore, E. B. Wiggins, A. T. Ahern, S. Zimmerman, L. Montgomery, P. C. Jost, C. E. Robinson, L. D. Ziemba, E. L. Winstead, B. E. Anderson, C. A. Brock, M. D. Brown, G. Chen, E. C. Crosbie, H. Guo, J. L. Jimenez, C. E. Jordan, M. Lyu, B. A. Nault, N. E. Rothfuss, K. J. Sanchez, M. Schueneman, T. J. Shingler, M. A. Shook, K. L. Thornhill, N. L. Wagner, and J. Wang, *Sizing response of the Ultra-High Sensitivity Aerosol Spectrometer (UHSAS) and Laser Aerosol Spectrometer (LAS) to changes in submicron aerosol composition and refractive index*, Atmospheric Measurement Techniques **14**, 4517 (2021).

[26] A. K. Vance, S. J. Abel, R. J. Cotton, and A. M. Woolley, *Performance of WVSS-II hygrometers on the FAAM research aircraft*, Atmospheric Measurement Techniques **8**, 1617 (2015).

[27] Tina Jurkat-Witschas and Johannes Lucke and Carsten Schwarz and Christoph Deiler and Falk Sachs and Simon Kirschler and Deniz Menekay and Christiane Voigt and Ben Bernstein and Olivier Jaron and Frank Kalinka and Alessandra Zollo and Lyle Lilie and Johanna Mayer and Christian Page and Benoit Vié and Aurelien Bourdon and Rogerio Pereira Lima and Luiz Vieira, *Overview of Cloud Microphysical Measurements during the SENS4ICE Airborne Test Campaigns: Contrasting Icing Frequencies from Climatological Data to First Results from Airborne Observations*, in *SAE Technical Paper Series* (SAE International, 2023).

[28] J. Lucke, A. L. Zollo, B. Bernstein, and T. Jurkat-Witschas, *SENS4ICE deliverable D4.3: Final report on airborne demonstration and atmospheric characterization*, Tech. Rep. (2024).

[29] S. Kirschler, *Effekte von Aerosol und Dynamik auf die Eigenschaften ozeanischer Wolken im Nordwestatlantik*, Ph.D. thesis, Johannes Gutenberg-Universität in Mainz (2023).

[30] E. De La Torre Castro, T. Jurkat-Witschas, A. Afchine, V. Grewe, V. Hahn, S. Kirschler, M. Krämer, J. Lucke, N. Spelten, H. Wernli, M. Zöger, and C. Voigt, *Differences in microphysical properties of cirrus at high and mid-latitudes*, Atmospheric Chemistry and Physics **23**, 13167 (2023).

[31] A. Gettelman, C. G. Bardeen, C. S. McCluskey, E. Järvinen, J. Stith, C. Bretherton, G. McFarquhar, C. Twohy, J. D'Alessandro, and W. Wu, *Simulating Observations of Southern Ocean Clouds and Implications for Climate*, Journal of Geophysical Research: Atmospheres **125**, 10.1029/2020jd032619 (2020).

8

[32] G. V. Cesana, T. Khadir, H. Chepfer, and M. Chiriaco, *Southern Ocean Solar Reflection Biases in CMIP6 Models Linked to Cloud Phase and Vertical Structure Representations*, Geophysical Research Letters **49**, 10.1029/2022gl099777 (2022).

[33] Y. Tsushima, S. Emori, T. Ogura, M. Kimoto, M. J. Webb, K. D. Williams, M. A. Ringer, B. J. Soden, B. Li, and N. Andronova, *Importance of the mixed-phase cloud distribution in the control climate for assessing the response of clouds to carbon dioxide increase: a multi-model study*, Climate Dynamics **27**, 113 (2006).

[34] Y. Seity, P. Brousseau, S. Malardel, G. Hello, P. Bénard, F. Bouttier, C. Lac, and V. Masson, *The AROME-France Convective-Scale Operational Model*, Monthly Weather Review **139**, 976 (2011).

[35] A. Tafferner, T. Hauf, C. Leifeld, T. Hafner, H. Leykauf, and U. Voigt, *ADWICE: Advanced Diagnosis and Warning System for Aircraft Icing Environments*, Weather and forecasting **18**, 184 (2003).

[36] F. Kalinka, K. Roloff, J. Tendel, and T. Hauf, *The In-flight icing warning system ADWICE for European airspace - Current structure, recent improvements and verification results*, Meteorologische Zeitschrift 26 (2017), Nr. 4 **26**, 441 (2017).

[37] J. R. Lucke, T. Jurkat-Witschas, D. Baumgardner, F. Kalinka, M. Moser, E. De La Torre Castro, and C. Voigt, *Characterization of Atmospheric Icing Conditions during the HALO-(AC)³ Campaign with the Nevzorov Probe and the Backscatter Cloud Probe with Polarization Detection*, in *SAE Technical Paper Series* (SAE International, 2023).

8

ACKNOWLEDGEMENTS

So this is it! Dear reader, you have arrived at the acknowledgments section, which free of any scientific content is going to recall these past years and express due thanks to everyone who supported me. I first of all want to thank my supervisor Tina, who was available for my questions basically all the time, everywhere, be it from the car or with screaming kids in the background. You provided great guidance and often asked the critical questions that I needed to improve my work! I want to thank my promotor Volker, for giving me the opportunity to pursue my PhD at TU Delft, for always swiftly taking care of all organizational matters that arose, and for his very valuable feedback that greatly improved the content, structure, and clarity of my thesis. Many thanks also to my second promotor and head of department at DLR, Christiane, for giving me the opportunity to work on my PhD at DLR, for ensuring that DLR IPA was part of the SENS4ICE project and by this making all the wonderful wind tunnel and flight campaigns happening. Thank you also for all the comments and input to my work.

Completing my PhD would first of all been impossible and secondly not nearly as memorable and joyful without my colleagues at DLR. I really appreciate all the scientific discussions we had, as well as all the events we did together. Therefore, many thanks to Dennis, for helping me work through tough Maths and for many game nights and pizza at his place. Many thanks to Manu, for spending days and hours organizing the AC^3 campaign, for taking superb photos during the campaign, and for spontaneous ski tours in the mountains, boat trips on the Ammersee and our ice hockey games. Thanks to Simon, for his efforts in creating a common base of code used for our instrument evaluation, for his support during the European SENS4ICE campaign, and for proofreading part of my thesis. Further thanks to Elena for all her help with evaluating the DMT grayscale probes and for her comments on my thesis, as well as to Johanna for keeping our paper discussions and Science seminars running, and for supporting the SENS4ICE campaign. Raphael, thank you very much for being part of the measurement campaign in Braunschweig and helping me obtain the measurements that were so valuable for my thesis. My time at DLR would have been much less structured if Tiziana hadn't ensured that 1) the laboratory was organized, 2) there was a coffee break at 3 pm, 3) lunch was at 11:30 sharp. I will always warmly remember our Chinese New Year's parties, thanks a lot to Ziming and Gregor for organizing them. Thanks to Romy and Valerian for carrying out the measurements at RTA that I used in my thesis and for being wonderful colleagues! Many thanks to Deniz, for being a great Master's student and photographer, for all the support in the SENS4ICE campaign, including helpful suggestions on the flight path («circle over Paris») and for all the amazing trips we did in France! Thank you to Natalie for taking care of so many organizational matters in such a cheerful way. I am furthermore grateful to all the

other colleagues from DLR and also Universität Mainz who provided their input to my work during many seminars and discussion rounds.

Amane, I believe us meeting during the SAE conference was the biggest luck of my entire PhD. Thank you for caring so much about me and for supporting me when I needed it. You are the person I have always been looking for and you for make my life so wonderful. 愛してるよ.

I would not have arrived where I am now without the support of my family, on which I could always count. To my siblings: You are a great source of joy in my life, always inspiring me with new ideas and funny stories. I warmly remember all the time we spent together, also during our home-office month during COVID. To my parents: You raised me in a way that taught me to view subjects from many different angles. You challenged me when I believed some things were too difficult and you supported me to help me reach my goals, all the time still making me feel loved. Thank you!

8

A

SUPPORTING INFORMATION

A.1. TEST POINTS FOR WIND TUNNEL MEASUREMENTS

Table A.1 shows all the test points used for the investigation of the Nevzorov probe properties and the tunnel speed, temperature, liquid water content (LWC) and median volume diameter (MVD) settings.

Collins IWT					Rail Tec Arsenal					BIWT				
Test point	TAS [ms^{-1}]	SAT [°C]	LWC [gm^{-3}]	MVD [μm]	Test point	TAS [ms^{-1}]	SAT [°C]	LWC [gm^{-3}]	MVD [μm]	Test point	TAS [ms^{-1}]	SAT [°C]	LWC [gm^{-3}]	MVD [μm]
Small droplet spray					Small droplet spray					Small droplet spray				
C1	40	-20	0.30	12	LWC29[*]	60	5	0.43	15	406	40	-10	0.27	22
C10	40	-20	1.50	18	LWC28[*]	60	5	0.43	20	416	40	-10	0.64	29
C2	40	-10	0.42	15	LWC27[*]	60	5	0.43	40	405	40	-10	0.18	34
C12	40	-10	0.42	25	LWC26[*]	60	5	0.44	50	409	40	-5	0.61	21
C3	40	0	0.54	18						410	40	-5	0.55	26
C11	40	0	2.50	16						419	40	-5	0.80	30
C5	67	-20	0.25	14						418	40	0	0.82	26
C14	67	-20	0.80	27						417	40	0	0.81	32
C6	67	-10	0.42	15										
C15	67	-10	1.40	19										
C19	67	-10	1.10	42										
C29	67	-10	1.30	46										
C30	67	-10	1.50	53										
C4	67	0	0.80	14										
C13	67	0	2.00	17										
C8	85	-20	0.30	13										
C17	85	-20	1.30	20										
C9	85	-10	0.34	19										
C18	85	-10	0.80	28										
C24	85	-10	0.90	41										
C25	85	-10	1.20	58										
Freezing Drizzle					Freezing Drizzle					Freezing Drizzle				
O2	76	-18	0.79	158	U13[†*]	40	5	0.22	24 (200)	522[†]	40	-5	0.72	16 (240)
O3	76	-18	1.08	221	U15[†*]	40	5	0.64	102 (131)	521[†]	40	-5	0.47	18 (225)
O4	76	-18	1.45	172	U19[*]	40	5	0.5	126	524[†]	40	-5	0.44	24 (166)
O5	76	-18	1.48	188	U18[†*]	60	5	0.43	102 (131)	525[†]	40	-5	0.38	34 (166)
O6	76	-18	1.66	152						537[†]	40	-5	0.36	61 (226)
O7	76	-18	1.65	128										
O8	76	-18	1.51	153										
Freezing Rain					Freezing Rain					Freezing Rain				
					TP10	50	-5	0.30	720					
					TP11	60	-5	0.25	720					
					TP7[†*]	60	3	0.33	534 (652)					
					TP8[†]	60	-5	0.33	534 (652)					

[†] Bimodal distribution, [*] For testing purposes the tunnel temperature was raised above the melting point.

Table A.1: Overview of the test points used for the investigation of the Nevzorov probe. The liquid water content (LWC) values stem from the internal tunnel calibrations. The median volume diameter (MVD) values were derived from Cloud Combination Probe (CCP) measurements at the Braunschweig Icing Wind Tunnel (BIWT) and the Collins IWT and from CAPS and Malvern measurements at Rail Tec Arsenal (RTA). For bimodal distributions, the diameter corresponding to the maximum of the large droplet mode is provided in brackets behind the MVD.
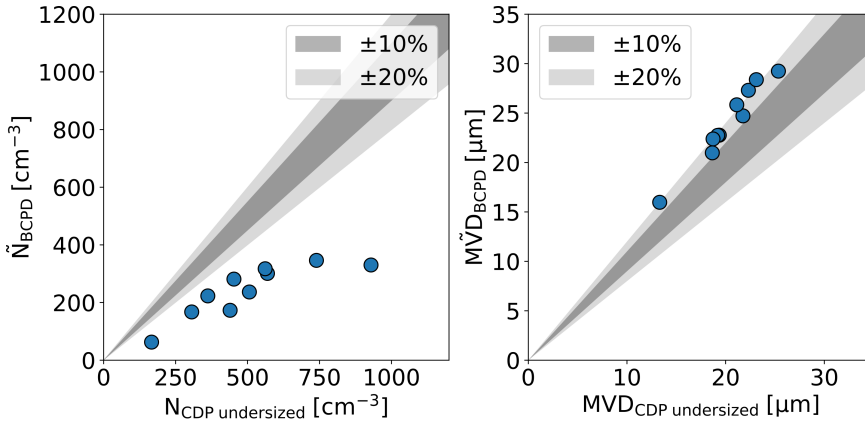
Figure A.1: Comparison of number concentrations (N) and median volume diameters (MVDs) computed from the BCPD and from CDP size distributions, to which the undersizing behavior of the BCPD was applied.

A.2. INVERSION PROCEDURE FOR THE BACKSCATTER CLOUD PROBE WITH POLARIZATION DETECTION

To investigate if the effect of the undersizing in the Backscatter Cloud Probe with Polarization Detection (BCPD) is significant, I apply matrix **A** to the Cloud Droplet Probe (CDP) measurement, which is assumed to be close to the true droplet size distribution (DSD). The resulting size distribution is designated as the «undersized CDP measurement». If the differences between CDP and BCPD were purely due to undersizing and the matrix **A** contained a perfect representation of the undersizing behavior of the BCPD, the measurements of the CDP and the BCPD should be the same. Consequently, all the remaining differences between CDP and BCPD cannot be explained by the undersizing behavior of the BCPD. The result can be seen in Fig. A.1.

There still exist very significant differences between the number concentrations of the BCPD and the CDP. Furthermore, the agreement between the MVDs of BCPD and CDP that was evident in Fig. 4.18b has worsened, the MVDs of the BCPD are now on average 18% higher than those computed from the CDP.

Fig. A.2 shows the number concentrations per bin, similar as in Fig. 4.19, but with the undersized CDP. The ratio between the number concentrations has improved, especially above a diameter of 15 μm the undersized CDP and BCPD agree closely.

A.3. DROPLET COINCIDENCE IN THE CLOUD DROPLET PROBE MEASUREMENTS

Droplet coincidence in the CDP was present for some of the high LWC test points. This was detected through an analysis of particle transit times, which increase if
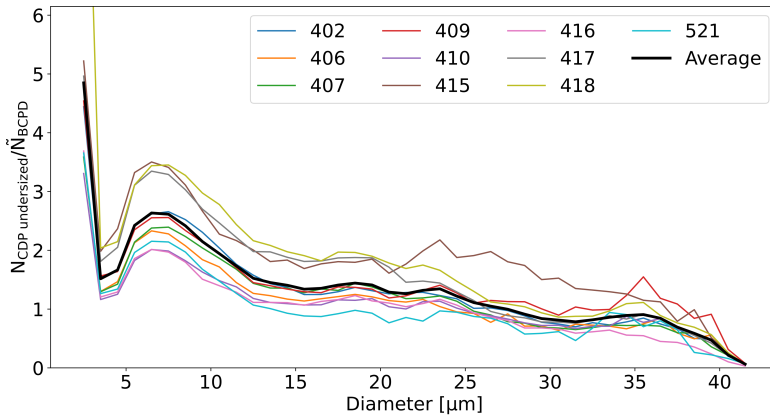
A

Figure A.2: Ratio between the number concentrations (N) per size bin of the undersized CDP and BCPD for all the test points in the BIWT.

coincidence is present [1]. Figure A.3 shows the average path length during which the CDP sizer was above the detection threshold, plotted versus the number concentration. The average path length is the average transit time multiplied by the airspeed. This was done in order to compare test points with different air speeds. Test points with larger MVDs produce longer average path lengths, which is to be expected simply due to the larger particle size. However, Fig. A.3 shows that longer average path lengths are also observed for test points with high number concentrations. Since I know that coincident droplets cause longer transit times, I deduce that coincidence occurred for these test points.
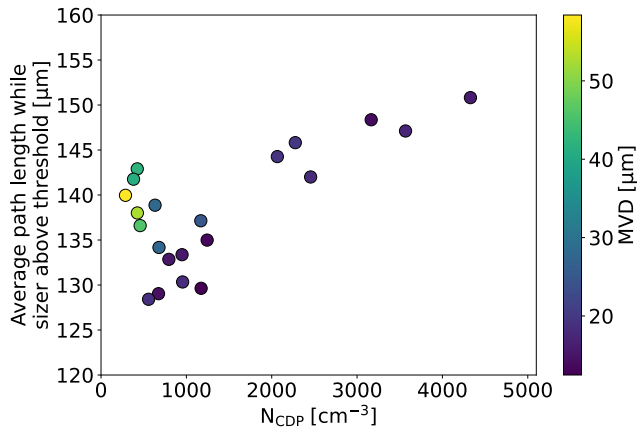

Figure A.3: Average path length while sizer above threshold plotted against the number concentration (N) for the small droplet spray test points measured at Collins. The average path length is a measure similar to the average transit time but multiplied by the airspeed in order to make test points with different airspeeds comparable.

A.4. Determination of dry air segments with the Nevzorov probe

Similar to the evaluation in icing wind tunnels (IWTs), also for the evaluation of the in-flight Nevzorov measurements information about the heat losses that are due to convection is required. These heat losses can be measured outside of clouds but, consequently, an algorithm is needed that determines the presence of a cloud/no cloud. Droplets cause spikes in the signal of the Nevzorov probe that was measured at a resolution of 100 Hz. Therefore, I investigated if it is possible to differentiate between clouds and dry air by the standard deviation of the Nevzorov measurements. At first, the maximum standard deviation that occurs in cloud-free air needs to be determined. As a case study, a flight from the MOSAiC ACA flight campaign [2] on 13th of September 2020 was chosen. The reason that this flight, and not one from the HALO-AC³ campaign, is used is that this technique was developed prior to the start of the HALO-AC³ campaign. I was not involved in the measurements of the campaign and only performed the data evaluation.

The Nevzorov sensor head used during the MOSAiC campaign did not have a 12 mm cone. This is not problematic, since the LWC sensor and the 8 mm cone are sufficient for the detection of dry air, because the only requirement is that particles impact the sensor.

Stretches where only dry air is present were selected based on the number concentration that was measured by the reference instruments. Only stretches where not a single particle was observed by the reference instruments over five seconds qualify as dry air. Subsequently, I plot histograms of the observed standard deviations of the Nevzorov signals during these stretches. The standard deviation is defined over a window of 200 measurements, which corresponds to a time of two seconds.

Figure A.4 shows that the standard deviation of the signals of the collector sensors only rarely exceeds 0.006 V. To demonstrate that dry and cloudy air are separable by the standard deviation, it is also necessary to verify the minimum standard deviation values that occur in cloudy air. I define stretches of cloudy air as periods of at least five seconds during which the number concentration exceeds 0.1 cm^{-3}. Fig. A.5 shows the observed standard deviations during these cloudy stretches. I observe that most of the standard deviations significantly exceed 0.006, however also a number of cases with standard deviations below 0.006 exist. From video data recorded with a GoPro, I discovered that most of the occurrences, during which the standard deviations of the Nevzorov sensors were low but a significant number concentration was detected, were in very patchy clouds. It is therefore possible that no particles impacted on the Nevzorov probe. Nonetheless, it does not seem to be sufficient to use a threshold of 0.006 V for the differentiation between dry and cloudy air, instead, I use a value of 0.004 V, which assures that all the values that fall into the bin with the highest number of points in all four plots of Fig. A.5 are classified as clouds.

To analyze how well the filtering works, I investigate the following:

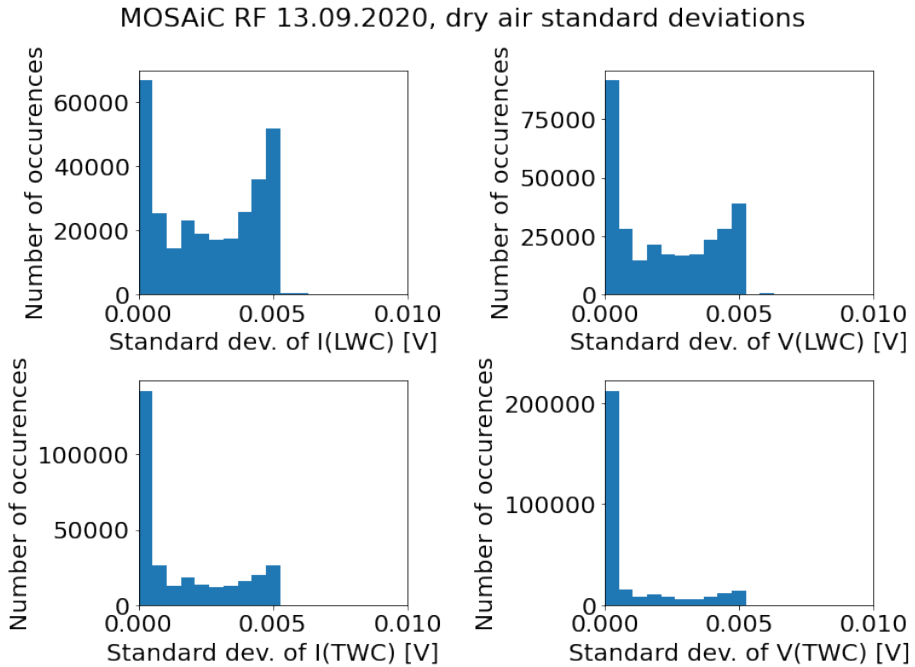- How often is no dry air detected but the TWC does not exceed 0.01 gm^{-3}?

Figure A.4: Histogram of the standard deviations of the current (I) and the voltage (V) measured by the Nevzorov LWC sensor (top row) and by the Nevzorov 8 mm cone (bottom row) during two-second intervals in dry air.

Such a scenario can indicate the presence of a very weak cloud but can also be due to very sudden changes in airspeed or fluctuations of the Nevzorov sensor head (Missed dry air detection).

- How often is dry air detected when the data from the optical probes shows a number concentration ≥ 1000 m^{-3}? What are the values of the number concentration (False positives of the dry air detection)?

The result can be seen in Fig. A.6. The probability that dry air is detected despite particles being present, i.e. the missed alarm probability, is 9.7%. The probability that, based on the standard deviations that were selected, air with an LWC below 0.01 gm^{-3}, i.e. essentially dry air, is not detected as such, is 34.6%. Both values appear high. However, the high false alarm probability does not represent a problem. Dry air needs to be detected to obtain data points from which the dry air term can be computed. This does not mean that every data point where dry air is present needs to be identified. Hundreds of thousands of data points with dry air at very similar pressures, temperatures and airspeeds were recorded. Detecting just some of them as dry air is sufficient.

The detection of dry air despite the presence of particles is more problematic, even though the probability is lower, but as mentioned before already, this is due
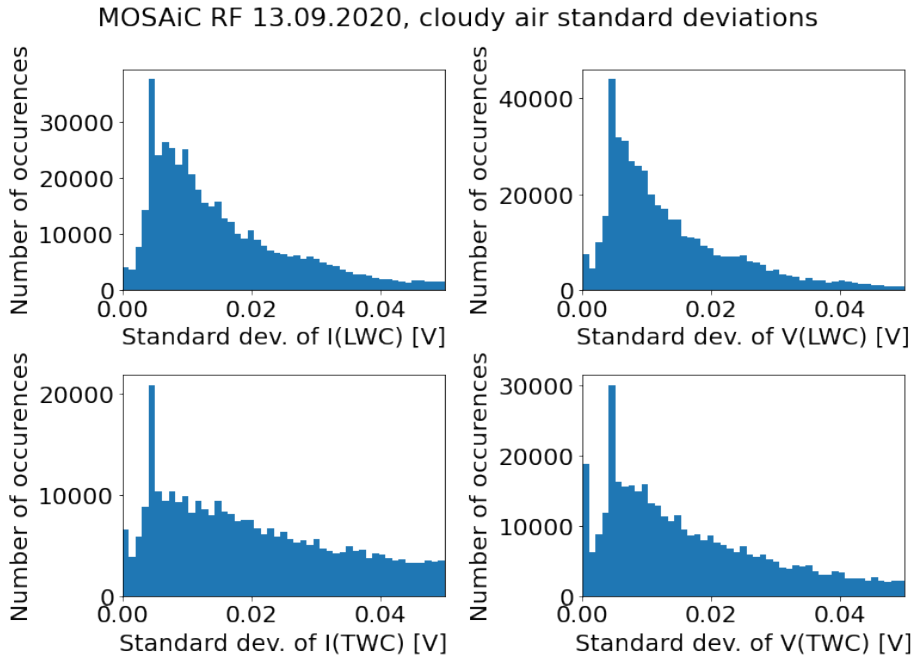
Figure A.5: Histogram of the standard deviations of the currents and voltages measured by the Nevzorov LWC sensor (top row) and the Nevzorov 8 mm cone (bottowm row) during two-second intervals in cloudy air.

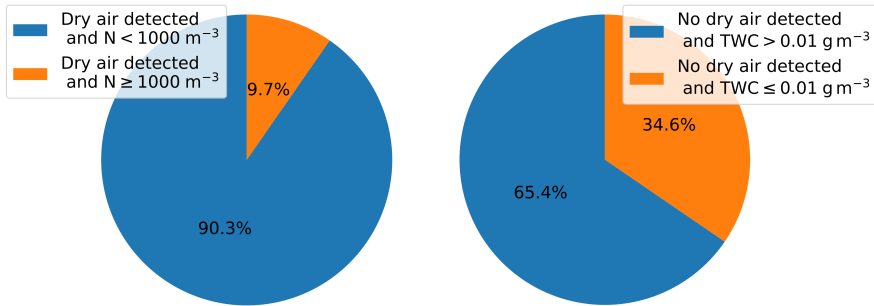to patchy clouds and I assume that at low standard deviations, no particles are impacting the Nevzorov sensors.

Figure A.6: Missed and false alarm probability of the dry air detection algorithm. The left plot shows the probability that dry air is detected when the number concentration is below (above) $1000 \ \mathrm{m}^{-3}$ in blue (orange). The right plot shows the probability that dry air is not detected when the total water content (TWC) of the 8 mm cone is larger (smaller) than $0.01 \ \mathrm{g \, m}^{-3}$ in blue (orange).
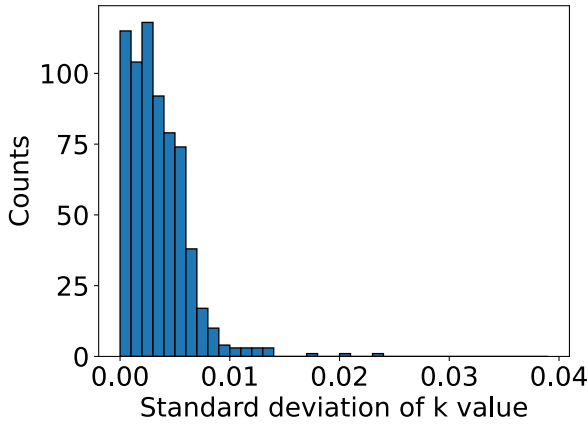
Figure A.7: Histogram of the standard deviation of the k values in the airspeed, pressure and temperature bins.

A.5. THRESHOLD SENSITIVITY OF THE NEVZOROV PROBE

The threshold sensitivity of the Nevzorov probe can be estimated from the standard deviation that is observed for the k values in the airspeed, pressure and temperature bins. A histogram of the standard deviation of the k values of the 8 mm TWC cone is shown in Fig. A.7. The standard deviation exceeds a value of 0.01 in only a few cases. Assuming that the k values in a bin are approximately Gaussian-distributed, the difference Δk between the estimated value $\hat{k}$ that is obtained from the binning procedure (see Section 5.5.2) and the correct value k will be smaller than 0.02 in 95% of the cases. Equation A.1 can be written as:

$$W = \frac{P_c - kP_r + \Delta kP_r}{\varepsilon L^* S_c U}. \tag{A.1}$$

In dry air, $P_c - kP_r = 0$, such that the uncertainty in the dry air measurement is:

$$\Delta W = \frac{\Delta kP_r}{\varepsilon L^* S_c U}. \tag{A.2}$$

Using $\Delta k = 0.02$ and typical values $L^* = 2700 \text{ Jg}^{-1}$, $P_r = 6$ W, $\varepsilon = 1$ and the sample area of the 8 mm cone for S_c, the threshold sensitivity of the Nevzorov 8 mm cone is obtained as 0.014 gm^{-3}. The sensitivity of the LWC sensor and the 12 mm cone is of a similar magnitude. In this work, to be on the safe side, a sensitivity of 0.025 gm^{-3} is assumed for the Nevzorov probe.

A.6. FLIGHT PATTERNS

Fig. A.8 shows some of the most common sampling patterns during research missions. The difference between racetrack patterns and staircase patterns is that racetrack patterns sample the same cloud at different altitudes, while during a staircase pattern the plane ascends along a straight line.
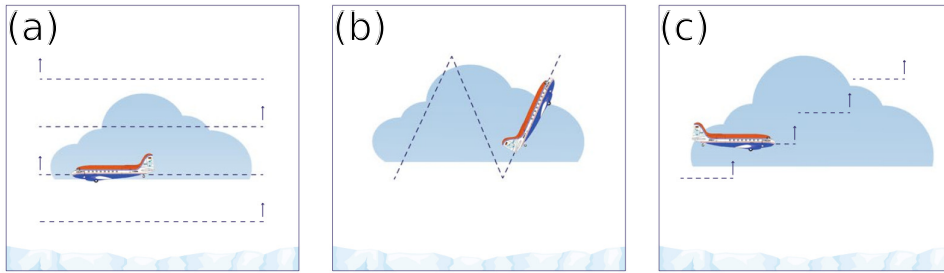
A.7. IDENTIFICATION OF ASPHERICAL PARTICLES IN MEASUREMENTS OF THE
BACKSCATTER CLOUD PROBE WITH POLARIZATION DETECTION   177

A

Figure A.8: Common flight patterns during research missions. (**a**): Racetrack pattern. **b**: Sawtooth pattern. **c**: Staircase pattern. Figure from Mech *et al.* [3].

A.7. IDENTIFICATION OF ASPHERICAL PARTICLES IN MEASUREMENTS OF THE BACKSCATTER CLOUD PROBE WITH POLARIZATION DETECTION

Chapter 5 discussed a technique for separating spherical and aspherical particles (which are assumed to represent liquid and ice particles respectively) in a bulk measurement of the BCPD. It is also mentioned that the presence of particles within a certain region can be used to unambiguously identify ice particles. This region is shown in Fig. A.9. The hatched area in the image is only the area where ice can be unambiguously identified. It is well possible that particles with diameters and δ values outside the area are also ice particles.
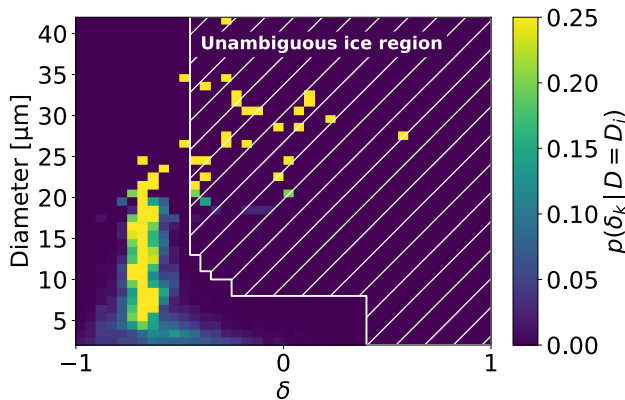

Figure A.9: Polarization ratio δ and particle diameter measured by the BCPD in a mixed phase cloud. The region where particles can unambiguously be identified as ice is hatched.
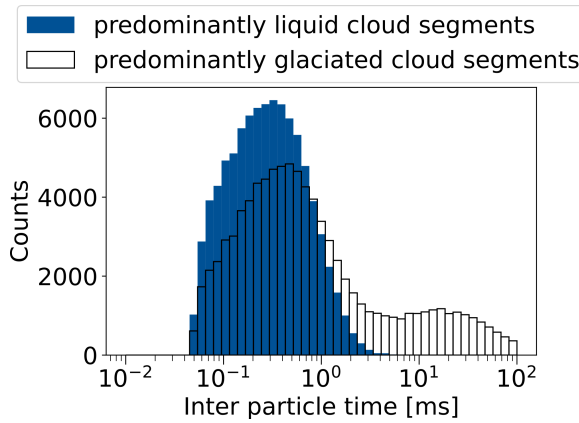
Figure A.10: IPTs for predominantly liquid and predominantly glaciated conditions. Predominantly liquid conditions were defined as those where the μ_l value from the Nevzorov probe was larger than 0.9.

A.8. INTER-PARTICLE TIMES IN GLACIATED CONDITIONS

Inter-particle times (IPTs) can be used for underwing probes to detect if a measurement is contaminated by ice particles that shatter on the arm of the instrument [4, 5]. IPTs are assumed to be approximately Poisson-distributed and the expected IPT depends on the number concentration. If shattering occurs, a second mode, with a mean that is significantly smaller than what would be expected from Poisson statistics, is observed in the IPT distribution. IPTs observed by the BCPD can be seen in Fig. A.10. Predominantly liquid and predominantly glaciated segments are distinguished. The lower mode is at approximately the same IPT for liquid and glaciated segments. This demonstrates that shattering for the BCPD cannot be distinguished with an IPT analysis, as the particles shatter significantly ahead of the BCPD sample volume and then disperse in all directions. The second mode, which is visible at larger IPTs for the glaciated segments, exits because segments with very low ice crystal number concentrations were measured.

A.9. IMAGES OF PARTICLES DURING APPENDIX O ENCOUNTERS FROM THE SENS4ICE CAMPAIGN

Section 6.4.3 analyses the detection of Appendix O conditions with the Icing Risk Assessment Algorithm. During the research flight on April 27, 2023, two longer segments with Appendix O conditions were observed from the reference measurements. The first encounter was approximately one minute long, from 14:14 - 14:15 UTC. The second encounter was approximately three minutes long, from 14:33 - 14:36 UTC. Images of the particles from the first encounter can be seen in Fig. A.11. SLDs but also ice crystals (marked in red) are present.

Images of the particles in the second encounter are depicted in Fig. A.12. Here, in contrary to Fig. A.11, no ice particles are visible.
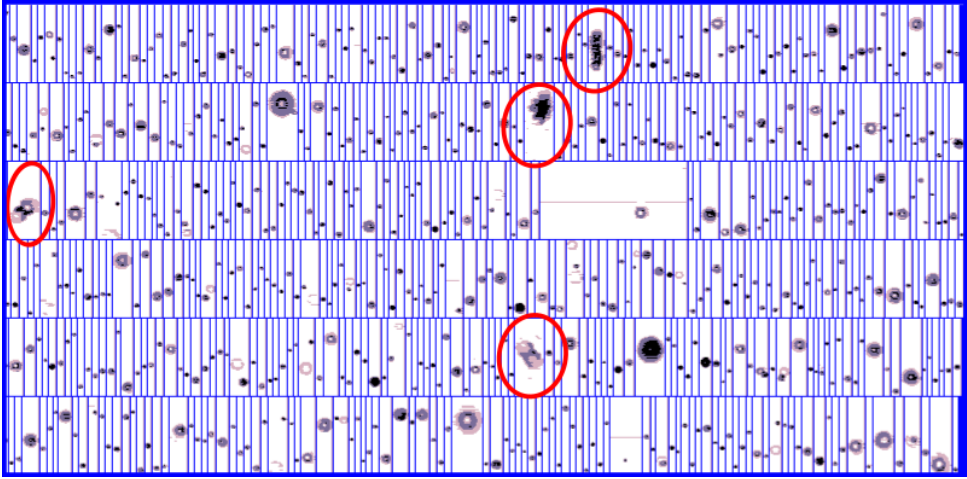
A

Figure A.11: Images of particles observed with the CIP during an Appendix O encounter on April 27, 2023 from 14:14-14:15 UTC. Ice crystals are marked in red.
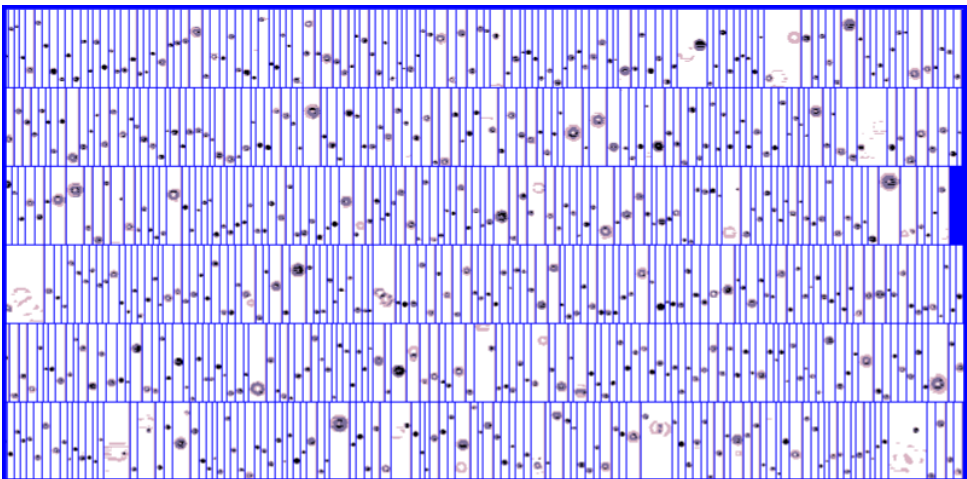

Figure A.12: Images of particles observed with the CIP during an Appendix O encounter on April 27, 2023 from 14:33-14:36 UTC.

A

REFERENCES

[1] S. Lance, *Coincidence Errors in a Cloud Droplet Probe (CDP) and a Cloud and Aerosol Spectrometer (CAS), and the Improved Performance of a Modified CDP*, Journal of Atmospheric and Oceanic Technology **29**, 1532 (2012).

[2] M. Moser, C. Voigt, T. Jurkat-Witschas, V. Hahn, G. Mioche, O. Jourdan, R. Dupuy, C. Gourbeyre, A. Schwarzenboeck, J. Lucke, Y. Boose, M. Mech, S. Borrmann, A. Ehrlich, A. Herber, C. Lüpkes, and M. Wendisch, *Microphysical and thermodynamic phase analyses of Arctic low-level clouds measured above the sea ice and the open ocean in spring and summer*, Atmospheric Chemistry and Physics **23**, 7257 (2023).

[3] M. Mech, A. Ehrlich, A. Herber, C. Lüpkes, M. Wendisch, S. Becker, Y. Boose, D. Chechin, S. Crewell, R. Dupuy, C. Gourbeyre, J. Hartmann, E. Jäkel, O. Jourdan, L.-L. Kliesch, M. Klingebiel, B. S. Kulla, G. Mioche, M. Moser, N. Risse, E. Ruiz-Donoso, M. Schäfer, J. Stapf, and C. Voigt, *MOSAiC-ACA and AFLUX - arctic airborne campaigns characterizing the exit area of MOSAiC*, Scientific Data **9**, 10.1038/s41597-022-01900-7 (2022).

[4] P. R. Field, A. J. Heymsfield, and A. Bansemer, *Shattering and Particle Interarrival Times Measured by Optical Array Probes in Ice Clouds*, Journal of Atmospheric and Oceanic Technology **23**, 1357 (2006).

[5] A. Korolev and P. R. Field, *Assessment of the performance of the inter-arrival time algorithm to identify ice shattering artifacts in cloud particle probe measurements*, Atmospheric Measurement Techniques **8**, 761 (2015).

LIST OF ABBREVIATIONS

2D-S 2D-Stereo Probe

ADC analog to digital converter

BCP Backscatter Cloud Probe

BCPD Backscatter Cloud Probe with Polarization Detection

BIWT Braunschweig Icing Wind Tunnel

CAPS Cloud Aerosol and Precipitation Spectrometer

CAS Cloud Aerosol Spectrometer

CAS-DPOL Cloud Aerosol Spectrometer with Depolarization Option

CC collision-coalescence

CCN cloud condensation nucleus

CCP Cloud Combination Probe

CDP Cloud Droplet Probe

CIP Cloud Imaging Probe

DLR Deutsches Zentrum für Luft- und Raumfahrt

D_{max} maximum drop diameter

DMT Droplet Measurement Techniques

DSD droplet size distribution

DWD Deutscher Wetterdienst

FCDP Fast Cloud Droplet Probe

FSSP Forward Scattering Spectrometer Probe

FZDZ freezing drizzle

FZRA freezing rain

IAGOS In-service Aircraft for a Global Observing System

ICD Ice Crystal Detector

IKP Isokinetic Probe

INP ice nucleating particle

IPT inter-particle time

IWC ice water content

IWT icing wind tunnel

LWC liquid water content

LYR Longyearbyen Airport

MVD median volume diameter

OAP optical array probe

PCD particle count distribution

PIP Precipitation Imaging Probe

PSD particle size distribution

RTA Rail Tec Arsenal

SAFIRE the French facility for airborne research

SDS small droplet spray

SENS4ICE SENSors and certifiable hybrid architectures for safer aviation in ICing Environment

SLD supercooled large droplet

TWC total water content

UAV unmanned aerial vehicle

UHSAS Ultra-High Sensitivity Aerosol Spectrometer

WP Waypoint

Curriculum Vitæ

Johannes Reinhard Lucke

13.04.1993   Born in Berlin-Kreuzberg, Germany.

Education

2012–2016   **Bachelor of Science**
Engineering Science
Technische Universität München

2016–2019   **Master of Science**
Earth Oriented Space Science and Technology (ESPACE)
Technische Universität München

2019–2024   **Doctoral student**
Detection and Differentiation of Supercooled Large Droplet Icing Conditions
Faculty of Aerospace Engineering
Delft University of Technology
&
Institute for Atmospheric Physics
German Aerospace Center

LIST OF PUBLICATIONS

1. **J. Lucke**, T. Jurkat-Witschas, R. Heller, V. Hahn, M. Hamman, W. Breitfuss, V. R. Bora, M. Moser, C. Voigt, *Icing wind tunnel measurements of supercooled large droplets using the 12 mm total water content cone of the Nevzorov probe*, Atmospheric Measurement Techniques, Vol. 15, No. 24, p. 7375-7394 (2022).

2. **J. Lucke**, T. Jurkat-Witschas, D. Baumgardner, F. Kalinka, M. Moser, E. De La Torre Castro, C. Voigt, *Characterization of Atmospheric Icing Conditions during the HALO-(AC)³ Campaign with the Nevzorov Probe and the Backscatter Cloud Probe with Polarization Detection*, SAE Technical Paper Series (2023).

3. B. M. Esposito, D. Orchard, **J. Lucke**, L. Nichman, N. Bliankinshtein, L. Lilie, P. Catalano, F. D'Aniello, J. W. Strapp, *Comparability of Hot-Wire Estimates of Liquid Water Content in SLD Conditions* SAE Technical Paper Series (2023).

4. E. de la Torre Castro, T. Jurkat-Witschas, A. Afchine, V. Grewe, V. Hahn, S. Kirschler, M. Krämer, **J. Lucke**, N. Spelten, H. Wernli and others, *Differences in microphysical properties of cirrus at high and mid-latitudes*, EGUsphere , Vol. 2023 p. 1-34 (2023).

5. M. Moser, C. Voigt, T. Jurkat-Witschas, V. Hahn, G. Mioche, O. Jourdan, R. Dupuy, C. Gourbeyre, A. Schwarzenboeck, **J. Lucke**, Y. Boose, M. Mech, S. Borrmann, A. Ehrlich, A. Herber, C. Lüpkes, M. Wendisch, *Microphysical and thermodynamic phase analyses of Arctic low-level clouds measured above the sea ice and the open ocean in spring and summer*, Atmospheric Chemistry and Physics, Vol. 23, No. 13, p. 7257-7280 (2023).